Flows induced by the settling and phase change of particles: iron rain and iron snow in planetary interiors

Quentin Kriaa

Aix*Marseille université
Socialement engagée

NNT : 2023AIXM0303

THÈSE DE DOCTORAT

Soutenue à Aix-Marseille Université
le 19 septembre 2023 par

Quentin KRIAA

Ecoulements induits par la sédimentation et le changement de phase de particules : pluie et neige de fer dans les intérieurs planétaires

Discipline
Sciences pour l'ingénieur

Spécialité
Mécanique et physique des fluides

École doctorale
ED 353 Sciences pour l'ingénieur : mécanique, physique, micro et nanoélectronique

Laboratoire
IRPHE

Partenaires de recherche
CNRS

Composition du jury

Philippe CLAUDIN DR CNRS, ESPCI, Paris	Rapporteur
Romain MONCHAUX Professeur, ENSTA, Paris	Rapporteur
Anne DAVAILLE DR CNRS, FAST, Orsay	Examinatrice
Jerome NEUFELD Professeur, DAMTP, University of Cambridge UK	Examinateur
Jacques MAGNAUDET DR CNRS, IMFT, Toulouse	Président du jury
Michael LE BARS DR CNRS, IRPHE, Marseille	Directeur de thèse
Benjamin FAVIER CR CNRS, IRPHE, Marseille	Co-directeur de thèse

irphé
Institut de Recherche sur les Phénomènes Hors Equilibre

cnrs

A mes anciens professeurs
qui m'ont tant inspiré

Affidavit

I, undersigned, Quentin Kriaa, hereby declare that the work presented in this manuscript is my own work, carried out under the scientific supervision of Michael Le Bars and Benjamin Favier, in accordance with the principles of honesty, integrity and responsibility inherent to the research mission. The research work and the writing of this manuscript have been carried out in compliance with both the french national charter for Research Integrity and the Aix-Marseille University charter on the fight against plagiarism.

This work has not been submitted previously either in this country or in another country in the same or in a similar version to any other examination body.

Marseille, June the 11th 2023

Liste de publications et participation aux conférences

Liste des publications réalisées dans le cadre du projet de thèse

1. Kriaa, Q., Subra, E., Favier, B., & Le Bars, M. (2022). Effects of particle size and background rotation on the settling of particle clouds. Physical Review Fluids, 7(12), 124302.
2. Kriaa, Q., Favier, B., & Le Bars, M. (2023). Two-way coupling Eulerian numerical simulations of particle clouds settling in a quiescent fluid. Physical Review Fluids, *accepted*

Participation aux conférences et écoles d'été au cours de la période de thèse

1. Summer school 'Fluid Dynamics of Sustainability and the Environment' (online with DAMTP, Cambridge, UK), Septembre 2021
2. Conférence 'GDR Navier-Stokes 2.00' (Saclay), Octobre 2021
3. Workshop GreZuMarOb (Zürich, Suisse), Novembre 2021
4. Conférence 'Rencontres du Non Linéaire' 2022 (Paris), Avril 2022
5. Workshop Copermix 'Fundamentals of mixing: a unified framework for mixing dynamics' (Marseille), Avril 2022
6. Conférence IUTAM 'Particles, Drops and Bubbles in Stratified Environments' (IMFT, Toulouse), Juillet 2022
7. Conférence 'Festival de théorie: Chaos Control, Feedback & Model Reduction' (Aix-Marseille Université), Juillet 2022
8. Workshop 'Particles in turbulence' (Marseille), Juillet 2022
9. Conference IUTAM 'From Stokesian suspension dynamics to particulate flows in turbulence' (IMFT, Toulouse), Août 2022
10. Séminaire invité, Institut de Physique du Globe de Paris, Septembre 2022
11. Conférence of the Royal Astronomical Society: Specialist Discussion on 'Solid-Liquid Interactions in Deep Planetary Interiors' (online with London UK), Octobre 2022
12. American Physical Society, Division of Fluid Dynamics 2022 (Indianapolis, USA), Novembre 2022
13. Séminaire invité, Université de Twente, Enschede, Pays-Bas, Avril 2023
14. Summerschool 'Fluid mechanics of planets and stars' (CISM, Udine, Italie), Avril 2023
15. Workshop GreZuMarOb (Marseille), Mai 2023
16. Séminaire invité, ETH Zürich, Zürich, Suisse, Mai 2023
17. Séminaire invité, LadHyX, Paris, Juin 2023
18. Geophysical Fluid Dynamics Program 2023 of the Woods Hole Oceanographic Institution, Woods Hole Massachusetts, USA, Juin-Août 2023

Résumé

La présente étude s'intéresse aux écoulements que génèrent elles-mêmes des précipitations, i.e. des écoulements qui émergent suite à la sédimentation de particules denses solides (flocons) ou liquides (gouttes), inertes ou réactives (changement de phase). Cette thèse est spécifiquement motivée par deux phénomènes géophysiques.

Lors de sa formation il y a 4,5 milliards d'années, la Terre a subi des impacts violents avec d'autres planètes telluriques. Lorsqu'ils étaient assez grands, ces impacteurs ont fait fondre le manteau terrestre en un océan de magma. Leur noyau de métal liquide a alors été projeté dans cet océan et a éclaté en gouttelettes, conduisant à la chute d'un nuage de gouttes de métal liquide qui a longtemps été modélisée comme une *pluie de fer*.

Aujourd'hui même, le lent refroidissement de Ganymède – un satellite naturel de Jupiter – conduirait à la solidification de son noyau métallique depuis la périphérie. Il en résulterait la formation de flocons solides de fer pur, plus denses que le métal liquide, qui chutent donc par gravité comme une *neige de fer*. Mais ces cristaux refondent en profondeur à cause des hautes températures. La neige fondue poursuit alors sa chute vers le centre de Ganymède, nourrissant une convection compositionnelle vraisemblablement à l'origine d'une dynamo.

Dès le départ de cette thèse, la flottabilité était identifiée comme principal moteur de ces écoulements, et la nature particulaire du forçage comme ingrédient central de leur complexité. Faisant fi des détails morphologiques des flocons, et de la dynamique de fragmentation et coalescence des gouttes, cette étude démarre au chapitre 1 par l'analyse expérimentale du couplage entre un fluide immobile et des nuages de particules sédimentant collectivement en son sein. Le choix de l'écoulement canonique de thermique turbulent a révélé les spécificités induites par la nature particulaire du forçage : un découplage gravitaire entre la turbulence et les particules, et un taux de croissance accru des nuages, présentant un maximum pour une taille précise des particules. Au-delà des interprétations fondées sur la phénoménologie classique des écoulements turbulents chargés en particules, les simulations eulériennes en two-way coupling du chapitre 2 révèlent que la turbulence n'est pas essentielle à l'optimum de croissance des nuages. Des simulations laminaires reproduisent en effet nos observations, qui sont dues à la déformation de la structure interne du nuage, dont la circulation est diminuée par la dérive gravitaire des particules, augmentant ainsi la capacité d'entraînement du nuage à grande échelle. Les expériences du premier chapitre ont également été menées avec une rotation de fond comme modèle de rotation planétaire. Celle-ci interrompt la croissance des nuages lorsque la force de Coriolis devient comparable à leur inertie : ils s'enroulent alors en colonnes tourbillonnaires. Le chapitre 3 révèle que cette dynamique réduit la dilution des nuages, atténuant l'efficacité d'équilibrage chimique entre gouttes de métal et océan de magma suite à un impact planétaire, d'autant plus que la planète tourne rapidement et que les éléments chimiques en jeu sont sidérophiles.

Le 4e chapitre ajoute alors le changement de phase : en tamisant continûment des grains de sucre au-dessus d'une cuve d'eau, leur dissolution assure la formation d'eau sucrée qui plonge en profondeur par flottabilité, fournissant un analogue de la neige de fer fondue. La microphysique de la suspension de grains contrôle une richesse de comportements, s'étendant du panache turbulent à la lente émergence d'un écoulement laminaire à grande échelle, dû aux forçages cumulés des sillages de grains. En guise d'ouverture, sont abordées dans le chapitre 5 les implications de ces expériences sur la transition sédimentation-convection et sur le forçage possible d'une dynamo par neige de fer.

Mots clés: Ecoulements diphasiques, sédimentation de particules, changement de phase, dissolution, fluides tournants, noyaux planétaires, accrétion

Abstract

The present study focuses on flows that are generated by precipitations, i.e. that emerge following the settling of dense particles, whether they be solid (snow flakes) or liquid (drops), inert or reactive (due to phase change). This thesis is specifically motivated by two geophysical phenomena. 4,5 billion years ago, during its formation, the Earth experienced violent impacts with other rocky planets. When sufficiently large, those impactors released enough energy to melt the rocky mantle of the Earth and form a magma ocean. As their metal core was thrown in this ocean, it shattered intro drops, leading to the fall of a cloud of liquid metal drops that has long been modelled as an "iron rain".

Presently, the secular cooling of Ganymede – a natural satellite of Jupiter – is likely responsible for the solidification of its metal core from the periphery inward. This would lead to the formation of solid iron snow flakes that are denser than the ambient liquid metal, hence that would fall like an "iron snow" due to gravity. But if these crystals reach excessive temperatures, they remelt. The resulting molten iron snow keeps sinking downward, nourishing a compositional convection that likely feeds a planetary dynamo.

Since the start of this PhD, it was identified that buoyancy is the main force driving those geophysical flows, and that the particulate nature of the buoyancy forcing is a key ingredient of their complexity. Disregarding morphological details about the snow flakes, as well as the specific dynamics of fragmentation-coalescence of drops, this study begins in chapter 2 with an experimental analysis of the coupling between a still fluid and a cloud of particles that settle collectively in this fluid. Comparing particle clouds with the canonical turbulent thermal reveals the specificities induced by the particulate nature of the buoyant material : a gravitational decoupling of the particles from the turbulence they initially generate, and an enhanced growth rate of the clouds that is maximum for a specific particle size.

Going beyond classical interpretations based on the well-known phenomenology of particle-laden turbulent flows, the 3D two-way coupled Eulerian simulations of Chapter 2 show that turbulence is not essential to the optimum growth of particle clouds. Indeed, laminar simulations recover our observations, which are due to the disruption of the cloud inner structure, whose circulation is weakened by the particles' gravitational drift, therefore enhancing the cloud growth. To model planetary rotation, the experiments of the first chapter were also performed on a spin table to include background rotation. The latter interrupts the growth of clouds when the Coriolis force becomes commensurate with their inertia: the clouds then roll up as vortical columns. Chapter 3 reveals that this dynamics reduces the clouds' dilution, diminishing the chemical equilibration efficiency between metal drops and a magma ocean, all the more as the planet rotates faster and as the chemical elements involved in the mass transfers are more siderophilic.

The 4th chapter adds a new ingredient: phase change. As sugar grains are continuously sieved above a water tank, their dissolution leads to the formation of sugary water that sinks down the tank due to its negative buoyancy, mimicking the behaviour of the molten iron snow. The microphysics of the suspension of sugar grains controls a wealth of behaviours, ranging from lazy turbulent plumes to the slow onset of a laminar large-scale flow, due to the cumulative forcing by successive wakes of large sugar grains. Some implications of these experiments are finally discussed in Chapter 5 on the transition from settling iron snow to compositional convection, considering the possibility of an iron-snow-driven dynamo in the core of small rocky planets.

Key words: Two-phase flows, particle settling, phase change, dissolution, rotating fluids, planetary cores, accretion

Remerciements

Je tiens à remercier l'ensemble des membres de mon jury pour l'intérêt dont ils ont fait preuve en acceptant d'évaluer mon travail, pour le temps qu'ils ont investi dans la lecture du présent manuscrit, pour leurs retours enthousiastes et leurs questions coriaces ! Nos échanges me laissent un souvenir enjoué de ma soutenance de thèse !

***

Je veux adresser un immense merci à William, Eric, Adrien, Léo et Mathieu pour leur aide technique. Travailler avec des gens aussi réactifs, à l'écoute et serviables a été un vrai plaisir ! Je vous suis reconnaissant et j'espère que les divers visuels présentés lors de ma soutenance ont fait honneur à votre travail – petite dédicace à Eric pour les porte-filtres imprimés 3D qui m'ont permis de faire de chouettes mesures et d'avoir de superbes images !

Merci à Sandra et Saida d'avoir été si aidantes, toujours prêtes à rendre service quand j'étais dans le besoin, et de m'avoir aidé notamment à organiser le pot ! Merci Frédéric d'être toujours si avenant et d'une aide rapide et efficace, en particulier lors des préparatifs de thèse tandis que mon ordinateur décidait de rendre l'âme 4 jours avant ma soutenance...

Pour avoir été un bénéficiaire privilégié de l'administration, j'exprime toute ma gratitude à Mikael, Cathy, Ulysse et Julie grâce à qui j'ai pu faire tant de missions à droite et à gauche. Je suis reconnaissant de tout le travail que vous avez fait pour moi, toujours au plus vite et parfois en un clin d'œil même quand j'abusais de votre gentillesse – et je m'en excuse – en vous donnant mes ordres de missions 3-4 jours avant déplacement... Merci infiniment de votre patience, votre indulgence et votre efficacité permanente.

***

J'adresse maintenant mes remerciements à deux collaborateurs que je suis chanceux d'avoir eu durant ma thèse.

Ludovic, travailler avec toi est tellement enrichissant ! Je regrette que notre temps commun à l'IRPHE ait été ma première année de thèse plutôt que les suivantes, car faute de maturité je n'ai pas su profiter de l'étendue de tes connaissances et ton expertise expérimentale. Chaque discussion que j'ai avec toi illumine des sentiers dont je n'avais parfois même pas connaissance. Je considère vraiment comme une chance de pouvoir travailler avec toi, et je te suis reconnaissant de tout le temps et de toute l'aide que tu as pu m'accorder.

J'adresse aussi mes remerciements à Maylis Landeau. J'ai une chance folle de t'avoir rencontrée au DAMTP à Cambridge. Merci de ta patience, tes conseils et pour tout ce que tu m'as transmis de ta passion pour ta recherche, de ta rigueur, de tes connaissances en géophysiques, de

ton expertise en tant qu'expérimentatrice. Pour chacune de nos interactions dont j'ai toujours hâte, merci beaucoup.

***

Michael, Benjamin, j'ai adoré ma thèse avec vous.

Merci pour votre temps, pour l'étendue de ce que vous m'avez transmis, et pour la qualité de votre transmission.

A me pousser à m'ouvrir à toute science, à tout sous-domaine de la physique, à aller à tout séminaire, à me soutenir à l'heure de chercher dans tous les coins possibles les analogies existantes. Cette ouverture et cette diversité sont quelque chose qui me tenait à cœur déjà avant ma thèse, qui me paraissait absolument nécessaire ; mais mon expérience à Woods Hole a rendu manifeste combien, en la matière, j'ai eu une chance formidable de bénéficier de votre symbiose, du foisonnement de science que vous faites fructifier et dont vous partagez les fruits à travers la dynamique de toute l'équipe. Merci mille fois – en mon nom et j'espère au nom de toute l'équipe – de nous fédérer, de cultiver une dynamique qui est une vraie source de richesse, qui est porteuse, qui donne une identité et une référence vers laquelle se tourner en cas de besoin. – Patrice Le Gal, Patrice Meunier et Stéphane, merci également !

J'ai beaucoup d'estime pour vous. Je suis sincèrement fier d'avoir travaillé avec vous, et je me sais extrêmement chanceux. Merci à vous deux de m'avoir fait confiance et de m'avoir donné de superbes opportunités de conduire une recherche exaltante durant 3 ans. Merci d'être présents dans les moments difficiles, de m'avoir tous les deux appris à prendre du recul, à comprendre les enjeux souvent cachés et les règles parfois ambiguës du jeu de la recherche.

Benjamin, merci d'être si généreux et pédagogue à l'heure de transmettre ton savoir. C'est terrible car tu donnes tellement de ton temps que trouver un créneau de libre pour discuter avec toi devient l'objet de manigances en messes basses dans les couloirs – et en même temps, quand on se retrouve enfin face à toi, on en deviendrait à son tour égoïste tellement le flot de tes connaissances est intarissable, mais aussi du fait, évidemment, de ton immense pédagogie, de ta positivité et ton entrain constants, de ton foisonnement d'idées et de ta curiosité permanente que tu transmets immanquablement. Discuter science avec toi n'est jamais assez long car c'est toujours une joie.

Michael, au-delà du recrutement, merci de ton immense confiance que tu m'as accordée tôt dans la conduite de mes travaux, dans les responsabilités que tu m'as données comme l'encadrement de stages, les opportunités de papier, de collaboration, de vulgarisation, de conférences innombrables où tu m'as envoyé vagabonder pour présenter mes travaux aux quatre vents. Michael, merci de ne pas t'être satisfait de ce que je peux faire, de m'avoir toujours poussé plus, en t'investissant toi-même en retour. Merci, car je pense que l'avancée de ma thèse doit beaucoup à ton exigence. Et malgré ces petits coups de pieds, j'ai toujours eu l'impression d'être dans un donnant-donnant, de travailler comme en duo, comme si en demandant plus tu t'investissais toi-même plus en retour, et était ainsi toujours présent, attentif, réactif, disponible, en faisant honneur à ton engagement de directeur.

Votre confiance a été extrêmement valorisante, et j'espère qu'à mon tour, si je suis amené à encadrer, je saurai être à la hauteur de votre exemple.

Le temps que vous m'avez accordé, et les sacrifices que vous avez pu être amenés à faire, je vous en suis infiniment reconnaissant. Je crois que votre manière de former m'a vraiment réussi

– en tout cas elle m'a vraiment plu. Il y a des hauts et des bas dans une thèse – la fin avant Woods Hole était particulièrement cauchemardesque – mais tout cela reste très superficiel et anecdotique quand je pense au fond. Vous avez restauré ce sentiment, que j'avais perdu depuis des années, d'excitation à l'idée de venir si tôt et de partir si tard pour faire de la science qui soit jouissive et exaltante. Cela faisait longtemps que je n'étais pas vraiment heureux dans mes études, mais ces trois années de thèse, j'ai vraiment été heureux. Et de ça, vous deux portez une belle part de la responsabilité. Merci beaucoup.

***

L'autre part de cette reponsabilité est portée par les doctorants et post-doctorants avec qui j'ai passé tant de temps. Ce n'est pas juste parce que je fais de la science intéressante que ça me plaît de passer tant de temps au labo, loin de là. Toute ma thèse a été fortement conditionnée par la joie que j'avais de venir au quotidien qui était, avant toute chose, due au plaisir de retrouver le groupe de doctorants. Cela faisait des années que je n'avais pas été aussi heureux au sein d'un groupe. A chacun je témoigne ma gratitude et mon affection : Daphné, Romain, Keshav, Amelie, Fabien, Pierre, Remi, Tommaso, Raul, Lucas Rotily, Marc, Nihal, Florian, Djihane, Selim, Elliot, Roman, Joris, Antoine, Lucas Gey, Valentin, Hugo, Louise, Omar, Eric, Marine, Aurore, et pardon si j'en oublie : je vous remercie collectivement pour votre sympathie, votre ouverture d'esprit, votre indulgence, votre soutien et votre amitié – et j'adjoins mes amis venus de loin, ainsi que ma famille, qui se sont fait un devoir de venir assister a ma soutenance. Merci de votre présence inflexible !

Contents

Introduction

The present work is a journey in a tiny yet fascinating fraction of the world of particle-laden flows. It revolves around the behaviour of a collection of melting-or-dissolving particles that settle in a fluid, to try to understand the coupled dynamics of the emerging fluid motions and of the particles themselves. As a typical example: some grains of sugar that are dropped in water. Despite the apparent banality of this everyday-life situation, this problem proves of fantastic wealth for the physicist, and an exciting analog to study precipitation-driven flows like rain and snow in the atmosphere... and even in planetary cores !

When considering particle-laden flows, a first complexity comes from the difficulty to accurately model the physics of the interaction between a flow and the particles it contains. This explains persistent challenges even to model systems where the particles are considered of negligible influence on the flow, like the dispersion of pollutants (figure 1a) or spray (figure 1b) in the atmosphere. The size, shape, isotropy, density, surface roughness, porosity of particles are some of many parameters that affect their evolution at the individual scale. As an example, the porosity of marine aggregates (figure 1c) enables them to retain some of the fluid that surrounds them while settling. This would partly explain why they decelerate when reaching the density jump of the 'pycnocline' in the ocean, due to the need for this retained lighter fluid to be renewed by diffusion before sedimentation can resume (Prairie et al., 2015; Magnaudet and Mercier, 2020).

Another inherent complexity of particle-laden flows arises when the influence of particles on the fluid is taken into account, because then particles can interact hydrodynamically. Even for suspensions of particles that evolve with negligible inertia in a Stokes flow, the long-range interactions of particles cannot be described by a simple pairwise summation (Guazzelli and Hinch, 2011). When particles have more inertia, the flow around them loses its fore-aft Stokes-flow symmetry, adding complexity to the microstructure of the suspension (Guazzelli and Morris, 2011) i.e., to the relative arrangement of neighbouring particles at the particle scale. The additional ingredient of gravity brings in sedimentation that is unfortunately coupled to the particles' inertia in experiments, unless gravity is compensated by an opposing acceleration of the experiment, or thanks to external forces like magnetism. Sedimentation biases the motion of the particles along the direction of gravity, resulting in a more complex microstructure that becomes anisotropic (Climent and Magnaudet, 1999).

These elements mean that the flow at the particle scale can have an impact on the whole suspension, with paramount consequences for supra-particle-scale flows. In this thesis, we are interested in particle clouds or suspensions that settle, meaning particles drift downward within the fluid. As they do so, each particle drags some fluid in its vicinity. Depending on the interparticle distance, the wakes of dragged fluid might be too far to influence one another (if

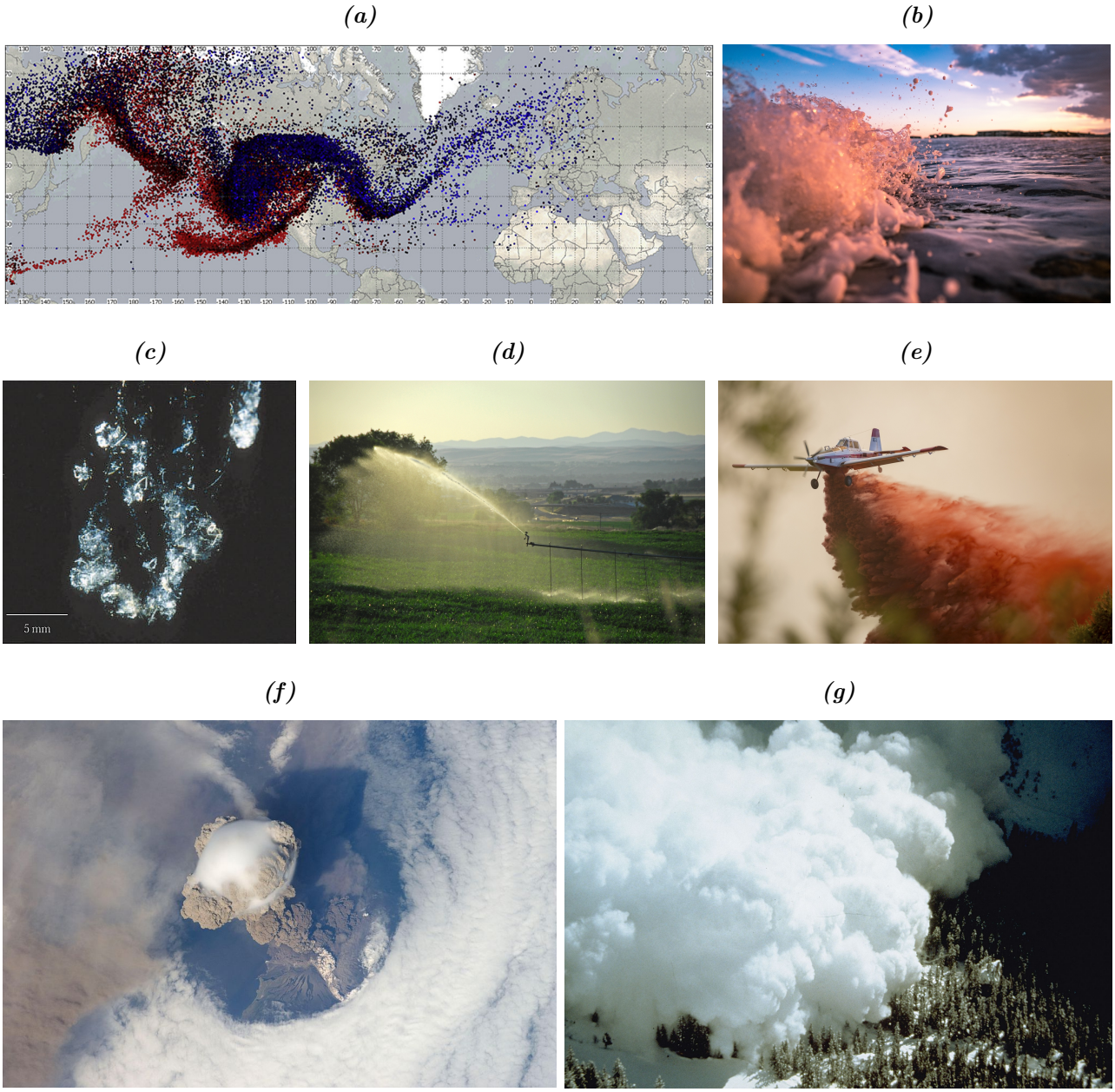

Figure 1: *(a) Dispersion of radioactive particles in the atmosphere eight days after the Fukushima nuclear accident (extracted from fig. 1 in Lujanienė et al. (2012)). (b) Formation of spray due to breaking waves (Bradley Beach, United States, public domain). (c) In situ micrograph of marine snow aggregates (from figure 2 in Kiørboe (2001)). (d) Dispersion and fall of drops produced by a sprinkler (Kirsten Strough, public domain). (e) Drop of flame retardant by an air tanker (The Pioneer Fire, Boise National Forest, Idaho, 2016, public domain). (f) Volcanic plume of the Sarychev Peak erupting on the Matua Island on June 12th (NASA, public domain, via Wikimedia Commons). (g) Avalanche (Irstea, CC BY-SA 4.0, via Wikimedia Commons).*

particles are extremely distant) or conversely combine and therefore lead to the formation of flow structures that are larger than the particle scale (Monchaux and Dejoan, 2017). It means the microstructure of the suspension/cloud plays a decisive role in driving a flow at a micro-to-macro scale, with a multiplicity of length scales and timescales – an observation that is central to the present work and that will be discussed in Chapter 4. Many examples of macroscopic sedimentation-driven flows can be found in the literature, like the settling drops of a sprinkler (figure 1d) or the flame retardant dropped by an air tanker (figure 1e), turbidity currents (Ouillon et al., 2019), volcanic clouds (Carazzo and Jellinek, 2012) (figure 1f), bubble curtains, landslides (Fritz et al., 2009) or avalanches (figure 1g). The variety of scales between large flow structures and individual particles is especially challenging in atmospheric, oceanographic and geophysical flows due to the orders of magnitude that separate them, and that result in very broad ranges of dynamical numbers – a conclusion that holds whether particles force the flow (e.g., avalanches) or not (e.g., pollutants dispersed by the winds), whether the flow itself be turbulent hence multiscale (although planktons migrate in the ocean which is a turbulent environment, at their own scale they observe a Stokesian world), or not.

Another exciting source of richness in the present work is the presence of phase change in the dynamics of these particles that force the fluid motions, due to the additional couplings it brings in. This thesis focuses on melting and dissolution that enforce a transition from a buoyant particle-laden mixture to a one-phase buoyant fluid. Before it ends drawing the system towards more familiar one-phase buoyant behaviours, this transition is massively constrained by the particulate nature of the buoyancy forcing since the mass or heat transfers are inherently associated with the boundary layers that develop at the surface of particles. The details of the flow and its heterogeneity at the particle scale become more decisive than ever with the introduction of delays or even blocking effects like saturation: this is classically illustrated by the persistence of sprays whose drops may survive over unexpectedly large timescales due to saturation of water vapour (Pal et al., 2021; Stiehl et al., 2022). The considerable sensitivity of the rates of heat-or-mass transfer with the size of particles is another crucial point that creates a strong asymmetry between two flows of identical macroscopic properties yet with differing microstructures (Houze Jr, 2014).

Superb examples of all these points that have guided my intuition all along this PhD are localised events of rain pouring from a cloud, as illustrated in figures 2a-2b. Such flows are essentially driven by the settling of hydrometeors. When substantial amounts of rain fall to the ground, the flow can be violent and develop as a *downburst*, a downward current of air that hits the ground and spreads radially outward with large wind velocities. An interesting distinction is that of *wet* versus *dry* downbursts: these violent downdrafts have been distinguished because the former are driven by large rates of precipitation, whereas the latter are typically driven by the evaporation of drops that increases the air density through evaporative cooling (Srivastava, 1985, 1987). This twofold forcing of the flow through the settling of drops and their cold vapour is an inspiring analog to keep in mind throughout the following pages.

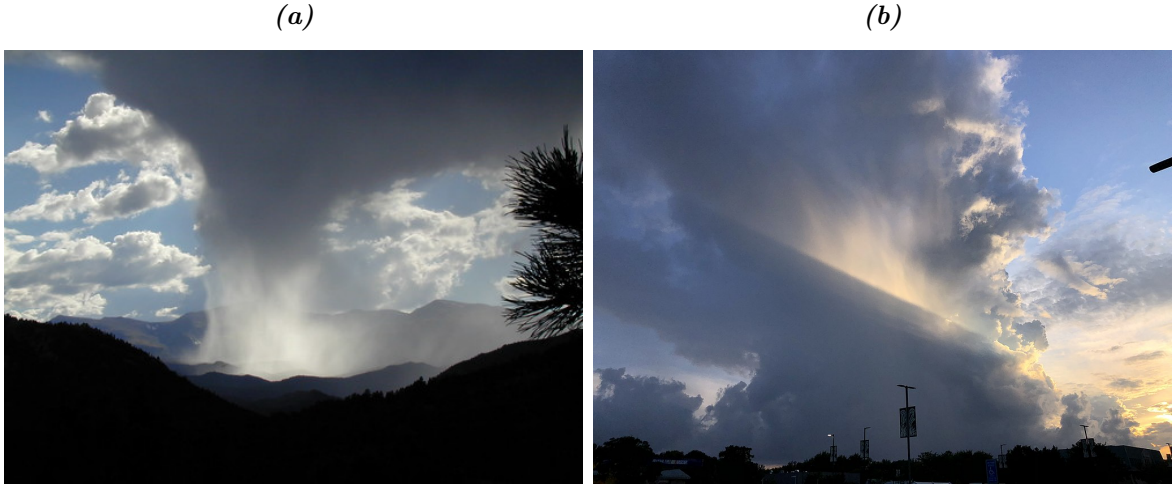

Figure 2: *(a) Rain on mount Evans in Evergreen, Colorado (Greg Younger, CC BY-SA 2.0). (b) Hail shaft (Famartin, CC BY-SA 4.0, via Wikimedia Commons).*

1 Two geophysical motivations

This PhD was motivated by two geophysical flows that are introduced before presenting the organisation of the manuscript.

1.1 Metal-silicate mixing during planet formation

The Earth is a very dynamical thermal machine whose efficiency is still today largely constrained by the initial composition and temperature it had at the end of accretion. Convection in the mantle has been decisive in shaping continents and controlling their motion through plate tectonics, while convection in the core is the source that presently sustains our global magnetic field, of paramount importance for our planet's habitability. These motions are notably driven by the release of heat in space, hence they are constrained by the amount of heat that accumulated in the Earth during its accretion, by the distribution of radioactive elements in the planet, and by the *differentiation* i.e. the core-mantle separation that redistributed heat and chemical elements. The initial composition of both the core and the mantle is also paramount as it influences their density, rheology, and it controls the existence of compositional convection in the Earth core that feeds the magnetic field.

To better understand the present state of the Earth, what can we learn about its initial thermo-chemical state? Numerical simulations in the field of astrophysics have shown that 4.5 Gyrs ago, rocky planets formed by accretion during different stages of planetary impacts between bodies that were finally as large as Mars or the Earth. Radiochronometry indicates that accretion occurred over $10 - 100$ Myrs. At a late stage of accretion, planetary embryos were already differentiated into a liquid metal core and an outer silicate mantle, as sketched in figure 3. Collisions between large impactors released enough energy to melt the rocks into magma in the mantle of both the target planet and the impactor (see the red region in figure 3). The dense metal core of the impactor was accelerated into this liquid magma and due to its

large inertia, it shattered into drops that fell as a cloud towards the centre of the Earth. How they sedimented in the magma ocean and possibly in the core determined how they contributed to the growth of the latter. In addition, the chemical and thermal transfers between the drops and the ambient controlled the initial temperature and composition of both the core and the mantle, with consequences on their respective convection.

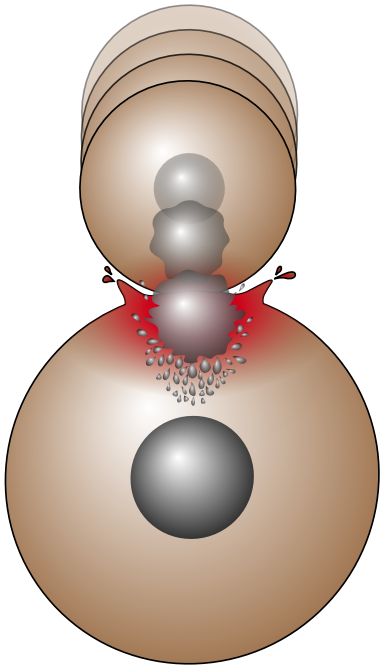

Figure 3: *Sketch of a planetary impact between a target planet and an impactor. Upon contact, the considerable energy released melts the mantle (in brown) which becomes 'magma' in which the core of the impactor (moving downward in time) bursts into drops.*

Not only are these considerations interesting to understand the initial state of the Earth, but they are also crucial to interpret present-day geochemical data that can be collected from meteorites and mantle rocks. Indeed, the composition of the core and the mantle today depends on the *partitioning* i.e. the distribution of chemical elements like Ni, Si, Co, Pb... between the core and the mantle. This distribution is controlled by partition coefficients that are functions of past conditions of pressure and temperature at the time of *chemical equilibration* i.e. at the time when metal and silicates were in chemical interaction (Rudge et al., 2010). However, the connection between the composition measured today and these past conditions can only be drawn if the *efficiency of chemical equilibration* between metal and silicates is known at the time of chemical transfers between metal and silicates (Rudge et al., 2010; Wade and Wood, 2005).

This efficiency of chemical equilibration has been modelled and refined over the years. Three categories of models have been proposed. The first model of *iron rain* (Rubie et al., 2003) envisaged the rapid emulsification of the metal core of the impactor into drops that sank down a magma ocean as a collection of isolated drops falling vertically. The second model of Dahl and Stevenson (2010) considered that the whole volume of metal fell as a unique volume that was

eroded by hydrodynamical instabilities at its boundary. The third model considered that the core of the impactor sank down with sufficient inertia for the flow in and around the metal to be turbulent, favouring its deformation and eventual fragmentation while sinking as a drop-laden *turbulent thermal* that entrains silicates down the magma ocean (Deguen et al., 2014).

So far, the effect of planetary rotation on metal-silicate equilibration has been largely disregarded, despite the strong rotation rate of the proto-Earth that has been suggested by impact simulations (Ćuk and Stewart, 2012). Does rotation affect the evolution of the sinking clouds of iron drops ? Under which conditions ? How much can it modify the efficiency of chemical equilibration?

1.2 Iron snow in the core of small rocky planets

Some small rocky planets have evidenced signs of a global magnetic field of internal origin. It is notably the case of Ganymede, a natural satellite of Jupiter which we also refer to as a 'rocky planet' for simplicity. This observation has intrigued the scientific community because the usual processes that generate magnetic fields in large rocky planets seem impossible on Ganymede. Why is that ?

The planet of reference for magnetic field production is the Earth, whose magnetic field is produced by *dynamo*. This process describes how the motion of an electrically conducting fluid can produce a magnetic field. Such a fluid is found at the centre of rocky planets as the liquid metal of their iron-rich core. The coupling between magnetism and fluid motions leads to the presence of electrical currents that feed the magnetic field, but which are constantly subject to ohmic dissipation. As a result, dynamo action can be sustained only as long as the inertia of the flow is sufficiently large compared to ohmic dissipation, which translates as a condition on the magnetic Reynolds number

$$Re_m = \frac{UL}{\eta_m} \gg 1 \ , \tag{1}$$

where U and L are respectively the characteristic velocity scale and length scale of the flow, and η_m is the magnetic diffusivity. This necessary yet insufficient requirement places constraints on the vigour of the flow. Then, a burning question when observing a magnetic field that is dynamo-generated is: What are the properties of the fluid motions that drive the dynamo?

Apart from mechanical forcings like tides and precession that are not considered in this work (see section 5 in the recent review by Landeau et al. (2022)), three contributions are usually mentioned that participate in sustaining the Earth's magnetic field: *thermal convection* due to the concentration of heat at the centre of the planet, that is released at the core periphery in the overlying mantle; *crystallisation* of the core at the centre, made possible by the existence of large pressures and the slow secular cooling of the Earth, that leads to a chemical separation between pure iron (that solidifies on the solid inner core) and lighter elements that rise in the liquid outer core, feeding a compositional convection; *latent heat release* during crystallisation, that warms the fluid near the inner core, hence boosting the thermal convection. These three elements have proven important in driving the Earth dynamo.

The second ingredient is of particular interest. To understand why, a very schematical description is given here, that is refined at the end of the manuscript. Schematically, the location for core crystallisation is determined by the competition between temperature (large tempera-

tures favour the presence of liquid rather than solid metal) and pressure (large pressures have the opposite influence). The Earth can be called a 'large rocky planet' because pressure overcomes the influence of temperature at the centre, hence the presence of a solid inner core. On a 'small rocky planet' like Ganymede, temperature is expected to counterbalance the influence of pressure, to such an extent that the core may not crystallise at the centre. What's more, Ganymede's core is expected to be thermally stably stratified because the thermal gradient is subadiabatic, making thermal convection inoperative in the core. Then, where could fluid motions originate from ? What flow nourishes Ganymede's magnetic field?

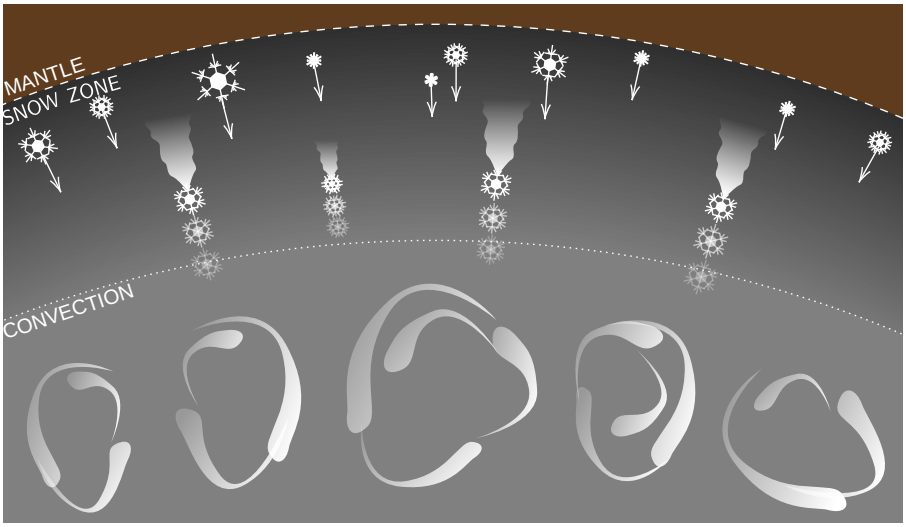

Figure 4: *Sketch of the scenario of iron snow in the metal core of a small rocky planet. Pure iron flakes (in white) crystallise anywhere in the snow zone – where the temperature lies between the liquidus and solidus of the Fe-FeS mixture – and settle because they are denser than the ambient. When crystalling, they release light sulfur-rich fluid that rises due to its positive buoyancy (white wakes behind snow flakes). At the bottom of the snow zone, crystals remelt; the molten snow nourishes convective overturns in the deeper convective region.*

A likely scenario is *iron snow*, that is sketched in figure 4. This scenario can be summarised like so: At the end of its formation, Ganymede's core was so hot that it was entirely molten. As it cooled down, the first location where the temperature became lower than the liquidus was the periphery of the metal core. There, the metal began solidifying. Ganymede's core is schematically a mixture of iron Fe and iron sulphide FeS at pressures around $6 - 10$ GPa. Therefore, crystallisation leads to the growth of pure iron crystals (white snow flakes in figure 4), while lighter sulfur-rich fluid is released by exsolution (white undulating plumes in figure 4). The iron snow flakes being denser than the Fe-FeS mixture, they settle due to gravity, whereas the light sulfur-rich fluid rises because it is lighter than the ambient, likely building a stratification in the zone of crystallisation. The chemical separation leads to the continuous settling of pure iron snow flakes in the region where the temperature is below the liquidus: this is the phenomenon of iron snow. As snow flakes keep falling towards larger and larger temperatures, they ultimately reach a region where the temperature is above the liquidus due to insufficient core cooling. There, snow flakes remelt. This delineates the bottom of the snow zone. Below, remelting of snow flakes produces a molten iron-rich fluid layer that is much more

concentrated in iron than the ambient. Consequently, the dense molten iron-rich fluid layer cannot accumulate at the bottom of the snow zone: it keeps sinking deep in the core, and nourishes a compositional convection, as sketched by convective loops of white molten snow in figure 4.

The ability of snow flakes to produce fluid motions when they settle remains to be clarified. Models of thermal evolution of Ganymede in Hauck II et al. (2006) have estimated a buoyancy flux from the sole consideration of the rate of solidification of iron flakes, with no consideration about their downward sedimentation. Hauck II et al. (2006) then used scaling laws from the literature on fully-fluid buoyancy-driven rotating convection to determine the typical zonal velocities that this flux may nourish. The underlying assumption that a buoyancy flux of particles produces the same flow as a buoyancy flux of fluid is daring and needs to be proven for the specific regime of iron snow. Other authors (Zhan and Schubert, 2012) considered that the dense snow flakes weight on the ambient fluid as a continuous field of buoyancy. The latter was advected by a pure advection-diffusion equation that was identical to that which is usually employed for the advection of temperature. There again, the specific influence of the particulate nature of the buoyancy forcing was disregarded. Also, both approaches disregarded the stable chemical stratification of the snow zone that results from the exsolution and rise of the sulfur-rich residual liquid during crystallisation, and that is usually assumed strong enough to prevent vertical fluid motions in the snow zone (Rückriemen et al., 2015, 2018; Christensen, 2015). As a result, some scepticism remained about the ability of snow flakes to nourish motions in the snow zone, and future investigation was called for (Rückriemen et al., 2015).

Compositional convection, nourished by the mass flux of remelting snow flakes, has been considered a plausible candidate to generate the magnetic field (Rückriemen et al., 2015, 2018; Christensen, 2015). The mass flux of snow flakes is controlled by their volume fraction and size, themselves controlled by the process of crystallisation, the size of the snow zone and its thermodynamical properties. Unfortunately, none of these quantities is known with exactitude, and no data are available about the mode of crystallisation, where it might happen, whether supercooling is involved, etc. Therefore, the buoyancy flux nourishing compositional convection is poorly constrained. The most recent models of iron snow are steady and one-dimensional i.e. they assume quasi-steadiness and uniformity in directions that are orthogonal to gravity (Rückriemen et al., 2015, 2018). Yet, most phenomena at stake in this scenario are fundamentally unsteady and they are sources of heterogeneities.

This PhD was therefore motivated by the will to better understand the fluid motions driven by iron snow flakes and their remelting. Some driving questions were: Can snow flakes behave collectively i.e. can their settling produce macroscopic fluid motions beyond the scale of an individual flake ? How do planetary rotation and stratification alter their settling ? What sizes of snow flakes are to be expected ? How daring is the approximation of instantaneous uniform melting ? Does remelting of snow flakes lead to a uniform buoyancy flux nourishing the compositional convection ?

2 Organisation of the manuscript

Gaining understanding on the physics described above has required to split the journey in simple successive steps, each being the basis to investigate the next one. This progression in complexity naturally corresponds to the progression of the chapters in this manuscript, that have been oriented by the following questions:

1. What flows can be induced by settling particles?
2. What is the influence of the particle size in these buoyant particle-laden flows?
3. What is the minimum physics describing these flows?
4. How does background rotation modify the dynamics of settling particle clouds?
5. How does phase change alter the forcing of fluid motions?

The present work is organised as follows:

- Since the start of this PhD, it was identified that buoyancy is the main force driving those geophysical flows, and that the particulate nature of the buoyancy forcing is a key ingredient of their complexity. Yet, it has not been taken into account up to now. Chapters 1 to 3 focus on clouds of non-reative particles that settle in a fluid, with the aim to gain understanding on the coupling between the clouds dynamics and the flow that emerges.
  - Chapter 1 presents laboratory experiments of clouds of glass spheres settling in a water tank. The canonical configuration of a *turbulent thermal*, i.e. a localised instantaneous release, enables to assess the specificities induced by the particulate nature of the buoyant material, and the role of the particles' size. A first series of experiments performed in a non-rotating water tank shows that particle clouds do not follow the universal growth predicted for turbulent thermals. To assess how planetary rotation might affect particle clouds, a second series is performed with the whole experimental setup mounted on a spin table. These experiments show that rotation eventually imposes a transformation of particle clouds into vortical columns.
  - Chapter 2 digs deeper in the dynamics of particle clouds when background rotation is absent. Thanks to Eulerian two-way coupled numerical simulations, the physics of the fluid-particle interaction is reduced to its minimum to understand why particle clouds behave differently than one-phase turbulent thermals.
  - Chapter 3 analyses how the transition of particle clouds to the regime of vortical column affects the efficiency of chemical equilibration between metal and silicates after a planetary impact.
- Chapters 4 and 5 consider the additional ingredient of phase-change in plumes of reactive particles.
  - Chapter 4 is directly motivated by the remelting of iron snow flakes in planetary cores. It presents an analog experiment where sugar grains are continuously sieved

above a water tank, their dissolution feeding a plume of sugary water that sinks due to its negative buoyancy, mimicking the behaviour of the molten iron snow. The mass rate and size of sugar grains are varied with the aim to characterise the structure and dynamics of the compositional convection that appears, its coupling with sugar grains, and how the flow affects the settling and phase transition of sugar grains.

– Chapter 5 finally opens on some preliminary implications of the experiments of Chapter 4 on the remelting of iron snow flakes and how it nourishes compositional convection.

Part I

Clouds of inert particles

Chapitre 1

Effects of particle size and background rotation on the settling of particle clouds

Summary

We experimentally investigate the behaviour of instantaneous localised releases of heavy particles falling as turbulent clouds in quiescent water, both with and without background rotation. We present the results of 514 systematic experiments for no rotation and for three rotation rates $\Omega = 5, 10, 20$ rpm, and for the size of particles in the range 5 μm to 1 mm, exploring four decades of the Rouse number $\mathcal{R} \in [6 \times 10^{-4}, 4]$ which quantifies the inertia of particles. In the canonical framework of turbulent thermals described by Morton *et al.*, [Proc. R. Soc. A: Math. Phys. Sci. **234**, 1 (1956)], we compare particle clouds with salt-water thermals to highlight specificities due to the particulate nature of the turbulence forcing. In the absence of rotation, particle clouds initially behave as salty thermals with a modulation of their entrainment capacity, which is optimally enhanced for a finite inertia $\mathcal{R} \simeq 0.3$ due to particulate effects. However this regime of turbulence is limited in time due to the inertial decoupling between turbulent eddies and particles. For the three values of Ω explored here, the particulate enhancement of entrainment is inhibited. Moreover the cloud's expansion is interrupted when the Coriolis force overcomes its inertia, forcing the cloud to transform into vortical columnar flows which considerably increase the residence time of particles.

1.1 Introduction

Interactions between a fluid and solid particles can take many forms. In granular media of maximum packing fraction, particles constrain the fluid motion. Conversely, in configurations of vanishingly small concentrations, particles are seemingly isolated and the fluid tends to constrain the motion of the particles. The continuous transition between these end-members

(Andreotti et al., 2012) and the influence of other particle properties like their size and density offer a vast spectrum of interactions and phenomena (see Brandt and Coletti (2022) for a review), which notably manifest in landslides (Fritz et al., 2009), the transport of sediments in rivers (Abramian et al., 2019), the performance of agricultural sprays (Lake, 1977), or the formation of planets in protoplanetary disks (Meheut et al., 2012).

When the size of particles, their volume fraction and the particle-to-fluid density anomaly are low, the fluid governs the motion of particles whose feedback on the flow is negligible, a situation called *one-way coupling* (Balachandar and Eaton, 2010). Many studies have considered the one-way coupling between particles and pre-established idealised isotropic turbulent flows whose properties are well controlled (Brandt and Coletti, 2022), evidencing that turbulence is a source of non-uniformities in the field of particle concentration (e.g. Aliseda et al., 2002; Yoshimoto and Goto, 2007; Salazar et al., 2008) and that turbulence alters the velocity and trajectory of settling particles (e.g. Maxey, 1987; Good et al., 2014).

Although these studies have brought substantial light on the interactions between the fluid and particles, in several situations the feedback of particles on the fluid has a non-negligible impact on the flow (Monchaux and Dejoan, 2017) – a situation referred to as *two-way coupling* (Balachandar and Eaton, 2010). This is especially true when the flow is nourished by the particles, as in downdrafts which can be accompanied by intense rainfalls and are accelerated by the evaporation of droplets (Kruger, 2020), or when the flow is produced by the particles themselves e.g., in turbidity currents (Ouillon et al., 2019; Necker et al., 2002). The initial motivation of the present study fits in this latter framework: past studies suggest that the magnetic field of small telluric planets and moons like Mercury or Ganymede results from the fluid motions generated by iron snow flakes settling into liquid metal – a phenomenon called *iron snow* (Rückriemen et al., 2015). As a first step to understand this phenomenon, this study focuses on the instantaneous release of heavy particles falling as a cloud in water.

The motion of buoyant clouds has been widely studied by releasing a finite volume of denser miscible fluid (often salt water) in fresh water, which almost immediately becomes turbulent. A decisive aspect of the dynamics of these clouds is the efficiency of turbulence to entrain ambient fluid at the cloud interface. Entrainment is actually key to modelling numerous structures like gravity currents (Ouillon et al., 2019; Necker et al., 2002), wildfire plumes (Paugam et al., 2016), moist convection cells (Yano, 2014) or heat plumes in ventilated spaces (Linden, 1999). By a simple modelling of entrainment through a single scalar coefficient, Morton et al. (1956) developed in 1956 the *turbulent thermal* model, which has proved a successful model of finite releases of buoyant fluid in a multitude of contexts (Turner, 1986), even for finite buoyant releases made of immiscible fluid (Landeau et al., 2014) and bubbles (Peñas et al., 2021) generated from different initial conditions. Similarly, past experiments on finite releases of heavy particles have shown that after an initial regime of acceleration, the dynamics of such clouds can be described with the turbulent thermal model (Rahimipour and Wilkinson, 1992; Bush et al., 2003; Lai et al., 2013, 2016). To the best of our knowledge, no specific influence of the particulate nature of the turbulence forcing has been observed on this initial dynamics. Yet, particles have proved capable of modulating turbulence in controlled turbulent flows (see Balachandar and Eaton (2010) for a review) as well as in recent experiments on particle-laden plumes (i.e. continuous injections of buoyancy), whose entrainment efficiency was altered by particles when they crossed the plume interface (McConnochie et al., 2021). The absence of

any such observation for instantaneous releases calls for systematic experiments to determine whether the particulate nature of the turbulence forcing can alter the entrainment efficiency of particle clouds with respect to miscible turbulent thermals. To do so, we investigate the role of particle inertia by covering a large range of particles' sizes from a regime dominated by the fluid motions (when particles have a low inertia) to a regime dominated by the inertia of particles.

Motivated by the influence of planetary rotation during iron snow, we also investigate the influence of background rotation on the clouds' dynamics. Various experimental studies exist on plumes in a rotating ambient (Fernando et al., 1998; Goodman et al., 2004; Frank et al., 2017, 2021; Sutherland et al., 2021). Some recent studies brought substantial light on their particular behaviour due to the solid body rotation, both for bubble-laden (Frank et al., 2021) and miscible plumes (Sutherland et al., 2021). These studies can qualitatively guide the analysis of thermals in a rotating ambient, but while plumes tend to reach a permanent regime, thermals are inherently transient so that scaling laws inevitably differ. A few experimental studies exist for instantaneous buoyant releases that are miscible with water (Ayotte and Fernando, 1994; Helfrich, 1994), but to the best of our knowledge, no such experiments have been conducted with particle clouds.

In this work, we present the results of 514 experiments performed by systematically varying the size of particles and the angular velocity of the background rotation. The experimental apparatus and governing dimensionless numbers are introduced in section 1.2. Section 1.3 analyses the behaviour of particle clouds in a still environment, starting from the reference saltwater thermals in the canonical framework of Morton et al. (1956) in section 1.3.1. The evolution of clouds is analysed by distinguishing two dynamical regimes, and we observe specific effects resulting from the particulate nature of the turbulence forcing when clouds behave as turbulent thermals. Section 1.4 analyses the additional influence of background rotation. Again distinguishing two regimes, we observe that rotation inhibits most of the particulate effects observed without rotation, and considerably increases the residence time of particles when they fall. In section 1.5, main results are summed up and final remarks are made. Lists of all experiments (table 1.2) and all notations (table 1.3) can be found in appendixes.

1.2 Experimental apparatus

1.2.1 Experimental setup

The apparatus is illustrated in figure 3.1. The experiments are performed in a Plexiglas tank of height 100 cm and cross-section area 42×42 cm^2 containing approximately 160 L of fresh water ($\rho_f = 998$ kg.m^{-3}, $\nu = 10^{-6}$ m^2.s^{-1}). The tank is filled long before the experiments to ensure that water is at room temperature, i.e. 22 °C on average. The tank is fixed in the middle of a rotating table whose angular velocity Ω varies from 0 (no rotation) to 20 rotations per minute (rpm). A lid is placed on top of the tank to limit air motions above the free surface during the experiments. A hole at the centre of the lid enables to insert a cylinder of inner diameter $D_{\text{cyl}} = 3.2$ cm to release the buoyant material.

Clouds are either made of salt water, or a mixture of 26.1 mL of fresh water and a fixed mass $m_0 = 1.0$ g of spherical glass beads of density $\rho_p = 2500$ kg.m^{-3} and a mean radius r_p ranging

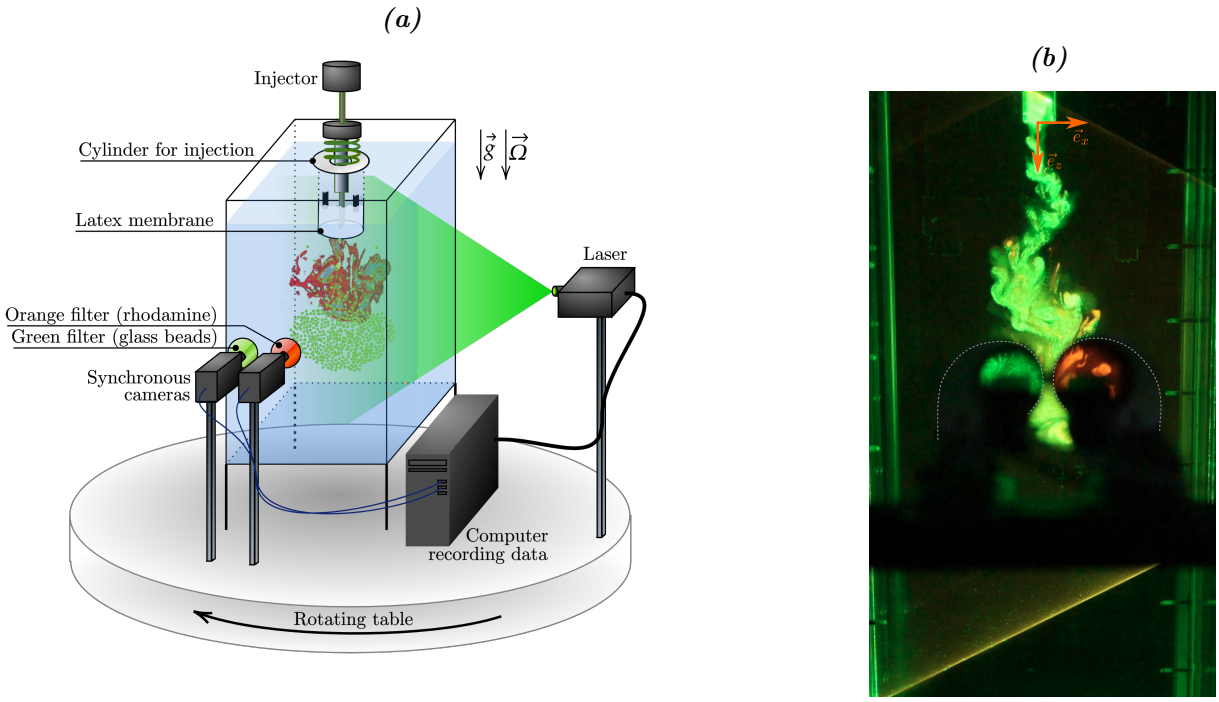

Figure 1.1: *(a) Schematic of the experimental apparatus; see main text for additional details. (b) Turbulent cloud falling with rhodamine. Dotted gray lines highlight the edges of the two filter holders. Particles (respectively, rhodamine) are visible through the filter located on the left-hand side (respectively, right-hand side).*

from 2.5 μm to 500 μm (see discussion in section 1.2.3). In all cases, the buoyancy introduced into the system is the same. Adding fresh water to particles has two motivations. First, in air, small particles tend to cluster because of electrostatic interactions which are easily removed by placing particles in water with a small amount of soap (typically one drop for 20 cl of water). Secondly, if particles fall from air into water, we observe that they entrain some air with them, form clusters, and expell air only gradually as ascending bubbles which are detrimental for the detection of particles and might affect the particle dynamics of interest here. These effects are therefore avoided; the reader is referred to Zhao et al. (2014) for more information about clouds containing such initial clumps of particles. After the cylinder's bottom nozzle has been sealed by a latex membrane which is stretched and taped onto the cylinder itself, the buoyant material is poured into the cylinder. Water in the cylinder always occupies a volume rising at a height $H_0 = 3.3$ cm above the latex membrane.

Initially there is no relative motion between water and the tank (either water and the tank are motionless, or they are in solid body rotation with the rotating table). At $t = 0$ the experiment starts by rupturing the latex membrane with a needle, releasing the content of the cylinder; see figure 1.2 for an illustration. The 1-mm-thick tip of the needle is sharpened to ensure an efficient and fast rupturing of the latex membrane in less than 0.02s according to the videos recorded. Once the membrane retracts, particles are observed to fall out of the cylinder because of their weight. For most particle sizes, the downward acceleration of particles quickly

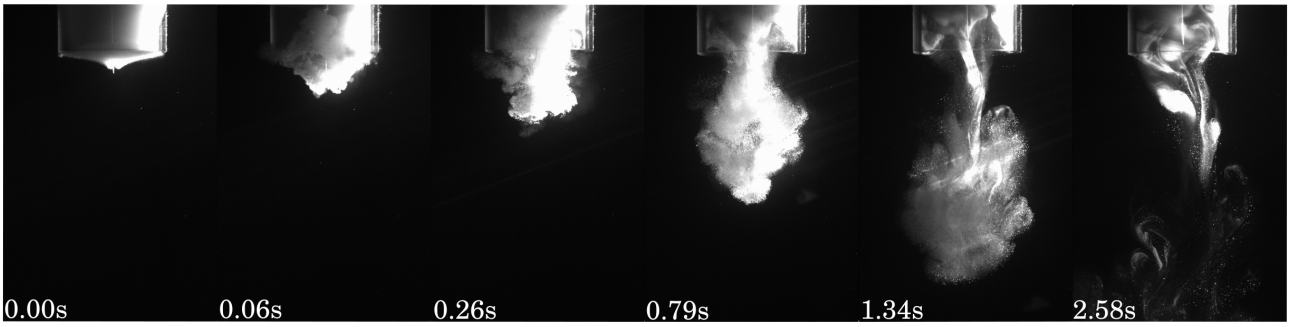

Figure 1.2: *Rupturing (first frame) of the latex membrane, releasing rhodamine and glass beads whose diameter is in the range* $90 - 150$ μm. *Photographs are recorded by a single monochrome camera with no filter. Particles are sufficiently large to be distinguished from the continuous field of rhodamine. The cylinder being transparent, the needle and recirculation of rhodamine are visible on the last two photographs.*

transmits to the fluid, the buoyant material rolls up and the cloud almost immediately becomes turbulent.

Visualisations are performed in a vertical laser sheet with half-angle of divergence 30°, using a Powell lens and a laser of wavelength 532 nm with a power of 1 W or 1.5 W depending on the series of experiments (Laser Quantum 532 nm CW laser 2 W). Since particles and water have different motions, two identical PointGrey cameras are synchronised and record the same experiment with two different filters. The first camera has a green filter (band-pass filter from Edmund Optics, CWL 532 nm, FWHM 10 nm) to record the motion of glass beads which reflect and refract the laser beam, while the second camera has an orange filter (high-pass filter above 570 nm). By colouring the fluid inside the cylinder with rhodamine, the second camera records the motion of the turbulent eddies which appear in orange in the laser sheet because of the fluorescence of rhodamine. In doing so, there is no overlap of information between the two cameras. Both of them save images in a format 960×600 pixels, corresponding to a field of view whose size is 45 cm in depth and 28 cm in width. Cameras are synchronised, recording images at 50 frames per second (fps). To minimise effects of parallax, they are placed as close as possible to one another, and as far as possible from the laser sheet. A calibration grid was placed in the plane of the laser sheet and photographed by both cameras. This enables to define a coordinate system for each of the two cameras, and to dewarp images so that synchronous photographs can be sumperimposed using Python's library OpenCV.

1.2.2 Initial conditions of release

The initial release of particles is notably controlled by the effective density of the fluid within the cylinder, which depends on the volume fraction in particles. Two initial volume fractions can be imposed. Either particles are stirred in the cylinder to form a suspension in water before rupturing the membrane, and in that case the initial release is said to be *dilute*. Otherwise, particles are left to settle before the experiment so that they form a compact layer at the bottom of the cylinder, directly lying on the latex membrane, and in that case the initial release is said to be *compact*.

Since larger particles settle faster, only particles with $r_p \leq 30$ μm could be maintained in suspension prior to puncturing the membrane. This is why to compare particle clouds of different particle sizes, experiments have been performed with a compact release for all particle ranges. Then, additionally, experiments have been performed with a dilute release when feasible. The motivation for these dilute releases is twofold: it enables to assess the effect of this initial condition on the cloud development, and it enables to compare the behaviour of particles with respect to salt water clouds, for which salt is always dilute in the whole volume of water within the cylinder.

Then, we want to consider a quasi-instantaneous release of particles, but the smallest ones can take up to 7 min to settle over the depth of the cylinder. Hence, the mass excess $m_0 = 1$ g needs to be expelled from the cylinder. Yet, we are interested in the flow generated only by the glass beads settling. A compromise consists in immersing the cylinder on the last 2.2 cm of the 3.3 cm-high volume of water. Once the membrane is ruptured, the resulting hydrostatic imbalance with the ambient fluid leads to a downward acceleration of the buoyant mixture which is released on a much shorter time scale, at first order independent from the beads' mean radius and the dilute or compact initial conditions.

In order to assess the robustness of our protocol, let us determine the depth beyond which this initial momentum has a negligible influence on the cloud evolution. When the buoyant material comes out of the cylinder, friction on the inner walls of the cylinder as well as shear on the sides of the buoyant fluid both generate circulation, forcing the buoyant fluid to roll up. The initial acceleration of all the fluid in the cylinder due to the hydrostatic imbalance actually adds some more circulation, which levels the difference between compact and dilute releases: in fact, we observe that for both dilute and compact releases in the range $r_p \leq 30$ μm, all clouds initially roll up and end up approximately spherical with typical size D_{cyl} at a depth of order 1-2D_{cyl}. For a buoyant cloud with initial momentum, the Morton length (Morton, 1959; Turner, 1986) quantifies the distance beyond which the cloud buoyancy predominates over the initial momentum. For our experiments, the Morton length can be expressed [see equation (A.15) in Deguen et al. (2011)]

$$l_M = \left[\frac{(\rho_0/\rho_f)^2 U_{\mathrm{ref}}^2 D_{\mathrm{cyl}}^3}{g(\rho_0/\rho_f - 1)} \right]^{1/4}, \tag{1.1}$$

with $g = 9.81$ m.s^{-2}. The initial cloud density ρ_0 relevant for its dynamics is computed once the cloud has rolled up as a sphere of radius D_{cyl} hence $\rho_0 = \rho_f + (1 - \rho_f/\rho_p) m_0/(4\pi D_{\mathrm{cyl}}^3/3)$. Then, the typical cloud velocity U_{ref} is prescribed by the cloud size and reduced gravity as

$$U_{\mathrm{ref}} = \sqrt{g \left(1 - \frac{\rho_f}{\rho_0}\right) D_{\mathrm{cyl}}}, \tag{1.2}$$

which is the same for all experiments. We find that $l_M \simeq D_{\mathrm{cyl}}$. Hence, after the cloud has rolled up and travelled a distance l_M, corresponding to a total distance of order 2-3D_{cyl}, the influence of the initial momentum can be neglected.

1.2.3 Particle distributions

Particles are provided by Sigmund Lindner (SiLibeads) in sets of polydisperse distributions. For every set of particles, a Gaussian is fitted on the histogram of the distribution of particles' radii. This provides the average radius r_p of the set of particles, as well as the standard deviation σ_p with respect to r_p. The ratio $\mathcal{S} = \sigma_p/r_p$ is a measure of the polydispersity of a given set of particles. The average radius r_p and the ratio $\mathcal{S}$ are listed in table 1.1 for polydisperse, monodisperse and bidisperse particle sets.

Monodisperse sets are obtained due to sieves, each of them corresponding to a given size which truncates the Gaussian. The distribution obtained is integrated to compute the resulting mean radius. The characteristic deviation σ_p is computed simply as the difference in radius between r_p and the cutoff value of the sieve.

Bidisperse sets are obtained by mixing together a percentage p of the total mass $m_0 = 1$ g from the monodisperse set $90 - 100$ μm, and a percentage $1 - p$ of m_0 from the monodisperse set $140 - 150$ μm. The characteristic deviation σ_p is computed as the difference between the resulting average radius r_p, and the average radius of the monodisperse set whose percentage (p or $1 - p$) is the largest.

	Range of diameters (μm)	Symbol	r_p (μm)	$\mathcal{R}$	Re_p	N_p	$\mathcal{S}$	Π ($\times 10^{-4}$)
Polydisp.	0-20	○	2.6	6.00×10^{-4}	1.16×10^{-4}	5.43×10^{9}	1.0	0.813
	40-70	○ or ●	29.9	7.57×10^{-2}	0.167	3.57×10^{6}	0.35	9.34
	90-150	●	64.4	0.308	1.47	3.58×10^{5}	0.3	20.1
	150-250	●	108.1	0.696	5.57	7.56×10^{4}	0.23	33.8
	250-500	●	192.4	1.48	21.1	1.34×10^{4}	0.22	60.1
	500-750	●	339.8	2.73	68.8	2.43×10^{3}	0.24	106
	750-1000	●	465.9	3.70	128	944	0.18	146
Monodisp.	90-100	■	45.7	0.168	0.567	1.00×10^{6}	0.029	14.3
	140-150	■	76.1	0.406	2.29	2.17×10^{5}	0.029	23.8
	224-250	■	120.8	0.814	7.28	5.42×10^{4}	0.07	37.8
	$\geq$ 1000	■	524.5	4.13	160	662	0.093	164
Bidisp.	$p = 80\%$	▲	51.8	0.210	0.805	6.87×10^{5}	0.118	16.2
	$p = 60\%$	▲	57.8	0.255	1.09	4.95×10^{5}	0.211	18.1
	$p = 40\%$	▲	63.9	0.304	1.44	3.66×10^{5}	0.191	20.0
	$p = 20\%$	▲	70.0	0.354	1.84	2.78×10^{5}	0.087	21.9

Table 1.1: *Governing numbers of all series of experiments. The column 'Range of diameters' describes the range of diameters of the glass spheres (in microns) as referenced by the trademark SiLiBeads. Percentages p of bidisperse clouds are defined in the main text. The symbols are those used in figures throughout the paper. Shapes depend on the dispersity of particle sets. Filled symbols correspond to a compact release of particles, and empty symbols correspond to a dilute release, as defined in the text. Particle clouds are also compared to salt water clouds of Rouse number $\mathcal{R} = 0$, also represented by an empty circle ○.*

1.2.4 Dimensionless numbers

In the present study, particles are considered to interact only through hydrodynamic interactions. This assumption is based on three arguments: particles of size $r_p \geq 2.5$ μm are non-Brownian at temperatures around 290-300K (Andreotti et al., 2012); soap was used during experiments to avoid physico-chemical interactions; finally, collisions are expected to play little part in the cloud dynamics except during the phase of acceleration when particles are released from a compact layer in the cylinder. Hence, particles interact by inducing a velocity perturbation on other particles with a magnitude decreasing with distance, or by wake interactions.

Thus, the following dimensional quantities describe the dynamics of the clouds and the particles they are laden with: gravity g, the fluid density ρ_f and kinematic viscosity ν, the particles' density ρ_p, the total mass of particles m_0, the average radius of particles r_p, the standard deviation σ_p of the supposedly Gaussian distribution of particles' radii, and finally the diameter of the cylinder D_{cyl}. The tank angular velocity is not included yet; effects of rotation are discussed in section 1.4. The tank dimensions are not considered, assuming they are large enough not to influence the dynamics.

These parameters enable us to define the terminal settling velocity w_s of a single particle for the two following end members. Very small particles have a negligible particulate Reynolds number $Re_p = 2r_p w_s/\nu \ll 1$ and therefore move in a Stokes flow. Assuming sphericity, the balance between their buoyancy and the linear Stokes drag leads to defining

$$w_s^{\text{Stokes}} = \frac{2gr_p^2(\rho_p - \rho_f)}{9\nu\rho_f} \propto r_p^2. \tag{1.3}$$

As for large particles characterised by a large particle Reynolds number $Re_p \gg 1$, the balance between their buoyancy and a quadratic drag law leads to

$$w_s^{\text{Newton}} = \sqrt{\frac{8g(\rho_p - \rho_f)}{3C_d\rho_f} r_p} \propto \sqrt{r_p}, \tag{1.4}$$

with C_d the drag coefficient, approximately constant and equal to 0.445 for a sphere in the range $Re_p \in [750, 3.5 \times 10^5]$ (see Crowe et al., 2011). Several empirical expressions exist in the literature to capture the smooth transition from regime (4.3) to regime (4.33) when r_p increases. For particulate Reynolds numbers lower than ∼800 as is the case here, a classical equation is provided by the Schiller-Naumann correction to the Stokes velocity (Crowe et al., 2011):

$$w_s = \frac{w_s^{\text{Stokes}}}{1 + 0.15Re_p^{0.687}}. \tag{1.5}$$

Finally, the eight quantities listed above involve three dimensions, thus according to the Vaschy-Buckingham theorem, five dimensionless numbers are defined as listed below:

$$\mathcal{S} = \frac{\sigma_p}{r_p}; \qquad N_p = \frac{3m_0}{4\pi r_p^3 \rho_p}; \qquad \Pi = \frac{r_p}{D_{\text{cyl}}}; \qquad Re_p = \frac{2r_p w_s}{\nu}; \qquad \mathcal{R} = \frac{w_s}{U_{\text{ref}}}. \tag{1.6}$$

The ratio $\mathcal{S}$ quantifies the dispersity of particle distributions. The total number of particles N_p plays an important part in the particles' interactions, and governs the initial fall. The ratio

Π is typically adequate to characterise the influence of the velocity perturbations induced by a single particle at initial times when the cloud size is of order D_{cyl} (Subramanian and Koch, 2008; Pignatel et al., 2011). The particulate Reynolds number Re_p compares advection and molecular diffusion in the flow produced around a particle as it settles. Finally, particles and water have different motions since particles have inertia, as quantified by their Rouse number $\mathcal{R}$ which compares the inertia of a particle (through its terminal velocity w_s) and that of the cloud which sustains that particle. Since the reference fluid velocity U_{ref} is the same for all experiments (equation (3.1)), in this study the Rouse number varies only with the particles' radius: the larger the particle, the larger its inertia, the larger the Rouse number. Dimensionless numbers for each set of beads are listed in table 1.1, and appendix 1.A additionally provides a complete list of the experiments performed.

1.3 Particle clouds in a still environment

1.3.1 The turbulent thermal as a one-phase reference

In this section, we focus on the release of salt water clouds in fresh water, and interpret our results in the framework of Morton et al. (1956) (the paper hereafter abbreviated as MTT56), whose equations have proved applicable in a multitude of contexts (see section 3.1), highlighting the role of attractor of the model of turbulent thermal. We then use this purely fluid case to highlight and understand any specificity due to the particulate nature of the turbulence forcing in the next sections.

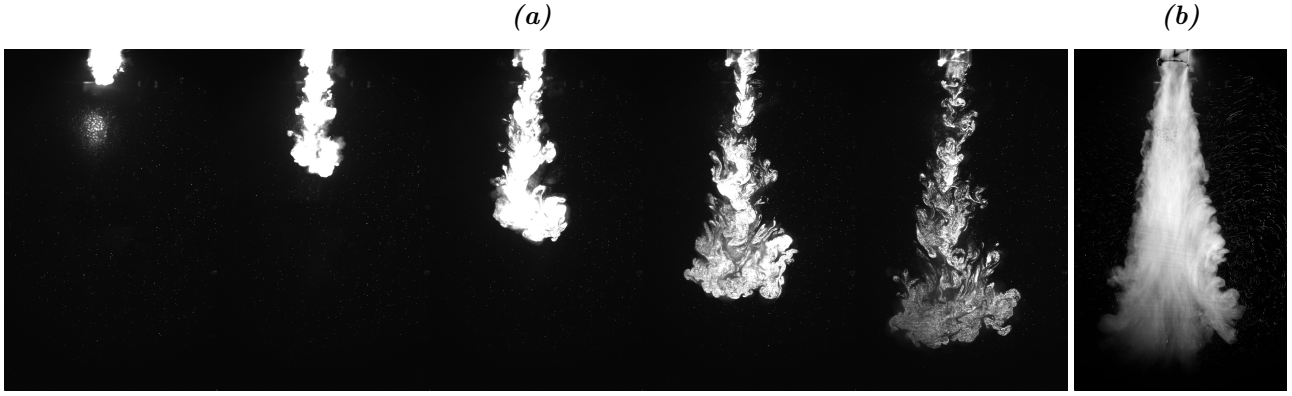

Figure 1.3: *(a) Salt-water cloud falling in still, fresh water. The time lapse between frames is 1.6s, and all photographs are 45cm high. (b) Pixel-by-pixel standard deviation of light intensity during the same experiment, over 8.0s.*

The robustness of MTT56 comes from its integral description of the main physics of the thermal as well as the small number of hypotheses required. The shape of the thermal is expected to play little part on its dynamics, and it is approximated by a sphere of radius $r(t)$ and uniform density $\rho(t)$ so that describing the thermal evolution only requires three variables:

$r(t)$, $\rho(t)$, and the vertical velocity $\dot{z}(t) = dz/dt$ whose integration leads to the thermal position in depth $z(t)$. Knowing the thermal velocity, these quantities can alternatively be computed as functions of z: $r(z)$, $\rho(z)$, $\dot{z}(z)$.

Figure 1.3 shows the evolution of a salt-water thermal of excess mass $m_0 = 1$g released in the same condition as any particle cloud. We observe that the turbulent cloud radius grows linearly with depth. This is captured by MTT56 through the entrainment hypothesis. The turbulence developing inside the cloud is considered responsible for a uniform inflow of ambient fluid into the spherical thermal – a process called *entrainment* – with a characteristic inflow velocity v_e. The *entrainment hypothesis* states that this velocity is proportional to the sole characteristic velocity scale of the system, the thermal vertical velocity $\dot{z}$, so that the entrainment velocity reads

$$v_e = \alpha \dot{z}, \tag{1.7}$$

with α a positive constant called the *coefficient of entrainment*. From this model, the mass of the thermal increases in time due to the uniform entrainment of ambient fluid over the thermal's surface. Neglecting any *detrainment*, i.e. any outflow of buoyant material which would be lost in the wake (or *stem*) behind the thermal, the mass anomaly m_0 remains constant within the cloud. Finally the evolution of the cloud's momentum is mainly driven by the constant buoyancy force $m_0 g$, and mitigated by a quadratic drag term. The resulting equations of evolution are

$$\begin{cases} \dfrac{d}{dt}\left[\dfrac{4}{3}\pi r^3 \rho\right] & = 4\pi r^2 v_e \rho_f = 4\pi r^2 \alpha \dot{z} \rho_f & \text{(1.8a)} \\ \dfrac{d}{dt}\left[\dfrac{4}{3}\pi r^3 (\rho - \rho_f)\right] & = \dfrac{dm_0}{dt} = 0 & \text{(1.8b)} \\ \dfrac{d}{dt}\left[\dfrac{4}{3}\pi r^3 \rho \dot{z}\right] & = m_0 g - \frac{1}{2}\rho_f \dot{z}^2 \pi r^2 C_D & \text{(1.8c)} \end{cases}$$

with C_D a drag coefficient. Combining the equations of conservation of mass (1.8a) and mass excess (1.8b) immediately yields $\dot{r} = \alpha \dot{z}$ which shows that α directly quantifies the constant growth rate of the thermal in depth with $\alpha = dr/dz$. Figure 1.3 confirms the linear growth of the turbulent thermal in depth with snapshots (figure 1.3a) and with the pixel-by-pixel standard deviation of light intensity captured by the camera over 8.0 s of the cloud fall (figure 1.3b). Knowing the couple (r, ρ) at a given depth z_0 enables to compute (r, ρ) at any depth z from the sole knowledge of α and conservation of m_0. Finally, integration of the whole model shows that the cloud decelerates as it entrains ambient fluid. With no specific assumption on C_D, self-similar solutions can be found at large times, which scale like (see Escudier and Maxworthy, 1973)

$$\begin{cases} r \sim z \sim t^{1/2}, & \text{(1.9a)} \\ \dot{z} \sim z^{-1} \sim t^{-1/2}, & \text{(1.9b)} \end{cases}$$

In the present context, particle clouds follow this regime only after an initial phase of acceleration and beyond the Morton length [equation (1.1)].

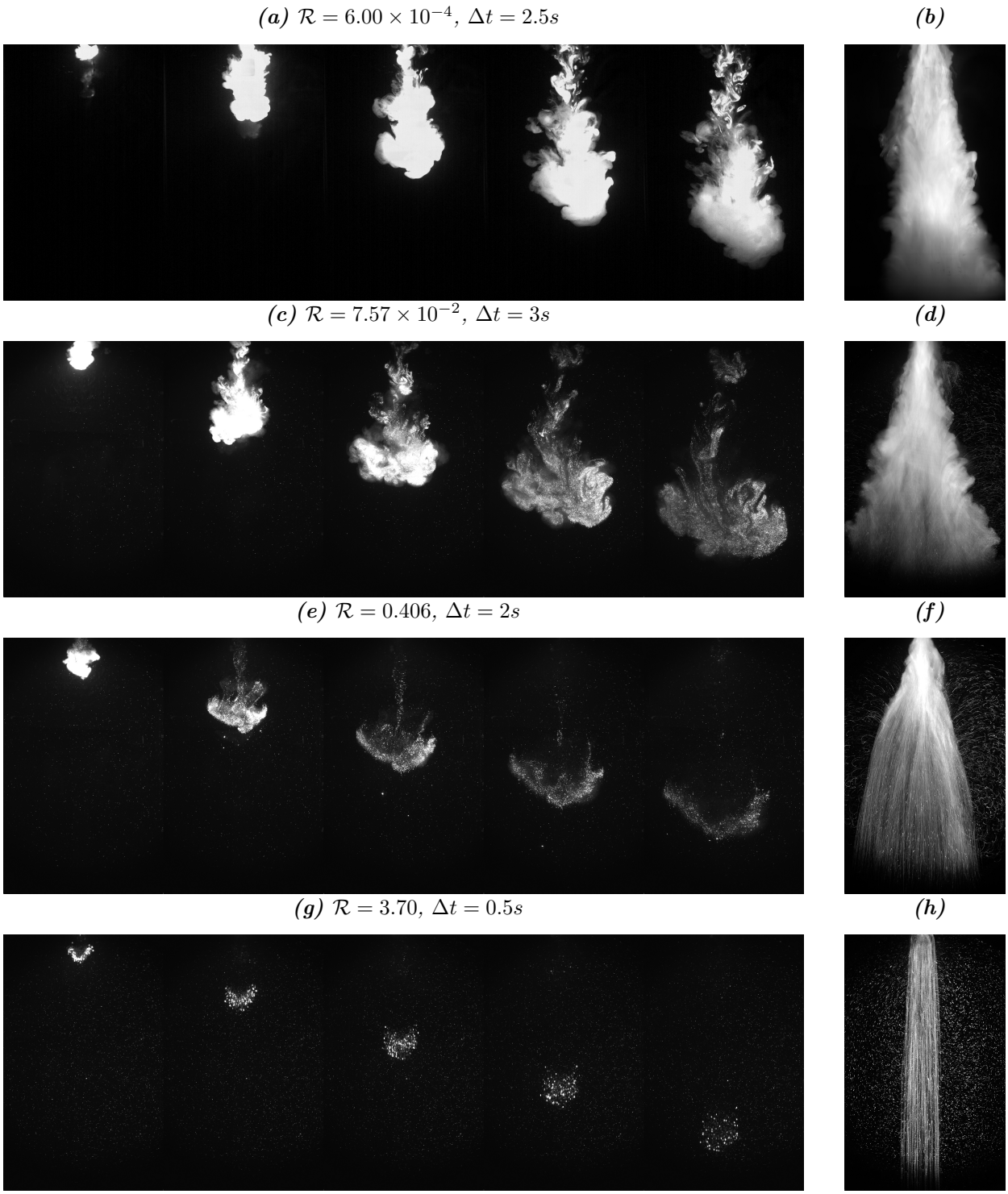

Figure 1.4: *(a,c,e,g): Particle clouds falling for different Rouse numbers $\mathcal{R}$ in the absence of background rotation. The height of all snapshots is 45cm and the time lapse between two successive snapshots Δt is indicated in each subtitle. (b,d,f,h): Pixel-by-pixel standard deviation of all photographs taken during the experiment on the same row, of respective durations (b) 20s, (d) 28s, (f) 16s, (h) 3.4s. Bright dots in the background correspond to remaining particles from previous experiments which have no influence during experiments.*

1.3.2 Thermal regime: specificities of particle-induced entrainment

The broad behaviour of particle clouds is now compared to the reference one-phase turbulent thermals. Figure 1.4 presents snapshots of particle clouds for four different Rouse numbers. At low Rouse numbers, clouds clearly appear to decelerate and linearly grow in depth, in much the same way as salt-water thermals. Yet, for large Rouse numbers, defining a coefficient of entrainment due to the cloud growth hardly seems feasible since the particle cloud spreads little during its fall. This observation is confirmed by the pixel-by-pixel standard deviation of light intensity computed over the fall of a cloud of Rouse number $\mathcal{R} = 3.70$ (see figure 1.4h), as opposed to similar visualisations for $\mathcal{R} \leq 0.406$ (see figure 1.4b). Note as well that for $\mathcal{R} = 3.70$, particles are observed to mostly fall vertically without swirling in eddies, as visible due to the particle trajectories in figure 1.4h.

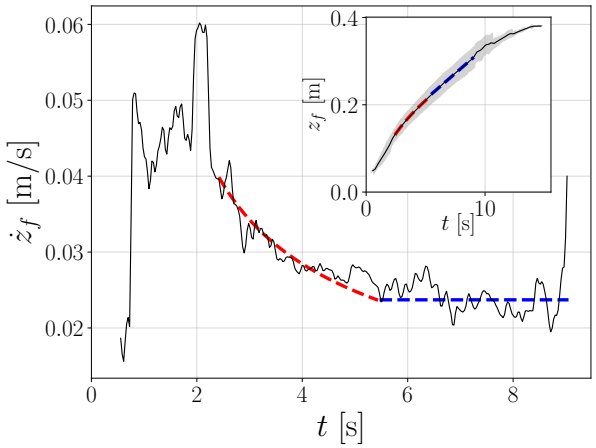

Figure 1.5: *For a cloud of Rouse number $\mathcal{R} = 0.308$, the main graph shows in dark solid line (——) the average cloud front velocity up to $t \simeq 9s$ after which the noise is too large. This velocity is computed from second order finite differences of the cloud front position $z_f(t)$, itself shown in inset (——). The gray shaded area corresponds to the standard deviation due to averaging of $z_f(t)$ from different realisations of the same experiment. On both curves are represented the model for the thermal regime (- - -) and the model of constant front velocity (- - -).*

These last observations emphasise a transition in the cloud dynamics which is due to a separation between particles and turbulent eddies, hereafter simply referred to as *separation*, which interrupts the turbulence forcing. This transition is confirmed by analysing the kinematics of the cloud front whose depth is denoted z_f (measuring techniques are described in Appendix 1.C). To do so, for a given Rouse number, the curves $z_f(t)$ from different realisations of the same experiment are averaged. Then, the resulting curve is filtered with a moving average to reduce noise, and the velocity $\dot{z}_f$ is computed. Finally, two laws can be fitted on $z_f(t)$: either we fit $z_f = C\sqrt{t - t_0}$ for the thermal regime where t_0 and C are arbitrary constants, or we fit an affine law on $z_f(t)$ which is adequate after separation has happened. Figure 1.5 shows that after an initial duration of acceleration of the cloud front up to 2.5s, the latter decelerates in the thermal regime (see red dashed curves in the range 2.5s-5.2s). This highlights the relevance of the analogy between particle clouds and turbulent thermals described by MTT56, as previously verified in the literature (e.g. Rahimipour and Wilkinson, 1992; Bush et al., 2003; Deguen et al.,

2011). However, after some time, the cloud front velocity becomes constant; see blue dashed curves in figure 1.5 after 5.2s. This transition is due to separation, which is further discussed in section 1.3.3. We now exclusively focus on the cloud evolution before separation.

As mentioned in section 1.3.1, one of the main features of turbulent thermals is their ability to efficiently entrain surrounding fluid. According to the literature, thermals typically entrain with an average entrainment coefficient $\alpha = 0.25 \pm 0.10$ (Deguen et al., 2011; Landeau et al., 2014), whose variability is due to the sensitivity of turbulence to initial conditions, and also to the dependence of α on the experimental configuration. The coefficient of entrainment of all clouds is measured following the procedure described in Appendix 1.D.1. Figure 1.6 shows the entrainment capacity of particle clouds for all Rouse numbers, with respect to the reference of salty thermals whose measured entrainment coefficient is in our case $\alpha_{\text{salt}} = 0.18 \pm 0.02$, which lies in the usual range. Note the drastic decrease of the entrainment coefficient for Rouse numbers above $\simeq$0.3. This drop is directly due to particles of large Rouse number quickly separating from turbulent eddies, resulting in a short-lived turbulence forcing and therefore a low entrainment rate (see section 1.3.3). Most importantly for the rest of this study, two regions are distinguished: clouds in the range $\mathcal{R} \leq 1$ go through the self-similar thermal regime, unlike those in the range $\mathcal{R} > 1$ (see the gray shaded area in figure 1.6) in which case α is still measured but does not have the same meaning (see Appendix 1.D.1).

Then, considering clouds in the range $\mathcal{R} \leq 1$, two main observations can be made. The first observation is that, in the thermal regime, particle clouds entrain more than salt water clouds using the same experimental apparatus, and for the same mass excess. The second observation is that this enhanced entrainment capacity operates most efficiently in a range of Rouse numbers centered on $\mathcal{R} \simeq 0.3$, since $\alpha/\alpha_{\text{salt}} \to 1$ when the Rouse number vanishes to zero, and $\alpha/\alpha_{\text{salt}} \to 0$ when the Rouse number largely exceeds 0.3.

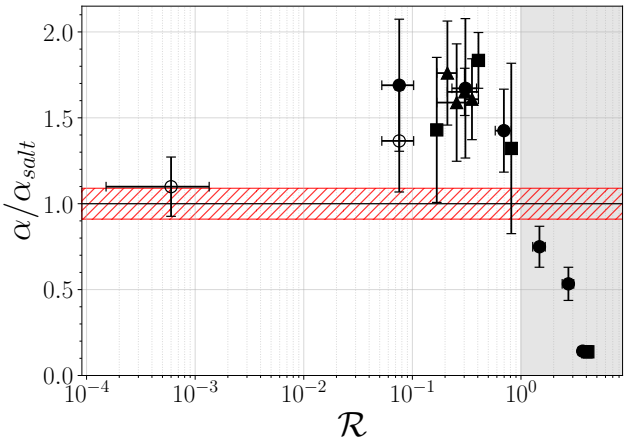

Figure 1.6: *Entrainment capacity of particle clouds with respect to the reference case $\alpha_{salt} = 0.18$. Symbols are listed in table 1.1. Red hatchings correspond to the errorbar for salt water whose Rouse number virtually corresponds to $\mathcal{R} = 0$. The gray shaded area highlights clouds which do not go through the thermal regime.*

This enhanced entrainment of particle-laden thermals compared to salt-water thermals is

now interpreted in the light of past results on inertial particles. Particles of very large $\mathcal{R}$ hardly respond to modifications of the flow around them because of their large inertia (Yoshimoto and Goto, 2007), hence they tend to settle vertically, whatever the flow direction around them. On the opposite, particles of vanishingly small $\mathcal{R}$ act as passive tracers in the fluid – salt water corresponding to the asymptotic case $\mathcal{R} = 0$. In the intermediate range where we observe that $\alpha > \alpha_{\text{salt}}$, particles of finite inertia follow the fluid, yet they also gravitationally slip with respect to the fluid in their vicinity (Nitsche and Batchelor, 1997). This gravitational slip is typically modelled by a vertical terminal velocity w_s which adds up to the local fluid velocity for particles of low inertia (Balachandar and Eaton, 2010; Nasab and Garaud, 2021). Consequently, through drag, such particles can accelerate the fluid and modify its streamlines so that the fluid follows the particles due to *two-way coupling* (Balachandar and Eaton, 2010; Monchaux and Dejoan, 2017). A single particle may be too small to efficiently modify the flow around it, however the more concentrated the particles, the more efficient their forcing (Balachandar and Eaton, 2010; Monchaux and Dejoan, 2017; Nasab and Garaud, 2021).

In our experiments two effects are observed which modify the concentration of particles inside the clouds. First, particles preferentially concentrate on the edges of eddies because their density is larger than that of the ambient. This effect of *preferential concentration* or *inertial clustering* is notably due to pressure effects centrifuging dense particles outside of eddies (see Brandt and Coletti, 2022, for further details). It can be derived from theory (see Balachandar and Eaton, 2010; McConnochie et al., 2021) and has been evidenced in numerous experimental (Aliseda et al., 2002) and numerical (Nasab and Garaud, 2021; Yoshimoto and Goto, 2007) past studies. Second, particles preferentially settle on the side of eddies that moves with a downward velocity (parallel to $+\vec{g}$). This effect of *fast-tracking* or *preferential sweeping* has been evidenced in numerical simulations (Maxey, 1987; Wang and Maxey, 1993), experiments (Aliseda et al., 2002), and recently atmospheric flows (Li et al., 2021).

The combination of both phenomena is shown in figure 1.7a. In this snapshot, the particle cloud has led to the formation of a vortex ring, whose cross-section evidences two vortical structures, centered on the toroidal vortex core. Many particles settle on the edges of these two vortices, and particles almost exclusively sweep on the downgoing side. Together, preferential concentration and preferential sweeping lead particles to fall on the inner sides of these eddies without rolling upwards with the fluid on the other side. Hence, the work of the buoyancy force exerted on particles is always positive, and no turbulent kinetic energy needs to be converted into potential energy to lift particles on the outer ascending side of those eddies. This enhances the efficiency of the particulate forcing and consequently the entrainment rate of particle clouds compared to salt-water thermals. Additionally, both phenomena increase the local effective density of the fluid on the downgoing side of eddies where eddies are being forced by particles, and they also enhance the gravitational slip of particle clusters with respect to the fluid; see in particular (Aliseda et al., 2002). This enhances the capacity of concentrated particles to impose their own trajectory to the fluid and force the turbulent flow through two-way coupling, as we initially observe during the cloud acceleration for all $\mathcal{R}$. All in all, figure 1.7c illustrates the ability of particles to modify the flow and force a new eddy through two-way coupling. On the first photograph particles aim at separating from a vortex, yet one observes the formation of an additional eddy on the following frames. This is likely due to the large concentration and fast downward velocity of the particles sweeping along the former vortex. This enhances

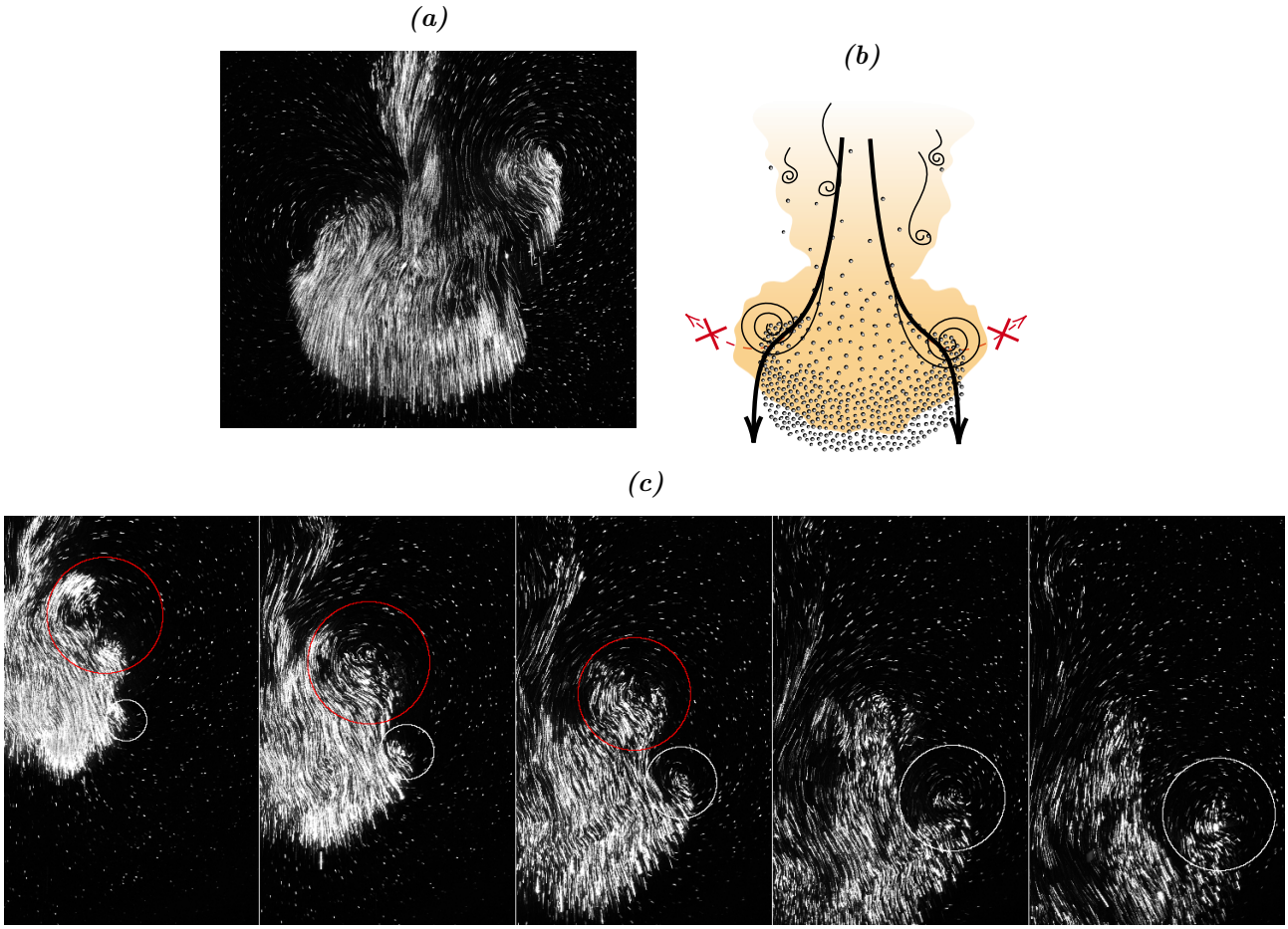

Figure 1.7: *(a) Particles ($\mathcal{R} = 0.304$) preferentially fall along the down-going sides of eddies (image height: 24.0cm). (b) Schematic of the situation photographed in (a), with particles going downward (see dark arrows) without rolling upward on the up-going sides of eddies (see red dashed arrows which are crossed out). (c) Illustration of the ability of particles ($\mathcal{R} = 0.308$) to force a new eddy (centred on the white circle) after they separate from a former one which vanishes (centred on the red circle). Each image is a pixel-by-pixel moving standard deviation of light intensity over 0.3s. The time interval between frames is $\Delta t = 1.4s$ and their height is 20.7cm. See the supplemental material Rouse0p308_0RPM.avi for an animation showing a particle cloud of Rouse number $\mathcal{R} = 0.308$ falling in a still ambient.*

entrainment and makes it longer-lasting.

Our observations of the enhancement of entrainment by particles contrast with the study of McConnochie et al. (2021) who studied particle-laden turbulent plumes whose buoyancy was due to two agents: particles as well as a difference in salinity. They observed that particles modify the entrainment coefficient *only* when they settle in the direction opposite to the plume fluid buoyancy flux. This modification was interpreted as being due to particle clusters crossing the plume interface and interacting with it, which requires particles to settle opposing the fluid buoyancy flux. The fact that, in the present study, particles modify the entrainment coefficient as they fall down with the turbulent thermal, might be due to the very distinct nature of a plume and a thermal: once the former reaches a steady state, particles evolve in a pre-established stream, while the particles of a thermal evolve in a fundamentally unsteady flow which develops because of their forcing. This distinction between plumes and thermals in the context of particle-laden flows remains to be fully explored.

1.3.3 Separation

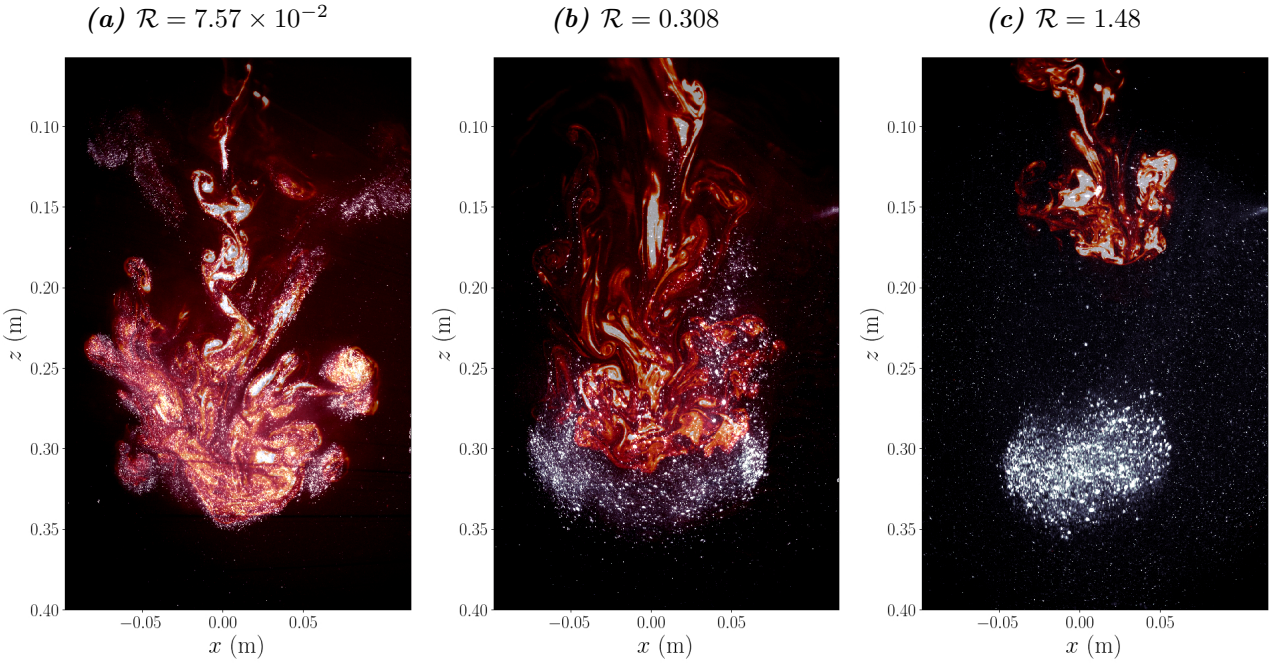

Figure 1.8: *Separation between glass beads (in gray/white) and rhodamine (in orange) for three different Rouse numbers, for the same front depth.*

To visualise separation, rhodamine was added to water in the cylinder of injection for a few experiments, and snapshots can be visualised in figure 1.8. For $\mathcal{R} = 7.57 \times 10^{-2}$ no separation is visible between particles (in gray/white) and rhodamine (in orange) over the depth of our set-up. On the opposite for large particles of Rouse number $\mathcal{R} = 1.48$, separation quickly takes place even above $z \simeq 10$ cm, and the rapid increase of the distance between rhodamine and particles emphasizes this process. Separation is a gradual phenomenon though, as evidenced by

particles of intermediate Rouse number $\mathcal{R} = 0.308$ which are still separating in the snapshot in figure 1.8b. This process can be understood by the fact that when the thermal velocity becomes lower than the particles' settling velocity w_s, the rms velocity in the cloud (which scales like $v_e = \alpha \dot{z}$) becomes unable to sustain particles in eddies (e.g. Rahimipour and Wilkinson, 1992; Bush et al., 2003). Hence they separate at a depth z_{sep} which is defined by $\dot{z}(z_{\text{sep}}) = w_s$. From this definition of separation, and from the self-similar behaviour $\dot{z} \sim z^{-1}$ of MTT56 [equation (1.9b)], the distance of separation is expected to scale like $\mathcal{R}^{-1}$, and we now attempt to verify this scaling experimentally.

Appendix 1.D.2 presents the protocol to measure the depth of separation z_{sep} between turbulent eddies and particles. Essentially, when particles separate from eddies, the patterns made by their trajectories transition from curved and randomly oriented (due to particles whirling inside eddies) to mostly straight and vertical; this enables to measure z_{sep}. Figure 1.9 shows the depth of separation as measured in experiments, and the associated forced-fit curve following a law $z_{\text{sep}} \propto \mathcal{R}^{-1}$. The curve confirms the decrease of z_{sep} with a larger particle size under the trend $z_{\text{sep}} \propto \mathcal{R}^{-1}$ provided by MTT56 in the thermal regime, which is also consistent with previous results in the literature (see the scaling laws in Wang et al., 2014).

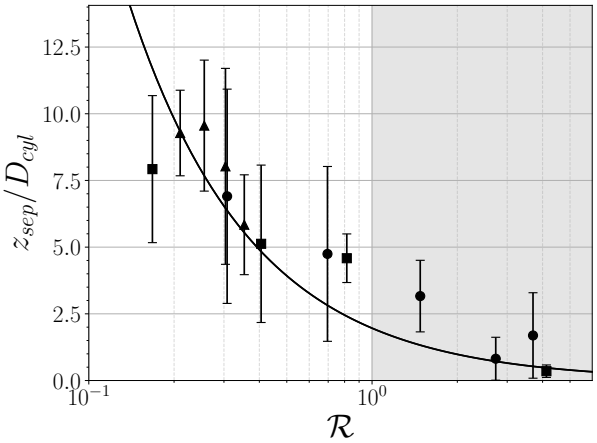

Figure 1.9: *Depth of separation of particles from eddies. The gray shaded area corresponds to the range $\mathcal{R} > 1$ (see figure 1.6) containing clouds which never behave as turbulent thermals. The dark solid line corresponds to the scaling $z_{sep} \propto \mathcal{R}^{-1}$ obtained from the equations of Morton.*

As soon as separation starts, the turbulent thermal has a decreasing mass excess which eventually vanishes to zero. After that, particles fall in a quiescent fluid. Hence, particle clouds can rigorously be considered as turbulent thermals only as long as particles have not separated yet. This has led previous authors (Rahimipour and Wilkinson, 1992; Bush et al., 2003; Lai et al., 2016) to distinguish mainly three regimes in the cloud's evolution: (i) the *acceleration regime*, (ii) the self-similar turbulent *thermal regime* of MTT56, and (iii) the *swarm regime* in which particles settle (mostly) vertically in a quiescent fluid, while the turbulent eddies are left behind particles and viscously decay. This latter regime is analysed in section 1.3.4. For now, we focus on the formation of the swarm *during* separation.

All swarms change morphology during their fall. The swarms which originate from a tur-

bulent thermal are shaped both by particles and by turbulent eddies over the course of separation. This results in a variety of possible swarm morphologies. Monodisperse (figure 1.10a) and polydisperse (figure 1.10b) swarms are illustrated in figure 1.10. We observe that monodisperse clouds produce thin swarms which are concentrated in particles and therefore very bright on the camera. Conversely, polydisperse clouds produce swarms of larger height σ_z, which keeps increasing in time because of the difference in settling velocities between the smallest and largest particles. Consequently, the brightness of these polydisperse swarms decreases in time (compare the brightness of the three snapshots in figure 1.10b). Finally bidisperse swarms evidence a gradual splitting between two particle fronts (not shown here), due to the bimodal distribution of particle sizes.

(a) $\mathcal{R} = 0.814$, $\mathcal{S} = 0.07$ ***(b)*** $\mathcal{R} = 0.696$, $\mathcal{S} = 0.23$

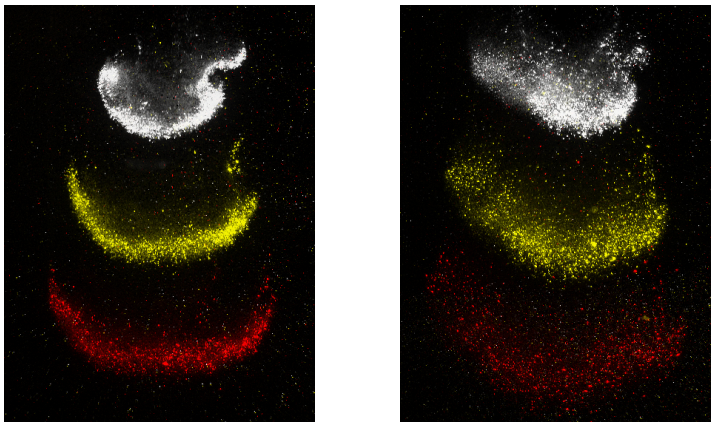

Figure 1.10: *Morphology of swarms for a monodisperse (a) or polydisperse (b) distribution of particles. Colours are used to superimpose snapshots of a swarm at different times. Both photographs are 24.4cm-high, and the time delay between snapshots is (a) 1.6s., (b) 2.0s.*

The role of turbulent eddies in shaping the swarm during separation can be visualised in the Supplemental Material [*Still-ambient-particles-and-rhodamine.avi* (see the case $\mathcal{R} = 0.31$) and *Rouse0p406_STD_0RPM.avi*]. Particles initially swirl within the turbulent thermal, until separation starts, as can be assessed from the vertical motion of particles at the cloud front. Then, two regions can be distinguished. On one hand, particles ahead of eddies have separated and fall vertically at a constant velocity $\dot{z}_{\mathrm{f,s}}$ which is the (front) velocity of the swarm (hence the subscript s), of order w_s. On the other hand, particles in the eddies keep swirling and fall faster than $\dot{z}_{\mathrm{f,s}}$, say at a velocity

$$\dot{z}_{p,e} = \dot{z}_{\mathrm{f,s}} + u(t), \tag{1.10}$$

with $u(t) > 0$ the velocity excess. The width of the swarm is equal to that of the turbulent region which feeds it with particles. During separation the turbulent cloud keeps growing so that particles are gradually shed outwards in the swarm (see figures 1.10a-1.10b).

From these observations, we can propose a model of swarm formation in the framework of MTT56. The description hereafter is for a cloud transitioning from thermal to swarm regime ($\mathcal{R} \leq 1$), but it is also valid for a cloud which directly accelerates to the swarm regime ($\mathcal{R} > 1$) if one cancels the velocity $\dot{z}_e(t)$ of eddies in equations (1.11) and (1.12). New notations

are introduced to rigorously distinguish the behaviours of eddies, particles within eddies, and particles which have separated from eddies.

During separation, consider that turbulent eddies fall with velocity $\dot{z}_e(t)$ (see the left column in figure 1.11) and, for simplicity, assume that they remain in the same self-similar regime despite the loss of particles. This notably implies that α remains constant during separation. Then, the radii of both the patch of turbulent eddies and the nascent swarm increase at a rate

$$\dot{\sigma}_x(t) = \alpha \dot{z}_e(t). \tag{1.11}$$

All particle sets are polydisperse to some extent. Hence, consider a cloud of minimum (respectively maximum) Rouse number $\mathcal{R}_{\min}$ (respectively $\mathcal{R}_{\max}$). The difference between the maximum and minimum settling velocities reads $\Delta w_s = w_s(\mathcal{R}_{\max}) - w_s(\mathcal{R}_{\min}) > 0$. Since the depth of separation $z_{\text{sep}} \propto \mathcal{R}^{-1}$ decreases with $\mathcal{R}$, the cloud's largest particles separate first, with a velocity $w_s(\mathcal{R}_{\max})$ in the reference frame of the laboratory (see the left column in figure 1.11). Meanwhile, smaller particles keep falling through turbulent eddies. Assuming that the drag and buoyancy of these smaller particles are balanced, their upper rear front falls with velocity $w_s(\mathcal{R}_{\min})$ in the reference frame of eddies (right column in figure 1.11). Since eddies fall at velocity $\dot{z}_e(t)$ with respect to the laboratory, it means that the smaller particles fall at velocity $\dot{z}_e(t) + w_s(\mathcal{R}_{\min})$ in the reference frame of the laboratory. Hence, the vertical extent of the particle cloud detected by the cloud-tracking algorithm varies with a rate

$$\dot{\sigma}_z(t) = w_s(\mathcal{R}_{\max}) - (\dot{z}_e(t) + w_s(\mathcal{R}_{\min})) = \Delta w_s - \dot{z}_e(t). \tag{1.12}$$

Let us finally turn to the transfer of particles from eddies to the swarm. We just concluded that in the reference frame of the laboratory, the velocity of the smallest particles inside the turbulent eddies is $\dot{z}_e(t) + w_s(\mathcal{R}_{\min})$. For the sake of simplicity, we adopt the definition $\dot{z}_{p,e} = \dot{z}_e(t) + w_s(\mathcal{R}_{\min})$. Since the largest particles separate first, we expect the swarm front to fall with a velocity $\dot{z}_{\text{f,s}} = w_s(\mathcal{R}_{\max})$. Combining these expressions of $\dot{z}_{p,e}$ and $\dot{z}_{\text{f,s}}$ with equation (1.10), we find $u(t) = \dot{z}_e(t) - \Delta w_s$. Consequently the volume flux $j_p(t) = \phi(t)u(t)$ of particles shed in the emerging swarm is

$$j_p(t) = \phi(t)[\dot{z}_e(t) - \Delta w_s] = -\phi(t)\dot{\sigma}_z(t). \tag{1.13}$$

In equation (1.13), $\phi(t) = N_p[r_p/r(t)]^3$ is the supposedly uniform particle volume fraction within turbulent eddies, with N_p the total number of particles in the cloud, r_p their radius and $r(t)$ the radius of the supposedly spherical cloud in the framework of MTT56. The whole process of swarm formation is sketched in figure 1.11.

The expressions of $\dot{\sigma}_x(t)$, $\dot{\sigma}_z(t)$ and $j_p(t)$ are controlled by the velocity of eddies $\dot{z}_e(t)$ which cannot instantaneously vanish as soon as particles reach the depth $z_{\text{sep}}(\mathcal{R}_{\max})$. Neglecting polydispersity for now ($\Delta w_s = 0$), the fact that eddies keep falling explains why the particle cloud is necessarily contracted ($\dot{\sigma}_z < 0$) and thus particles are compacted ($j_p > 0$) from the thermal to the swarm: this explains why monodisperse swarms have a large aspect ratio σ_x/σ_z even though they originate from an approximately spherical cloud. During separation, eddies keep widening ($\dot{\sigma}_x > 0$) so that particles are gradually shed outward and behind former particles. As a result the swarm takes a bowl shape (see figure 1.10 and Wang et al., 2014, for a clear numerical illustration). However, polydispersity acts against the cloud contraction, and therefore against

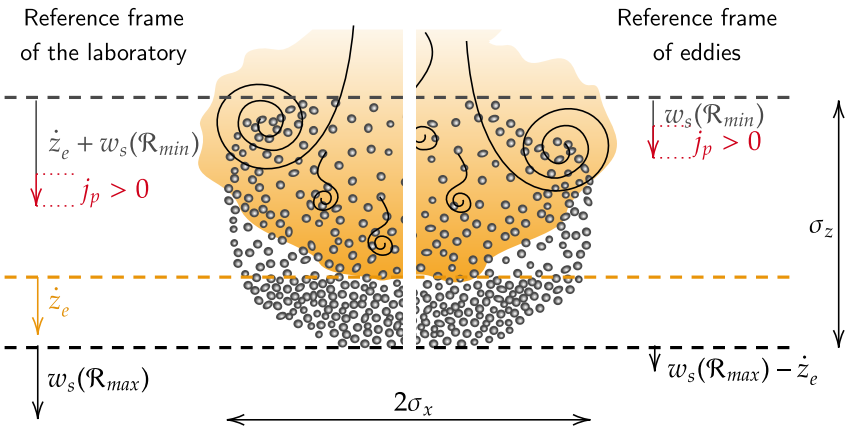

Figure 1.11: *Sketch of the process of cloud contraction and compaction of particles during separation for* $\dot{z}_e(t) > \Delta w_s$.

the compaction of particles. Once separation is over, in the swarm regime the volume flux j_p loses meaning, the cloud keeps a constant lateral extension ($\dot{\sigma}_x = 0$), and it grows vertically at a constant rate $\dot{\sigma}_z = \Delta w_s$ exclusively governed by polydispersity (see below, section 1.3.4).

This simple description captures the evolution of large polydisperse clouds whose particles do seem to keep the entrainment active during separation; see the Supplemental Material *Still-ambient-particles-and-rhodamine.avi* for $\mathcal{R} = 0.308$. It also captures the evolution of particle clouds which never go through the thermal regime for $\mathcal{R} > 1$ (see discussion in section 1.3.4). To sum up, the larger $\mathcal{R}$, the lower the depth of separation, hence the thermal at the start of contraction so the more efficient contraction; a lower depth of separation also implies that the thermal has a smaller size, and so does the swarm. Polydispersity, however, acts to increase the swarm height, hence monodisperse swarms are the thinnest (see figure 1.10).

Note that the role of $\mathcal{R}$ in shaping clouds is not straightforward: the dependency of $\dot{\sigma}_z(t)$ and $j_p(t)$ with $\mathcal{R}$ is not explicit in equations (1.12)-(1.13). One can easily show that $\phi(t)$ is independent of $\mathcal{R}$ for a spherical cloud of constant m_0, and the velocity difference Δw_s is not a function of the mean settling velocity w_s. The role of $\mathcal{R}$ is only implicit in the velocity of eddies $\dot{z}_e(t)$: since during separation the eddies are expected to fall at velocity $\dot{z}(z_{\text{sep}}) = w_s(\mathcal{R})$, at first order we have $\dot{z}_e(t) \simeq \dot{z}(z_{\text{sep}}) = w_s(\mathcal{R})$ during separation. Consequently, for a given velocity difference Δw_s, a cloud of larger particles experiences a larger $\dot{z}_e(t)$ during separation and compacts more than a cloud of smaller particles (see the expression of $\dot{\sigma}_z$ in equation (1.13)). This trend is consistent with the observation of our clouds in experiments.

1.3.4 Swarm regime

Swarms are produced in different ways depending on the size of particles. Particles in the range $\mathcal{R} \leq 1$ initially accelerate, then transition to the thermal regime and finally separate as a swarm. On the opposite, particles in the range $\mathcal{R} > 1$ directly transition from their initial acceleration to the swarm regime, which is characterised by a constant fall velocity. This distinction introduced in figure 1.6 is confirmed in figure 1.12a, which complements the previous figure 1.5 with the kinematics of a cloud directly accelerating to the swarm regime; see blue

dashed curves for $\mathcal{R} = 1.48$.

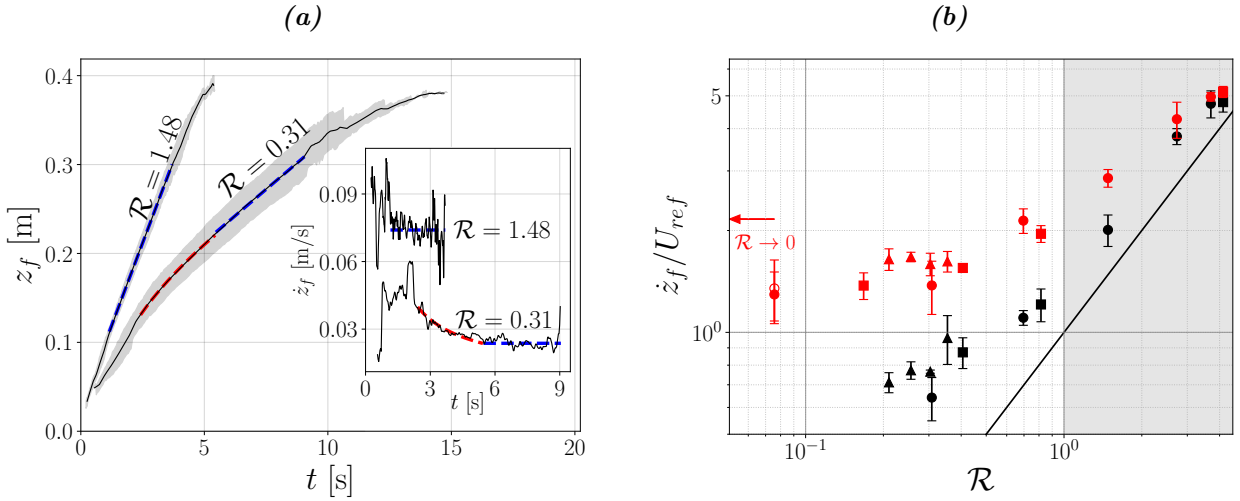

Figure 1.12: *(a) Kinematics of two clouds of different Rouse numbers. (——) Average cloud front position in time with the standard deviation due to averaging indicated in gray shaded area; (- - -) fit of thermal regime; (- - -) fit of swarm regime. (b) ● Average cloud front velocity $\dot{z}_{f,s}$ during the swarm phase; ● maximum cloud front velocity $\dot{z}_{f,max}$; (——) line of equation $\dot{z}_f = w_s$. The red arrow shows the measured value for the asymptotic limit $\mathcal{R} \to 0$ corresponding to salty thermals, and the gray shaded area corresponds to clouds which never behave as a turbulent thermal.*

Recall that particles are expected to separate from eddies at their terminal velocity so that the constant swarm velocity $\dot{z}_{\mathrm{f,s}}$ should be of order w_s. Particles having $\mathcal{R} < 0.2$ separate too deep in the tank for the swarm regime to be analysed. For other clouds, the constant velocity $\dot{z}_{\mathrm{f,s}}$ is measured and visible in figure 1.12b in dark symbols. Up to a constant offset of order $O(1)$, measurements prove to be reasonably close to the reference value w_s in dark solid line, all the more as $\mathcal{R}$ is larger. The fact that swarms of smaller particles fall faster than w_s is interpreted as a consequence of the capacity of numerous smaller particles to drag fluid downward with them through their hydrodynamical interactions by displacing fluid (Yamamoto et al., 2015; Pignatel et al., 2011), whereas fewer larger particles behave individually and modify only the flow close to themselves in a small wake (Subramanian and Koch, 2008).

The maximum cloud front velocity $\dot{z}_{\mathrm{f,max}}$ measured during every experiment is also computed and shown with red symbols in figure 1.12b. As $\mathcal{R}$ increases, the velocities $\dot{z}_{\mathrm{f,s}}$ and $\dot{z}_{\mathrm{f,max}}$ get closer. This is due to the reduced duration of the thermal regime, which is ultimately shut off, leading clouds of large Rouse number to directly accelerate to reach their maximum velocity as a single particle would, hence $\dot{z}_{\mathrm{f,max}} \simeq w_s$.

1.4 Particle clouds in a rotating environment

1.4.1 Formation of a columnar flow

From the previous section, we can expect – as the following section will confirm – that clouds containing particles of vanishingly small Rouse number behave similarly as salt-water clouds,

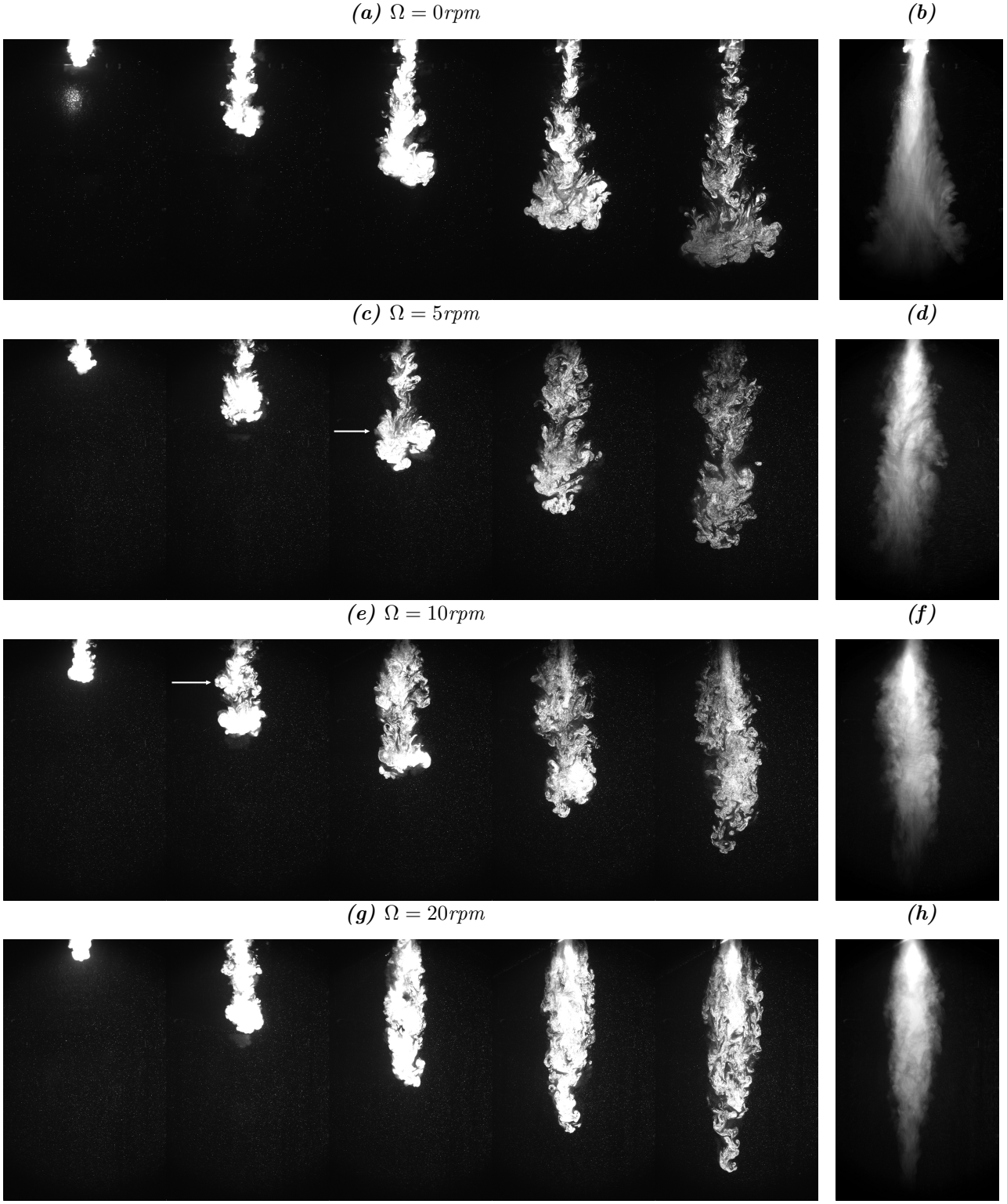

Figure 1.13: *(a,c,e,g): Salt water clouds for varying Ω. The time lapse between snapshots is always 1.6s, and photographs are always 45cm-high. When observable, the depth $z_{f,col}$ where the cloud becomes columnar is indicated by a white arrow. (b,d,f,h): Pixel-by-pixel average of light intensity of all photographs taken during the experiment on the same row, of respective duration (b) 8.3s, (d) 9.1s, (f) 9.8s, (h) 7.8s.*

and the larger $\mathcal{R}$ the larger the discrepancy between their behaviours. Therefore, we start by analysing the influence of rotation on salt-water clouds.

In figure 1.13, the most striking observation is that rotation interrupts entrainment at some depth $z_{f,\mathrm{col}}$, marking a transition from a regime of expanding cloud to a vortical columnar flow of constant radial extension for $z \geq z_{f,\mathrm{col}}$ (see white arrows in figures 1.13c and 1.13e; the transition is also visible in a video in the Supplemental Material [*SaltWater_10RPM.avi*]). Initially the cloud inertia is large, hence as long as the cloud is expanding, one may neglect the influence of rotation and consider that the cloud follows the model of MTT56: the cloud grows and decelerates due to the entrainment of ambient fluid, gradually reducing the cloud inertia. Simultaneously, entrainment enables the ambient fluid in solid body rotation to gradually penetrate through the turbulent thermal and increase its total kinetic momentum. The transition is expected to happen when the Coriolis force predominates over the cloud inertia (Ayotte and Fernando, 1994; Helfrich, 1994; Fernando et al., 1998). This can be quantified with a Rossby number based on the inflow of ambient fluid at the thermal interface. There, the entrained fluid is subject to the Coriolis force $2\Omega v_e$ with v_e the entrainment velocity [equation (1.7)], and its inertia reads $(\dot{z}_f/r)v_e$, leading to

$$Ro(z) = \frac{\dot{z}_f}{2\Omega r}. \tag{1.14}$$

The front velocity $\dot{z}_f$ is used rather than $\dot{z}$ because the front is easily traceable from videos, and more meaningful due to a modification of the residence time of particles when $\Omega > 0$, as discussed in section 1.4.4.

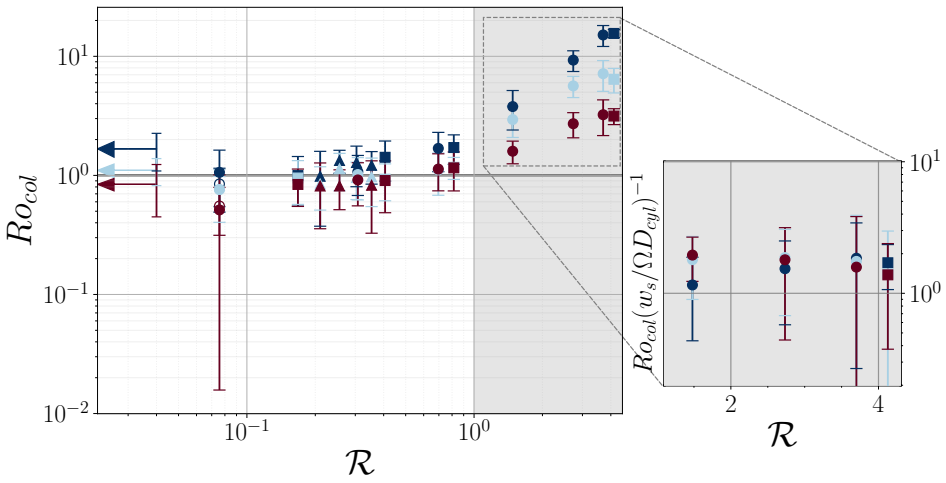

Figure 1.14: *Transitional Rossby number Ro_{col} computed at depth $z \geq z_{f,col}$. The inset validates the scaling $Ro_{col} \simeq w_s/\Omega D_{cyl}$ in the range $\mathcal{R} > 1$ (gray shaded area) corresponding to clouds which are columnar due to particles falling as swarms. Colour code: (●) $\Omega = 5rpm$, (●) $\Omega = 10rpm$, (●) $\Omega = 20rpm$.*

The transition is expected when the Rossby number is of order unity. For simplicity and up to a constant factor, we will consider $Ro_{\mathrm{col}} = Ro(z_{f,\mathrm{col}}) = 1$ as the condition of transition to a vortical columnar flow. To test this condition, we compute the transitional Rossby number

from the automatic cloud-tracking algorithm of Appendix 1.C. The depth of transition is defined due a change in the clouds' kinematics, from an initial phase of deceleration when $z < z_{f,\mathrm{col}}$ to a phase of constant velocity when $z > z_{f,\mathrm{col}}$ (see section 1.4.4). Then, measurements of the Rossby number $\dot{z}_f(z)/2\Omega\sigma_x(z)$ are approximately constant for $z \geq z_{f,\mathrm{col}}$, hence the values of this Rossby number are averaged for $z \geq z_{f,\mathrm{col}}$ where noise is low enough. Results are shown in figure 1.14 in ordinate, as a function of $\mathcal{R}$. For any given Ω, measurements confirm that $Ro_{\mathrm{col}} \simeq 1$ within the uncertainty margin of experiments in the range $\mathcal{R} \leq 1$. Therefore, in a rotating environment, this range of Rouse numbers corresponds to clouds whose particles fall in a vortical columnar flow below $z_{\mathrm{f,col}}$.

Before transition $Ro(z) > 1$ so inertia predominates over the Coriolis force, and if one neglects rotation, clouds are expected to behave as turbulent thermals. According to this simple picture, which is rigorously applicable when $Ro(z) \gg 1$, the condition $Ro_{\mathrm{col}} = 1$ yields $z_{\mathrm{f,col}} \sim \Omega^{-1/2}$. Although we lack additional values of Ω to quantitatively confirm this scaling, it is compatible with our present measurements made for three different values of $\Omega > 0$, and was already verified in past experiments with one-phase thermals (see Ayotte and Fernando, 1994; Helfrich, 1994). Thus, the faster the spinning, the lower the depth of transition, as observed in figure 1.13.

In figure 1.14, in the range $\mathcal{R} > 1$ the transitional Rossby number Ro_{col} is larger than unity. This is because such clouds are columnar not due to rotation, but because particles behave as swarms. Hence particles fall with a constant velocity of order w_s and clouds hardly grow so their diameter is approximately equal to D_{cyl}. Consequently $Ro_{\mathrm{col}} \simeq w_s/\Omega D_{\mathrm{cyl}}$, as confirmed by the inset of figure 1.14.

1.4.2 Thermal regime with background rotation: entrainment levelling

Let us focus on the evolution of clouds before the transition to a vortical columnar flow. As long as $Ro(z) > 1$ and after a phase of acceleration, the cloud is considered to evolve as a turbulent thermal which entrains ambient fluid and grows linearly in depth. The entrainment capacity of all particle clouds is compared to the reference of salt water thermals in figure 1.15. This entrainment capacity is not presented for $\Omega = 20$ rpm because at such rotation rate, the depth of transition $z_{\mathrm{f,col}}$ is too low for the entrainment rate to be measurable above $z_{\mathrm{f,col}}$.

At both $\Omega = 5$ rpm (figure 1.15a) and $\Omega = 10$ rpm (figure 1.15b), the entrainment coefficient suddenly drops for $\mathcal{R} > 1$ as previously seen for $\Omega = 0$ rpm. This is again due to particles decoupling from the fluid due to their inertia. Most interestingly, in the range $\mathcal{R} \leq 1$ figures 1.15a and 1.15b show that $\mathcal{R}$ hardly has any influence on $\alpha/\alpha_{\mathrm{salt}}$, and the entrainment capacity α is levelled to a value close to α_{salt}. This contrasts with observations at $\Omega = 0$ in figure 1.6. In other words, because of rotation, particulate effects appear to be inoperative, hence particle clouds entrain approximately as much as their salt-water counterparts, as evidenced by the overlap of most data points with the errorbar of α_{salt} in red hatchings.

It may come as a surprise that rotation suppresses any local maximum value of $\alpha/\alpha_{\mathrm{salt}}$ in the range $z < z_{f,\mathrm{col}}$ even though $Ro(z < z_{f,\mathrm{col}}) > 1$ i.e. inertia predominates over the Coriolis force. In a still environment, we observe an enhancement of the entrainment rate for $\mathcal{R} \simeq 0.3$ where particles concentrate, especially in the peripheral eddies of the particle cloud (see figure 1.7).

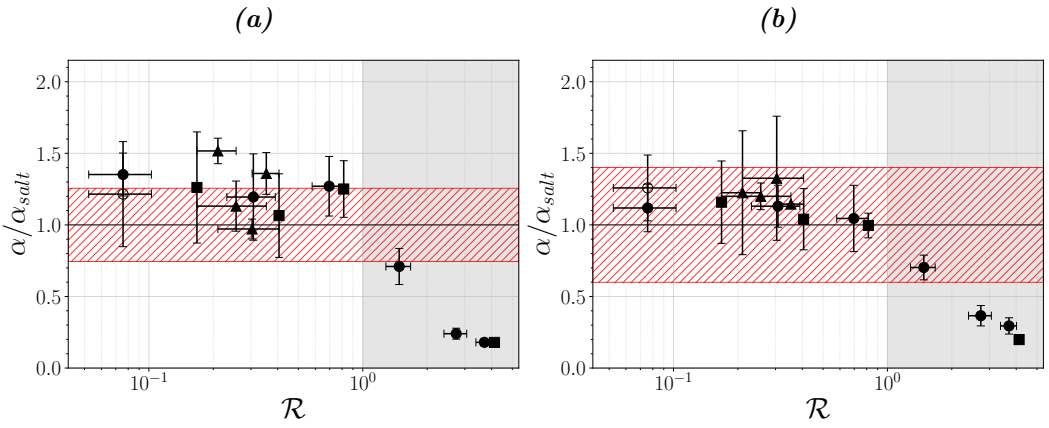

Figure 1.15: *Entrainment capacity of particle clouds for different Rouse numbers at (a)* $\Omega = 5rpm$ *and (b)* $\Omega = 10rpm$. *For further information on colours and symbols, see figure 1.6.*

At the particles' scale, the Coriolis force has a negligible dynamical influence (it is three to four orders of magnitude lower than the particles' inertia), so the disappearance of the enhancement of α is necessarily due to the influence of the Coriolis force on the fluid. This influence acts before $z = z_{f,\mathrm{col}}$, because the condition $Ro(z_{f,\mathrm{col}}) = 1$ holds for a transition of the *entire* cloud, i.e. when rotation starts to fully govern the cloud dynamics. Conversely, the particulate effects at stake are rather *localised* at the interface between the cloud and the ambient fluid, where the entrainment flux affects the flow as soon as the inflow starts. Consequently, rotation is expected to have a non-negligible influence on the outer shell of the cloud for a Rossby number $Ro(z)$ larger than unity (i.e. before $z_{f,\mathrm{col}}$ is reached) by modifying the structure of the flow and gradually tilting vortices along $\vec{e}_z$. Such modifications likely prevent particles from concentrating and sweeping on the downward sides of eddies, thus switching particulate effects off. Because in our experiments at $\Omega \geq 5$ rpm, the Rossby number never exceeds 6 when $\mathcal{R} \leq 1$, clouds are never sufficiently inertial for their interface to be unaffected by rotation (as pointed out by Frank et al. (2017); Fabregat Tomàs et al. (2017) in the case of continuous injections of buoyancy, rotation modifies a plume's dynamics even for modest Rossby numbers; furthermore, rotation eventually influences *any* plume as long as its injection is long enough, due to the conservation of angular momentum, see Frank et al. (2017)). Although the study of Sutherland et al. (2021) bears upon the behaviour of plumes in background rotation, it inspired our reflections on the transition to vortical columnar flows and we refer the reader to this study for additional information on the flow that develops with a starting plume in background rotation. Further investigation on the behaviour of particles and the structure of the flow close to the interface requires additional visualisations of particles in horizontal planes and quantification of the velocity field, which is beyond the scope of the present study.

Another ingredient which may act to inhibit particulate effects is the centrifugal force. In fact, although this force is negligible compared to gravity (the ratio $r\Omega^2/g$ is only of order 10^{-1} for the largest rotation rate $\Omega = 20$rpm and for $r = 7D_{\mathrm{cyl}}$ which corresponds to the maximum radial distance to the axis of rotation), depending on the value of Ω we observe that the centrifugal force due to the rotating table is comparable with the centrifugal force exerted

on particles when they swirl in eddies at 0rpm. Hence, the centrifugal force due to $\Omega > 0$ may switch off preferential concentration as well as preferential sweeping, so that particles cannot concentrate to force the flow through two-way coupling.

1.4.3 Swarm regime

Figure 1.16a illustrates the influence of rotation due to the overlay of integral images for different rotation rates and identical Rouse numbers: the faster the rotation, the narrower the column (see also the Supplemental Material *Rouse0p406_0-5-10RPM.avi*), which is consistent with past observations for miscible thermals (Ayotte and Fernando, 1994; Helfrich, 1994) and bubble-laden plumes (Frank et al., 2021). To confirm this observation, we perform quantitative measurements of the width of columns through the quantity $\sigma_{x,\infty}$. For a given experiment, it corresponds to the average value of $\sigma_x(z)$ (the cloud width detected by the cloud-tracking algorithm; see appendix 1.C) after it becomes approximately constant. Figure 1.16b confirms that the larger Ω, the narrower the column. For $\Omega = 20$ rpm, the column half width is approximately $\sigma_{x,\infty} = D_{\text{cyl}}/2$ because $z_{f,\text{col}}$ is so low that the cloud has no time to grow through turbulent entrainment before becoming columnar, so it remains as large as the cylinder of injection. Similarly, all clouds in the range $\mathcal{R} > 1$ never grow as a thermal and therefore have a width $\sigma_{x,\infty} = D_{\text{cyl}}/2$.

The decreasing column width with increasing Ω can be explained from geometrical arguments. Before transition when $Ro(z) > 1$, for simplicity one may assume that clouds behave as self-similar turbulent thermals. Then, from the scalings (1.9a)-(1.9b) of MTT56, the width of a cloud should scale like $\sim \Omega^{-1/2}$ when $z_f = z_{f,\text{col}}$, as argued and verified by Ayotte and Fernando (1994); Helfrich (1994). Our experiments are performed for three different values of $\Omega > 0$ which is insufficient to quantitatively confirm this scaling, yet we note that it is compatible with our present measurements, using $\sigma_{x,\infty}$ as a measurement of the cloud radius at $z = z_{f,\text{col}}$. In other words, as Ω increases, the condition $Ro(z) = 1$ is reached at lower depths hence columns are narrower.

A remark should be made on the fact that the constant width of columns is a robust observation for low Rouse numbers, but for large Rouse numbers it is an approximation whose accuracy is quantified by the error bars in figure 1.16b. In fact, for the largest Rouse numbers, particles ultimately fall as swarms. In the absence of background rotation, the latter slowly expand along their fall. In fact, Subramanian and Koch (2008) in the range $Re_p \ll 1$, and later Daniel et al. (2009) in the range $Re_p \in$[93-425], showed that hydrodynamical interactions between particles result in a growth of swarms as $\sigma_x \sim t^{1/3}$. Because of the variability between several realisations, and due to our limited field of view after separation happens, our measurements do not enable us to discriminate between a sublinear or linear evolution of σ_x in depth for the swarm regime. Hence, we compute indicative constant values of the growth rate of swarms $d\sigma_x/dz$ obtained from linear regressions in the range $z > z_{\text{sep}}$ if $\Omega = 0$, and we perform the same analysis in the range $z_f > z_{f,\text{col}}$ when $\Omega > 0$. Results are shown in figure 1.17 for clouds which slightly grow indeed, behaving as swarms. In the range $\mathcal{R} > 1$, we observe that the more inertial the particles, the more the curves collapse on the dark symbols for $\Omega = 0$, indicating that particles are less and less sensitive to rotation due to their decoupling from the fluid. In the range $\mathcal{R} \leq 1$, the minimum Rouse number for which $d\sigma_x/dz > 0$ is measurable

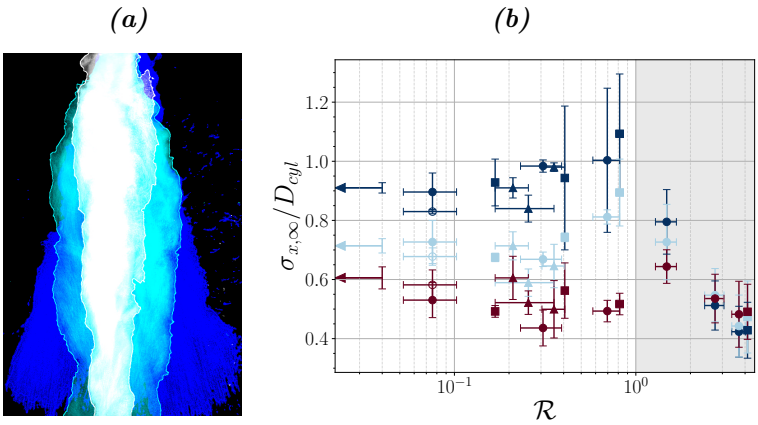

Figure 1.16: *(a) Overlay of colourised images of height 37.8cm, corresponding to pixel-by-pixel standard deviations of light intensity of three different experiments of Rouse number $\mathcal{R} = 0.168$ at 0rpm (blue), 5rpm (cyan) and 20rpm (white). (b) Dimensionless width of the rotating columns in the range $z \geq z_{f,col}$ as a function of $\mathcal{R}$. Arrows and their errorbars correspond to values for salty thermals. Colour code: (●) $\Omega = 5rpm$, (●) $\Omega = 10rpm$, (●) $\Omega = 20rpm$.*

tends to increase with Ω; additionally, for a given Rouse number, the larger Ω the more $d\sigma_x/dz$ differs from the reference values in a still environment. Both of these observations are due to the larger azimuthal inertia of the fluid and the increasing stiffening of radial motions when Ω increases, which require a larger particle inertia to be overcome.

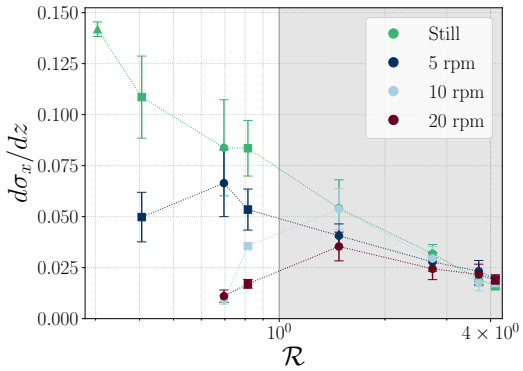

Figure 1.17: *Lateral growth rate of clouds which behave as swarms and thus slightly grow in depth. Measurements are performed with least squares linear regressions on $\sigma_x(z)$, i.e. assuming that $d\sigma_x/dz$ is constant.*

1.4.4 Kinematics and residence time

The influence of rotation on a cloud front velocity is now assessed. The front velocity is observed to be approximately constant below the depth $z_{f,\mathrm{col}}$. Since we can hardly distinguish between particles which fall in a vortical columnar flow, and swarms which are decoupled from

the fluid, in both cases the constant velocity for $z > z_{f,\mathrm{col}}$ is denoted $\dot{z}_{\mathrm{f,s}}$ to be consistent with notations used for clouds in a still environment, and we talk about a swarm regime. This velocity is determined from a linear fit of $z_f(t)$ as illustrated in figure 1.18a. Results for the velocities are shown in figure 1.18b. In the range $\mathcal{R} > 1$, the influence of Ω noticeably decreases with increasing $\mathcal{R}$ and curves collapse on the $\Omega = 0$ curve. This is due to particles being more and more insensitive to the swirling flow, especially as Ω is lower. In the range $\mathcal{R} \leq 1$, the larger the rotation rate, the larger the front velocity (see also the Supplemental Material *Rouse0p406_0-5-10RPM.avi*). This trend is mainly interpreted through the reduction of the column radius $r \simeq \sigma_{x,\infty}$ (see figure 1.16b) which, in turn, increases the particle volume fraction $\phi = 3m_0/4\pi\rho_p r^3$. From a macroscopic point of view, this results in a larger effective cloud density $\rho = \phi\rho_p + (1-\phi)\rho_f$, enhancing the cloud velocity through the reduced gravity $g(\rho/\rho_f - 1)$.

It should be mentioned that fitting an affine model on the average curve $z_f(t)$ is at odds with past measurements which seem in agreement with the scaling $z_f(t) \sim t^{1/2}$ proposed by Ayotte and Fernando (1994) and Helfrich (1994). There seems to be no physical reason for columnar clouds to keep decelerating as turbulent thermals following the law $z_f(t) \sim t^{1/2}$ after the turbulent entrainment and lateral cloud growth are interrupted by rotation, thus cancelling the mixing drag. Conversely, the previous arguments are consistent with a constant cloud front velocity. Yet, we still note a subtle decrease of the clouds' velocity in time for the lowest Rouse numbers. This slight decrease is ultimately expected since a lot of the buoyant material remains in suspension behind the cloud front, to such an extent that the cloud front gradually thins out (see figure 1.13) thus reducing the front effective density and velocity. We expect the front deceleration to depend on the rate of detrainment of buoyant material in the columnar cloud wake, which cannot be measured from our planar visualisations.

Further understanding can come from analysing how particles distribute and settle in columnar clouds. Figure 1.19 combines snapshots and Hovmöller diagrams of the light intensity obtained for every image of an experiment after averaging the values of all pixels along every row. For very large Rouse numbers (see figures 1.19j-l), particles decouple from the fluid due to their inertia and fall as swarms with a constant velocity. For lower Rouse numbers (see figures 1.19a-i), compared to clouds falling in a still environment, the Hovmöller diagrams confirm that due to rotation, the cloud front velocity is approximately constant and detrainment is enhanced since the residence time of particles at any depth is visibly increased. On the Hovmöller diagrams, the fast concentrated frontal blob falling with constant velocity corresponds to the cloud. Conversely, the slow dilute region where particles settle on a much larger time scale on average corresponds to the stem of detrained particles (see respectively red and white regions in figures 1.19g-h). Furthermore, images with rhodamine confirm that the frontal blob corresponds to the turbulent cloud initially dyed with rhodamine, since this blob drags rhodamine down the tank (see figure 1.19i in particular). Thus, detrainment is enhanced by rotation; in addition, we observe that the frontal blob laterally shrinks as it falls in the tank. These observations might result from the interaction between the rotating ambient and the turbulent cloud at its interface, where the cloud seems to be gradually peeled off by a strong shear, thereby switching off particulate effects. Further investigation would require additional observation in a horizontal plane, as well as measurements of the fluid velocity field.

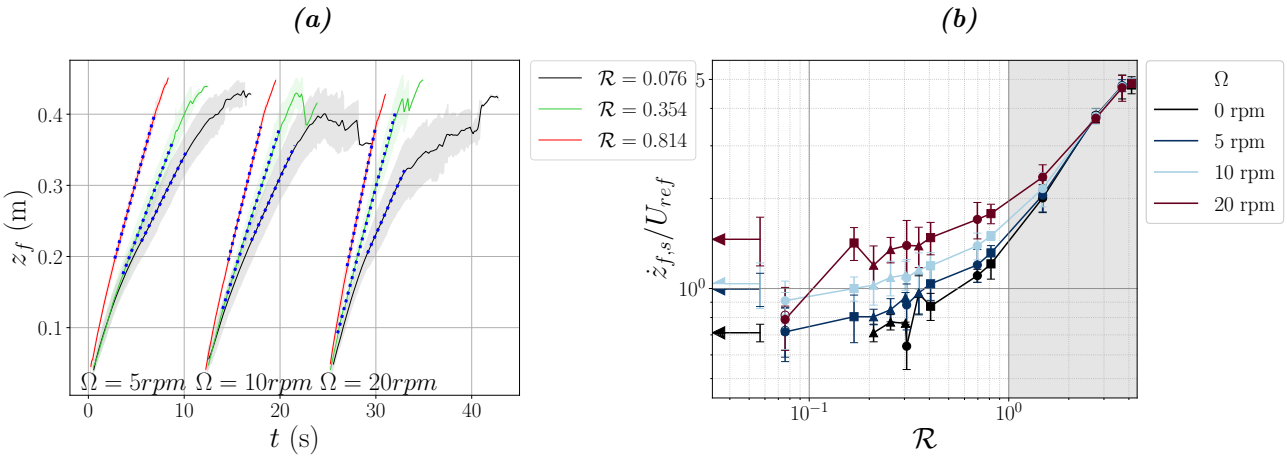

Figure 1.18: *(a) Examples of the determination of the constant front velocity during the swarm regime. Solid lines correspond to $z_f(t)$ averaged over all realisations, and shaded areas correspond to uncertainty margins, which are extremely small for large Rouse numbers. Colours vary with the Rouse number, and the curves are horizontally shifted for $\Omega = 10$ rpm and $\Omega = 20$ rpm for clarity. The linear fits are shown as dotted blue lines in the time ranges that minimise the error. (b) Evolution of the cloud front velocity in the swarm regime for various angular velocities of the rotating table. Arrows and their errorbars correspond to values for salty thermals.*

1.5 Summary and conclusion

Instantaneous releases of a buoyant material in still water behave differently if the material is salt water or heavy particles. Particle clouds initially behave as turbulent thermals, and the difference manifests through an increase of their entrainment capacity compared to salty clouds, with a maximum of enhancement for a finite inertia corresponding to $\mathcal{R} \simeq 0.3$ (figure 1.6). The origin of this enhancement likely stems from particulate effects which have already been observed in canonical turbulent flows, mainly preferential concentration and preferential sweeping. A second difference is due to a transition from the thermal regime to the swarm regime because particles decouple from turbulent eddies due to their inertia and eventually separate from them.

Adding background rotation, the particulate enhancement of entrainment is inhibited (figure 1.15), likely due to the influence of the Coriolis force on the inflow of entrained fluid at the cloud interface. When the Coriolis force predominates on the dynamics of the whole cloud ($Ro \leq 1$), the latter transitions to a regime of vortical columnar flow (figure 1.14). Together with the decoupling of particles from the flow (separation), this transition adds a new limitation on the duration of turbulence. The model of Morton et al. (1956) appears like an efficient framework to anticipate the different regimes experienced by the particle clouds throughout their fall.

Polydisperse, bidisperse and monodisperse particle sets were used to assess the role of polydispersity in the clouds dynamics. It appears that polydispersity plays little part in turbulent clouds and vortical columnar flows. It essentially modifies the morphology of swarms during and after separation (section 1.3.3).

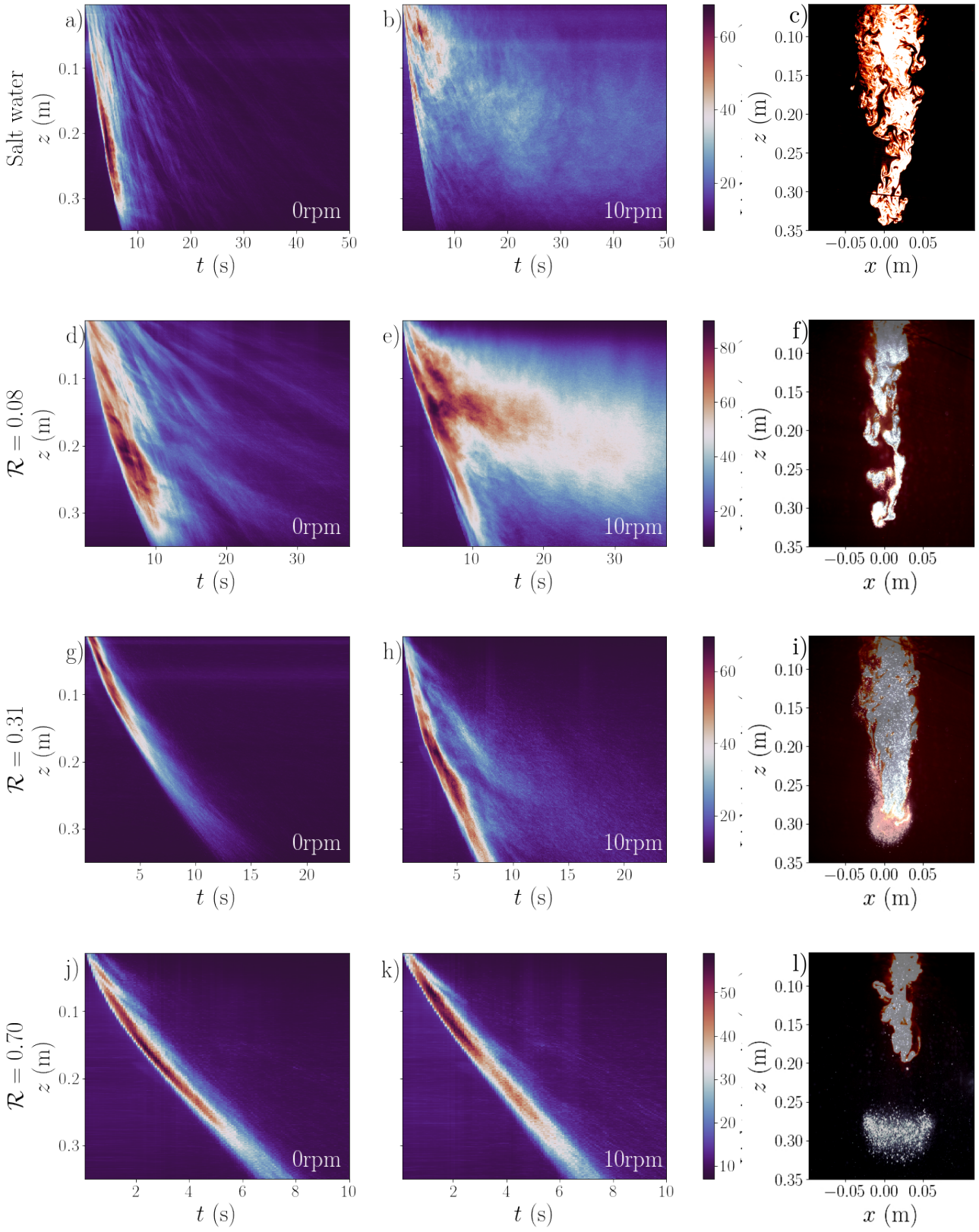

Figure 1.19: *Left and middle columns respectively correspond to the Hovmöller diagrams of the horizontally-averaged light intensity of clouds falling respectively at 0rpm and 10rpm. Every row corresponds to a different Rouse number as indicated on the left-hand side. Right column: snapshots of particles falling with rhodamine at 10rpm.*

It is worth mentioning that the inhibition of the enhancement of entrainment due to background rotation is likely due to the fact that the clouds' inertia is not large enough for them to be completely insensitive to rotation. Increasing their initial inertia by releasing a larger mass excess m_0 could enable to observe a range of depths where rotation leaves them unaffected. Additional measurements for other (lower) values of Ω would also be beneficial to extract quantitative scalings with the rotation speed Ω.

Some open questions remain. According to the literature on particle-laden turbulent flows (e.g. Balachandar and Eaton, 2010; Monchaux and Dejoan, 2017) we expect inertial effects to be optimal when the ratio of the settling velocity w_s over the *local* flow velocity within the cloud is of order one – in other words when a *local* Rouse number is of order unity. For our smallest particles, this velocity ratio remains small because the clouds never fall deep enough to decelerate until this local Rouse number becomes of order unity. The entrainment rates of turbulent thermals and our clouds are constant before separation. Yet, if α varies on a length scale larger than our field of view (so that its variation could not be assessed), one can imagine that in a larger tank, these clouds would experience a further increase of α when the local Rouse number gets close to unity. This hypothesis cannot be ruled out without additional experiments at a larger scale.

Further work on such particle clouds requires to quantify the flow produced by particles through PIV in a vertical laser sheet. Additional visualisations of the glass beads and of PIV particles in horizontal planes would prove enlightening to understand the structure of clouds in the presence of background rotation. It could clarify the mechanism through which the influence of rotation gradually contaminates an entire cloud from its periphery to its entirety, following similar work on plumes (Sutherland et al., 2021). To this end, we would also benefit from experiments at a larger scale with a larger mass excess m_0 to better separate scales and dynamical regimes.

1.6 Acknowledgements

The authors acknowledge funding by the European Research Council under the European Union's Horizon 2020 research and innovation program through Grant No. 681835-FLUDYCO-ERC-2015-CoG. The authors thank V. Dorel and L. Huguet for the setting of a first version of the experiment and metrology, as well as for their preliminary results that guided the present work.

1.A List of experiments

Table 1.2 lists the number of experiments processed for each couple $(\Omega, \mathcal{R})$. Numbers tend to be higher when particles are more sensitive to initial conditions, or when measurements are very sensitive to noise because of the considerable dilution of particles when the cloud falls. Numbers also vary because some experiments were not processed, because clouds occasionally went out of the laser sheet, or pieces of latex membrane fell with clouds in the laser sheet, introducing a bias in measurements.

Ω \ $\mathcal{R}$	Salt water	6.00×10^{-4}	7.57×10^{-2} ○	7.57×10^{-2} ●	0.308	0.696	1.48	2.73	3.70
0 rpm	6	5	16	8	5	6	5	4	10
5 rpm	12	0	19	7	15	10	10	5	5
10 rpm	13	0	21	6	15	9	11	10	5
20 rpm	17	0	18	3	12	15	15	5	9

Ω \ $\mathcal{R}$	0.168	0.406	0.814	4.13	0.210	0.255	0.304	0.354
0 rpm	8	5	6	6	6	3	2	4
5 rpm	9	14	9	5	4	4	4	4
10 rpm	10	5	5	5	5	7	5	5
20 rpm	5	6	5	5	6	5	5	5

Table 1.2: *Number of experiments which are processed for each couple* $(\Omega, \mathcal{R})$*. For* $\mathcal{R} = 6.00 \times 10^{-4}$*, experiments were conducted only to determine the entrainment coefficient of clouds at 0rpm (see section 1.3.1).*

1.B List of notations

Table 1.3 lists the notations used in this study for reference.

Defined in	Variable	Description
Section 3.2.1	ρ_f	Density of ambient fluid
Section 3.2.1	ν	Viscosity of ambient fluid
Section 3.2.1	Ω	Angular velocity of the rotating table
Section 3.2.1	D_{cyl}	Diameter of the cylinder
Section 3.2.1	m_0	Total mass excess (1g)
Section 3.2.1	ρ_p	Density of the glass beads
Section 3.2.1	r_p	Mean radius of a particle set
Section 3.2.1	H_0	Water height above the latex membrane
Section 1.2.2	l_M	Morton length
Section 1.2.2	g	Acceleration of gravity
Section 1.2.2	ρ_0	Initial cloud density
Section 1.2.2	U_{ref}	Reference velocity of clouds
Section 1.2.3	σ_p	Standard deviation of a distribution of particles' radii
Section 1.2.3	$\mathcal{S}$	Dimensionless number quantifying polydispersity
Section 1.2.3	p	A percentage to define bidisperse particle sets
Section 3.2.2	w_s	Terminal velocity of a single particle
Section 3.2.2	Re_p	Particulate Reynolds number
Section 3.2.2	w_s^{Stokes}	Stokes terminal velocity
Section 3.2.2	w_s^{Newton}	Newton's terminal velocity
Section 3.2.2	C_d	Drag coefficient of a spherical particle
Section 3.2.2	N_p	Total number of particles in a cloud
Section 3.2.2	Π	Dimensionless average radius of a particle set
Section 3.2.2	$\mathcal{R}$	Rouse number
Section 1.3.1	r	Radius of a spherical thermal
Section 1.3.1	ρ	Density of a uniform spherical thermal
Section 1.3.1	z	Vertical position of the centre of mass of a uniform spherical thermal
Section 1.3.1	$\dot{z}$	Vertical velocity of the centre of mass of a thermal; by extension in experiments, vertical velocity of the barycentre of particles within a cloud
Section 1.3.1	v_e	Entrainment velocity
Section 1.3.1	α	Coefficient of entrainment
Section 1.3.1	C_D	Drag coefficient of a spherical thermal
Section 1.3.2	z_f	Depth of a cloud's front
Section 1.3.2	$\dot{z}_f$	Vertical velocity of a cloud's front
Section 1.3.2	α_{salt}	Entrainment coefficient of salt water thermals
Section 1.3.3	z_{sep}	Depth of separation between particles and eddies
Section 1.3.3	σ_x	Radius of a cloud computed as a standard deviation
Section 1.3.3	σ_z	Height of a cloud computed as a standard deviation
Section 1.3.3	$\dot{z}_{\text{f,s}}$	Constant vertical front velocity in the swarm or vortical columnar regimes
Section 1.3.3	$\dot{z}_{p,e}$	During separation: vertical velocity of particles still present inside eddies
Section 1.3.3	$u(t)$	During separation: velocity excess of swirling particles wrt separated particles
Section 1.3.3	$\dot{z}_e$	During separation: vertical velocity of eddies
Section 1.3.3	$\dot{\sigma}_x$	Growth rate of the cloud radius
Section 1.3.3	$\dot{\sigma}_z$	Growth rate of the cloud height
Section 1.3.3	$\mathcal{R}_{\text{min}}$	Rouse number of the smallest particles within a cloud
Section 1.3.3	$\mathcal{R}_{\text{max}}$	Rouse number of the largest particles within a cloud
Section 1.3.3	Δw_s	Difference of terminal velocities between the largest and smallest particles
Section 1.3.3	j_p	During separation: volume flux of particles shed in the emerging swarm
Section 1.3.3	ϕ	Particles' volume fraction
Section 1.3.4	$\dot{z}_{\text{f,max}}$	Maximum cloud front velocity
Section 1.4.1	$z_{\text{f,col}}$	Depth of transition from a thermal to a vortical columnar flow
Section 1.4.1	$Ro(z)$	Cloud Rossby number
Section 1.4.1	Ro_{col}	Rossby number computed at the depth $z_{\text{f,col}}$
Section 1.4.3	$\sigma_{x,\infty}$	(Possibly asymptotically) constant radius of a vortical columnar cloud

Defined in	Variable	Description
Appendix 1.C	N_0	Otsu's method: number of pixels in class 0
Appendix 1.C	N_1	Otsu's method: number of pixels in class 1
Appendix 1.C	I_0	Otsu's method: average intensity in class 0
Appendix 1.C	I_1	Otsu's method: average intensity in class 1
Appendix 1.C	δ^*	Cloud-tracking: interparticle distance where a cloud has low concentration
Appendix 1.C	Δ^*	Cloud-tracking: interparticle distance outside of clouds
Appendix 1.C	I_{thr}	Cloud-tracking: threshold intensity to binarise images
Appendix 1.C	σ	Cloud-tracking: size of the Gaussian kernel defining a hull around a cloud
Appendix 1.D	N^*	A number of snapshots to compute standard deviations of light intensity
Appendix 1.D	Σ_{sep}	Expanded uncertainty on the value of z_{sep}

Table 1.3: *List of variables, the section in which they are defined, and a short description.*

1.C Measurements from the automatic cloud tracking

Several quantities are computed from an automatic processing of videos of falling glass beads (visualised by the camera with a green filter). This processing consists of an automatic detection of the particle cloud as follows. The signal received by the camera is never a flat field, even before cloud launching at $t = 0$: this means that inhomogeneities are always present in the light intensity, even in the absence of particle cloud. To correct them, a background photograph is always saved at $t < 0$. Then, all photographs of the cloud at $t > 0$ are divided by this initial background image, so that pixels without particles should have a value of 1, while pixels with particles should have larger values of relative light intensity. The aim, then, is to define a threshold on light intensity to binarise the image. This threshold should be time-dependent since the cloud keeps diluting so that its average light intensity keeps decreasing. An appropriate binarisation therefore depends on the histogram of each photograph, and Otsu's method (Otsu, 1979) is adopted to process experiments. It consists in an optimisation algorithm which maximises the inter-class variance between the two resulting levels of intensity (denoted 0 or 1), the inter-class variance being proportional to $N_0 N_1 (I_0 - I_1)^2$ with $N_{i\leq 1}$ the number of pixels in the level i, and $I_{i\leq 1}$ the average intensity in the level i. The second image in figure 1.20 shows the binarisation of the first image using Otsu's method to define the threshold.

A first limitation of this naive binarisation is that the tank is only emptied after several experiments, so that the background image usually contains some of the smallest particles from previous experiments which settle very slowly and behave as isolated tracers (see the background around the cloud in the second image in figure 1.20). These isolated particles pollute the field of view, which makes it necessary to define a criterion to distinguish the falling cloud on one hand, and old remaining particles on the other hand. Otherwise, a naive binarisation either detects the cloud *and* remaining particles (if the threshold is too low), or does not detect all the particles within the cloud (if the threshold is too large). Regions of high particle concentration are always very bright and easily detected. The main issue is to distinguish between regions of the cloud with low concentration, and detrimental particles from past experiments, since both of these appear in dark shades of gray.

A solution to this problem lies in the interparticle distance. Small particles from past experiments are far away from one another, with a typical interparticle distance Δ^*. Particles falling with the cloud in regions of low concentration have a typical interparticle distance

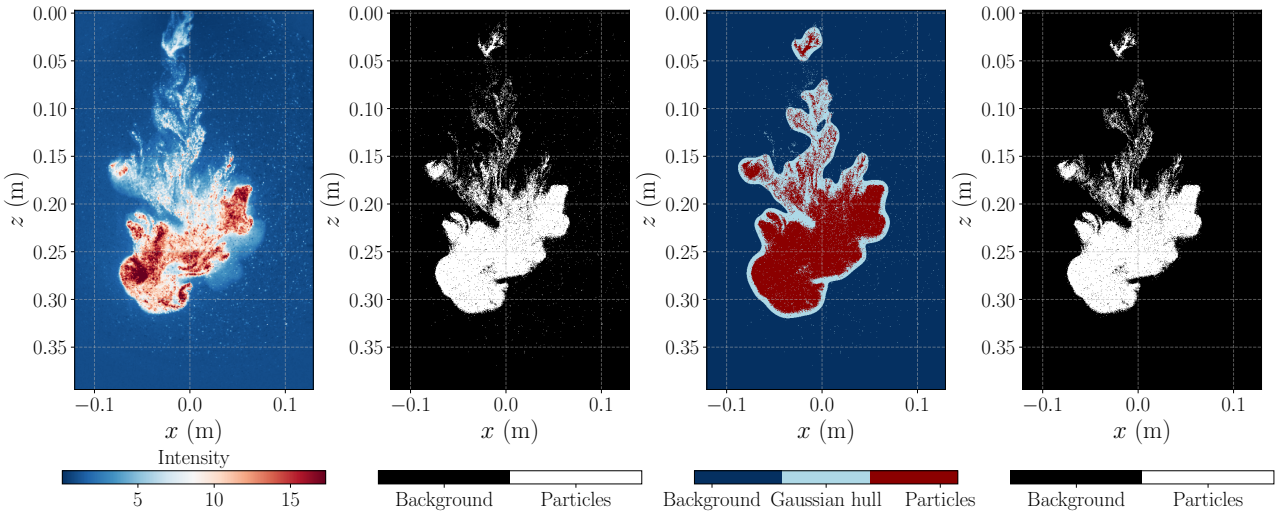

Figure 1.20: *Illustration of the automatic cloud tracking. From left to right, the first image is the ratio of a raw image over a background image taken when no cloud is visible; the second image is a raw binarisation of the first image; the third image shows how to discriminate between the cloud (in the Gaussian hull) and old remaining particles; the last image corresponds to the final result i.e. the restriction of the second image to the Gaussian hull.*

$\delta^* < \Delta^*$ (first image in figure 1.20). Then, the idea is to perform a naive binarisation with a threshold of intensity denoted I_{thr} (second image in figure 1.20), then blur the result with a Gaussian kernel of size σ which verifies $\delta^* < \sigma < \Delta^*$. In doing so, regions of low concentration in the cloud will connect because $\delta^* < \sigma$, which means that blurred particles now overlap, resulting in a signal which is above the threshold I_{thr}. On the opposite, isolated particles from past experiments do not overlap after blurring the image since $\sigma < \Delta^*$, hence their signal is lost in noise below I_{thr}. Then, the resulting blurred image is binarised with the same threshold I_{thr} as before, creating a "Gaussian hull" which only contains regions of both large intensity compared to I_{thr}, and whose interparticle distance is small compared to σ; see the third image in figure 1.20. To finish with, the final result is the initial naive binarisation of faw images *restricted* to the Gaussian hull only (fourth image in figure 1.20). As observed in figure 1.20, the Gaussian hull is able to capture some particles in regions of low concentration in the vicinity of the brightest regions, and gets rid of most particles in the background.

Once finally binarised, images are used to compute several quantities: the cloud front position $z_f(t)$ is that of the lowermost white pixel; the coordinates $x(t)$ and $z(t)$ of the cloud centroid are computed as averages of the coordinates of all white pixels; the cloud vertical $\sigma_z(t)$ and lateral $\sigma_x(t)$ dimensions are computed as standard deviations of white pixels with respect to the centroid. Errorbars on these quantities correspond to a confidence interval of 95% around the mean value, computed as 1.96 times the uncertainty obtained by averaging results of several realisations of an experiment, and from least squares regressions if any.

1.D Measurements from raw images

1.D.1 Coefficient of entrainment

The coefficient of entrainment α quantifies the growth rate of clouds, measured as the slope described by the edges of clouds as they fall in the water tank. The simplest and most robust way of quantifying this slope is by using all the photographs of a movie, as well as two integral images computed with the macro ZProject of ImageJ: the average and the pixel-by-pixel standard deviation of light intensity over the entire cloud fall (see figure 1.21). With these three visualisations, the cloud edges are tracked, the slope $\alpha = dr/dz$ is determined by hand in each case, and we retain the mean value of the three methods for each realisation of an experiment. Finally we compute α and its error bar respectively as the mean and standard deviation of all the realisations of a given set $(\mathcal{R}, \Omega)$.

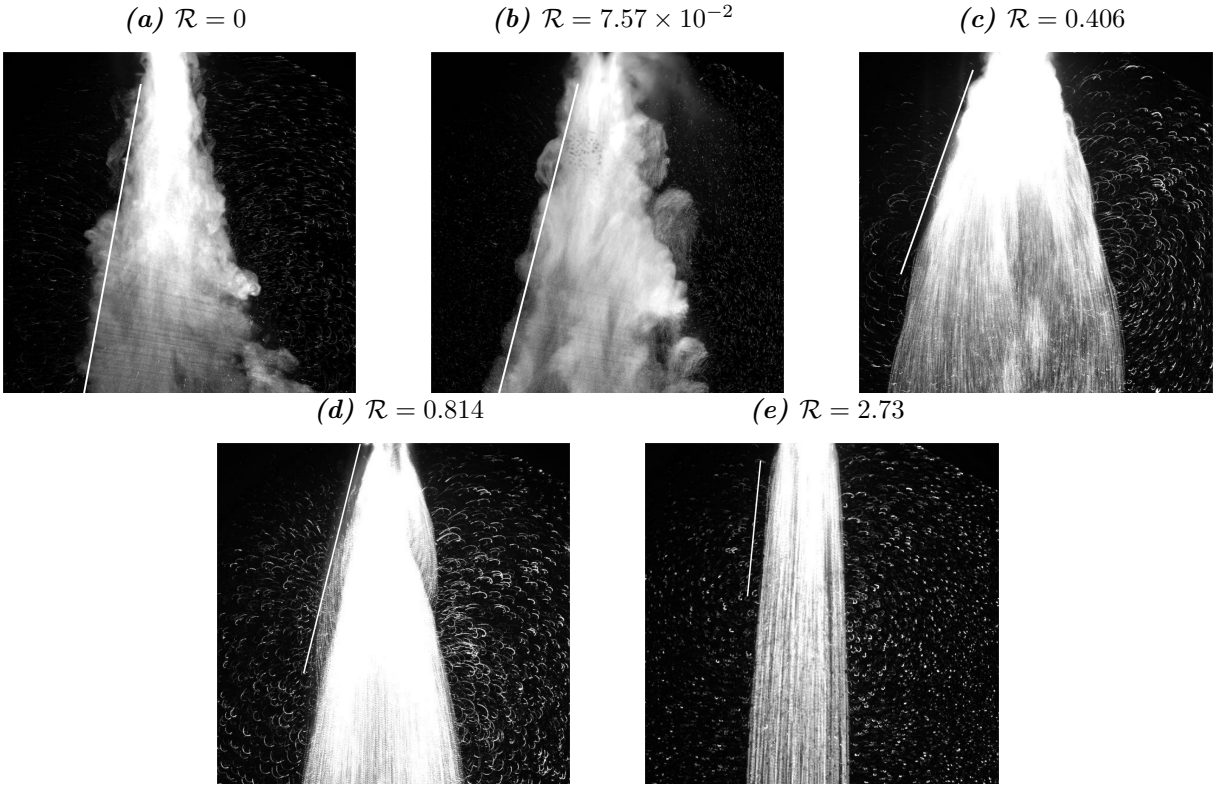

Figure 1.21: *For five Rouse numbers, images show a moving standard deviation of the light intensity during a typical experiment. Before separation, the angle of opening of clouds can be compared to the angle predicted from the average coefficient of entrainment $\alpha(\mathcal{R})$, shown by a thick solid white line.*

The slope α is determined over the distance where the cloud grows linearly, before separation and before transition to a vortical columnar flow. When a cloud never grows linearly (because particles are so large that the Rouse number $\mathcal{R}$ is above unity), an indicative value of α is measured: it corresponds to the initial growth rate of the cloud after rupturing the membrane, in the phase of acceleration of the cloud (see figure 1.21e).

1.D.2 Depth of separation

Experimentally, the depth of separation can be measured in two different ways. For the first one, the overlay of images from both cameras enables to compute the surface area of overlap between rhodamine and particles, both regions being defined from the cloud-tracking algorithm presented in appendix 1.C. Initially both regions are superimposed. Their overlap gradually shrinks in time or depth, evidencing an inflexion point which is considered as defining separation. Depending on experiments, the inflexion point may not be well defined. In that case the asymptotic states of complete overlap and nil overlap are detected, and separation is considered to happen at mid-time. This first method presents the advantage of being quantitative, but only a few experiments were performed with rhodamine. The second method is based on the trajectories of particles. Moving standard deviations are performed over a chosen number N^* of snapshots (typically 30), which enables to observe the trajectory of individual particles over the N^* snapshots at 50 fps (see an example in figure 1.7a). When particles separate from eddies, the patterns made by their trajectories transition from curved and randomly oriented (due to particles whirling inside eddies) to mostly straight and vertical. When half the visible particles have a vertical trajectory, separation is considered to occur. The difficulty to assess the proportion of particles having transitioned affects the determination of the depth of separation z_{sep}. This is accounted for by expanded uncertainties Σ_{sep}: they are measured in such a way that for z lower than $z_{\text{sep}} - \Sigma_{\text{sep}}$ almost all particles swirl in eddies, and for z larger than $z_{\text{sep}} + \Sigma_{\text{sep}}$ almost all particles have a vertical trajectory.

The two methods to identify separation were both implemented for the same series of particle clouds of average Rouse number $\mathcal{R} = 0.308$; the difference between their respective mean value of z_{sep} corresponded to a low relative error of 2.1%, which was considered satisfactory enough to validate the use of the second approach for all experiments.

Chapitre 2

Two-way coupling Eulerian numerical simulations of particle clouds settling in a quiescent fluid

Summary

To get a deeper understanding of our laboratory experiments [Kriaa *et al.*, Phys. Rev. Fluids 7(12) 124302 (2022)], we numerically model settling clouds produced by localised instantaneous releases of heavy particles in a quiescent fluid. By modelling particles as a field of mass concentration in an equilibrium Eulerian approach, our two-way coupling simulations recover our original experimental observation of a maximum growth rate for clouds laden with particles of finite Rouse number $\mathcal{R} \approx 0.22$, where $\mathcal{R}$ is the ratio of the individual particle settling velocity to the typical cloud velocity based on its initial radius and total buoyancy. Consistent with the literature on buoyant vortex rings, our clouds verify the relation $\alpha \propto \Gamma_\infty^{-2}$ between the clouds' growth rate α as firstly defined by Morton *et al.*, [Proc. R. Soc. A: Math. Phys. Sci. **234**, 1 (1956)] and their eventually constant circulation Γ_∞. As the Rouse number approaches $\mathcal{R} \approx 0.22$, the baroclinic forcing of the circulation reduces down to a minimum, thus optimising the cloud growth rate α. This analysis highlights the role of the mean flow in the enhanced entrainment of ambient fluid by negatively buoyant clouds. Our results also validate, on the basis of direct comparison with experimental results, the use of a one-fluid two-way coupling numerical model to simulate particle clouds in the limit of weak particle inertia.

2.1 Introduction

The present study follows up on a series of 514 systematic laboratory experiments presented in Kriaa et al. (2022) (Chapter 1) which focus on the evolution of instantaneously-released particle-laden clouds settling from rest in initially quiescent water, under the sole action of their buoyancy. By varying the size of particles yet keeping an identical buoyancy for all clouds,

the latter proved to grow linearly in depth, with a growth rate α that reaches a maximum for a finite particle inertia $\mathcal{R} \simeq 0.3 \pm 0.1$, where the Rouse number $\mathcal{R} = w_s/U_{\text{ref}}$ is the ratio of the terminal velocity of an isolated particle w_s over the reference fall velocity U_{ref} of the cloud due to the sole action of its buoyancy. This new observation was unexpected because the theory of turbulent thermals (Morton et al., 1956), commonly used to model such clouds, predicts that all clouds should grow similarly as a salt-water cloud of identical buoyancy. Yet, our measurements revealed that the particle inertia can increase the growth rate by up to 75%. Our experiments did not enable us to answer some remaining questions: Through which mechanism do particle clouds entrain more than salt-water clouds of identical buoyancy? In particular, does the particle inertia alter the mean flow around the cloud or does it modulate the intensity of the turbulence that develops inside the cloud? The aim of the present study is to gain understanding on these questions thanks to complementary numerical simulations. The numerical approach to be adopted should capture the macroscopic physics of particle clouds as observed in our experiments, yet with the minimum ingredients to keep a low numerical cost, with a motivation to later apply the method to a planetary-scale multiphase flow called 'iron snow' (Rückriemen et al., 2015).

When the size of particles, their volume fraction and the particle-to-fluid density anomaly are low, the fluid governs the motion of particles whose feedback on the flow is negligible, a situation called *one-way coupling* (Balachandar and Eaton, 2010). Many studies have considered the one-way coupling between particles and fluid motions (e.g. Brandt and Coletti, 2022; Good et al., 2014; Yoshimoto and Goto, 2007; Goto and Vassilicos, 2008; Falkinhoff et al., 2020) and evidenced that inertia is a source of non-uniformities in the field of particle concentration (Maxey, 1987): despite the incompressibility of the fluid phase, inertia allows the disperse phase to be compressible. Maxey (1987) showed that very small particles behave as passive tracers due to their low inertia; conversely, large particles are insensitive to local modifications of the flow due to their large response time (see also Yoshimoto and Goto, 2007; Ghosh et al., 2005). Due to this low-pass 'inertial filtering' of timescales, dense particles of intermediate size partly decouple from fluid motions. For some finite inertia they have been observed to optimally couple with the surrounding flow and concentrate in some specific regions. This phenomenon of 'preferential concentration' (Maxey, 1987; Aliseda et al., 2002; Yoshimoto and Goto, 2007; Salazar et al., 2008; Toschi and Bodenschatz, 2009; Falkinhoff et al., 2020) leads to the accumulation of small particles in regions of large strain rate or equivalently of low vorticity (Maxey, 1987), possibly due to centrifuging of particles outside of vortices (Falkinhoff et al., 2020; Brandt and Coletti, 2022), while larger dense particles rather concentrate in regions of vanishing fluid acceleration (Bec et al., 2006; Goto and Vassilicos, 2008).

With the addition of gravity, another heterogeneity originates from the tendency of heavy particles to fall on the side of downward velocity of eddies (Wang and Maxey, 1993), which can be grasped by simple advective arguments even in laminar flows (e.g. Nielsen, 1993). This phenomenon of 'fast tracking' or 'preferential sweeping' is also optimum for a finite particle inertia (Wang and Maxey, 1993); it has been observed in 2D periodic laminar vortices (Maxey and Corrsin, 1986) and in turbulent flows (e.g. Good et al., 2014; Falkinhoff et al., 2020; Hassaini and Coletti, 2022; Elghobashi and Truesdell, 1993; Bosse et al., 2006). Additionally, due to their inertia, falling particles lag behind fluid motions so their trajectories are biased in the direction of gravity. As particles cross upwelling and downwelling regions, they spend more

time in upwelling regions, increasing their sensitivity to velocity variations in these upwellings. This 'loitering' (Nielsen, 1993) is a third example of preferential sampling of the flow.

All these phenomena of preferential sampling determine the distribution of particles in time and space. This observation is paramount if the flow is altered by the feedback of particles on the fluid, a situation referred to as *two-way coupling* (Balachandar and Eaton, 2010). Inclusion of this feedback in numerical simulations has proved to be essential as it further modifies the structure of particle-laden flows even in well-controlled idealised isotropic turbulent flows (Monchaux and Dejoan, 2017; Hassaini and Coletti, 2022; Elghobashi and Truesdell, 1993; Bosse et al., 2006), especially in the presence of gravity which breaks the flow isotropy. As an example, experiments (Aliseda et al., 2002) and simulations (Monchaux and Dejoan, 2017; Bosse et al., 2006) have shown that the non-linear modification of the settling velocity due to preferential concentration and preferential sweeping is further favoured by two-way coupling since clusters of particles drag fluid with them as they sweep downward, producing downward acceleration of the fluid which enhances the fluid velocity and therefore the particle settling velocity. Most importantly, even in the presence of low mass loadings, the feedback of particles on the fluid is essential if the flow is driven by the particles themselves, e.g. in downdrafts (Kruger, 2020), turbidity currents (Ouillon et al., 2019; Necker et al., 2002), and presumably iron snow (Rückriemen et al., 2015). The present work fits in this framework: in our experiments (Kriaa et al., 2022) particles were released from rest in quiescent water, hence all fluid motions resulted from the drag exerted by particles on water during their fall.

Thus, in this study we adopt an equilibrium Eulerian approach (Balachandar and Eaton, 2010) to model our settling particle clouds at reasonably low numerical cost, while still accounting for the two essential ingredients of (i) the feedback of particles on the fluid through a drag term which forces the flow, and (ii) a differential motion between water and settling particles through a gravitational drift, a formalism already used in the literature to model particle-laden flows (Fabregat Tomàs et al., 2017; Boffetta et al., 2007; Reali et al., 2017; Lemus et al., 2021; Chou and Shao, 2016). The latter effect is quantified by a Rouse number which is about $\mathcal{R} = 0.3$ for the optimum growth rate in experiments, and which lies below unity for most of our clouds. Our experiments therefore fit in the range of validity of the equilibrium Eulerian model, as pointed out by Boffetta et al. (2007). Note however that we extend our analysis up to $\mathcal{R} \simeq 3$ as in our experiments. Boffetta et al. (2007) showed that such particles have so much inertia that they undergo the 'sling effect' i.e. particles tend to converge and thereby form caustics, so that the continuum modelling of particle motions through a unique velocity field locally breaks down. Yet, our results using the equilibrium Eulerian formalism up to $\mathcal{R} \simeq 3$ show good agreement with our experiments, supporting the fact that if the sling effect plays any part in experiments, it still has no strong statistical signature on the macroscopic quantities we measured in experiments and reproduce numerically here.

The paper is organised as follows. Section 2.2 introduces the equations of motion to model particles as a field of mass concentration verifying an advection-diffusion equation and forcing the flow through a drag term. Section 2.3 presents the numerical setup of the three-dimensional numerical simulations. Then, section 2.4 presents the two main regimes of cloud settling; it notably evidences the same maximum of the cloud growth rate α as observed in our experiments (Kriaa et al., 2022). Section 2.5 is devoted to the analysis of this effect, showing that particles with a Rouse number close to the optimum impose a weaker baroclinic forcing of the clouds'

circulation, resulting in an enhanced growth rate according to the theory of buoyant vortex rings. Further discussion and concluding remarks are presented in section 2.6. Appendix 2.A provides details on the robustness of the numerical simulations, and appendix 2.B gives numerical results for particle clouds of larger Reynolds number than those presented in the core of this study.

2.2 Equations of motion

If a particle has finite inertia and is not neutrally buoyant, it moves with a velocity $\boldsymbol{v}_p$ which is different from that of the fluid $\boldsymbol{v}$ in its vicinity, and the particle acceleration verifies its own momentum equation. This momentum equation for a small spherical particle was established in 1983 by Maxey and Riley (1983) under the assumptions that the particle of radius r_p is much smaller than the characteristic macroscopic length scale L of the flow, that the particle Reynolds number based on the slip velocity of the particle is much lower than unity (so the disturbance flow due to the particle can be considered a Stokes flow), and that the diffusive timescale r_p^2/ν is much lower than the advective timescale L/U_0 (ν being the kinematic viscosity of the fluid and U_0 a characteristic velocity scale of the flow). With these assumptions, the leading terms boil down to the particle acceleration, its buoyancy and the Stokes drag exerted by the fluid. Furthermore, in the equilibrium Eulerian formalism, assuming that all particles have very small inertia (limit of vanishingly small Stokes number i.e. vanishing particle response time compared to the timescale of the flow at the particle scale), the particle acceleration can be neglected (Balachandar and Eaton, 2010) so that the particle velocity is solely prescribed by the balance between buoyancy and drag (Berk and Coletti, 2021; Falkinhoff et al., 2020). This balance yields

$$\boldsymbol{v}_p = \boldsymbol{v} + w_s \boldsymbol{e}_z \ , \tag{2.1}$$

as derived in Nasab and Garaud (2021), where $\boldsymbol{v}$ is the fluid velocity, $\boldsymbol{v}_p$ is the particle velocity, w_s is the terminal velocity of the particle in quiescent fluid and $\boldsymbol{e}_z = \boldsymbol{g}/||\boldsymbol{g}||$ is aligned with the gravity field $\boldsymbol{g}$. In the present study we use this approximation to the momentum equation even for particles with non negligible inertia, and try to assess the accuracy of this approach. To keep a moderate numerical cost, as in previous studies of particle-laden flows (Fabregat Tomàs et al., 2017; Boffetta et al., 2007; Magnani et al., 2021; Jacobs et al., 2015; Reali et al., 2017; Lemus et al., 2021; Chou and Shao, 2016) we model particles as a continuum with a field of concentration $\mathcal{C}$ (mass of particles per unit volume) that is advected at the velocity $\boldsymbol{v}_p$, hence, mass conservation reads

$$\partial_t \mathcal{C} + \boldsymbol{v}_p \cdot \nabla \mathcal{C} = 0 \ . \tag{2.2}$$

In practice, such modelling neglects particle dispersion at the particle scale. In fact, even in dilute suspensions for which collisions are negligible, and even in the absence of Brownian motions, particles induce long-range perturbations, particle-wake interactions and collective-settling effects in the fluid depending on their particulate Reynolds number (e.g. Guazzelli and Morris, 2011; Subramanian and Koch, 2008; Pignatel et al., 2011; Daniel et al., 2009). These perturbations lead to a dispersion which has been analysed analytically (Koch, 1994), numerically (Ladd, 1993) and experimentally (Ham and Homsy, 1988; Nicolai and Guazzelli, 1995; Martin et al., 1994; Xue et al., 1992; Lee et al., 1992), and which can be approximated

by a diffusive process. Together with other ingredients such as concentration gradients and shear (Davis, 1996), these effects are referred to as a hydrodynamic diffusion (Guazzelli and Hinch, 2011). They are often approximated at a macroscopic level by a term of diffusion in the mass conservation above (Elghobashi, 1994; Martin et al., 1994; Nasab and Garaud, 2021; Lee et al., 1992). In addition, including a diffusive term in the mass conservation equation is necessary to prevent the formation of caustics in the field of particle concentration, which would lead to numerical instabilities in the current Eulerian framework (Magnani et al., 2021). By introducing the effective particle diffusivity κ_p, and using equation (2.1), the new equation of mass conservation reads

$$\partial_t \mathcal{C} + \boldsymbol{v} \cdot \nabla \mathcal{C} = \kappa_p \nabla^2 \mathcal{C} - w_s \frac{\partial \mathcal{C}}{\partial z}, \tag{2.3}$$

where the last term accounts for the gravitational drift of particles.

Fluid motions are constrained by the condition of incompressibility

$$\nabla \cdot \boldsymbol{v} = 0, \tag{2.4}$$

which also prescribes the incompressibility of the field of concentration using equation (2.1). The fluid velocity $\boldsymbol{v}$ verifies the Navier-Stokes equation for a Newtonian fluid

$$\frac{\partial \boldsymbol{v}}{\partial t} + \boldsymbol{v} \cdot \nabla \boldsymbol{v} = -\frac{1}{\rho_f} \nabla p + \nu \nabla^2 \boldsymbol{v} + \frac{1}{\rho_f} \boldsymbol{f}_{\text{drag}}, \tag{2.5}$$

where ρ_f is the fluid density, p is the pressure field including the hydrostatic contribution, ν is the constant fluid kinematic viscosity, and $\boldsymbol{f}_{\text{drag}}$ is the average drag force exerted by particles on the fluid per unit volume. This drag term in equation (2.5) describes how particles force the flow: the field of concentration and the fluid are now two-way coupled. The present model is derived for supposedly spherical particles of vanishingly small Reynolds number, hence they fall in the Stokes regime with a settling velocity

$$w_s^{\text{Stokes}} = \frac{2 g r_p^2 (\rho_p - \rho_f)}{9 \nu \rho_f}, \tag{2.6}$$

with ρ_p the density of a spherical particle of radius r_p, and $g = ||\boldsymbol{g}||$ corresponds to gravity. Then, using equation (2.1), the Stokes drag exerted by the fluid on a particle reads $-6\pi\rho_f \nu r_p w_s^{\text{Stokes}} \boldsymbol{e}_z$. Summation on all the particles in the unit volume requires to multiply this individual acceleration by the number of particles per unit volume i.e. $3\mathcal{C}/4\pi r_p^3 \rho_p$. Using Newton's third law, the drag force reads

$$\boldsymbol{f}_{\text{drag}} = \mathcal{C} \frac{\rho_p - \rho_f}{\rho_p} \boldsymbol{g}. \tag{2.7}$$

The previous equations are non-dimensionalised using the length scale D_{cyl} which corresponds to the diameter of the vertical cylinder that was initially containing the particles in our water tank experiments (Kriaa et al., 2022, see Chapter 1). This cylinder was immersed at the top of our tank and closed by an elastic membrane, until this membrane was ruptured at $t = 0$

to instantly release the particles. As for the velocity scale, we use the characteristic velocity that clouds can build up when accelerating from rest which is

$$U_{\text{ref}} = \sqrt{g\left(1 - \frac{\rho_f}{\rho_0}\right) D_{\text{cyl}}}\ , \tag{2.8}$$

where $\rho_0 = \rho_f + (1 - \rho_f/\rho_p)m_0/(4\pi D_{\text{cyl}}^3/3)$ is the typical initial effective density of particle clouds (see Chapter 1 for details). Time t, pressure p and concentration $\mathcal{C}$ are respectively non-dimensionalised by the advective timescale $D_{\text{cyl}}/U_{\text{ref}}$, the characteristic dynamic pressure $\rho_f U_{\text{ref}}^2$, and the fluid density ρ_f. With the dimensionless variables, equation (2.4) is unmodified while mass conservation now reads

$$\partial_t \mathcal{C} + \boldsymbol{v} \cdot \nabla \mathcal{C} = \frac{1}{Pe}\nabla^2 \mathcal{C} - \underbrace{\mathcal{R}\frac{\partial \mathcal{C}}{\partial z}}_{\text{gravitational drift}}\ , \tag{2.9}$$

where $Pe = U_{\text{ref}} D_{\text{cyl}}/\kappa_p$ is the Péclet number, and $\mathcal{R} = w_s/U_{\text{ref}}$ is the Rouse number which characterises the gravitational drift of particles. When $\mathcal{R} \ll 1$ particles hardly drift with respect to the fluid and tend to follow fluid motions, whereas particles having $\mathcal{R} \gg 1$ largely decouple by vertical settling so their trajectories largely differ from those of fluid particles in their vicinity. Using equation (4.4), similar non-dimensionalisation of equation (2.5) leads to

$$\frac{\partial \boldsymbol{v}}{\partial t} + \boldsymbol{v} \cdot \nabla \boldsymbol{v} = -\nabla p + \frac{1}{Re}\nabla^2 \boldsymbol{v} + \underbrace{Ri\mathcal{C}\boldsymbol{e}_z}_{\text{drag term}}\ , \tag{2.10}$$

where $Re = U_{\text{ref}} D_{\text{cyl}}/\nu$ is the Reynolds number and $Ri = gD_{\text{cyl}}(1-\rho_f/\rho_p)/U_{\text{ref}}^2$ is the Richardson number which boils down to a ratio of density contrasts $Ri = (1 - \rho_f/\rho_p)/(1 - \rho_f/\rho_0)$ for our specific choice of U_{ref} used to non-dimensionalise the equations.

2.3 Numerical setup

The numerical setup aims at reproducing the experimental conditions for the generation of our particle clouds (Kriaa et al., 2022, Chapter 1), released with no initial velocity from the top centre of a tank of still water. Every particle cloud is composed of $m_0 = 1$ g of spherical glass beads with a mean radius r_p chosen in the range 5 μm$-$1 mm, as well as some water, sometimes dyed with rhodamine. All this material is initially contained in a cylinder of diameter $D_{\text{cyl}} =$ 3.2 cm partially immersed in water and sealed by a latex membrane. When an experiment starts, the membrane is ruptured by a needle, it quickly retracts and lets particles settle from rest in the tank with the dyed fluid. Visualisations are performed in a vertical green laser sheet with two cameras: the one with a green filter records the motion of particles only, while the camera with an orange filter records only motions of turbulent eddies dyed with rhodamine, see figure 2.1a for an illustration. Some reference clouds without particle inertia contained an identical mass excess $m_0 = 1$ g of salt water and were generated in the same way. Their dynamics is characterised by a Rouse number $\mathcal{R} = 0$. Experiments were performed in a tank

of depth 1 m with horizontal square cross section of 42×42 cm^2 surface area; the side walls of the tank were considered far enough from particle clouds to have a negligible influence on the settling of particles. In the present simulations, the computational domain represents a cube of volume 1 m^3 with side length $L_{\text{domain}} = 31.25 D_{\text{cyl}}$. Figure 2.1b shows a numerical analog of our experimental clouds in a simulation having $\mathcal{R} = 0.221$ at time $t = 34$.

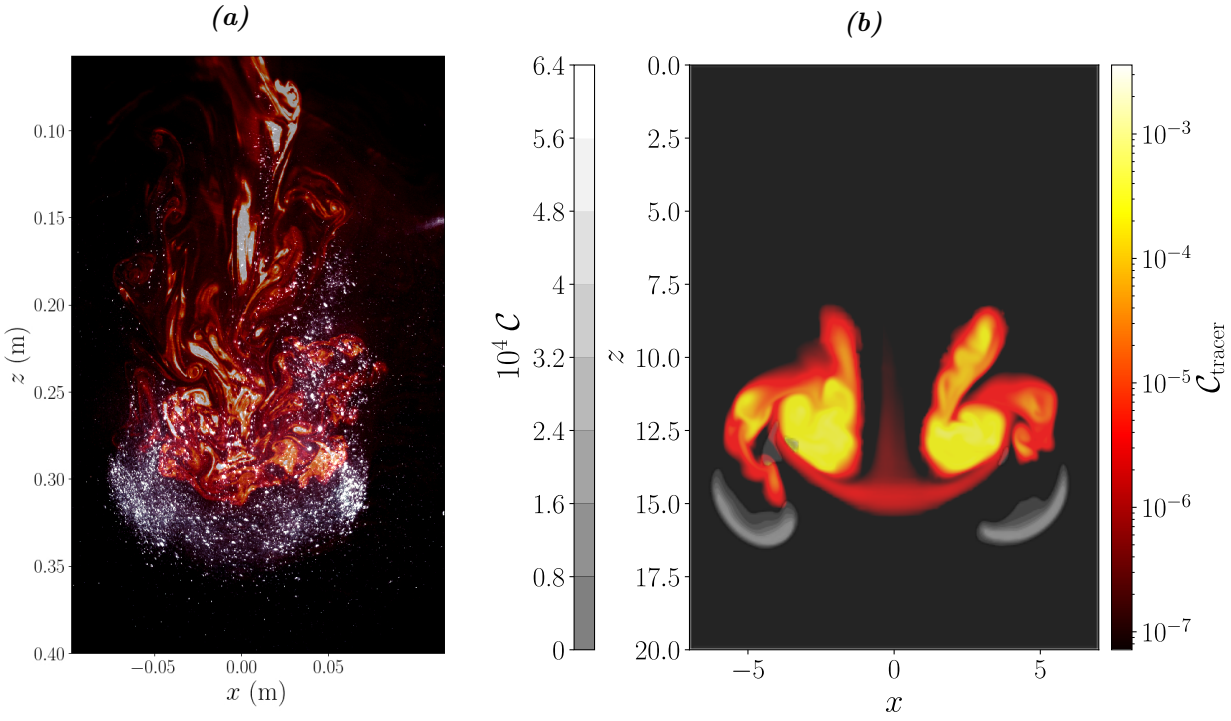

Figure 2.1: *(a) Visualisation of an experimental particle cloud in a vertical laser sheet with particles in grey (set of polydisperse particles of Rouse number $\mathcal{R} = 0.308 \pm 0.080$) and dye (rhodamine) in orange. (b) Numerical analog in the plane $y = 0$ of the previous photograph with a grey field of concentration $\mathcal{C}$ modelling particles and an orange tracer concentration $\mathcal{C}_{tracer}$ modelling dye (cloud of Reynolds number $Re = 1183$ as in the experiment (a), with a fixed Rouse number $\mathcal{R} = 0.221$). The larger vertical spread of particles in (a) compared to (b) is due to the polydispersity of the former, whereas simulations are performed for monodisperse particle clouds (for further details, see Kriaa et al., 2022, Chapter 1). The coordinates x and z in (b) are non-dimensionalised by D_{cyl} (see section 2.2).*

To model the instantaneous release of particles from the cylinder, the field of concentration is initialised in a narrow cylindrical region of diameter D_{cyl}, horizontally centred and localised at distance $1.5 D_{\text{cyl}}$ below the top of the computational domain. In experiments particles rested at the bottom of the cylinder on the latex membrane as a very thin layer of height H_{compact}. To smooth the initial concentration gradients that are required to model the initial layer, the field of concentration is initialised in a cylindrical region of height $10 H_{\text{compact}}$, and the lateral and vertical edges of this cylindrical region are smoothed by a hyperbolic tangent with typical length scale H_{compact}. The factor 10 on the initial height of the pile of particles is expected to have negligible influence: indeed, our experiments showed that varying the height of the pile of particles from H_{compact} to $40 H_{\text{compact}}$ had negligible impact on the dynamics we aim

to model here (for further details, see Kriaa et al., 2022, Chapter 1). To compensate for the errors introduced the hyperbolic tangent smoothing, the exact mass of particles is enforced (in dimensional form, $m_0 = 1$ g) by an appropriate rescaling. The uniform fluid is initially motionless, save for a cylindrical envelope around particles at time $t = 0$ in which the velocity field is perturbed by a random uniform infinitesimal noise.

A passive tracer is implemented to mimic rhodamine in simulations. This tracer is initialised exactly like the concentration $\mathcal{C}$ and satisfies equation (2.9) with its own Rouse number $\mathcal{R} = 0$ so it does not drift vertically as particles do. Importantly, unlike the field of particle concentration $\mathcal{C}$, the passive tracer does not force any flow (it is absent of equation (2.10)).

On all walls, the velocity field satisfies no slip boundary conditions, while the concentration $\mathcal{C}$ and the passive tracer satisfy no-flux Neumann boundary conditions.

Equations (2.4), (2.9) and (2.10) are integrated in three dimensions with the solver Basilisk (Popinet, 2009) that is second-order accurate in space and time, using a time-splitting pressure-correction discretisation of the Navier-Stokes equation (2.10). The second-order advection scheme of Bell et al. (1989) is used for equation (2.10) and for the two advection terms in equation (2.9). The concentration gradient $\partial\mathcal{C}/\partial z$ is computed with the generalised minmod slope limiter to reduce spurious oscillations due to sharp concentration gradients at initial times, with negligible impact on our numerical measurements (see appendix 2.A). Due to the large scale separation between the domain size and the initial cloud size ($L_{\text{domain}} = 31.25 D_{\text{cyl}}$), an adaptive mesh refinement is adopted. This octree mesh is made of hierarchically organised cubic cells, each refinement of a cell corresponding to a division of this cell in 8 identical cubes. This refinement is based on local values of the concentration $\mathcal{C}$ and on the local viscous dissipation, see an illustration in figure 2.2a. The smallest mesh cell has a size fixed to $L_{\text{domain}}/1024$ while the largest mesh cell has a size $L_{\text{domain}}/128$.

Our main focus is to analyse the influence of gravitational settling on the evolution of particle clouds by varying the Rouse number from $\mathcal{R} = 0$ to $\mathcal{R} = 3.03$. Consequently, with a fixed density $\rho_p = 2500$ kg/m^3 for all particles (the density of the fluid is $\rho_f = 1000$ kg/m^3), the Richardson number $Ri = 138$ does not vary between simulations, and the same conclusion holds for Re and Pe. These last two numbers are equal because we assume $\nu = \kappa_p$ as a first approximation. The value $Re = 454$ is chosen by following this conservative estimate: if the particle clouds were highly inertial and if their turbulence was homogeneous and isotropic with a fully-developed energy cascade from the integral cloud scale of order $\sim 3D_{\text{cyl}}$ to the Kolmogorov scale, then the latter would have a size $3D_{\text{cyl}}Re^{-3/4}$. By prescribing that this smallest length scale should have a size $L_{\text{domain}}/1024$, this prescribes the value of $Re = (L_{\text{domain}}/3072D_{\text{cyl}})^{-4/3} = 454$. This calculation is conservative as no flow structure reaches such a small length scale in our simulations. In fact, the transient cloud formation does not permit the development of an energy cascade down to the Kolmogorov scale. Instead, the clouds we model are close to laminar, with a predominating coherent structure of size $\sim 3D_{\text{cyl}}$, confirming that all length scales are appropriately resolved. An example of the fields obtained is shown in figure 2.2b. For completeness, additional simulations at $Re = 1183$ (which is the Reynolds number of particle clouds in our experiments Kriaa et al., 2022) are presented in appendix 2.B which show similar results as those presented in the core of the present analysis.

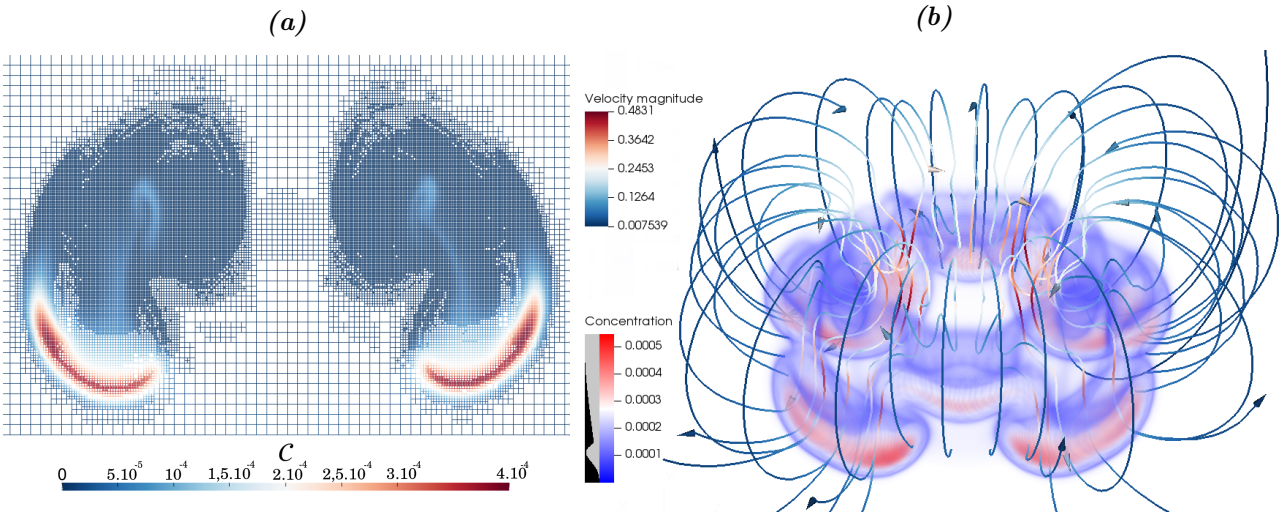

Figure 2.2: *(a) Adaptive mesh refinement on the field of concentration $\mathcal{C}$ for $\mathcal{R} = 0.221$ in the plane $y = 0$ at time $t = 35$. (b) Bird's eye view of the 3D structure of $\mathcal{C}(x, y, z, t = 33.75)$ for $\mathcal{R} = 0.221$ in blue-red colours (colorbar and opacity in the bottom left-hand corner). Streamlines show the toroidal velocity field, with blue-red colours for the velocity magnitude $||\boldsymbol{v}||$ (colorbar in the top left-hand corner).*

2.4 Regimes of cloud settling

2.4.1 Overview

Figure 2.3 shows snapshots as well as an average image of the field of concentration $\mathcal{C}(x, y = 0, z, t)$ in a vertical cross section of the computational domain. They faithfully account for all the qualitative morphological features observed in our experiments (see figure 1.4 in Chapter 1). Particle clouds initially grow as they propagate downward. For the lowest Rouse numbers this regime of growth and dilution lasts over the entire fall of the cloud. For intermediate Rouse numbers, this regime is more prominent (see figure 2.3c), yet this growth gradually vanishes and stops (see in particular average images in figures 2.3d, 2.3e). This transition is due to separation of the field of concentration from eddies, which is why the field of concentration deforms less and less, and settles more and more vertically.

The cloud evolution can be quantified by tracking the vertical position $z_f(t)$ of its front, defined as the lowermost position of the iso-contour of concentration $\mathcal{C}(x, y, z, t) = 10^{-8}$ (this low value ensures that measurements are independent of the specific threshold), and by tracking the vertical position $z(t)$ of the centre of mass, defined as the weighted average of the vertical coordinate z in the whole computational domain as $z(t) = \int_V z\mathcal{C}dV / \int_V \mathcal{C}dV$. Figure 2.4 shows the evolution of these two positions in time; for all figures we use dashed lines if $\mathcal{R} > 0.221$ and solid lines otherwise, with grey shades diverging from the thick darkest line of $\mathcal{R} = 0.221$. For low Rouse numbers ($\mathcal{R} < 1$), after a short phase of acceleration, the positions $z_f(t)$ and $z(t)$ evidence a concave evolution revealing the cloud deceleration. For intermediate Rouse numbers, a smooth transition occurs that leads to a regime of constant settling velocity when particles

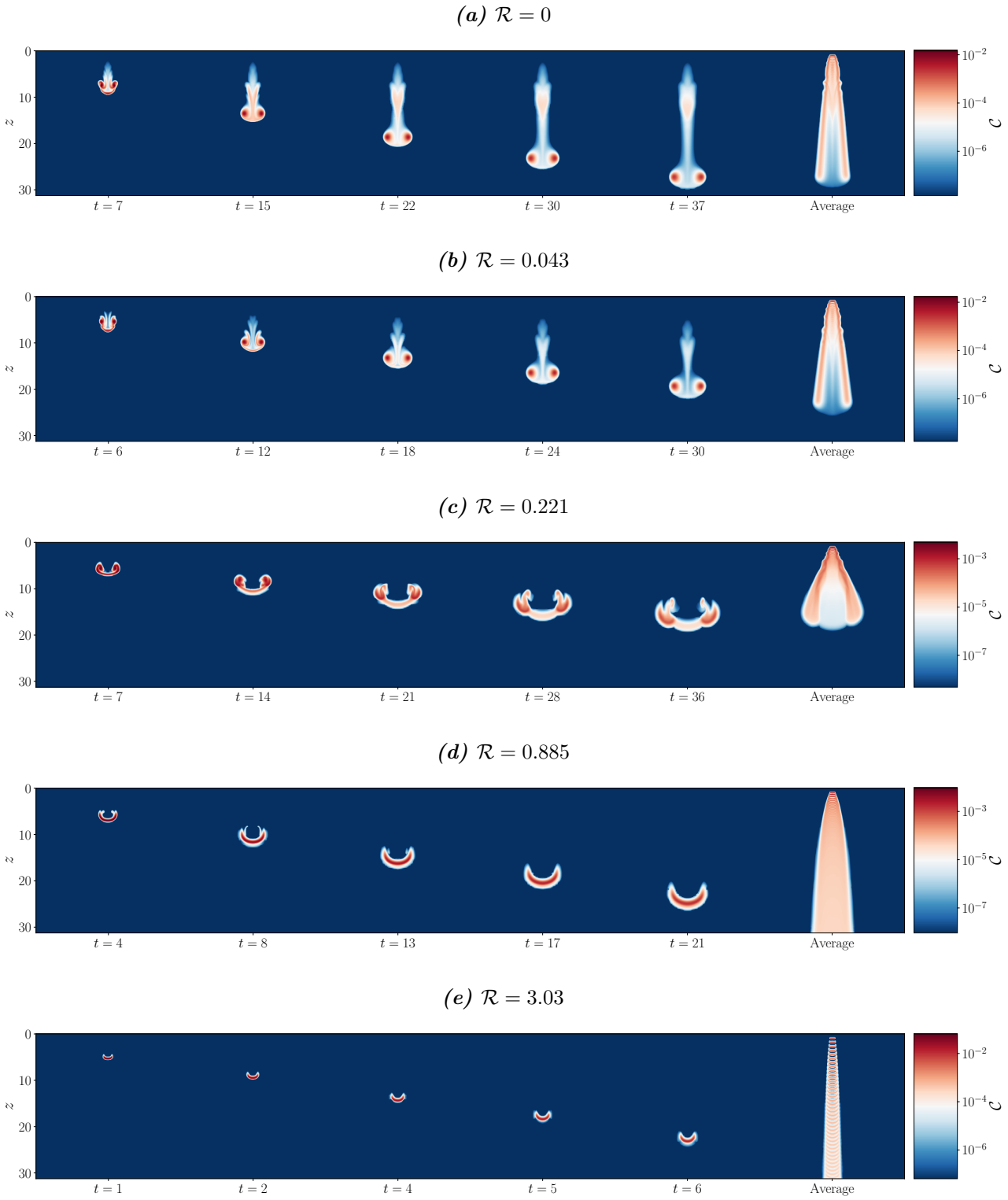

Figure 2.3: *Each row shows snapshots of the field of concentration $\mathcal{C}(t, x, z)$ in the plane $y = 0$ for a different Rouse number, as well as the average of 40 snapshots taken with a constant timestep $\Delta t = 1$ over the fall.*

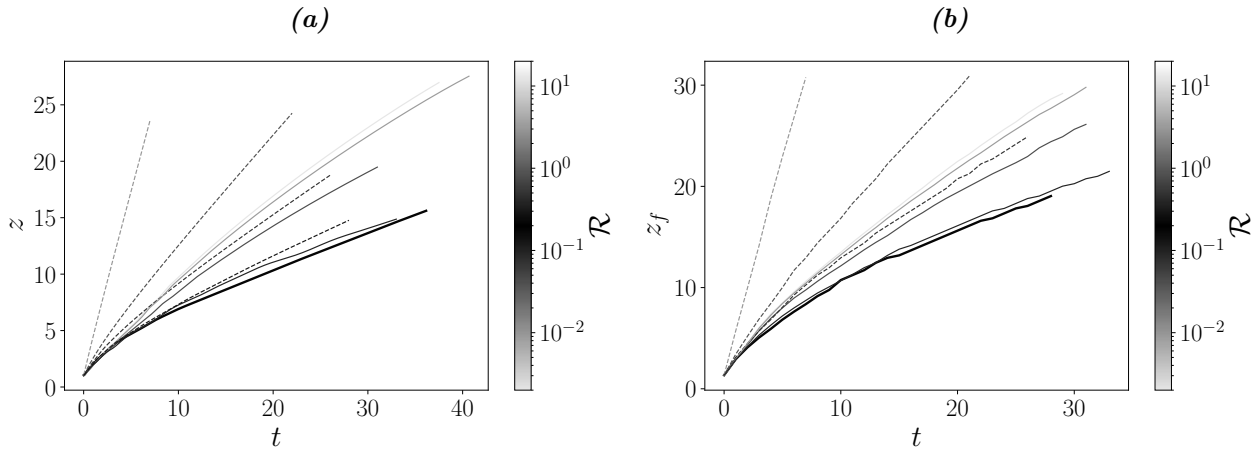

Figure 2.4: *For several Rouse numbers, evolution in time of the vertical position of (a) the centre of mass of particles, and of (b) the cloud front. Lines are dashed if* $\mathcal{R} > 0.221$ *and solid otherwise.*

separate from fluid motions and settle in quiescent liquid. For the largest Rouse numbers ($\mathcal{R} > 1$), clouds almost immediately transition from the regime of acceleration to the regime of constant settling velocity. The literature (Rahimipour and Wilkinson, 1992; Bush et al., 2003; Lai et al., 2016; Kriaa et al., 2022) distinguishes between the first regime of turbulent thermal, or equivalently of buoyant vortex ring, and the second regime of swarm. All these observations are consistent with our experimental observations, which were obtained by tracking the front of the light intensity reflected by the glass spheres in time, which is analogous to z_f here. In the next sections, the two regimes of buoyant vortex ring and swarm are described separately.

2.4.2 Buoyant vortex ring regime (*aka* thermal regime)

Due to the lower cloud Reynolds number in numerical simulations than in experiments (see appendix 2.B for results at higher Reynolds number), numerical results evidence clear buoyant vortex rings whose toroidal structure is less apparent in our more turbulent thermals in the laboratory. Yet, several studies have shown that turbulent thermals (i.e. instantaneous releases of a finite volume of buoyant fluid with no initial momentum) are formed like buoyant vortex rings (Pottebaum and Gharib, 2004; Gharib et al., 1998), and have a very similar structure (Bond and Johari, 2005; Lherm, 2021; Lecoanet and Jeevanjee, 2019; McKim et al., 2020) and dynamics (Turner and Taylor, 1957; Landeau et al., 2014), to such an extent that thermals have been considered as buoyant vortex rings whose circulation is fully determined by their buoyancy (Bond and Johari, 2010; Zhao et al., 2013). Consistently, turbulent thermals at the cap of starting plumes (Turner, 1962), immiscible thermals (Landeau et al., 2014) and settling particle clouds (Ruggaber, 2000; Lai et al., 2013; Moghadaripour et al., 2017) have all been successfully modelled as vortex rings. In fact, different models of turbulent thermals (for example Morton et al., 1956; Scorer, 1957) and models of buoyant vortex rings (Turner and Taylor, 1957; McKim et al., 2020; Nikulin, 2014) lead to the same scalings after the transient formation of these structures. Given the morphology of clouds in figure 2.3, we present the essential equa-

tions governing the evolution of buoyant vortex rings, which will prove enlightening to analyse the clouds' growth.

When buoyant particles start settling, the cloud initially rolls up as a buoyant vortex ring. After a transient, one observes that vorticity concentrates inside a toroidal core. It is often assumed, and appropriate in our simulations as we shall see, that the vortex ring is sufficiently thin-cored to guarantee the absence of any buoyant material along the vortex centreline (axis of symmetry of the vortex ring, parallel to $\boldsymbol{e}_z$ and passing through the centre of symmetry of the torus), and that no vorticity diffuses through this line, leading to the conclusion that the circulation Γ of the vortex ring remains constant after the short transient of spin-up (see equation 4 in reference McKim et al., 2020), as verified in numerical simulations for a cloud Reynolds number of 630 and 6300 (McKim et al., 2020). Consequently, the initial spin-up of the vortex is paramount because it sets the ultimately constant value of the circulation which plays a key role in determining the cloud growth rate.

The impulse of a thin-cored vortex ring of radius R under the Boussinesq approximation reads $\pi\rho_f\Gamma R^2$ (McKim et al., 2020; Turner and Taylor, 1957). This impulse varies in time due to buoyancy which is the sole external force, hence we have

$$\frac{d}{dt}\left[\pi\rho_f\Gamma R^2\right] = m_0 g \ , \tag{2.11}$$

from which it is clear that in the absence of buoyancy, the impulse would be constant hence the vortex ring would keep a constant radius, as verified in the literature (Didden, 1979; Gharib et al., 1998) for vortex rings of Reynolds number up to 10^4 (Didden, 1979). Assuming a constant circulation, the previous equation simplifies to

$$R^2(t) - R^2(t=0) = \frac{m_0 g}{\pi\rho_f\Gamma} t \ . \tag{2.12}$$

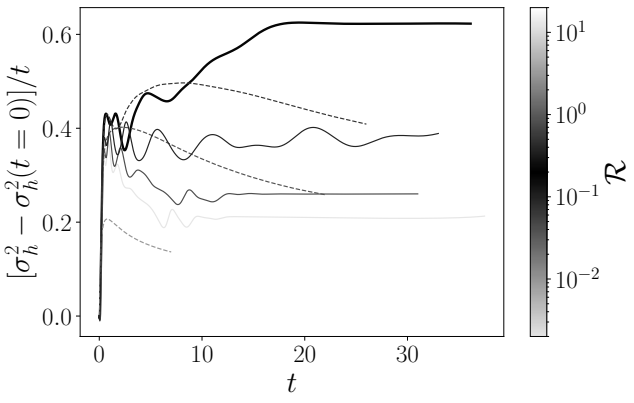

Figure 2.5: *Time evolution of the increment of square radius compensated with time* $[\sigma_h^2(t) - \sigma_h^2(t=0)]/t$*, measured in simulations for several Rouse numbers. Lines are dashed if* $\mathcal{R} > 0.221$ *and solid otherwise.*

To verify this scaling, the cloud radius is measured in numerical simulations with the quantity σ_h, which is the horizontal standard deviation of the particles' spatial distribution with

respect to the cloud centre of mass

$$\sigma_h(t) = \sqrt{\frac{\int \mathcal{C}(x', y', z', t)(x'^2 + y'^2)}{\int \mathcal{C}(x', y', z', t)}} \,, \tag{2.13}$$

where the origin of coordinates (x', y', z') corresponds to the cloud centre of mass, and integrals are computed in the whole computational domain. From this definition, the scaling (2.12) is verified in figure 2.5: aside from slight oscillations, clouds of low Rouse number ($\mathcal{R} \leq 0.221$) eventually grow as $\sigma_h \sim t^{1/2}$ as evidenced by the plateau of the compensated quantity $[\sigma_h^2 - \sigma_h^2(t=0)]/t$. Conversely, clouds with large Rouse numbers ($\mathcal{R} > 0.221$) grow slower than $\sigma_h \sim t^{1/2}$ so the quantity $[\sigma_h^2 - \sigma_h^2(t=0)]/t$ eventually decreases in time, meaning that these clouds do not follow the scaling (2.12). Note that according to equation (2.12), the plateaus in figure 2.5 are inversely proportional to the circulation Γ, suggesting the existence of a minimum of circulation for intermediate Rouse numbers close to $\mathcal{R} = 0.221$; this observation will receive considerable attention in section 2.5.

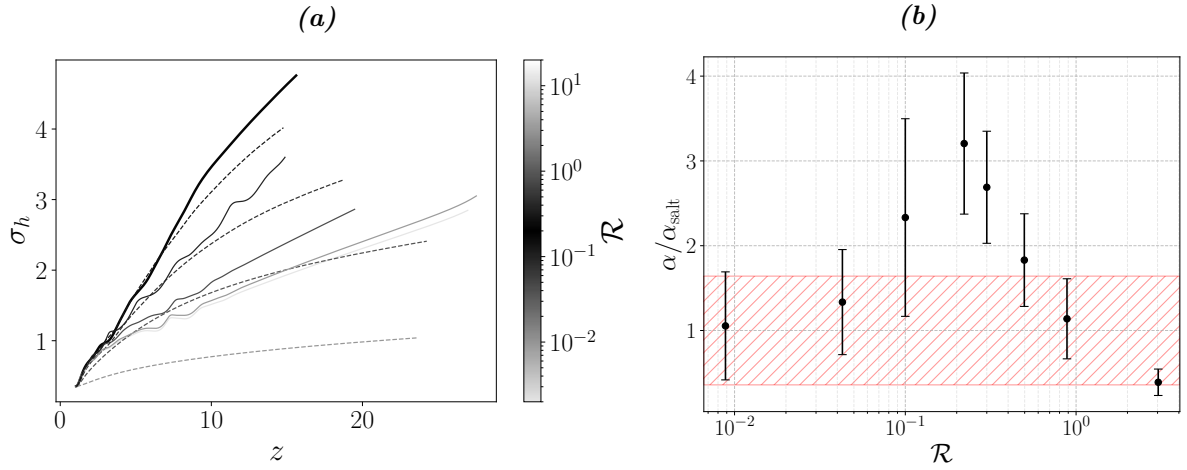

Figure 2.6: *(a) Evolution of the clouds' radius σ_h along depth. Lines are dashed if $\mathcal{R} > 0.221$ and solid otherwise. (b) Growth rate α computed in the range $z < 0.45 L_{domain}$, divided by the reference value α_{salt} of a salt-water cloud i.e. of a cloud with no particle settling ($\mathcal{R} = 0$).*

The clouds' growth is generally analysed along depth z rather than in time. Figure 2.6a shows the evolution of the radius $\sigma_h(z)$ for all clouds. For $\mathcal{R} \ll 1$ clouds tend to grow linearly in depth after a short transient. For $\mathcal{R} = 0.221$ a noticeable decrease of the slope $d\sigma_h/dz$ is visible at depth $z = 10$, as already observable in figure 2.3c, which is due to the transition to the swarm regime. For large Rouse numbers, typically above unity, it is manifest that the slope $d\sigma_h/dz$ is never constant, it keeps decreasing as clouds fall deeper.

More importantly, figure 2.6a shows that the growth rate $d\sigma_h/dz(z)$ tends to be maximum for an intermediate Rouse number close to $\mathcal{R} = 0.221$. To compare this growth rate with the entrainment rate measured in our experiments over a 45cm-deep field of view, the value of $d\sigma_h/dz(z)$ is computed in simulations, then averaged in the range $z < 0.45 L_{\mathrm{domain}}$. The resulting average value is denoted α and results are shown in figure 2.6b. Consistently with our

experiments (see figure 1.6 in Chapter 1), we observe an asymptote towards a constant growth rate as $\mathcal{R} \to 0$, a local maximum for a finite Rouse number which lies in the range $\mathcal{R} \simeq 0.3 \pm 0.1$ determined from experiments, and a clear decrease of the growth rate as $\mathcal{R}$ increases beyond $\mathcal{R} = 0.3$. The maximum amplitude of the enhancement $\alpha(\mathcal{R} = 0.221)/\alpha_{\text{salt}} = 3.20 \pm 0.83$ is larger than the value found in experiments $\alpha(\mathcal{R} \simeq 0.3)/\alpha_{\text{salt}} = 1.75 \pm 0.30$. This is likely due to the difference of cloud Reynolds number between experiments ($Re = 1183$) and simulations ($Re = 454$). In appendix 2.B, numerical results for clouds of Reynolds number $Re = 1183$ yield $\alpha(\mathcal{R} = 0.221)/\alpha_{\text{salt}} = 2.20 \pm 0.42$ as a new maximum, which is in agreement with our experiments. The important point here is that the present Eulerian approach is capable of reproducing the physical effect we observed in laboratory experiments.

We now turn to the swarm regime before analysing the role of the gravitational drift in enhancing the growth rate α in Section 2.5.

2.4.3 Swarm regime

During the gradual transition from the buoyant vortex ring to the swarm regime, particles increasingly decouple from fluid motions. This gradual decoupling is analysed thanks to the concentration $\mathcal{C}_{\text{tracer}}$ of the passive tracer, which is implemented in four additional simulations of Rouse numbers $\mathcal{R} = 0.100, 0.221, 0.498, 0.885$. As a wish to perform similar processings as in our experiments where the flow was visualised in a vertical laser sheet, the decoupling is illustrated with space-time diagrams in figures 2.7a-2.7d after averaging the fields $\mathcal{C}$ and $\mathcal{C}_{\text{tracer}}$ along x in the plane $y = 0$ (this averaging process is made explicit with the brackets $\langle\cdot\rangle_x$). The space-time diagrams reveal that increasing $\mathcal{R}$ leads to a faster separation between the field $\langle\mathcal{C}\rangle_x$ (in blue-red colours) and the passive tracer $\langle\mathcal{C}_{\text{tracer}}\rangle_x$ (in yellow-red contours) which is left behind particles. By construction, the sole ingredient responsible for this decoupling is the gravitational drift in equation (2.9) which only concerns the field $\mathcal{C}$, not the passive tracer.

A quantification of the decoupling between $\mathcal{C}$ and $\mathcal{C}_{\text{tracer}}$ is possible by defining a correlation coefficient which computes the overlap between $\mathcal{C}$ and $\mathcal{C}_{\text{tracer}}$ as a percentage of the total region occupied by these two fields. In practice, minimum thresholds are applied on the fields, whose values ensure the convergence of the correlation coefficient. As in figure 2.7, the correlation coefficient is computed in the plane $y = 0$ (denoted Oxz below) as

$$C_{\mathcal{C},\mathcal{C}_{\text{tracer}}}(t) = \frac{\int_{Oxz} \xi_1(t)\mathrm{d}x\mathrm{d}z}{\int_{Oxz} \xi_2(t)\mathrm{d}x\mathrm{d}z} \,, \tag{2.14}$$

where the booleans $(\xi_1(t), \xi_2(t))$ are defined as

$$\xi_1(t) = \begin{cases} 1, & \text{if } \mathcal{C}(t) > \mathcal{C}_1(t) \text{ and } \mathcal{C}_{\text{tracer}}(t) > \mathcal{C}_2(t) \\ 0, & \text{otherwise} \end{cases} ; \; \xi_2(t) = \begin{cases} 1, & \text{if } \mathcal{C}(t) > \mathcal{C}_1(t) \text{ or } \mathcal{C}_{\text{tracer}}(t) > \mathcal{C}_2(t) \\ 0, & \text{otherwise} \end{cases} , \tag{2.15}$$

with $\mathcal{C}_1(t) = \max\{\mathcal{C}(t)\} \times 10^{-4}$, $\mathcal{C}_2(t) = \max\{\mathcal{C}_{\text{tracer}}(t)\} \times 10^{-4}$. The time evolution of $C_{\mathcal{C},\mathcal{C}_{\text{tracer}}}(t)$ is shown in figure 2.8a for the same four simulations as above. The correlation coefficient is initially equal to unity because both fields of concentration are identical. Then, the correlation coefficient decreases as particles gradually shift away from the passive tracer due to the gravitational drift, all the faster as the Rouse number is larger. Finally figure 2.8b confirms

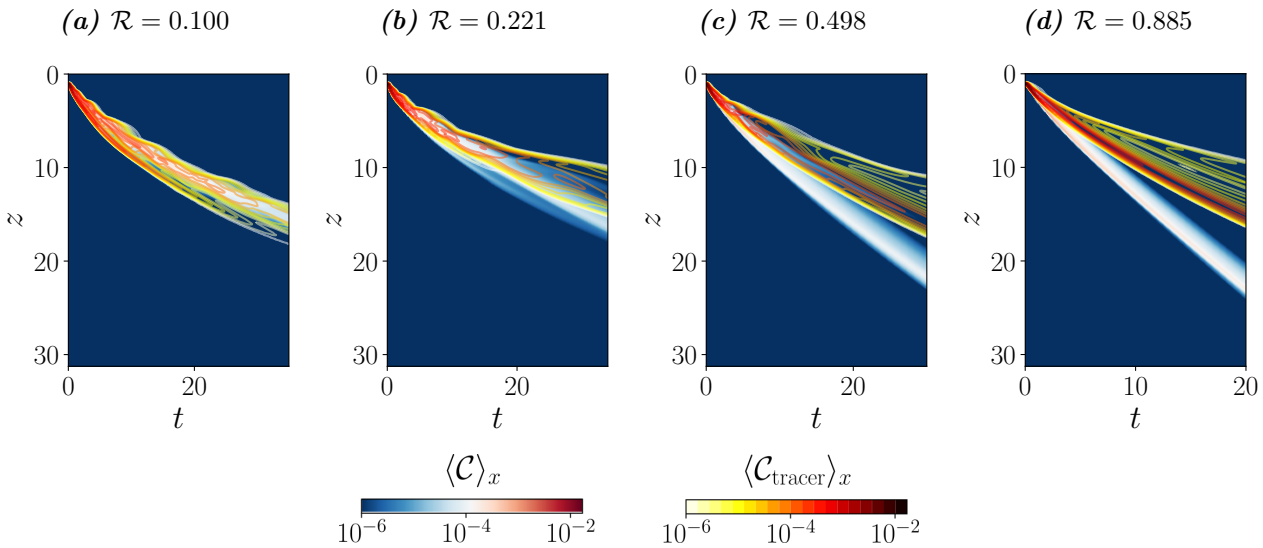

Figure 2.7: *Hovmöller diagrams for four increasing Rouse numbers showing the gradual decoupling in the plane $y = 0$ between the field of concentration $\langle \mathcal{C} \rangle_x$ (in blue-red colours) and the passive tracer $\langle \mathcal{C}_{tracer} \rangle_x$ (in yellow-red contours). The values shown for both concentrations are horizontal averages along x in the plane $y = 0$ at each time step.*

that the settling velocity of swarms approaches a constant value after separation, equal to the individual settling velocity which is equal to the Rouse number $\mathcal{R}$ in our dimensionless units (see inlet in figure 2.8b). Figure 2.6a already showed that the growth rate of swarms starts reducing after separation (the concave deflection of $\sigma_h(z)$ is most visible for $\mathcal{R} = 0.221$), so swarms ultimately fall with constant velocity, retaining a bowl shape without deforming, as shown by the snapshots in figure 2.3e for $\mathcal{R} = 3.03$.

2.5 Role of the Rouse number on the enhanced growth rate

The linear growth in depth of buoyant clouds is usually described as resulting from entrainment of ambient fluid into the cloud, leading to its growth and dilution, and consequently its deceleration through mixing drag. One reference to describe the process of entrainment for turbulent thermals is the model of Morton et al. (1956). It is based on the entrainment hypothesis which states that the inflow velocity at the interface of the turbulent thermal is proportional to the vertical velocity of the cloud's centre of mass; this inflow velocity is considered to be produced by turbulent motions.

Yet, our observation of a maximum growth rate α even for moderate Reynolds numbers ($Re = 454$ here) suggests that the enhanced entrainment due to the finite gravitational drift finds an origin in the large-scale buoyancy-induced mean flow (which, in the case of turbulent particle clouds, is obtained by an average over realisations) rather than in turbulent fluctuations. Actually, this question of the origin of entrainment in turbulent flows has long been debated: does it originate from the large-scale mean flow incorporating ambient fluid into the turbulent

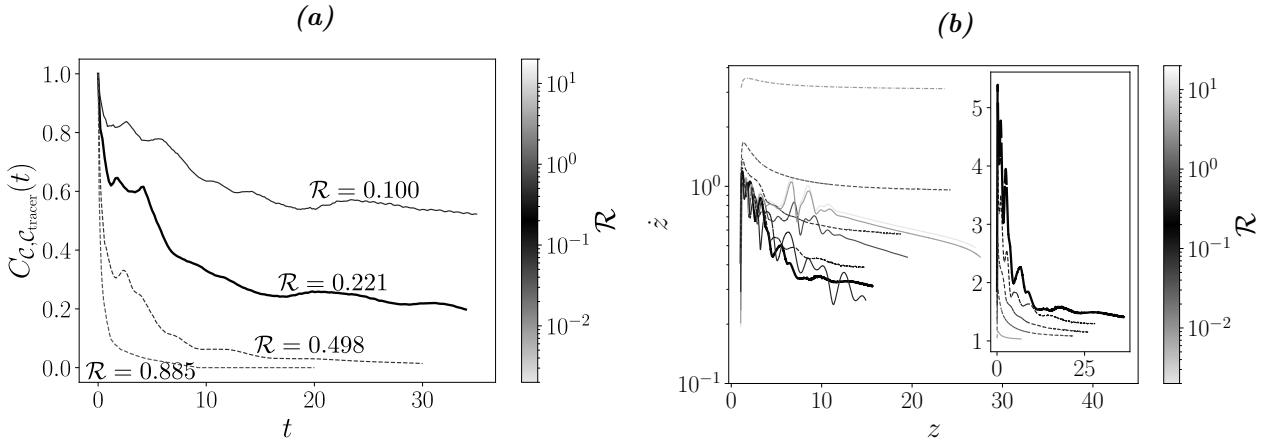

Figure 2.8: *(a) Time evolution of the correlation coefficient $C_{\mathcal{C},\mathcal{C}_{tracer}}(t)$ between particle and passive tracer concentrations for $\mathcal{R} \in \{0.100, 0.221, 0.498, 0.885\}$, from top to bottom. (b) Evolution in depth of the vertical velocity of the clouds' centre of mass for all simulations. Lines are dashed if $\mathcal{R} > 0.221$ and solid otherwise. The inset shows the normalised velocity $\dot{z}/\mathcal{R}$ as a function of time t only for clouds verifying $\mathcal{R} \geq 0.221$.*

region through 'engulfment'? Or from small-scale fluctuations and diffusive processes which mix the ambient material in the turbulent structure close to its interface through 'nibbling'? While Mathew and Basu (2002) observed that mixing in a cylindrical turbulent jet seemed to be driven by nibbling close to the jet interface, Townsend (1950) showed that large-scale eddies of increasing intensity produce more energy in the turbulent wake past a cylinder and consequently favour a larger growth rate of this wake, suggesting that the mean flow drives entrainment through engulfment. Discriminating between engulfment and nibbling can be complex because large and small scales may be insufficiently separated at moderate Reynolds numbers, and because fluxes at both scales can be connected through some relationships (Mathew and Basu, 2002). For example, in Odier et al. (2012), Reynolds stresses at the mixing interface of a gravity current are modelled based on Prandtl mixing length theory, thus enabling, through the use of a large-scale quantity based on the mean flow, the description of entrainment in the mixing layer by fundamentally local fluxes.

Importantly, the reason for this ambiguity is that both processes contribute to entrainment, as evidenced by Fox (1970) who derived the equations of evolution of a self-similar plume while considering the equation of conservation of energy, hence lifting the constraint of modelling entrainment to guarantee a closure of the equations. In doing so, he showed that entrainment depends both on the Reynolds stress and on a contribution from the mean flow due to buoyancy. This was confirmed by van Reeuwijk and Craske (2015) who carried this analysis further and showed that a third contribution comes from possible deviations from self-similarity in the streamwise direction. By analysing data from the literature, van Reeuwijk and Craske (2015) showed that the term of turbulence production due to shear hardly varies between a pure jet and a pure plume, even though plumes have a larger growth rate than jets. Hence this last difference between jets and plumes is attributed to the contribution of the mean flow due to buoyancy, as later confirmed by van Reeuwijk et al. (2016) in Direct Numerical Simulations.

These conclusions about entrainment apply similarly for plumes and thermals, as pointed out by Landeau et al. (2014). From the model of Morton et al. (1956), Landeau et al. (2014) proved experimentally that the growth rate of an immiscible thermal verifies a linear relationship with respect to the thermal's Richardson number, which is exactly analogous to the entrainment model of Priestley and Ball (1955) for plumes, see van Reeuwijk and Craske (2015) for details. Consistently with these conclusions, Lecoanet and Jeevanjee (2019) showed that turbulence only enhances entrainment by 20% between turbulent thermals of Reynolds number 630 and 6300, whereas an artificial sudden shut off of buoyancy during the same numerical simulations drastically reduces the entrainment rate of turbulent thermals (McKim et al., 2020), highlighting the driving role of buoyancy in entrainment.

Consequently, in the present section we focus on mean flow azimuthally-averaged quantities to try to understand the optimum growth rate of particle clouds for a Rouse number around $\mathcal{R} \simeq 0.22$. Past studies have shown that in the absence of buoyancy, the circulation of a vortex ring generated from a nozzle increases from zero to a constant value during the transient rolling-up of the viscous boundary layer in the nozzle (Didden, 1979), with this constant circulation increasing as the ratio of the nozzle length over its diameter increases. When the vortex ring is buoyant, buoyancy provides a new contribution to the total circulation, which was fully derived by McKim et al. (2020) for a thin-cored Boussinesq vortex ring, yielding the following scaling for the growth rate α (see Nikulin (2014); Bond and Johari (2005) but also Turner and Taylor (1957); Lecoanet and Jeevanjee (2019); Scorer (1957) for turbulent thermals)

$$\alpha \propto \frac{m_0 g}{\rho_f \Gamma_\infty^2}, \tag{2.16}$$

with a proportionality constant accounting for the cloud added mass and its morphology (McKim et al., 2020), and with Γ_∞ the asymptotically constant value of the circulation. The key result here is that since all clouds undergo the same buoyancy force $m_0 g$ in our simulations, their growth rate α is dictated by Γ_∞ only. Consequently, vortex rings of lower circulation should have a larger growth rate – crudely speaking, they should entrain more, as consistently observed in Bond and Johari (2005); Landeau et al. (2014).

To verify this scaling, the vortex ring circulation is computed *a posteriori* for several snapshots after (i) interpolating the mesh on a regular cartesian grid, (ii) averaging the azimuthal vorticity ω_θ along the azimuth $\boldsymbol{e}_\theta$ in radial and vertical bins (when ambiguity is possible, we denote azimuthally-averaged quantities with an overline such as $\overline{\omega}_\theta$), (iii) integrating the resulting average azimuthal vorticity over the whole radial extent and in the range $z \in [0.3, L_{\text{domain}} - 0.3]$ (top and bottom walls are removed from this range to avoid integration of vorticity near those boundaries). Results are shown in figure 2.9a. We verify that the circulation produced by the particle clouds ultimately reaches a plateau, except when $\mathcal{R} \gg 1$ i.e. for clouds which are not expected to behave as buoyant vortex rings due to separation. From previous sections, figure 2.9a already suggests that the circulation Γ_∞ is all the lower as the cloud grows faster; this is confirmed in figure 2.9b where the scaling $\alpha \propto \Gamma^{-2}$ of equation (2.16) is in excellent agreement with the best fit (see the solid dark line in figure 2.9b) of measurements of the circulation when the cloud centre of mass is at mid-depth in the computational domain i.e. with the definition $\Gamma_\infty \equiv \Gamma(z = L_{\text{domain}}/2)$.

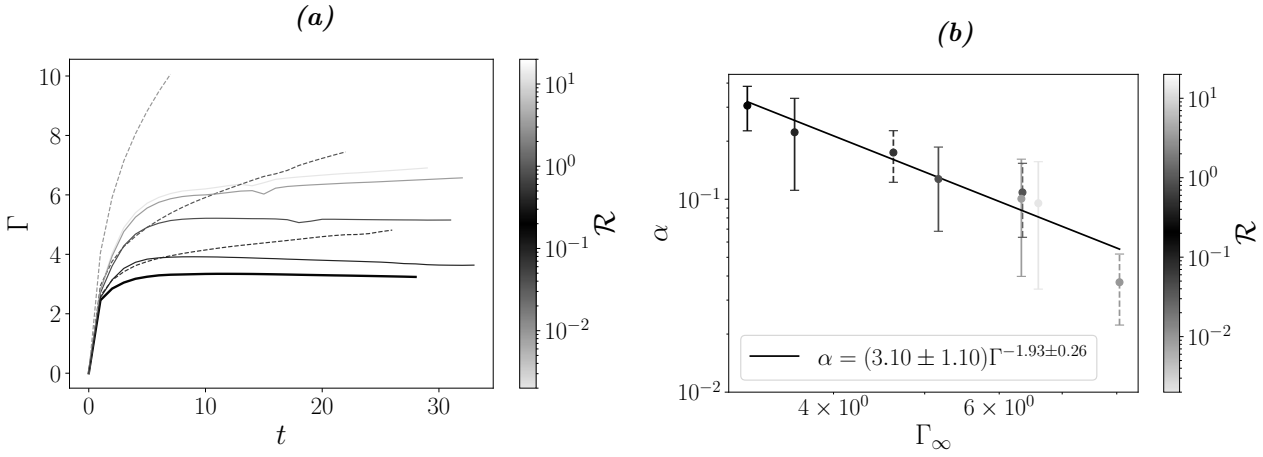

Figure 2.9: *(a) Time evolution of the axisymmetric circulation in the whole computational domain. Lines are dashed if* $\mathcal{R} > 0.221$ *and solid otherwise. (b) Correlation between the growth rate* α *averaged over the range* $z < 0.45L_{\text{domain}}$*, and measurements of* Γ_∞*. The solid dark line is the linear least square fit of* $\ln(\alpha)$ *vs.* $\ln(\Gamma_\infty)$*.*

Another remarkable observation is the modification of the structure of the vortical core when increasing the Rouse number, as illustrated in figure 2.10. When $\mathcal{R} = 4.28 \times 10^{-2}$ (figure 2.10a) the vortex core is neatly defined, centered around a maximum of azimuthal vorticity whose structure is at first order isotropic in a plane $(\boldsymbol{e}_r, \boldsymbol{e}_z)$ of fixed azimuth. Conversely when $\mathcal{R} = 0.221$ (figure 2.10c), the vortex core is made up of sheets of vorticity of alternate sign and varying intensity which occupy a much larger region than observed for $\mathcal{R} = 4.28 \times 10^{-2}$ at the same depth. Let us show that as $\mathcal{R}$ gets closer to 0.221 the vortical core induces circulation farther and farther away, thus expanding the region of entrainment through the toroidal mean flow. After defining the core centroid as the barycentre of the azimuthal vorticity, the following normalised circulation is computed

$$\Gamma^*(r) = \frac{1}{\pi r^2} \int_0^{2\pi} \int_0^r < \omega_\theta >_\theta r' \mathrm{d}r' \mathrm{d}\theta, \tag{2.17}$$

where (r', r, θ) here correspond to polar coordinates centered on the core centroid. The size of the vortex core is defined as $\text{argmax}\{\Gamma^*(r)\}$ i.e. as the radial distance from the core centroid where the circulation $\Gamma^*(r)$ is maximum. Consistently, figure 2.11a shows that this circulation Γ^* spreads further away from the core centroid when $\mathcal{R} = 0.221$, meaning that this vortex ring induces velocity farther away, therefore incorporating more ambient fluid within the particle cloud, hence the latter grows faster. This trend is even clearer in figure 2.11b where the core size is computed at the same depth $L_{\text{domain}}/2$ for all clouds: one verifies that the core extension is maximum when the Rouse number is closest to $\mathcal{R} = 0.221$.

The key question is then: How come vortex rings have a wider core and a lower circulation when the particle Rouse number is closer to 0.221? The vortex circulation is only produced during a short initial transient, mainly by the baroclinic torque as long as its contribution along the vortex centreline is non-negligible. As soon as the buoyant material has spun up

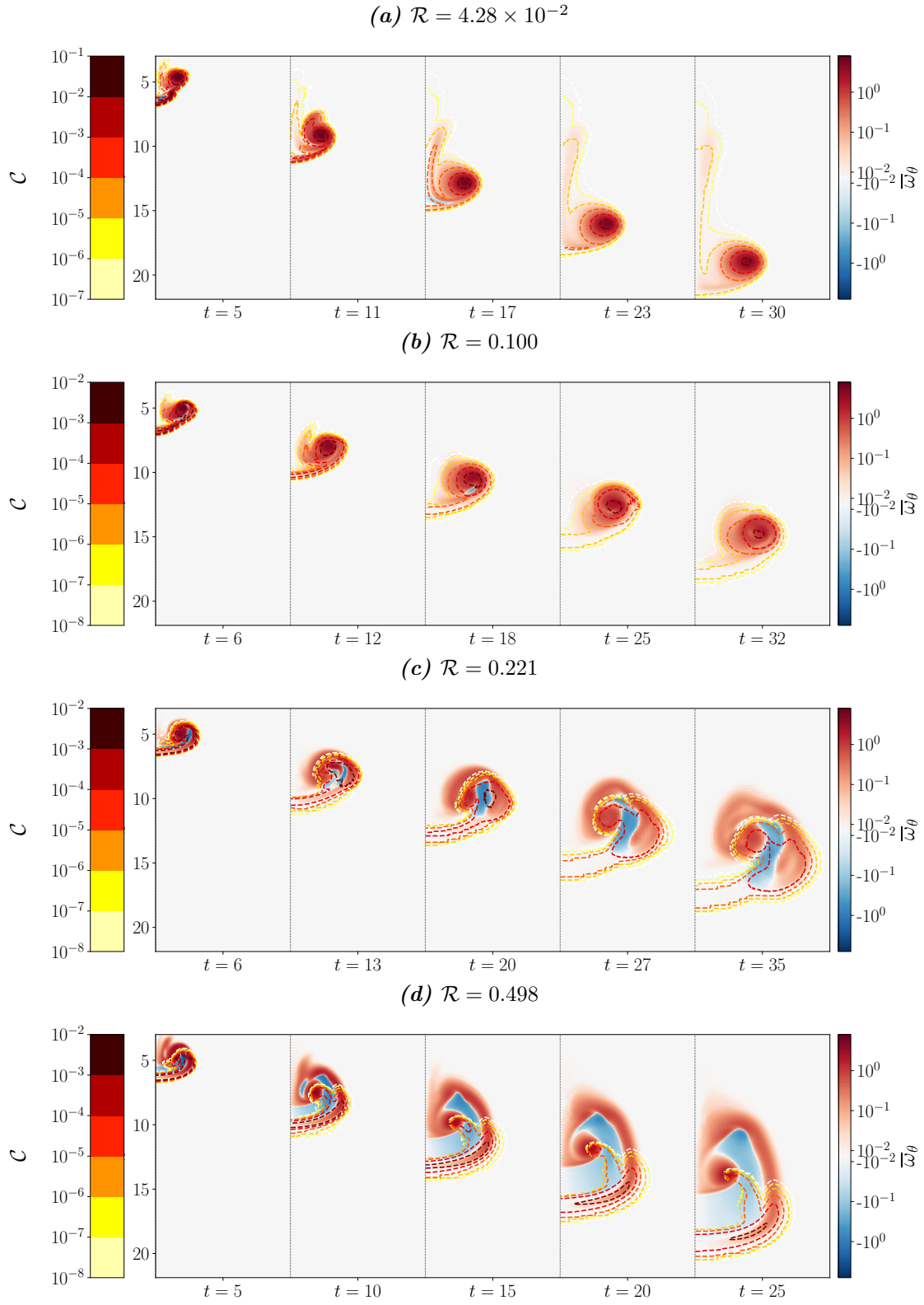

Figure 2.10: *Each row shows snapshots of the azimuthally-averaged vorticity $\overline{\omega}_\theta$ in blue-red colours, and the azimuthally-averaged concentration $\mathcal{C}$ with dashed contours in yellow-red shades (see colorbars on the left-hand side). Each snapshot is visualised in the plane (r, z) in the range $3 < z < 22$ and $0 < r = \sqrt{x^2 + y^2} < 10$.*

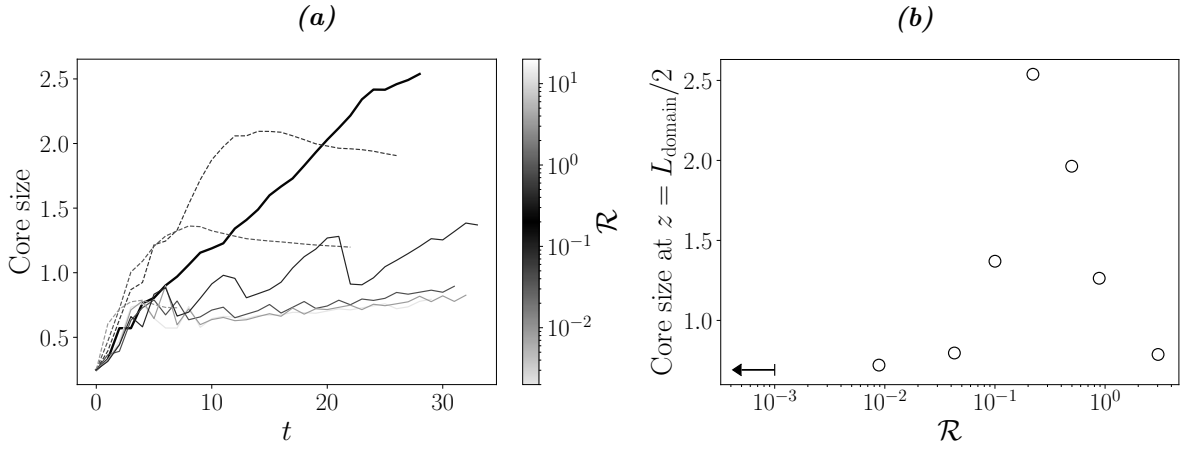

Figure 2.11: *(a) Time evolution of the size of the vortical core for all clouds. Lines are dashed if* $\mathcal{R} > 0.221$ *and solid otherwise. (b) Size of the core at depth* $z = L_{domain}/2$ *for all clouds. The dark arrow corresponds to the value for* $\mathcal{R} = 0$*.*

and widened sufficiently, one can define a closed contour encircling the core where no vorticity diffuses and no buoyant material is present, so that circulation is conserved (e.g. McKim et al., 2020). The vorticity equation along the azimuth $\boldsymbol{e}_\theta$ reads

$$\frac{\mathrm{D}\omega_\theta}{\mathrm{D}t} = \underbrace{\frac{\omega_\theta v_r}{r}}_{\text{stretching}} + \overbrace{\frac{g'}{\rho_f}\frac{\partial \mathcal{C}}{\partial r}}^{\text{baroclinic torque}} + \underbrace{\nu\left[\frac{1}{r}\frac{\partial}{\partial r}\left(r\frac{\partial \omega_\theta}{\partial r}\right) + \frac{\partial^2 \omega_\theta}{\partial z^2}\right]}_{\text{diffusion}}, \tag{2.18}$$

which shows that azimuthal vorticity is produced by vortex stretching, the baroclinic torque and diffusion of vorticity. The quantity $\omega_\theta v_r$ is at first order symmetrical around the vortex core, so for a thin-cored vortex ring having a radius much larger than the vortex core, the stretching term should be vanishingly small, as previously argued by other authors (McKim et al., 2020). Then, if diffusion is assumed negligible, most forcing is expected to originate from the baroclinic torque. This is especially true at initial times when the stretching and diffusion terms vanish while the baroclinic torque remains finite. The baroclinic torque is therefore the leading source of circulation at initial times (McKim et al., 2020). To verify this, the dimensionless baroclinic torque $Ri\partial_r\mathcal{C}$ along $\boldsymbol{e}_\theta$ is first averaged along the azimuth (the resulting axisymmetric torque is denoted $\overline{Ri\partial_r\mathcal{C}}$). Then the axisymmetric torque is integrated in the plane $(\boldsymbol{e}_r, \boldsymbol{e}_z)$ and integrated in time until $t = 10$ when we observe that the torque has vanished for all simulations. Results are shown in figure 2.12. We verify that Rouse numbers close to $\mathcal{R} = 0.221$, which correspond to the largest growth rate α (figure 2.6b) and lowest circulation (figure 2.9a), also correspond to the lowest baroclinic forcing. This observation is robust: integrating the baroclinic torque in time even just up to $t = 1$ modifies the value of the integrated torque, but leaves the curve in figure 2.12 unchanged. As an indication, the errorbars in figure 2.12 show the little influence of integrating the baroclinic torque up to $t = 8$ or $t = 10$ which respectively correspond to the lower and upper bound of errorbars.

The picture that emerges from these results is the following: under the assumption that baroclinicity is the leading forcing of the vortex rings' circulation, the maximum of entrainment capacity of particle clouds with a Rouse number close to $\mathcal{R} = 0.221$ seems to be due to the gravitational drift and two-way coupling of particles with the fluid which reduces the baroclinic torque, thus reducing the cloud circulation. Since all clouds undergo an identical buoyancy force $m_0 g$, these same clouds have a larger growth rate α as predicted by equation (2.16). Similar results have been obtained at a larger Reynolds number $Re = 1183$ (see Appendix B), in good agreement with experiments. Note however that the role played by fluctuations in the limit of very large Reynolds numbers remains to be explored and might have an influence on our conclusions derived from moderate Reynolds numbers only.

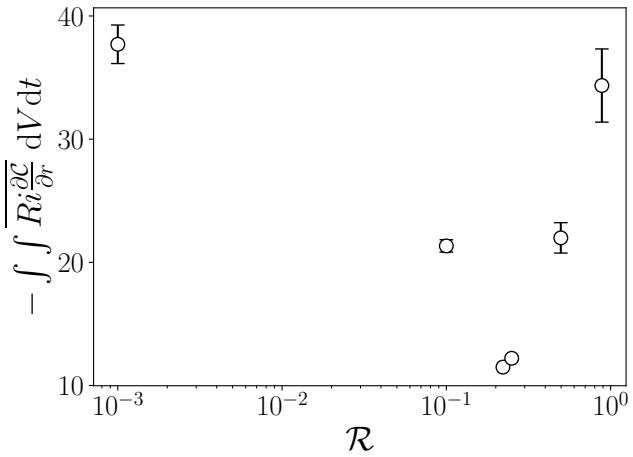

Figure 2.12: *Results of time and volume integration up until $t = 10$ of the axisymmetric baroclinic torque as a function of the Rouse number.*

2.6 Concluding discussion

The previous section showed that the gravitational drift modifies the distribution in space and time of the field of particle concentration $\mathcal{C}(x, y, z, t)$ compared to that of a passive tracer. This modification alters the forcing by the drag force, minimises the baroclinic torque and concurs to a maximum growth rate α for a Rouse number around $\mathcal{R} = 0.221$. All these modifications are observed at moderate Reynolds numbers and notably quantified by the azimuthally-averaged circulation and baroclinic torque; this is consistent with the literature pointing towards the leading role of the mean flow and buoyancy in controlling entrainment and the growth of thermals (see section 2.5). A key conclusion is that the present Eulerian two-way coupling numerical simulations successfully reproduce our experimental observation of a maximum growth rate $\alpha/\alpha_{\text{salt}}$ of particle clouds for a Rouse number $\mathcal{R} \approx 0.22$ lying within the experimental range $\mathcal{R} \simeq 0.3 \pm 0.1$. While results at $Re = 454$ yield a maximum growth rate slightly above the experimental value $\alpha(\mathcal{R} \simeq 0.3)/\alpha_{\text{salt}} = 1.75 \pm 0.30$, results at $Re = 1183$ lie in the experimental range within uncertainty margins. A systematic study with varying Reynolds numbers might clarify whether the mechanism identified in this paper persists in the presence of intense

turbulent fluctuations.

Our results raise a new question: How does the gravitational drift of particles contribute to reducing the baroclinic forcing ? Some light could be shed on this matter by analysing the properties of the flow induced by a canonical laminar vortex ring while the field of concentration drifts radially outward until separation, but the evolution of the structure of the vortex core in figure 2.10 suggests that the feedback of particles on the vortex ring itself probably plays a non-negligible part. Furthermore, even though the robust agreement between our experiments and the present results supports the responsibility of the mean flow in the maximisation of α for a finite Rouse number, it remains to be investigated whether other physical ingredients could be at play in experiments, in particular velocity fluctuations due to turbulence at much higher Reynolds numbers than considered here.

In the present numerical simulations, fluctuations are very low compared to the mean flow due to the low Reynolds number $Re = 454$ at the scale of the particle cloud. Our experiments, on the opposite, were characterised by a Reynolds number $Re = 1183$. Even though this value is too low to have a well-developed turbulent flow with a clear separation of scales between the integral cloud scale and the scale of the smallest dissipative eddies, our experimental clouds evidenced some more fluctuations than in numerical simulations. On one hand, these may modify the cloud circulation during its transient increase, hence during a limited amount of time. On the other hand, after this transient, entrainment can be increased by the term of production of turbulent kinetic energy (TKE), as shown by van Reeuwijk and Craske (2015) in their entrainment relations. This production term may differ for one-phase turbulent thermals vs. particle-laden turbulent thermals due to turbulence modulation by particles (Brandt and Coletti, 2022), as observed in simulations (Bosse et al., 2006; Elghobashi and Truesdell, 1993) and experiments (Hassaini and Coletti, 2022; Berk and Coletti, 2021). These studies notably showed a redistribution of energy from small to large wave numbers known as 'pivoting', which may favour nibbling-like entrainment at small scales rather than engulfment by the mean flow. Consequently, the possible enhancement of α by fluctuations in a more vigorous turbulent flow cannot be ruled out, calling for further investigation with a dedicated larger experimental setup and numerical simulations with a clear separation of scales. Answering these questions also probably requires a more advanced model such as a two-fluids approach where the particles have their own velocity field (e.g. Nasab and Garaud, 2021; Magnani et al., 2021; Nakamura et al., 2020), or a point-force Lagrangian model (e.g. Chou and Shao, 2016; Yamamoto et al., 2015; Climent and Magnaudet, 1999; Mazzitelli and Lohse, 2009).

2.7 Acknowledgements

This work was supported by the Programme National de Planétologie (PNP) of CNRS-INSU co-funded by CNES. Centre de Calcul Intensif d'Aix-Marseille is acknowledged for granting access to its high performance computing resources. This work was granted access to the HPC resources of IDRIS under the allocation 2022-A0120407543 and 2023-A0140407543 made by GENCI.

2.A Robustness of numerical measurements

We verified that numerical measurements of key quantities are invariant with respect to three numerical parameters: (i) the Schmidt number $Sc = \nu/\kappa_p$, (ii) the size $h_{\min}$ of the finest mesh cell and (iii) the numerical scheme implemented to compute the concentration gradient. For all simulations presented in the core of this study, the concentration gradient was computed with the generalised minmod slope limiter, which reads along the direction $\boldsymbol{e}_z$

$$\left(\frac{\partial \mathcal{C}}{\partial z}\right)_i \simeq \frac{1}{\Delta z} \max\left\{0, \min\left(\theta(\mathcal{C}_{i+1} - \mathcal{C}_i), \theta(\mathcal{C}_i - \mathcal{C}_{i-1}), \frac{\mathcal{C}_{i+1} - \mathcal{C}_{i-1}}{2}\right)\right\}, \tag{2.19}$$

with Δz the size of a mesh cell in the direction $\boldsymbol{e}_z$, θ a scalar ranging between 1 (the most dissipative scheme) and 2 (the least dissipative scheme), and $\mathcal{C}_{j\in\mathrm{N}}$ is the evaluation of $\mathcal{C}$ in a mesh cell j along the direction $\boldsymbol{e}_z$. The default value $\theta = 1.3$ of Basilisk was adopted. We verified that adopting a second-order centered scheme

$$\left(\frac{\partial \mathcal{C}}{\partial z}\right)_i = \frac{\mathcal{C}_{i+1} - \mathcal{C}_{i-1}}{2\Delta z} \tag{2.20}$$

does not alter our measurements. Results are presented in table 2.1, providing the average and standard deviation of (a) the growth rate α, (b) the cloud vertical velocity $\dot{z}$ and (c) the work of the drag term $\int \mathcal{C} v_z$ responsible for the transfer of energy from particles to the fluid during the cloud fall. These three quantities are averaged when the cloud position verifies $z(t) < 0.45 L_{\mathrm{domain}}$, which is the range we analysed with our experiments (Kriaa et al., 2022, Chapter 1). Reported values evidence little to negligible impact of the three numerical parameters on average measurements of α, $\dot{z}$ and $\int \mathcal{C} v_z$.

Varying numerical parameter	Fixed Re	$\alpha \times 10^3$	$\dot{z} \times 10^2$	$\int \mathcal{C} v_z \times 10^3$
$Sc \in \{1, 2, 5, 10\}$	1183	172 ± 7	640 ± 2	13.8 ± 2.3
$L_{\text{domain}}/h_{\min} \in \{256, 512, 1024, 2048\}$	180	328 ± 31	42.9 ± 3.4	6.4 ± 1.0
$L_{\text{domain}}/h_{\min} \in \{256, 512, 1024, 2048\}$	454	321 ± 29	44.1 ± 4.9	6.7 ± 1.5
$L_{\text{domain}}/h_{\min} \in \{512, 1024, 2048\}$	1183	343 ± 28	56 ± 14	12.7 ± 7.4
$\nabla \mathcal{C}$: minmod2 or 2nd order centered	454	305.64 ± 0.03	38.7870 ± 0.0004	5.422522 ± 0.000006
$\nabla \mathcal{C}$: minmod2 or 2nd order centered	1183	295 ± 8	39.9 ± 0.6	5.7 ± 0.2

Table 2.1: *Variability of the macroscopic quantities α, $\dot{z}$ and the work of the drag force $\int \mathcal{C} v_z$ in the range $z < 0.45 L_{domain}$ when varying the Schmidt number, the size h_{min} of the finest mesh cell, or the numerical scheme used to compute the concentration gradient.*

2.B Key results for clouds of Reynolds number $Re = 1183$

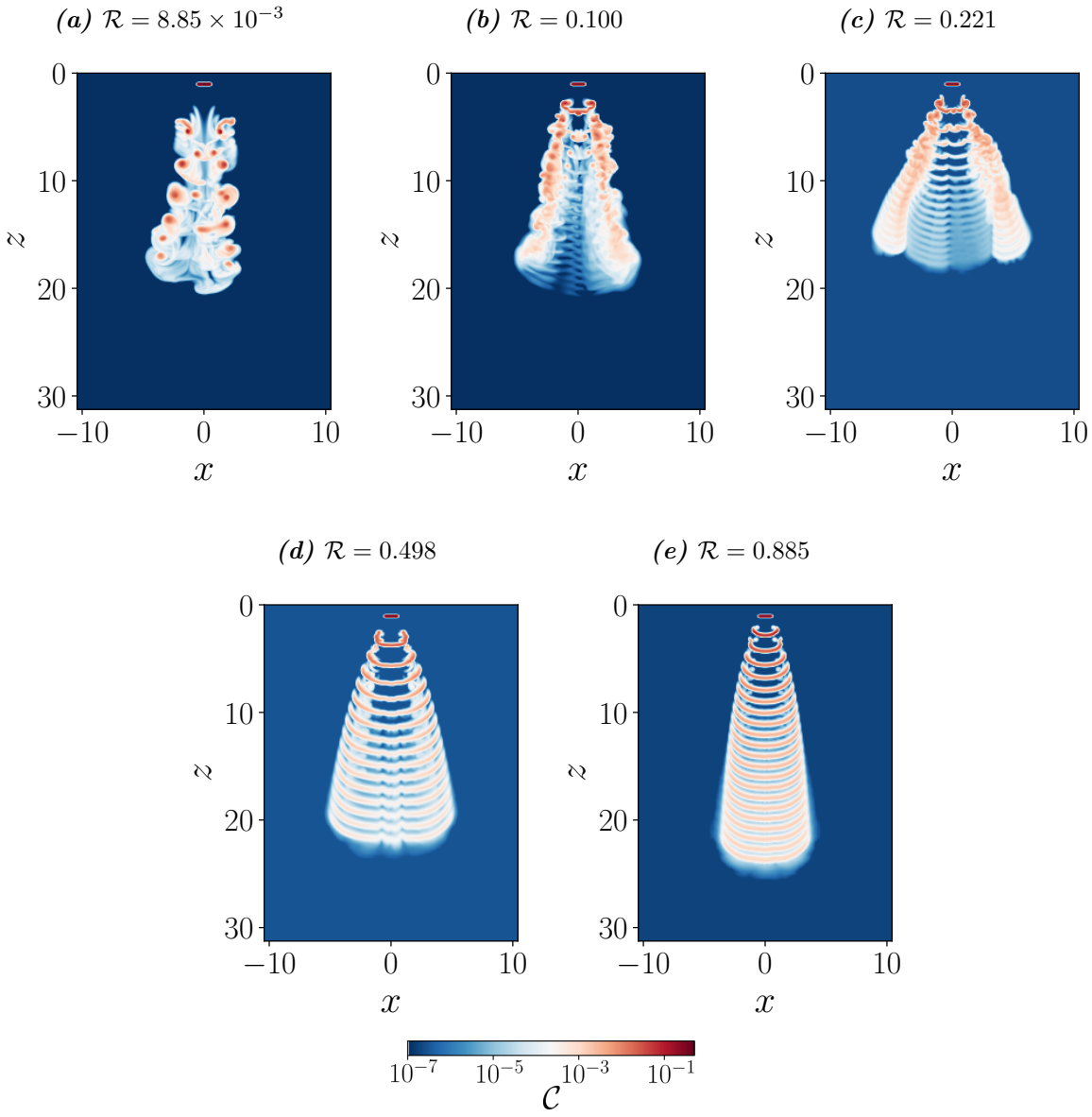

Figure 2.13: *Field of concentration $\mathcal{C}$ in the plane $y = 0$ averaged over up to 20 snapshots taken with a constant timestep $\Delta t = 2.5$ over the cloud fall for clouds of Reynolds number $Re = 1183$.*

For completeness, we briefly present numerical results for clouds of Reynolds number $Re = 1183$ as in our experiments (Kriaa et al., 2022, Chapter 1). Figure 2.13 shows time averages in the plane $y = 0$ of the field of concentration $\mathcal{C}$ for a set of clouds with varying Rouse numbers. More fluctuations do appear at low Rouse numbers (figures 2.13a-2.13c), whereas clouds of large Rouse numbers still evidence a thin bowl shape due to rapid particle separation from fluid motions (figures 2.13d, 2.13e). Importantly, these images show the existence of a maximum growth rate as $\mathcal{R} \to 0.221$, as quantitatively confirmed by figure 2.14, similarly as

in section 2.4.2 and consistently with our experiments (Kriaa et al., 2022, Chapter 1). The maximum amplitude of the enhancement $\alpha(\mathcal{R} = 0.221)/\alpha_{\text{salt}} = 2.20 \pm 0.42$ is lower than the one measured for $Re = 454$ in section 2.4.2, and in good agreement with the maximum measured in experiments $\alpha(\mathcal{R} \simeq 0.3)/\alpha_{\text{salt}} = 1.75 \pm 0.30$. A systematic study as a function of the Reynolds number might clarify what determines the amplitude of the optimum $\alpha/\alpha_{\text{salt}}$, but this is beyond the scope of the present work which focuses on the origin of this amplification, and on the capacity of the numerical model to reproduce it.

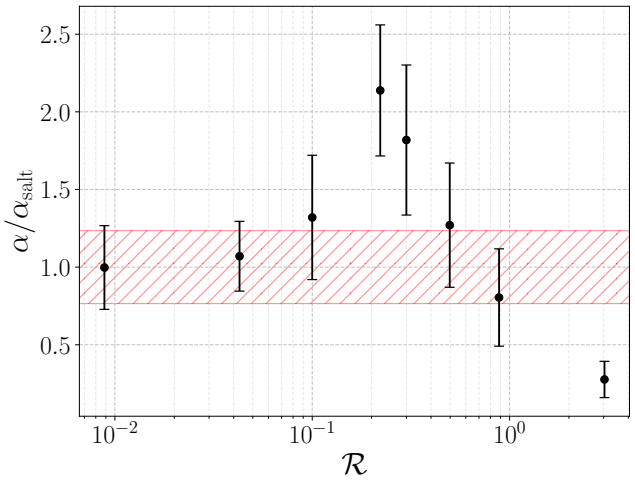

Figure 2.14: *Growth rate α computed in the range $z < 0.45L_{domain}$, divided by the reference value α_{salt} of a salt-water cloud i.e. of a cloud with no particle settling ($\mathcal{R} = 0$). The Reynolds number is $Re = 1183$.*

Chapitre 3

Influence of planetary rotation on metal-silicate mixing and equilibration in a magma ocean

This chapter is a work that has been led in collaboration with Maylis Landeau from IPGP, Paris

Summary

At a late stage of its accretion, the Earth experienced high-energy planetary impacts. Following each collision, the metal core of the impactor sank into molten silicate magma oceans. The efficiency of chemical equilibration between these silicates and the metal core controlled the composition of the Earth interior and left a signature on geochemical and isotopic data. These data constrain the timing, pressure and temperature of Earth formation, but their interpretation strongly depends on the efficiency of metal-silicate mixing and equilibration. We investigate the role of planetary rotation on the dynamics of the sinking metal and on its chemical equilibration using laboratory experiments of particle clouds settling in a rotating fluid. Our clouds initially sink as spherical turbulent thermals, but after a critical depth, rotation becomes important and they transition to a vortical columnar flow aligned with the rotation axis. In contrast with a thermal that grows in all directions, this vortical column grows vertically but keeps a constant horizontal extent. The slower dilution in vortical columns reduces chemical equilibration compared to previous estimates that neglect planetary rotation. Applied to Earth formation, our results predict that rotation strongly affects the fall of metal in the magma ocean for impactor cores smaller than 200 km in radius on a proto-Earth that rotates twice faster than today. On a fast-spinning proto-Earth, rotation becomes important for impactor cores up to 600 km in radius. We find that rotation significantly affects the degree of equilibration for highly siderophile elements with partition coefficients larger than 10^3. In this case, the degree of equilibration decreases by up to a factor 2 compared to previous estimates that neglect the effect of rotation.

3.1 Introduction

The present-day rocky planets of the solar system were formed 4.5 Gyrs ago (Patterson et al., 1955) by a series of impacts between planetary bodies. Moon-to-Mars-sized planetary embryos collided to form planets in $10-100$ Myrs (Chambers, 2004). This timing is confirmed by Hf-W radiochronometry which suggests that the Earth and the Moon were formed within the first 100 Myrs (Kleine et al., 2002; Rudge et al., 2010) of the solar system. At this time, planetary embryos were already differentiated into a liquid metal core and an outer silicate mantle (Kleine et al., 2002). During impacts, some of the metal core of impactors was mixed with silicates of the target planet, enabling thermal and chemical transfers. This mixing controlled the initial temperature and composition of rocky planets which determined the initial rheology of the mantle and the emergence of plate tectonics (Bercovici and Ricard, 2014), the time when a solid inner core started to grow (Labrosse, 2015), or the driving of an early dynamo in the Earth's core by exsolution of light elements (Badro et al., 2018).

Accretion of rocky planets goes through several successive stages involving ever larger impactors. The size of impactors varies from small kilometre-sized bodies to proto-planets as large as Mars or the Earth (Tonks and Melosh, 1993; Canup and Asphaug, 2001; Ćuk and Stewart, 2012; Canup, 2012). When the target embryo is the size of Mars or larger, the energy released during the impact is sufficient for shock waves to melt the silicate mantle much beyond the impact area (Brian Tonks and Jay Melosh, 1992; Nakajima et al., 2021). Previous studies (Tonks and Melosh, 1993; Nakajima et al., 2021) showed that a Mars-sized impactor hitting the Earth at a velocity larger than 11 km/s produces enough melt to uniformly cover the Earth surface down to a depth of 1000 km or more. The smaller the impactor or the target, the lower the volume of molten silicates produced by the shock in the target planet (Brian Tonks and Jay Melosh, 1992; Tonks and Melosh, 1993). Yet a series of small impactors may release sufficient energy to melt silicates at large depths, especially if the target surface is blanketed by a steam atmosphere (Abe and Matsui, 1985) reducing heat losses to space. Finally, during the first million years of accretion, radioactive elements like ^{26}Al (Dodds et al., 2021) released enough energy to melt the entire mantle of the target planet. In the following, we consider that any combination of the former ingredients enables the existence of a deep magma ocean, in which the impactor core sinks after an impact.

The fall of the impactor core in the magma ocean is strongly conditioned by the outcome of the impact. Numerical simulations are valuable tools to investigate the dynamics of impacts with various impactor sizes, impact angles or impact velocities (e.g., Ćuk and Stewart, 2012; Nakajima et al., 2021; Maas et al., 2021). Yet, evaluating chemical transfers requires to resolve mixing and diffusive processes at the metal-silicate interface. The length scale for chemical diffusion during the fall of metal in a magma ocean, which typically lasts a few hours, is on the order of 1 cm (Dahl and Stevenson, 2010). Unfortunately, numerical simulations are only able to resolve length scales which are typically 7 orders of magnitude larger than this diffusive length scale. Landeau et al. (2021) and Lherm et al. (2022) recently investigated the phase of mixing by impacts using laboratory experiments with miscible fluids, approaching dynamical regimes of planetary collisions. These experiments evidenced substantial mixing down to small scales during the impact stage, increasing the volume of silicates mixed and equilibrated with the impactor metal. They also suggest that much of the impactor kinetic energy is imparted

to the silicates during impact, so that metal from the impactor starts sinking with negligible velocity (see Fig. 3 and Fig. 7a in Landeau et al., 2021).

One of the key parameters controlling chemical transfers is the surface area of the metal-silicate interface per unit mass of metal. Past studies have investigated metal-silicate mixing through mainly two modelling approaches. The first approach considered that, after impact, the impactor core quickly emulsified into millimetre-to-centimetre-sized spherical drops, which settle downward. This so-called *iron rain* model (Rubie et al., 2003) has been refined by several analytical and numerical studies, which incorporated subtle aspects of the drops dynamics and diffusive transfers (Ichikawa et al., 2010; Ulvrová et al., 2011; Qaddah et al., 2019; Maas et al., 2021).

While emulsification during impact remains to be investigated, fluid mechanics experiments showed that breakup happens after a descent of a few initial radii of the sinking core (Landeau et al., 2014; Wacheul and Le Bars, 2018). These experiments showed that drops do not settle individually as an iron rain. Instead they favoured a second modelling approach. As the impactor core falls in the magma ocean, it forms a turbulent cloud that entrains silicates at a rate proportional to the cloud surface area and downward velocity, with a proportionality constant $\alpha = 0.25 \pm 0.10$ called the coefficient of entrainment (Morton et al., 1956). This entrainment dilutes the metal within the cloud, which therefore decelerates while its radius r increases linearly in depth z at a rate $dr/dz = \alpha$. In this model the cloud is called a turbulent thermal; it accurately accounts for stirring between miscible (Morton et al., 1956; Deguen et al., 2014; Landeau et al., 2021), immiscible (Landeau et al., 2014; Wacheul and Le Bars, 2018; Lherm and Deguen, 2018) and particle-laden fluids (Deguen et al., 2011; Kriaa et al., 2022). Thus, this model predicts stirring before and after the core breaks up into droplets (Deguen et al., 2014; Wacheul and Le Bars, 2018). A major consequence for chemical transfers is that metal equilibrates only with the finite volume of silicates that is entrained in the cloud. Yet, these previous studies have ignored the effect of planetary rotation on metal-silicate equilibration (Dahl and Stevenson, 2010), despite the strong rotation rate of the proto-Earth that has been suggested by impact simulations (Ćuk and Stewart, 2012).

This neglect likely originates from considering the earliest models for metal-silicate mixing. In the iron-rain scenario (Rubie et al., 2003; Ichikawa et al., 2010; Ulvrová et al., 2011; Qaddah et al., 2019) metal drops of $\sim$ 1 cm in radius fall in the magma ocean at a velocity of $\sim 0.2 - 0.5$ m/s, meaning that they settle in 10 to 100 days at the bottom of a 1000 km-deep magma ocean. Although this timescale is much longer than the length of day, the size of such drops is too small for planetary rotation to influence their dynamics. The strength of rotation is quantified by the ratio of inertial forces over the Coriolis force, the so-called Rossby number, which is on the order of 10^5 for an individual drop. This high value suggests that rotation is negligible at the scale of a drop. To estimate the effect of rotation at larger length scales, one can assume that an entire impactor core of 100 to 1000 km in radius falls as a whole under the buoyancy force. The resulting sinking velocity is on the order of 1 km/s, meaning that the impactor core reaches the bottom of the ocean in a few hours (Dahl and Stevenson, 2010). This fall time is now too short compared to the length of day for rotation to be important. The corresponding Rossby number is indeed larger than 10. However, this latter estimate entirely neglects the formation of a turbulent cloud of metal and silicates. Previous fluid mechanics experiments have found that the large-scale flow in a thermal or a particle-laden cloud is

easily affected by rotation (Ayotte and Fernando, 1994; Helfrich, 1994; Kriaa et al., 2022). In the present study, we show that planetary rotation affects the fall of metal-silicate clouds in magma oceans because the clouds grow with depth by turbulent entrainment, which enhances the magnitude of the Coriolis force, and they also decelerate, which reduces the magnitude of inertial forces.

The influence of planetary rotation on the fate of the impactor core has recently been investigated with numerical simulations by Maas et al. (2021) for a few scenarios of impacts on Earth in a global magma ocean. These simulations showed that planetary rotation, and the latitude of the impact point, do affect the dispersion and settling of iron drops in the magma ocean. However, because of the high numerical cost, the smallest drop size is 100 m in these simulations. In addition, the authors do not quantify the effect of rotation on the turbulent mixing in a metal-silicate cloud.

In the present study we focus on the scenario of an impact at the pole, with gravity and rotation aligned, and we model the post-impact flow using our recent laboratory experiments of rotating particle clouds (Kriaa et al., 2022, and Chapter 1). We quantify the role of planetary rotation varying the angular velocity and gravity of the target planet, the drop size and the impactor size.

Section 3.2 introduces the experimental framework for modelling the post-impact flow using particle-laden clouds settling in a water tank in solid body rotation. Section 3.3 summarises the key features of the dynamical regimes of these clouds on the basis of the results presented in Chapter 1. We show that clouds initially behave as turbulent thermals, but transform into vortical columns aligned with the axis of rotation when the thermal's Rossby number becomes lower than unity. This columnar flow is modelled in section 3.4, and its consequences on the dilution of metal in silicates is presented in section 3.5. Section 3.6 then considers the implications of these results on the efficiency of chemical transfers between metal and silicates. We discuss the limitations of our work and we suggest ideas for future investigations in section 3.7.

3.2 Experimental modelling

3.2.1 Experimental setup

We summarise the essential elements about the experimental setup of our experiments of settling particle clouds, which are presented with more details in Chapter 1. The apparatus is illustrated in figure 3.1. The experiments are performed in a Plexiglas tank of height 90 cm and cross-section area 42×42 cm^2 containing 160 L of fresh water which is our analogue for the magma ocean ($\rho_f = 998$ kg.m^{-3}, $\nu = 10^{-6}$ m^2.s^{-1}). The tank is fixed in the middle of a rotating table whose angular velocity Ω varies from 0 (no rotation) to 20 rotations per minute (rpm). A lid is placed on top of the tank with a hole at the centre. Placed in this hole, a cylinder of inner diameter $D_{\text{cyl}} = 3.2$ cm contains the buoyant material. The cylinder's bottom nozzle is sealed by a latex membrane, which is stretched and taped onto the cylinder. We then pour the buoyant material into the cylinder.

The released fluid is either made of salt water, which stands as a particle-free reference, or it is composed of a mixture of 26.1 mL of fresh water and a fixed mass $m_0 = 1.0$ g of

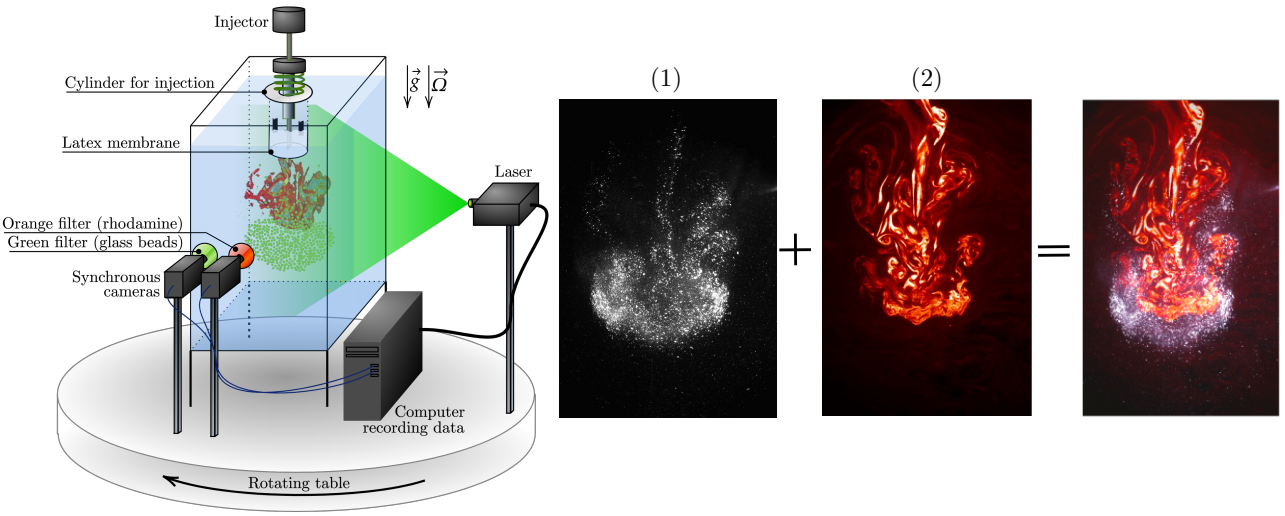

Figure 3.1: *Schematic representation of the experimental apparatus, and examples of images of (1) the glass beads using a green filter and (2) the released water volume using an orange filter.*

spherical glass beads of density $\rho_p = 2500$ kg.m^{-3}. The mean radius r_p of the beads ranges from 2.6 μm to 524.5 μm (see table 3.1). In all the experiments the total mass excess introduced into the system is the same. In this setup, the ambient water in the tank is an analogue for the silicate magma ocean and the released particles are analogues for the drops of liquid metal, as previously proposed by Deguen et al. (2011).

The ambient water and the tank are either both motionless or in solid-body rotation. At $t = 0$ the experiment starts by rupturing the latex membrane with a needle, releasing the content of the cylinder. Once the membrane retracts, the particles fall out of the cylinder because of their weight. For most particle sizes, the downward acceleration of the particles quickly transmits to the fluid, the buoyant material rolls up and the cloud becomes turbulent after a distance of about $1D_{\rm cyl}$.

The typical cloud velocity at a depth $1 - 2D_{\rm cyl}$ reads

$$U_{\rm ref} = \sqrt{g\left(1 - \frac{\rho_f}{\rho_0}\right) D_{\rm cyl}}, \tag{3.1}$$

with $g = 9.81$ m.s^{-2} and ρ_0 the initial cloud density once it has rolled up as a sphere of typical radius $D_{\rm cyl}$, hence

$$\rho_0 = \rho_f + \left(1 - \frac{\rho_f}{\rho_p}\right) \frac{3m_0}{4\pi D_{\rm cyl}^3}. \tag{3.2}$$

Note that the values of ρ_0 and $U_{\rm ref}$ are respectively fixed to 1033 kg/m^3 and 3.7 cm/s for all experiments.

Visualisations are performed in a vertical laser sheet (532 nm). Since particles and water have different motions, two identical black-and-white cameras are synchronised and record at 50 fps the same experiment with two different filters. The first camera has a green filter to record the motion of glass beads, which reflect and refract the laser beam, while the second camera has an orange filter. By colouring the fluid inside the cylinder with a fluorescent dye called

rhodamine, the second camera records the motion of the released water volume which appears in orange in the laser sheet. Both of them record the same field of view of size 45 cm × 28 cm.

r_p (μm)	2.6	29.9	45.7	51.8	57.8	63.9	64.4
$\mathcal{R}$	6.00×10^{-4}	7.57×10^{-2}	0.168	0.210	0.255	0.304	0.308
Re_p	1.16×10^{-4}	0.167	0.567	0.805	1.09	1.44	1.47

r_p (μm)	70.0	76.1	108.1	120.8	192.4	339.8	465.9	524.5
$\mathcal{R}$	0.354	0.406	0.696	0.814	1.48	2.73	3.70	4.13
Re_p	1.84	2.29	5.57	7.28	21.1	68.8	128	160

Table 3.1: *Properties of the particle-laden experiments used in this study. The numbers $\mathcal{R}$ and Re_p are defined below in equation (3.4). More details can be found in Chapter 1.*

3.2.2 Governing dimensionless numbers

The motion of particles is characterised by their settling velocity w_s. To compute w_s we use the model proposed by Samuel (2012)

$$w_s = \frac{20\nu_f}{r_p}\left[\sqrt{1+\frac{(\rho_p-\rho_f)gr_p^3}{45\rho_f\nu_f^2}}-1\right], \tag{3.3}$$

where ν_f is the kinematic viscosity of the ambient fluid, ρ_f is the density of the ambient fluid, r_p is the radius of a particle of density ρ_p, and g is gravity. The two following dimensionless numbers characterise the motion of particles

$$Re_p = \frac{2r_p w_s}{\nu_f}; \qquad \mathcal{R} = \frac{w_s}{U_{\text{ref}}}. \tag{3.4}$$

The particulate Reynolds number Re_p compares inertial and viscous forces at the scale of a settling particle, and hence, it controls the flow behind the particle. The Rouse number $\mathcal{R}$ – usually used for sediment transport (de Leeuw et al., 2020) and previously used to study metal-silicates mixing in experiments (Deguen et al., 2011) – compares the settling speed of a particle w_s and that of the cloud U_{ref}. Since the reference fluid velocity U_{ref} is the same for all experiments (equation (3.1)), the Rouse number only varies with the particles' radius: the larger the particle, the larger the Rouse number. As particles get smaller and smaller, their Rouse number goes to 0 so their gravitational drift due to settling vanishes, hence they behave more and more as salt water, which corresponds to the asymptote $\mathcal{R} = 0$. Conversely when their Rouse number is larger than unity, the settling speed of particles is so large that the motions of water and particles are decoupled. Our experiments explore the transition between these end members.

Finally, a key parameter is the angular velocity Ω of the tank, whose influence on the flow is quantified by the depth-dependent Rossby number

$$Ro(z) = \frac{\dot{z}_f(z)}{2\Omega r(z)}, \tag{3.5}$$

where $\dot{z}_f(z)$ is the vertical velocity of the front of a spherical particle cloud with radius $r(z)$ at depth z. The Rossby number is the ratio of the cloud inertia over the Coriolis force. In experiments $Ro(z=0) > 1$, so that particle clouds are initially weakly influenced by rotation. However, the Rossby number decreases as the cloud falls, and rotation starts affecting the dynamics when the Rossby number becomes equal to unity.

3.3 Dynamical regimes in particle-cloud experiments

Along with past studies in the literature (Rahimipour and Wilkinson, 1992; Bush et al., 2003; Lai et al., 2016), our experiments (Kriaa et al., 2022) showed that, throughout their evolution in depth, particle clouds experience transitions in dynamical regimes. This section recalls the essential features of these regimes.

3.3.1 Transition from turbulent thermals to swarms

3.3.1.1 Regime of turbulent thermal

In our experiments, particle clouds start their motion in the same way as salt water clouds: they form a so-called thermal, which is a finite volume of buoyant fluid whose motion is entirely governed by its total buoyancy. Our thermals quickly become turbulent during a short phase of acceleration at depths $\lesssim 1 - 2D_{\text{cyl}}$. Subsequently, turbulence entrains ambient fluid into the clouds and hence leads to their growth with depth. Because of this progressive entrainment and dilution, the clouds eventually decelerate. Entrainment can be modelled by assuming that the inflow velocity v_e of ambient fluid entrained into the thermal is proportional to the vertical velocity $\dot{z}$ of the turbulent thermal (Morton et al., 1956). In a uniform ambient fluid, this model predicts that the cloud radius r is proportional to the cloud depth z so that $r = r_0 + \alpha z$, with r_0 the initial cloud radius and $\alpha = 0.25 \pm 0.1$ the entrainment coefficient (Deguen et al., 2011; Landeau et al., 2014).

3.3.1.2 Transition to a swarm: separation of released fluid and particles

Figure 3.2 shows that after some depth, particles rain out of the turbulent cloud, a process referred to as 'separation'. This separation has already been observed in the literature (Rahimipour and Wilkinson, 1992; Bush et al., 2003; Deguen et al., 2011). When a turbulent thermal develops, it initially accelerates and reaches a maximum velocity $\sim U_{\text{ref}}$ that is larger than the individual settling velocity w_s of particles. Consequently, particles are forced to swirl inside the fast turbulent eddies. However, as the turbulent thermal grows in size, it decelerates. When its velocity eventually becomes lower than the settling velocity w_s, eddies are not vigorous enough to sustain the particles which rain out of the cloud. Separation happens when the cloud velocity approaches the individual settling velocity of particles i.e. $\dot{z}(z_{\text{sep}}) \simeq w_s$ where z_{sep} is the depth of separation. After separation, particles fall as a *swarm*: the cloud vertical velocity is constant and approximately equal to w_s, and the swarm keeps an approximately constant horizontal extent.

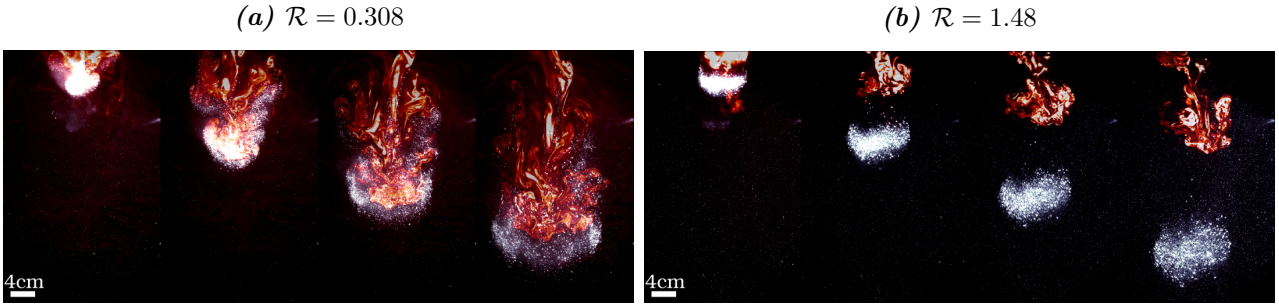

Figure 3.2: *Snapshots showing the gradual separation between particles (in white) and the released fresh water (in orange), all the faster as the Rouse number $\mathcal{R}$ increases from (a) to (b). Time intervals Δt between snapshots are (a) $\Delta t = 3.0s$ and (b) $\Delta t = 1.2s$.*

To predict separation, we use a *local* Rouse number $\mathcal{R}^*(z)$ that compares the settling velocity w_s of a particle with the *local* cloud velocity $\dot{z}(z)$ at depth z, i.e.

$$\mathcal{R}^*(z) = \frac{w_s}{\dot{z}(z)}. \tag{3.6}$$

When $\mathcal{R}^*(z) < 1$, eddies are vigorous enough to sustain particles so the cloud behaves as a thermal. Conversely, when $\mathcal{R}^*(z) > 1$, particles fall as a swarm. Our own experimental measurements (Kriaa et al., 2022, and Chapter 1) as well as past studies (Deguen et al., 2011; Wang et al., 2014) validated this criterion of separation. In equation (3.6), the velocity $\dot{z}(z)$ is estimated following the model of Escudier and Maxworthy (1973) for a turbulent thermal in which buoyancy is the sole volume force. Neglecting added mass as suggested by Bush et al. (2003); Deguen et al. (2011), we obtain

$$\dot{z}(z) = \sqrt{\frac{gD_{\text{cyl}}}{2\alpha}\left(\frac{\rho_0}{\rho_f} - 1\right)} \times \frac{\sqrt{\frac{1}{2}((1+\alpha\overline{z})^4 - 1) + \frac{\alpha\overline{z}}{2}(\frac{\rho_0}{\rho_f} - 1)}}{(1+\alpha\overline{z})^3 + \frac{\rho_0}{\rho_f} - 1}, \tag{3.7}$$

where $\overline{z} = 2z/D_{\text{cyl}}$. The transition $\mathcal{R}^*(z) = 1$ is shown in figure 3.3 with a solid red line in the plane $(\mathcal{R}, z)$: clouds behave as a thermal in the red region below this line, and fall as a rain otherwise. Note that the initial velocity of any cloud is $\dot{z}(z = 0) = 0$ so that $\mathcal{R}^*(z = 0) = \infty$; it takes a short falling distance before the Rouse number $\mathcal{R}^*(z)$ is lower than 1, which explains the slight curvature of the red solid line around $\mathcal{R} \simeq 1$ and $z/D_{\text{cyl}} \gtrsim 0$ in figure 3.3. When particles are too large ($\mathcal{R} > 1.15$ in figure 3.3), the cloud velocity $\dot{z}(z)$ is never larger than w_s and particles always fall as a swarm (see Kriaa et al. (2022) and Chapter 1 for more details).

3.3.2 Transition to vortical columns

3.3.2.1 Onset of the columnar flow

Our experiments showed that rotation interrupts the growth of the thermal at some depth z_{col}, marking a transition from the regime of turbulent thermal to a vortical column of constant radial extension for $z \geq z_{\text{col}}$. This transition is visible when comparing the linear growth of

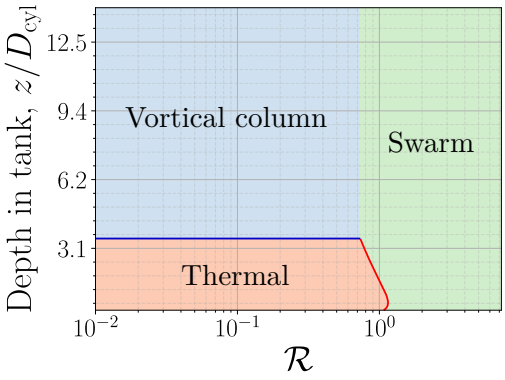

Figure 3.3: *Regime diagram up to $z/D_{cyl} = 14.1$ which is the depth of our field of view. Background colours indicate the different regimes: red stands for turbulent thermals, green stands for swarms, and light blue stands for vortical columns. Transitions correspond to $\mathcal{R}^*(z) = 1$ (——), $Ro(z_{col}) = 1$ (——) for $\Omega = 5$ rpm.*

a thermal in the absence of rotation (figure 3.4a) with the constant width of the cloud when $\Omega = 5$ rpm (figure 3.4b). Integrated photographs in figure 3.4c further evidence the constant width of the cloud below some depth when $\Omega = 5$ rpm in orange. Initially the cloud inertia is large compared to rotation ($Ro(z) > 1$) and the cloud behaves as a non-rotating thermal (Morton et al., 1956): it grows linearly with depth (regime above the orange arrow in figure 3.4c or for $z_f < 22$ cm in figure 3.5a). Equation (3.5) predicts that, as the cloud radius r increases and its velocity decreases with depth, the local Rossby number decreases. When $Ro(z) = 1$, the Coriolis force becomes comparable to the cloud inertia and hence, the flow transitions towards a regime influenced by rotation. This criterion of transition is illustrated with an example in figure 3.5a at depths $z_f > 22$ cm and we verify it for different particle radii r_p and rotation rates Ω in figure 3.5b. These results are consistent with past measurements in the literature for salt-water thermals falling in a rotating ambient (Ayotte and Fernando, 1994; Helfrich, 1994; Fernando et al., 1998). All these studies consistently show that the constant width of the column is the diameter of the turbulent thermal at depth z_{col} (as visible in figures 3.4c and 3.5a; see also figures 1.16 and 1.13 in Chapter 1). The transition to a vortical column is shown in figure 3.3 (solid blue line) assuming the transition from a thermal to a vortical column occurs when $Ro(z_{\text{col}}) = 1$.

We also observe that vortical columns penetrate through the solid body rotation with a constant front velocity. This explains why $Ro(z)$ remains close to 1 when $z > z_{\text{col}}$ in figure 3.5a (see figures 1.18a, 1.18b and 1.19 in Chapter 1 for more details). In addition, the vortical column is made of two different regions: (1) a frontal region (see the red circles in figure 3.4b), that we will assume spherical for simplicity, which corresponds to the former turbulent thermal and which no longer grows due to entrainment; (2) a columnar wake of particles detrained from the frontal sphere, which settle much slower than the frontal sphere (see figure 1.19 in Chapter 1).

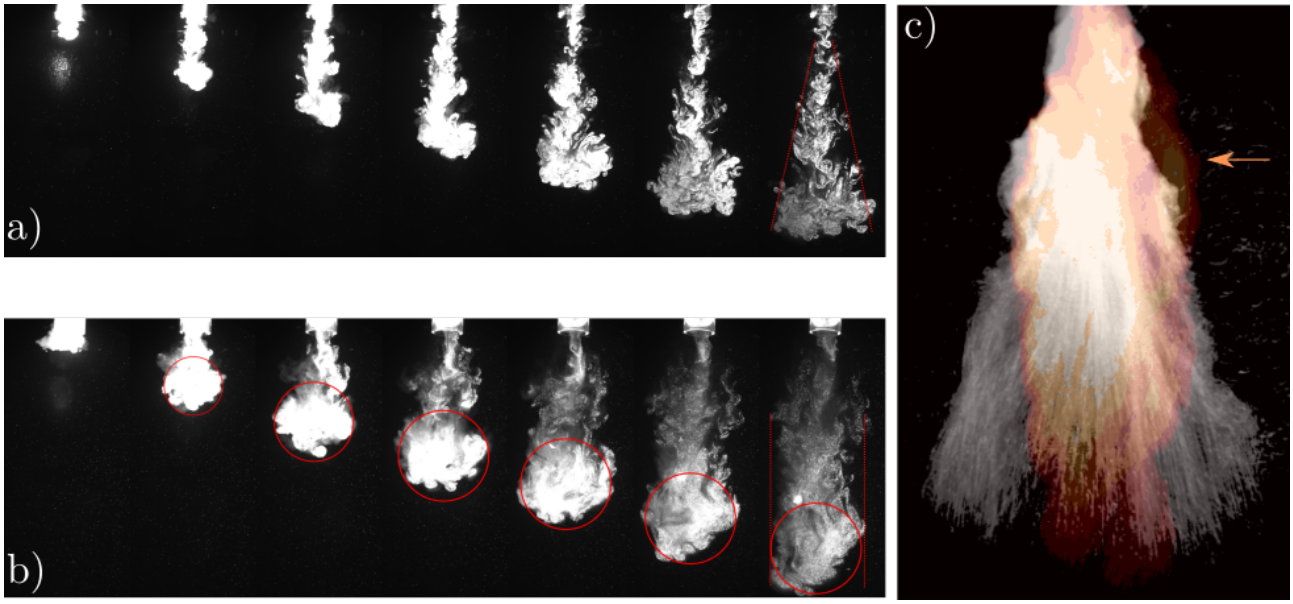

Figure 3.4: *Transition from the regime of turbulent thermal to the regime of vortical column. (a) Snapshots of a buoyant cloud of salt-water ($r_p = 0$) in the thermal regime ($\Omega = 0$, the time lapse between snapshots is 1s). (b) Snapshots of a buoyant cloud of small particles ($r_p = 29.9$ μm) in the vortical regime ($\Omega = 5$ rpm, the time lapse between snapshots is 1.7s). The red circles indicate the location of the frontal sphere; the dotted red lines show the growth of the thermal in (a) and the constant width of the vortical column in (b); the top cylinder has a diameter $D_{cyl} = 3.2$ cm in (a) and (b). (c) Overlay of two integral images (pixel-by-pixel standard deviation of light intensity during the cloud fall) for particle clouds with $r_p = 64.4$ μm respectively at 0rpm (grey shades in the background) and 5rpm (orange shades). The arrow indicates the typical depth of transition to the vortical regime.*

3.3.2.2 Comparison with previous studies on columnar rotating flows

When a rotating flow is dominated by the Coriolis force and the pressure gradient, these forces impose a geostrophic balance. Under these conditions, the flow is invariant along the rotation axis and forms columnar structures, the so-called Taylor columns (Taylor, 1922; Maxworthy, 1970).

The vortical columns we observe in our experiments when $Ro(z) < 1$ are reminiscent of Taylor columns. Our experiments are consistent with past studies on the dynamics of such columns. The constant speed at the column front agrees with a drag force proportional to the falling speed and balancing the buoyancy force. Similar dynamics were predicted for an object falling along the axis of rotation in a bounded or unbounded domain (Maxworthy, 1970; Moore et al., 1969; Vedensky and Ungarish, 1994). In the latter case the constant cloud velocity reads $\dot{z}_\infty \propto (\rho/\rho_f - 1)g/\Omega$ (see Stewartson, 1952; Moore et al., 1969; Bush et al., 1995). As the object moves along the vertical axis, it stretches vortex tubes downstream and generates a converging flow and a cyclonic swirl in a Taylor column behind the object. In this column, the amplitude of the swirling flow $v_{\text{swirl}} \sim \dot{z}_\infty$ (Bush et al., 1995).

Note that these results hold for $Ro \ll 1$. When the cloud Rossby number is on the order of unity, the vertical extent of the Taylor column decreases (Maxworthy, 1970; Minkov et al., 2002). Minkov et al. (2002) showed that the column behaves as if it were in an unbounded

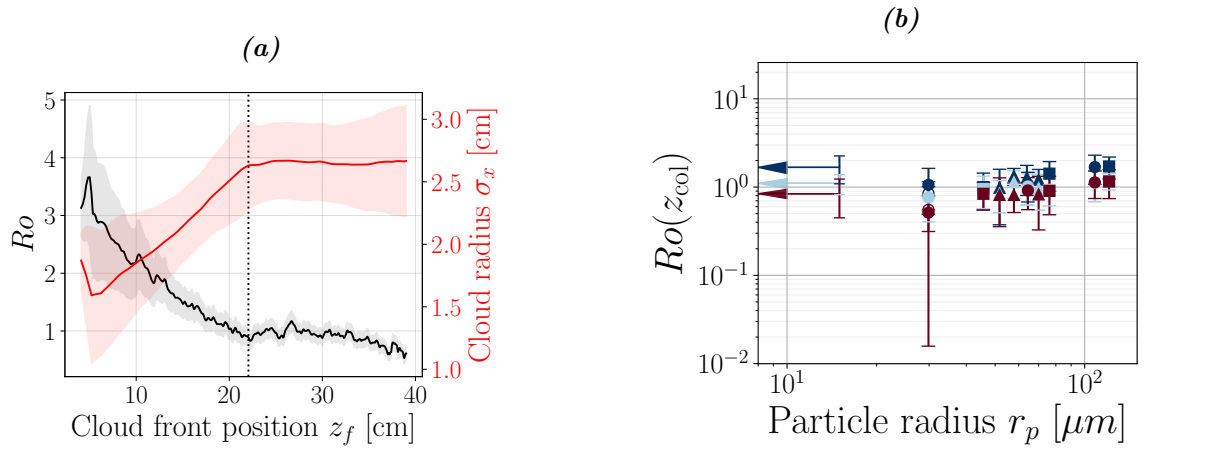

Figure 3.5: *(a) Rossby number Ro and experimental measure of the cloud radius σ_x (see section 1.C for details about the measurement of σ_x) as a function of the position of the cloud front. In this experiment $\Omega = 5$ rpm and $r_p = 29.9$ μm. The transition to the vortical regime occurs at the depth shown by the vertical dotted line where $Ro = 1$ and the cloud radius becomes constant (see Chapter 1 for details on measurements). (b) Average Rossby number after transition to the vortical regime for all rotation rates and particle sizes; adapted from figure 1.14 in Chapter 1.*

domain as long as inertial waves do not have enough time to propagate away from the moving cloud and reflect back to it, consistently with the interpretation of Greenspan (1968). Since our particle clouds verify $Ro(z \geq z_{\text{col}}) = 1$, the waves having the largest group velocity propagate as fast as the cloud falls. Consequently, these waves cannot propagate the information before the cloud reaches the bottom of the domain. This suggests that these clouds behave as if they were in an unbounded domain, falling with a velocity that scales like $\dot{z}_\infty \propto (\rho/\rho_f - 1)g/\Omega$.

In the light of these elements, together with the observations drawn in section 3.3.2, we model a vortical column using the following assumptions. We consider that particle clouds penetrate through the ambient as a leading frontal sphere of constant radius r_{col} and with constant velocity $\dot{z}_f$. We also neglect the effect of the walls. We assume that particles are gradually detrained behind the frontal sphere, nourishing a cylindrical vortical column. The typical swirl velocity in the column is equal to the velocity of the frontal sphere $\dot{z}_f$, so that vertical motions stir the particles in the columnar flow. For simplicity we will assume that these motions are vigorous enough to homogenise the particle concentration in the vortical column. The next section presents a model of column growth that is consistent with these key points.

3.4 Model of column growth through detrainment

Based on the above experimental observations, we now derive a minimalist model for the evolution of a particle cloud in the presence of rotation. Figure 3.6 provides an illustration of this model. The cloud initially grows as a turbulent thermal (A). At depth z_{col}, $Ro = 1$ and the thermal transitions to a frontal sphere of constant radius and speed (B). Particles are detrained behind the falling sphere and into a swirling column (B). After some distance, the sphere has detrained all its particles in the swirling column (C). Eventually, particles will fall down to the

bottom of the tank, possibly before the kinetic enegy of the column dissipates viscously (D). Particles can drag the fluid with them along their fall, or decouple from it, as we have seen in experiments. Which of these two configurations occurs depends on subtle hydrodynamical interactions between particles that enable the interstitial fluid between them to be dragged downward. These aspects require further investigation, as discussed in section 3.7. In this study, we speculate that particles drag a negligible amount of fluid when they decouple from the swirling column. Consequently, they rain out in quiescent liquid.

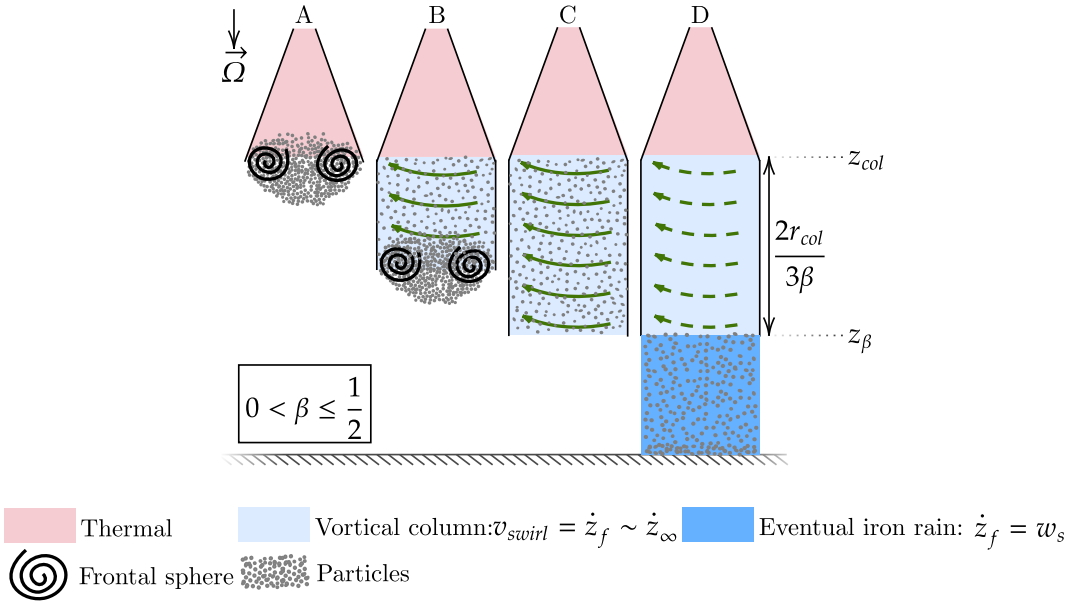

Figure 3.6: *Sketch of the cloud evolution. (A) The cloud initially grows as a turbulent thermal until $Ro(z) = 1$; (B) then the frontal sphere falls with constant speed while detraining particles in the swirling column; (C) all particles are detrained in the column of depth $2r_{col}/3\beta$ and swirl with the fluid; (D) ultimately, because of gravitational drift (i.e. settling) and viscous dissipation, particles rain out of the column until reaching the bottom where they accumulate.*

By analogy with models of entrainment (Morton et al., 1956), the detrainment (Taylor and Baker, 1991; de Rooy et al., 2013) of particles into the columnar wake is modelled through a single coefficient of detrainment β which is analogous to the coefficient of entrainment α (Baines, 2001; de Rooy and Siebesma, 2008). The coefficient of detrainment β is the ratio of the outward velocity transporting particles out of the spherical frontal blob, over the downward velocity of the cloud. The mass conservation of particles then reads

$$\frac{d}{dt}\left[\frac{4}{3}\pi r_{\mathrm{col}}^3 \phi \rho_p\right] = \frac{4}{3}\pi r_{\mathrm{col}}^3 \rho_p \frac{d\phi}{dt} = -2\pi r_{\mathrm{col}}^2 \beta \dot{z}_f \phi \rho_p, \tag{3.8}$$

where the only unknown $\phi(t)$ is the particle volume fraction within the frontal sphere of downward velocity $\dot{z}_f$ and radius r_{col}. The term $(\beta \dot{z}_f)$ is the detrainment velocity taking particles out of the cloud. The factor $2\pi r_{\mathrm{col}}^2$ on the right-hand side indicates that detrainment is considered to happen only on the upper half of the frontal sphere. Taking $t = 0$ when the cloud is at depth

z_{col}, the solution of this Ordinary Differential Equation (ODE) reads

$$\phi(t) = \phi(t=0)\exp\left[-\frac{t}{\tau_\beta}\right] \iff \phi(z) = \phi(z_{\mathrm{col}})\exp\left[-\frac{3\beta(z-z_{\mathrm{col}})}{2r_{\mathrm{col}}}\right], \tag{3.9}$$

where

$$\tau_\beta = \frac{2r_{\mathrm{col}}}{3\beta\dot{z}_f} \tag{3.10}$$

the characteristic duration of detrainment. Hence the column completes detrainment in a time of order τ_β. Since the column front moves with constant velocity $\dot{z}_f$, the column height after complete detrainment is of order $\dot{z}_f\tau_\beta = 2r_{\mathrm{col}}/3\beta$ and the depth of complete detrainment

$$z_\beta = z_{\mathrm{col}} + \frac{2r_{\mathrm{col}}}{3\beta}. \tag{3.11}$$

Particles are always detrained in the column behind the frontal sphere, hence $\beta > 0$. The maximum value for β is determined with a geometrical argument. During a time dt, the frontal sphere detrains buoyant material in a volume $2\pi r_{\mathrm{col}}^2\beta\dot{z}_f dt$; in the meantime the column grows by a volume $\pi r_{\mathrm{col}}^2\dot{z}_f dt$; equating them yields $\beta = 1/2$ as an upper bound. With this value, a frontal sphere of volume $4\pi r_{\mathrm{col}}^3/3$ typically detrains its particles in an identical volume $\pi r_{\mathrm{col}}^2(4r_{\mathrm{col}}/3) = 4\pi r_{\mathrm{col}}^3/3$ (see equation (3.11) for $\beta = 1/2$), meaning the sphere only adapts its shape to become a cylinder of radius r_{col} and depth $4r_{\mathrm{col}}/3$.

The range $0 < \beta < 1/2$ corresponds to the sketch in figure 3.6. Particles are detrained in a column of large depth-to-radius ratio. In this case, the volume of metal and silicates detrained by the frontal sphere is lower than the volume gained by the vortical column. This implies that the volume of the column is complemented by ambient fluid through entrainment, likely in the near wake of the frontal sphere where the flow converges towards the column (see section 3.3.2.2). Additionally, since the frontal sphere keeps a constant volume while detraining both fluid and particles, the sphere also entrains new ambient fluid that compensates the detrained volume.

In our experiments, we observe that detrainment of the frontal sphere ends at depths in the range $[45-90]$ cm. Since our columns had a typical width $r_{\mathrm{col}} \simeq 2D_{\mathrm{cyl}}$, equation (3.11) yields $\beta \in [0.05-0.12]$, a range that is consistent with typical values quantifying entrainment for turbulent jets and plumes (e.g. van Reeuwijk and Craske, 2015; Turner, 1986; Wang and Law, 2002; Carlotti and Hunt, 2017). A larger β value translates into a weaker effect of rotation. In this study, we aim at demonstrating that rotation can affect metal-silicate equilibration after an impact. To be conservative, we therefore use the end-member value $\beta = 0.12$ in what follows.

According to equation (3.9), the column is nourished by the frontal sphere with a mass flux of detrained particles that decays exponentially in depth. Yet, our visualisations in a vertical laser sheet evidence no stratification in the vortical column. This observation suggests that the buoyant material substantially stirred by turbulent motions in the column. To keep our model as simple as possible, we assume that stirring is sufficient behind the frontal sphere to neglect heterogeneities within the vortical column, so that its concentration is uniform.

3.5 Dynamical regimes in a magma ocean

In this section, we apply our experimental results to the fall of liquid metal into a magma ocean following a planetary impact. We use the following notations (see a list in table 3.2): the densities of metal ρ_m and silicates ρ_s, their respective kinematic viscosities (ν_m and ν_s) and mass diffusivities (κ_m and κ_s), the angular velocity Ω of the target planet, the radius R_t of the target planet, the radius R of the impactor, and f_m the volume fraction of metal within the impactor; we use the value $f_m = 0.16$ that corresponds to the same core fraction as in the present-day Earth. The acceleration of gravity g is assumed uniform in the magma ocean (see Fig. 5b in Olson, 2015).

Quantity	Notation	Value	Reference
Density of metal	ρ_m	7800 kg.m^{-3}	[1]
Density of silicates	ρ_s	3500 kg.m^{-3}	[2]
Kinematic viscosity of metal	ν_m	1.28×10^{-6} m^2.s^{-1}	[1]
Kinematic viscosity of silicates	ν_s	1.43×10^{-5} m^2.s^{-1}	[3]
Mass diffusivity of metal	κ_m	10^{-8} m^2.s^{-1}	[1,4]
Mass diffusivity of silicates	κ_s	10^{-8} m^2.s^{-1}	[1,4]
Metal volume fraction in the impactor	f_m	0.16	[5]
Radius of the target planet	R_t	6371 km	[6]
Angular velocity of the target planet	Ω	$2\Omega_\oplus - 5\Omega_\oplus$	-
Radius of the impactor	R	$< R_t$	-
Acceleration of gravity	g	$0.25g_\oplus - 2g_\oplus$	-

Table 3.2: *Governing quantities in the context of metal-silicate mixing following a planetary impact. The last three lines give ranges for the parameters that are varied, with $\Omega_\oplus = 7.3 \times 10^{-5}$ rad.s^{-1} and $g_\oplus = 9.81$ m.s^{-2}. References correspond to: [1] Lherm and Deguen (2018); [2] Qaddah et al. (2019); [3] Karki and Stixrude (2010); [4] Deguen et al. (2014); [5] Landeau et al. (2021); [6] Kono (2010).*

Both Ω and g are varied in the next sections; the subscript $\oplus$ denotes the values on Earth today. The constant entrainment coefficient is fixed to $\alpha = 0.25$ (Deguen et al., 2014; Landeau et al., 2021).

Finally, during an impact the metal of the impactor mixes with silicates from the target planet so that the metal dilutes in a larger volume, with an effective radius r_0 (Landeau et al., 2021). In all that follows, we assume that impactors approach the target planet at the escape velocity and we account for mixing during an impact using the scaling law from Landeau et al. (2021). Past studies have shown that the impactor core behaves as a turbulent thermal of radius r_0 immediately after an impact (Wacheul and Le Bars, 2018; Deguen et al., 2014; Landeau et al., 2021).

For simplicity we consider that the cloud contains spherical drops from the very start of its fall. The experiments of Landeau et al. (2021) suggest that, after an impact, the impactor core fragments after less than 7.5 times its initial radius (see figure 14 in Landeau et al., 2021). For such breakup lengths, Deguen et al. (2014) predict that the drop size is less than 4 mm (see their figure 7 and the discussion in section 8). As this is only an order of magnitude estimate,

we chose to explore a wide range of r_p values in what follows, with a particular focus on the case $r_p = O(10^{-3})$ m.

3.5.1 Three cases of reference for the Earth

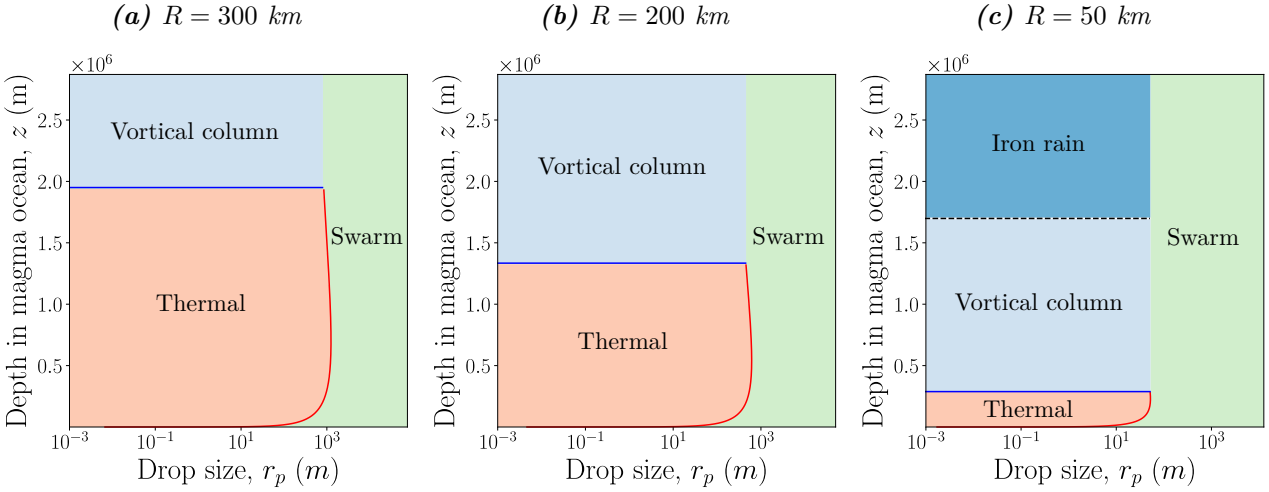

Figure 3.7: *Evolution of a cloud of metal drops after an impact on Earth by an impactor with a radius R equal to (a)* 300 km*, (b)* 200 km *or (c)* 50 km*. We fix $R_t = 6371$ km, $g = g_\oplus$ and $\Omega = 2\Omega_\oplus$, where $g_\oplus = 9.81$ m.s^{-2} and $\Omega_\oplus = 7.3 \times 10^{-5}$ rad.s^{-1} are values for the present-day Earth. Transitions correspond to $\mathcal{R}^*(z) = 1$ (——), $Ro(z_{col}) = 1$ (——), $z = z_\beta$ (- - -) for $\beta = 0.12$. As in figure 3.3, the red background stands for turbulent thermals, the light green stands for swarms, and the light blue stands for vortical columns. Additionally, the deep blue for $z > z_\beta$ stands for the regime of iron rain.*

Figure 3.7 shows a regime diagram for three different impactors, respectively of radius $R = 300$ km, 200 km and 50 km impacting a planet with the same gravity as the Earth ($g = g_\oplus$) and spinning twice faster than the present Earth ($\Omega = 2\Omega_\oplus$). Such rotation rates in the early Earth are suggested by estimates of the tidal dissipation of the Earth-Moon system (Touma and Wisdom, 1994; Daher et al., 2021).

We first focus on the case of small particle radius < 10 m. As the impactor radius R decreases from 300 km (figure 3.7a) to 50 km (figure 3.7c), the transition from a thermal to a vortical column happens at a lower depth, from $z_{\text{col}} = 1.95 \times 10^6$ m to $z_{\text{col}} = 2.88 \times 10^5$ m respectively (solid blue line in figure 3.7). This observation is paramount: assuming a magma ocean with a depth $\gtrsim 1000-1500$ km (Siebert et al., 2012; Fischer et al., 2015), a giant impactor with $R > 1000$ km is little affected by planetary rotation and never transitions to a vortical column (figure 3.7a). However, small impactors with $R < 200$ km transition to vortical columns before reaching the bottom of the magma ocean (figures 3.7b-3.7c). In this case, rotation affects the flow and may therefore affect the efficiency of chemical equilibration.

If the magma ocean is sufficiently deep for detrainment to complete, the same clouds of small particles transition from the vortical regime to the regime of iron rain. How does this transition happen? After detrainment, iron drops swirl with the fluid inside the wake at most

until viscosity has fully dissipated the swirl. Let us show that in practice, iron drops rain out of the vortical column before the swirl is dissipated. While iron drops are spiralling azimuthally, they keep settling downwards because of gravity with velocity w_s, as can be derived from the momentum equation of an individual drop. The time required for the topmost drops to settle down to the bottom of the vortical column is the ratio of the column height over the settling velocity w_s. This timescale is compared to the timescale of viscous dissipation $r_{\rm col}^2/\nu_s$ of the vortical column, and to the shorter timescale $\Omega^{-1}Ek^{-1/2}$ that should be taken into account if Ekman pumping develops in the magma ocean (Greenspan, 1968), with $Ek = \nu_s/\Omega z_{\rm ocean}^2$ the Ekman number based on the depth $z_{\rm ocean}$ of the magma ocean. For millimiter-sized drops that will be the main focus of the next sections, and for all possible sizes of $R < R_t$ hitting a planet of gravity $g = g_\oplus$ and angular velocity $\Omega = 2\Omega_\oplus$, the settling timescale is 4-5 orders of magnitude lower than $\Omega^{-1}Ek^{-1/2}$ which is itself 2-3 orders of magnitude lower than $r_{\rm col}^2/\nu_s$. Therefore iron drops are expected to rain out of the wake before the swirl is dissipated. This conclusion also held in our experiments (Kriaa et al., 2022, and Chapter 1): our slowest particles ($\mathcal{R} = 7.57 \times 10^{-2}$) settled over the column height in about 2.5 min which was an order of magnitude lower than $\Omega^{-1}Ek^{-1/2}$, hence we observed that particles rained out of the vortical column before the dissipation of the swirl. In this situation, we call 'iron rain' the regime in dark blue in figure 3.7c, when drops settle after detrainment from a vortical column.

The transition to iron rain is only visible for the smallest impactor in figure 3.7c. This is because the larger the impactor, the wider the vortical column ($r_{\rm col}$) and the deeper the depth $z_{\rm col}$, hence the deeper the depth of complete detrainment $z_{\rm col} + 2r_{\rm col}/3\beta = z_\beta$. This depth turns out to be deeper than the present-day core-mantle boundary for $R \geq 200$ km.

In figure 3.7a, drops larger than $r_p = 1.25$ km fall too fast for a turbulent thermal to sustain them: the cloud behaves as a swarm from the very start of its fall (light green region). Drops in the range $r_p \in [0.82, 1.25]$ km initially fall as a turbulent thermal (red background) but eventually rain out as a swarm before rotation affects the dynamics (transition from red to light green). However, metal drops in a magma ocean are likely smaller than 0.82 km in radius (Deguen et al., 2014; Landeau et al., 2014). Thus, in what follows we focus on smaller particles.

3.5.2 Regimes for a cloud of millimetre-sized drops

Figure 3.8a shows the different regimes experienced by a falling cloud of millimetre-sized drops for various impactor-to-target radius ratios R/R_t up to a depth corresponding to the present-day core-mantle boundary in Earth. As in previous figures, the solid blue line marks the depth $z_{\rm col}$ where clouds transition to a vortical column for $\Omega = 2\Omega_\oplus$ and $g = g_\oplus$, and the dashed dark line marks the transition to the regime of iron rain. We observe that the larger the impactor-to-target radius ratio R/R_t, the larger the initial buoyancy of the cloud of droplets, the larger the cloud inertia, hence the deeper the transition from the thermal to the vortical column.

When $R/R_t \leq 4.99 \times 10^{-3}$ (left of the red solid line), impactors have so little initial buoyancy that their Rossby number is never larger than unity. Consequently they experience the influence of background rotation from the very start of their fall. This scenario is consistent with the numerical simulation of a polar impact by Maas et al. (2021).

Conversely, impactors in the range $R/R_t \geq 0.19$ reach the core-mantle boundary before ever transitioning to the regime of vortical column. Such clouds always behave as turbulent thermals.

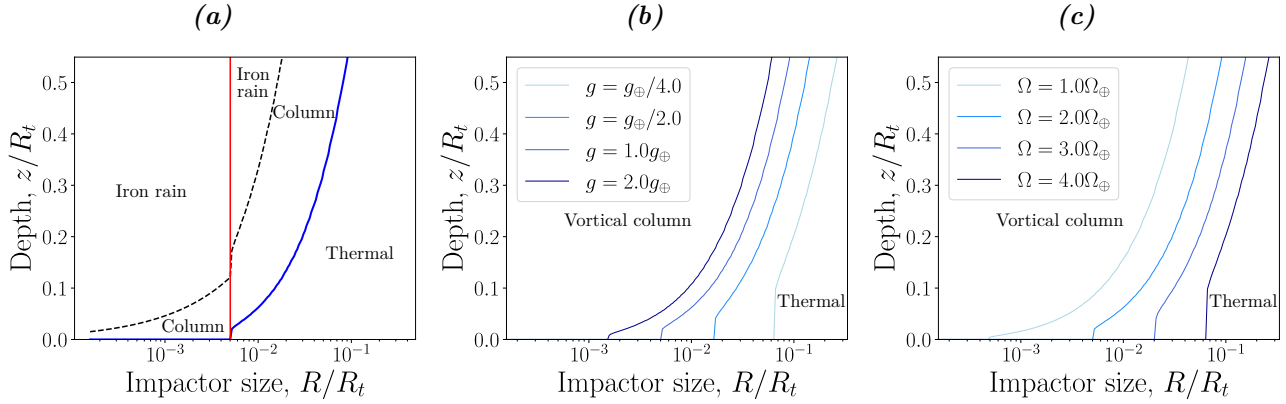

Figure 3.8: *(a) Dynamical regimes of a cloud of millimetre-sized drops for various impactor-to-target radius ratios for $\Omega = 2\Omega_\oplus$. Transitions correspond to the depth z_{col} (——) and the depth of complete detrainment z_β for $\beta = 0.12$ (- - -). Clouds in the range $R/R_t \leq 4.99 \times 10^{-3}$ verify $z_{col} = 0$ because their Rossby number remains below unity at all depths; they are separated from other clouds by the vertical solid red line (——). (b) Influence of gravity on the transition from a thermal to a vortical column at $z = z_{col}$; the angular velocity is $\Omega = 2\Omega_\oplus$. (c) Influence of the angular velocity on the same transition; the gravity is $g = g_\oplus$.*

Gravity g and the angular velocity Ω of the target planet are important parameters affecting the transition from the thermal to the swirling column stage. Their respective influence is illustrated in figure 3.8b and figure 3.8c. For a given impactor-to-target radius ratio, the larger gravity the deeper the depth of transition $z_{\rm col}$. As g increases, the cloud velocity increases during its phase of acceleration. It therefore takes a larger cloud radius $r_{\rm col} = r_0 + \alpha z_{\rm col}$ for the Coriolis force to overcome the cloud inertia and verify the condition $Ro = 1$. Thus, the transition to a vortical column is delayed deeper in the magma ocean. Figure 3.8c shows that the faster the background rotation Ω, the shallower the depth $z_{\rm col}$. This is straightforward from the definition of the Rossby number $Ro \propto \Omega^{-1}$: for a given impactor on a target planet of given gravity, the larger the angular velocity Ω the earlier the Coriolis force overcomes the cloud inertia to verify $Ro = 1$, hence $z_{\rm col}$ decreases. Consistently, when g decreases and Ω increases, larger and larger impactors are subject to the influence of rotation from the very start of their fall at depth $z = 0$ (figures 3.8b and 3.8c). On a fast-spinning Earth with $\Omega > 5\Omega_\oplus$ as proposed by Ćuk and Stewart (2012), rotation affects the flow even for large impactors with $R > 1000$ km.

3.6 Implications for mixing and equilibration after a planetary impact

3.6.1 Definitions of mixing and equilibration efficiency

As a cloud of metal drops falls in the magma ocean, the metal phase is stirred with silicates. This favours chemical transfers between the two phases. The present section models this equi-

libration between metal and silicates on the basis of previous studies (Deguen et al., 2014; Landeau et al., 2021), but including the effect of rotation and the regime of swirling columns.

We quantify mass transfers using the *equilibration efficiency* (Deguen et al., 2014; Landeau et al., 2021). This quantity compares the very initial state when no mass transfer has happened yet, to a state of thermodynamical equilibrium between the metal phase of the impactor and a given mass of silicates. For a chemical element i (e.g. tungsten), the equilibration efficiency is the ratio of the mass $\mathcal{M}_i$ of i transferred between these two states, over the maximum mass $\mathcal{M}_{\mathrm{i,max}}$ that could be transferred if (1) the metal was diluted in an infinite volume of silicates and (2) all the metal of the impactor fully equilibrated. Consequently the equilibration efficiency reads (Deguen et al., 2014)

$$\mathcal{E}_i(z) = \frac{\mathcal{M}_i(z)}{\mathcal{M}_{\mathrm{i,max}}} = \frac{m_m(z)|c_m^{\mathrm{eq}}(z) - c_m^0|}{\mathcal{M}_{\mathrm{i,max}}}, \tag{3.12}$$

with $m_m(z)$ the mass of metal that equilibrates, c_m^0 the initial mass concentration of element i in the metal, and $c_m^{\mathrm{eq}}(z)$ the concentration of i in the metal when thermodynamical equilibrium is reached. In the following the quantity $\mathcal{E}_i(z)$ will simply be referred to as the 'efficiency'.

From its definition, the efficiency is a 'state function' in the sense that it only depends on both the initial and final states of metal and silicates, not on the thermodynamic path that connects these states. Thus, the efficiency (3.12) quantifies chemical transfers provided that a thermodynamical equilibrium is reached by metal and silicates during the cloud fall, and that the cloud is uniform in composition. These conditions are assumed in our next calculations and discussed in Appendix 3.A.

3.6.1.1 Efficiency of turbulent thermals

In the case of turbulent thermals, previous studies (Deguen et al., 2014) have already established that the equilibration efficiency reads

$$\mathcal{E}_i^{\mathrm{th}}(z) = \frac{k}{1 + \frac{D_i}{\Delta_{\mathrm{th}}(z)}}, \tag{3.13}$$

where the quantity $\Delta_{\mathrm{th}}(z)$ is the *metal dilution*, defined as the ratio of the mass of silicates over the mass of metal contained in the thermal (Deguen et al., 2014). The dilution increases with depth as

$$\Delta_{\mathrm{th}}(z) = \frac{\rho_s}{\rho_m}\left[\left(\frac{r_0 + \alpha z}{R}\right)^3 \frac{1}{f_m} - 1\right], \tag{3.14}$$

with ρ_s the density of silicates, ρ_m the density of metal, r_0 the initial thermal radius, α the coefficient of entrainment, z the cloud depth, R the radius of the impactor, and f_m the volume fraction of metal in the impactor.

In equation (3.13), the superscript 'th' distinguishes between the general notation $\mathcal{E}_i(z)$ and the efficiency $\mathcal{E}_i^{\mathrm{th}}(z)$ of turbulent thermals specifically, since this latter efficiency serves as a reference for mass transfers. In equation (3.13), k is the mass fraction of impactor core that equilibrates chemically. Its value can be lower than unity, for example if the liquid metal is not

vigorously stretched by the turbulence, which would allow some fraction of the impactor core to keep its initial composition. Based on the conclusions of Deguen et al. (2014), we will consider that the entire impactor core equilibrates with silicates, hence we set $k = 1$ in our estimates of the efficiency. In equation (3.13), D_i is the partition coefficient of element i, that is to say the ratio between the concentration (in weight %) of i in the metal to the concentration of i in the silicates, both considered *at thermodynamical equilibrium*.

3.6.1.2 Efficiency of vortical columns

Equation (3.13) also applies to the columnar regime after substituting the general notation $\mathcal{E}_i(z)$ for $\mathcal{E}_i^{\mathrm{col}}(z)$, and replacing the metal dilution of a thermal $\Delta_{\mathrm{th}}(z)$ by its equivalent expression $\Delta_{\mathrm{col}}(z)$ in the regime of vortical column:

$$\mathcal{E}_i^{\mathrm{col}}(z) = \frac{k}{1 + \frac{D_i}{\Delta_{\mathrm{col}}(z)}}, \tag{3.15}$$

where we assume $k = 1$ as before. The mass of metal involved in chemical transfers is unchanged in this regime, however the mass of silicates now includes those present in the frontal sphere and those present in the wake, so that the metal dilution reads

$$\Delta_{\mathrm{col}}(z) = \underbrace{\frac{\rho_s}{\rho_m}\left[\left(\frac{r_0 + \alpha z_{\mathrm{col}}}{R}\right)^3 \frac{1}{f_m} - 1\right]}_{\Delta_{\mathrm{th}}(z_{\mathrm{col}})} + \frac{3\rho_s}{4\rho_m}\frac{(z - z_{\mathrm{col}})r_{\mathrm{col}}^2}{f_m R^3}, \tag{3.16}$$

which is applicable for $z_{\mathrm{col}} \leq z \leq z_\beta$. In equation (3.16) the terms on the right-hand side respectively correspond to the metal dilution $\Delta_{\mathrm{th}}(z_{\mathrm{col}})$ of a turbulent thermal at the depth z_{col}, and to the metal dilution within the vortical column.

3.6.1.3 Efficiency of an iron rain

As soon as metal drops have separated from silicates, one can no longer define a volume of silicates that would accompany the metal drops and mix with them during their fall. Instead, drops cross an ever-renewed volume of silicates and deposit (or absorb) some element i in the quiescent magma ocean, thus modifying the profile of concentration of i with respect to its initially uniform value c_s^0. Therefore no metal dilution is defined in this regime. Mass transfers are quantified by the evolution of the concentration in element i within the metal drops. Since mass transfers are transient during this regime of iron rain, no equilibrium concentration is reached in the drops, so the equilibration efficiency now reads

$$\mathcal{E}_i^{\mathrm{rain}}(z) = \frac{\mathcal{M}_i(z)}{\mathcal{M}_{\mathrm{i,max}}} = \frac{m_m(z)|c_m(z) - c_m^0|}{\mathcal{M}_{\mathrm{i,max}}}, \tag{3.17}$$

where the superscript 'eq' has been removed from the concentration $c_m(z)$ in the metal drops. Modelling of transfers between a settling spherical drop and the surrounding ambient liquid has been investigated in several studies (Wacheul and Le Bars, 2018; Qaddah et al., 2019; Samuel, 2012; Ulvrová et al., 2011; Lherm and Deguen, 2018). From mass conservation and

after modelling the diffusive flux at the metal-silicates interface, these studies show that the concentration in element i varies exponentially in depth to reach the equilibrium concentration $D_i c_s^0$ on a characteristic length scale l_{eq} called the 'equilibration length scale'. For a spherical drop, Lherm and Deguen (2018) established that this length scale reads (see their equation 36 and appendix C)

$$l_{\text{eq}} \sim w_s \frac{r_p^2 D_i}{6\kappa_s} Pe^{-1/2} \left(1 + \frac{1}{D_i}\sqrt{\frac{\kappa_s}{\kappa_m}}\right), \tag{3.18}$$

with $Pe = r_p w_s/\kappa_s$. With this, one can establish the expression of the efficiency in the iron rain regime, as detailed in appendix 3.C. The final expression of the efficiency reads

$$\mathcal{E}_i^{\text{rain}}(z) = 1 + [\mathcal{E}_i(z_\beta) - 1] \exp\left(-\frac{z - z_\beta}{l_{\text{eq}}}\right). \tag{3.19}$$

which is applicable for $z > z_\beta$. Consistently, the efficiency is continuous at depth z_β, and it evolves towards a state of complete mass transfer when z goes to infinity since $\mathcal{E}_i(z) \underset{z\to\infty}{\longrightarrow} 1$. Interestingly, in the thermal and vortical column regimes, the size of drops only influenced the depth of transition from one regime to another. However in the present regime of iron rain, the drop size explicitly determines the efficiency $\mathcal{E}_i^{\text{rain}}(z)$ through l_{eq}, whose value is 42.5 m when $r_p = 10^{-3}$ m.

To minimise notations, in the following the efficiency is always denoted with the general notation $\mathcal{E}_i(z)$ defined as

$$\mathcal{E}_i(z) = \begin{cases} \mathcal{E}_i^{\text{th}}(z), & \text{if } z < z_{\text{col}} \\ \mathcal{E}_i^{\text{col}}(z), & \text{if } z_{\text{col}} \leq z \leq z_\beta \\ \mathcal{E}_i^{\text{rain}}(z), & \text{if } z > z_\beta \end{cases}. \tag{3.20}$$

Similarly the metal dilution is denoted under the general form $\Delta(z)$, which corresponds to $\Delta_{\text{th}}(z)$ in the thermal regime and to $\Delta_{\text{col}}(z)$ in the columnar regime.

3.6.2 Dilution and mixing

Focusing on mixing in thermals and vortical columns, the metal dilution $\Delta(z)$ is computed at any depth for all drop sizes. Past studies which neglected the influence of planetary rotation showed that particles are expected to remain in a turbulent thermal from the start to the end of their fall in the magma ocean (Deguen et al., 2011, 2014; Landeau et al., 2021). Consequently the metal dilution $\Delta(z)$ is compared to the value $\Delta_{\text{th}}(z)$ which would be experienced by the cloud if planetary rotation had no influence on its dynamics. Results are shown in figure 3.9. By definition, $\Delta(z)/\Delta_{\text{th}}(z) = 1$ where clouds behave as turbulent thermals.

In figure 3.9, we observe that dilution reduces in the columnar regime. This originates from the slower growth of vortical columns compared to thermals: along a depth increment dz, the ratio of the volume increment of a turbulent thermal of radius r over the volume increment of a column of radius r_{col} is $4\alpha(r/r_{\text{col}})^2 \simeq (r/r_{\text{col}})^2$. So the deeper the vortical column, the larger the deviation between $\Delta(z)$ and $\Delta_{\text{th}}(z)$.

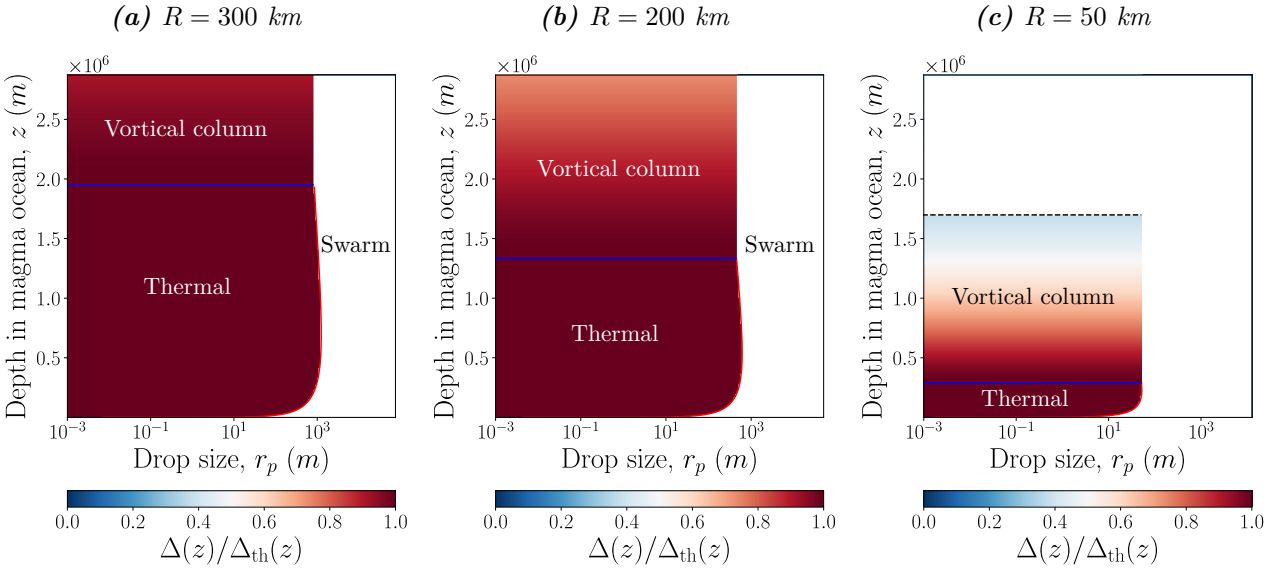

Figure 3.9: *Evolution of the ratio of metal dilution $\Delta(z)/\Delta_{\text{th}}(z)$ along depth z in the magma ocean for the three reference cases of figure 3.7, where Δ is the mass of equilibrated silicates divided by the mass of impactor metal and Δ_{th} is the value of Δ for a pure thermal i.e. in the absence of rotation. Transitions correspond to $\mathcal{R}^*(z) = 1$ (——), $Ro(z_{col}) = 1$ (——), $z = z_\beta$ (- - -) for $\beta = 0.12$.*

3.6.3 Efficiency of clouds made of millimetre-sized drops

The equilibration efficiency $\mathcal{E}_i(z)$ computed from equations (3.13)-(3.20) is shown in figure 3.10a for an impactor of radius $R = 50$ km falling onto Earth. The value of the equilibration efficiency at the surface of the planet ($z/R_t = 0$) is positive because we account for the dilution occurring during the impact (Landeau et al., 2021). It also varies with D_i consistently with equation (3.13): the lower the partition coefficient D_i, i.e. the less siderophile the element i, the larger the efficiency $\mathcal{E}_i^{\text{th}}(z = 0)$.

As the cloud of drops falls deeper in the magma ocean, it dilutes more and more so the efficiency always increases with depth. Once the cloud goes beyond the depth z_{col} (vertical solid blue line), it transitions to the regime of vortical columns, which is less efficient than turbulent thermals at diluting the metal drops. Hence, at a given depth, the slope of the curve $\mathcal{E}_i(z)$ is smaller than that of thermals (dotted lines) until the cloud reaches the depth of complete detrainment z_β.

Importantly, the final value of the equilibration efficiency is that recorded at the bottom of the magma ocean. If a cloud reaches the bottom of the magma ocean while it is in the vortical regime, then accounting for planetary rotation leads to a decrease in the equilibration efficiency. This is even clearer in figure 3.10b which compares the efficiency $\mathcal{E}_i(z)$ of a cloud in the vortical regime with the reference value $\mathcal{E}_i^{\text{th}}$ of a turbulent thermal at the same depth. The efficiency is always reduced in the vortical regime ($\mathcal{E}_i(z)/\mathcal{E}_i^{\text{th}}(z) < 1$) and the discrepancy between the actual efficiency $\mathcal{E}_i(z)$ and that of a thermal reaches 50% at depth $z = 0.26R_t$ for highly siderophile elements with $D_i = 10^4$.

When $z > z_\beta$ (on the right of the vertical dashed dark line in figure 3.10a), the regime of

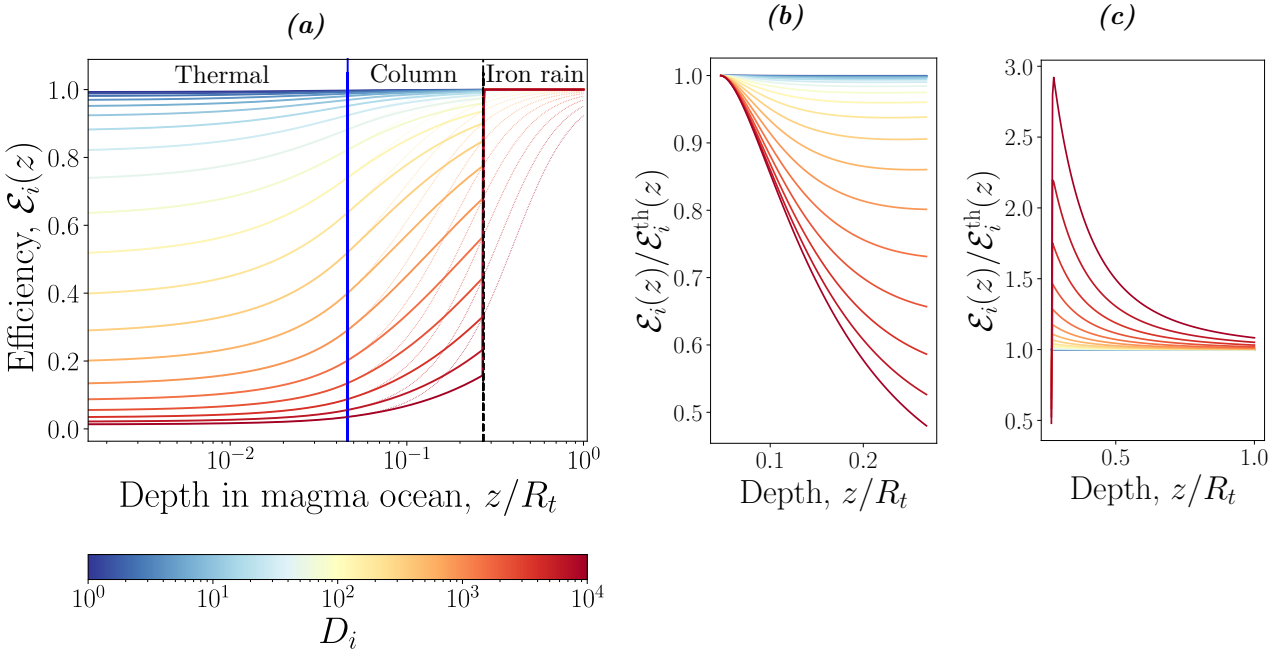

Figure 3.10: *Evolution of the efficiency for an impactor of radius $R = 50$ km hitting the planet Earth ($R_t = 6371$ km, $\Omega = 2\Omega_\oplus$, $g = g_\oplus$, $\beta = 0.12$). (a) Solid curves show the efficiency $\mathcal{E}_i(z)$, while thin transparent dotted lines show the evolution of $\mathcal{E}_i^{\rm th}(z)$ for reference. Vertical lines indicate the depth z_{col} (——) and the depth z_β (- - -). The next two figures show the evolution of the ratio $\mathcal{E}_i(z)/\mathcal{E}_i^{\rm th}(z)$ (b) in the vortical regime and (c) in the iron rain regime. The size of drops is fixed to $r_p = 10^{-3}$ m.*

iron rain ensures a rapid equilibration and $\mathcal{E}_i(z)$ quickly reaches unity. Figure 3.10c shows that the ratio $\mathcal{E}_i(z)/\mathcal{E}_i^{\rm th}(z)$ becomes larger than unity for most partition coefficients: despite the reduction of equilibration in the vortical regime, mass transfers are so efficient in the regime of iron rain that this delay is caught up and $\mathcal{E}_i$ becomes larger than $\mathcal{E}_i^{\rm th}$.

The previous conclusions are generalised in figures 3.11a-3.11c, which show the evolution of the efficiency $\mathcal{E}_i(z)$ along depth for various impactor-to-target radius ratios R/R_t. For all impactors, the efficiency slowly increases with depth until $z = z_\beta$, where the iron rain regime abruptly leads to $\mathcal{E}_i = 1$. Figures 3.11d-3.11f show the ratio $\mathcal{E}_i(z)/\mathcal{E}_i^{\rm th}(z)$ as a function of depth. Expectedly, the ratio is equal to unity at depths $z \leq z_{\rm col}$ in the thermal regime. Then, the ratio lowers in the vortical regime until the depth z_β. Finally, equilibration is so fast in the iron rain regime that the ratio $\mathcal{E}_i(z)/\mathcal{E}_i^{\rm th}(z)$ becomes larger than unity for $z > z_\beta$, all the more so as D_i is larger. Consequently, modelling clouds as turbulent thermals at all depths is all the more inaccurate as elements are more siderophile. This is especially true for the largest impactors that transition to iron rain in figure 3.11f, where the efficiency $\mathcal{E}_i(z)$ largely overshoots $\mathcal{E}_i^{\rm th}(z)$ for $z > z_\beta$. Note that this dependency with respect to the size of the impactor is not due to the iron rain regime (the equilibration length $l_{\rm eq}$ is independent of the impactor size R/R_t) but to the lower efficiency $\mathcal{E}_i^{\rm th}(z)$ of turbulent thermals produced by larger impactors.

Results for a target planet spinning faster at $\Omega = 4\Omega_\oplus$ (figure 3.12) highlight that vortical

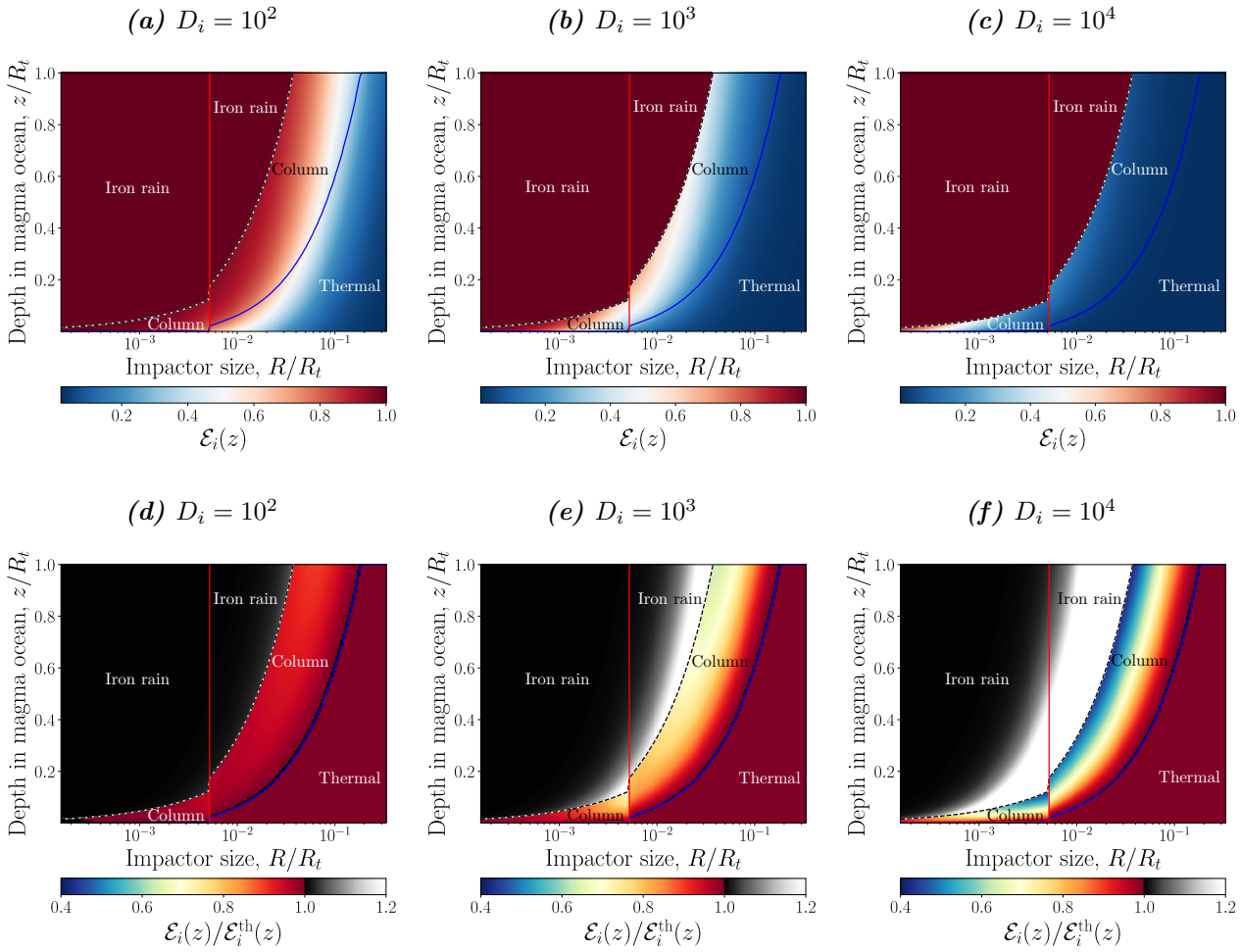

Figure 3.11: *Equilibration efficiency $\mathcal{E}_i$ (a-c) and ratio $\mathcal{E}_i/\mathcal{E}_i^{th}$ (d-f) as a function of impactor size and magma ocean depth for partition coefficients $D_i = 10^2$ (a and d), $D_i = 10^3$ (b and e) and $D_i = 10^4$ (c and f), on a planet spinning at $\Omega = 2\Omega_\oplus$. The size of drops is fixed to $r_p = 10^{-3}$ m. The solid blue line denotes z_{col}, the black-and-white dashed line denotes the depth z_β, and the solid red line separates the impactors that are influenced by rotation in the aftermath of the impact (on the left-hand side) from those that are affected by rotation deeper in the mantle (on the right-hand side).*

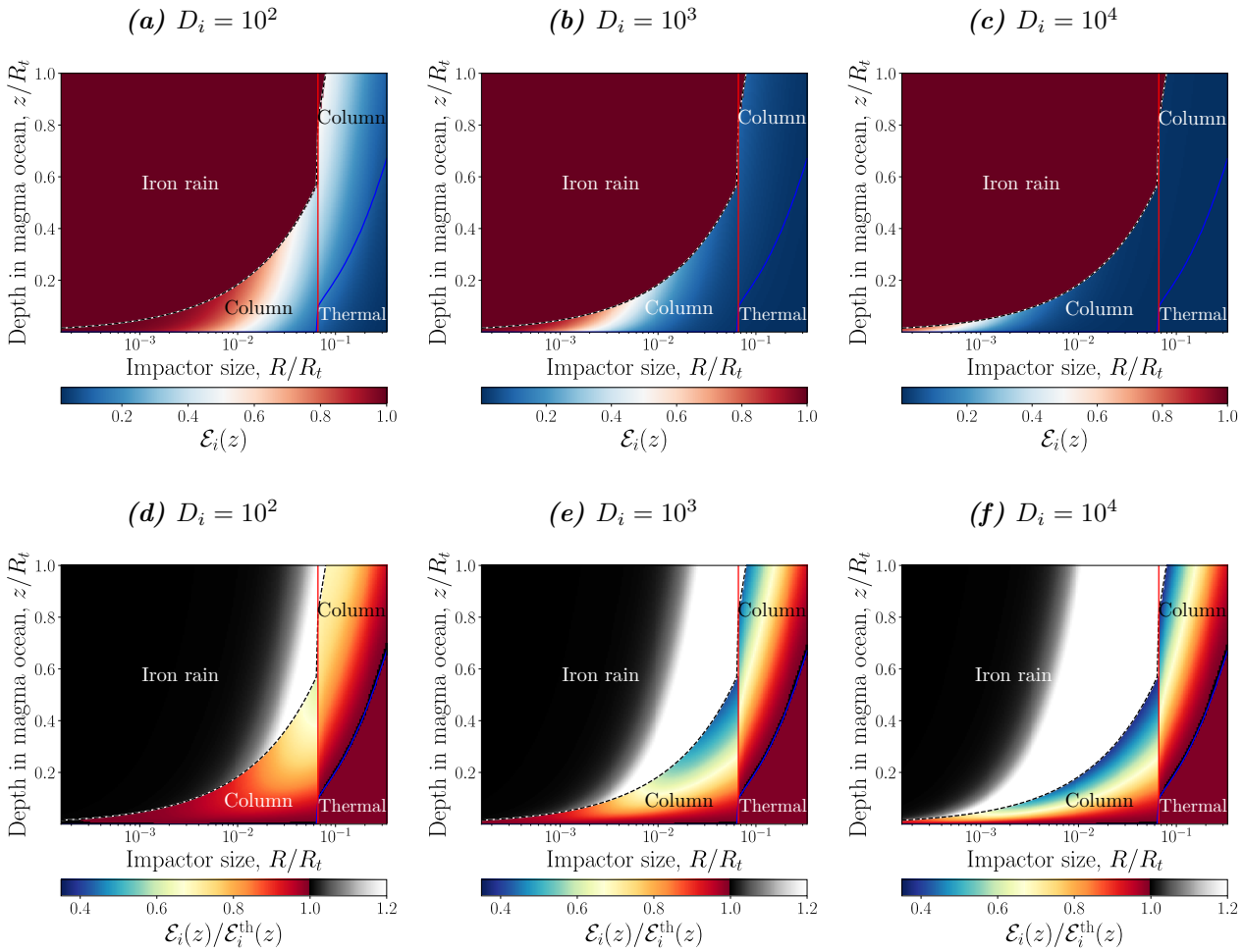

Figure 3.12: *Equilibration efficiency $\mathcal{E}_i$ (a-c) and ratio $\mathcal{E}_i/\mathcal{E}_i^{th}$ (d-f) as a function of impactor size and magma ocean depth, for $D_i \in \{10^2, 10^3, 10^4\}$ on a planet that is now spinning at $\Omega = 4\Omega_\oplus$. Regime boundaries as in figure 3.11.*

columns form at lower depths when rotation is stronger. As a result the efficiency $\mathcal{E}_i(z)$ is lower than in figure 3.11 when the cloud reaches the depth $z = z_\beta$, hence the discrepancy between $\mathcal{E}_i(z)$ and $\mathcal{E}_i^{\mathrm{th}}(z)$ is exacerbated.

This conclusion, however, only holds for impactors verifying $z_{\mathrm{col}} > 0$ on the right-hand side of the vertical red line in figures 3.11 and 3.12. In fact, clouds verifying $z_{\mathrm{col}} = 0$ are unaffected by any further increase of Ω, as illustrated in figure 3.13a. As long as Ω is sufficiently low (on the left-hand side of the vertical red line), a faster spinning reduces both z_{col} and z_β and thus the efficiency $\mathcal{E}_i(z_\beta)$. Conversely, when Ω is above the critical value Ω_c indicated by the vertical red line, impactors verify $z_{\mathrm{col}} = 0$ and we observe that the efficiency becomes independent of Ω. Indeed, the efficiency of vortical columns only depends on the metal dilution (see equation (3.27)) which becomes independent of Ω when $z_{\mathrm{col}} = 0$ (see equation (3.16)).

For a given impactor radius R, all angular velocities above the critical threshold Ω_c have an identical influence on the cloud evolution and on metal-silicate mixing. This critical threshold

is measured for several values of the gravity g and shown in figure 3.13b as a function of the impactor radius R/R_t. The increase of Ω_c with R when $R < 0.33R_t$ originates from larger impactors having more buoyancy and hence inertia. Thus, a larger angular velocity is required to guarantee that this inertia does not overcome the Coriolis force. Yet this intuitive result is not trivial since both $\dot{z}_f(z)$ and $r(z)$, which enter the definition of the Rossby number (3.5), increase with R/R_t. In the range $R/R_t \leq 0.33$, the ratio $\dot{z}_f(z)/r(z)$ increases with R/R_t, and hence the critical angular velocity Ω_c increases with R/R_t. Conversely, in the range $R/R_t \geq 0.33$, the critical angular velocity Ω_c is a decreasing function of R/R_t because of the decrease of $\dot{z}_f(z)/r(z)$ with increasing R/R_t.

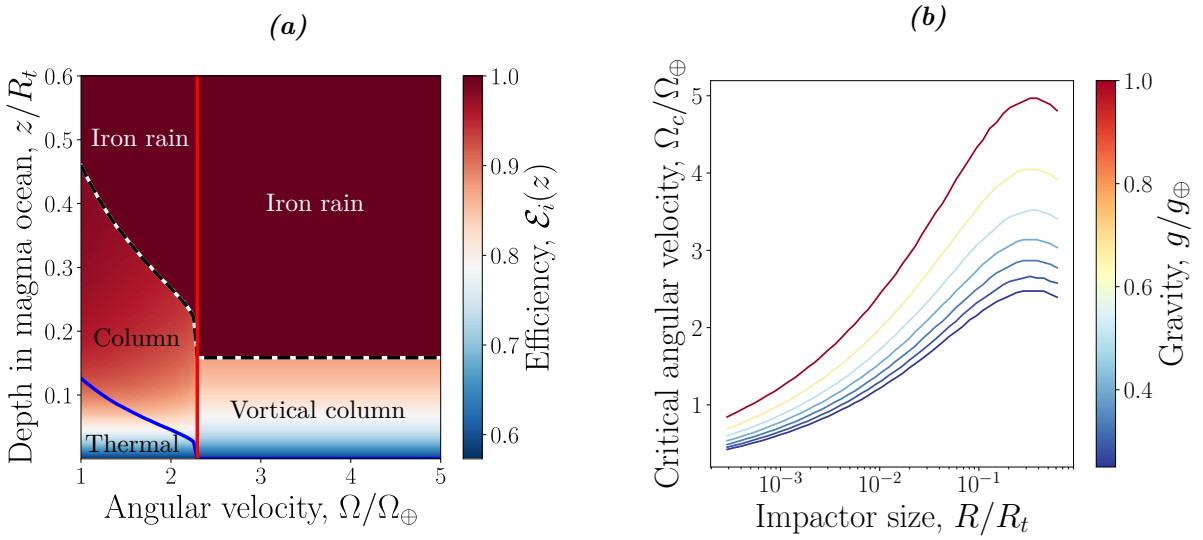

Figure 3.13: *(a) Influence of the angular velocity Ω on the transitions between dynamical regimes (from thermal to vortical column z_{col} (——), from vortical column to iron rain z_β (- - -), critical angular velocity Ω_c at which the thermal regime disappears and the flow is influenced by rotation in the aftermath of the impact (——)) and on the evolution of the efficiency $\mathcal{E}_i(z)$ with depth. (b) Evolution of the critical angular velocity Ω_c as a function of impactor size and for various values of g. For both figures, the size of the metal drops is $r_p = 10^{-3}$ m.*

3.7 Discussion and concluding remarks

Accounting for planetary rotation reconciles the existing models of a turbulent thermal and an iron rain, which appeared to be in contradiction (figures 3.6 and 3.7). Our results suggest that, after each impact, a turbulent thermal of metal and silicates sinks in the magma ocean, but transitions first to a swirling column strongly influenced by rotation, and then to a rain of iron drops. The transition from a thermal to a swirling column occurs at a critical depth $z_{\rm col}$, at which the inertia of the cloud equals the Coriolis force, meaning that the Rossby number Ro (3.5) equals unity. In this regime, a vortical column grows by detrainment of metal drops from a drop-laden frontal sphere to a swirling wake. This regime ends when detrainment completes (figure 3.6). At depths larger than z_β, we predict that metal drops rain out from the column

into an iron rain.

These effects of rotation on the dynamics of the cloud of metal drops have consequences on their chemical equilibration with silicates. At depths larger than z_{col} but smaller than z_β, the equilibration happens in a swirling column and is limited by the mass of silicates entrained in this column. Indeed the entrainment of ambient silicates is reduced in this regime compared to that in turbulent thermals. Thus, the regime of vortical columns is characterised by a reduced metal dilution $\Delta(z)$ compared to the dilution $\Delta_{\mathrm{th}}(z)$ of a reference turbulent thermal at the same depth (figure 3.9). We therefore predict an equilibration efficiency that is lower than previous estimates that neglect planetary rotation. Conversely, at depth larger than z_β, during the regime of iron rain, metal drops interact with a continuously-renewed volume of silicates. Thanks to this renewal of silicates, chemical transfers are efficient and full equilibration is reached at a typical depth $z_\beta + l_{\mathrm{eq}}$ with l_{eq} the equilibration length scale on the order of 100 m.

In the first two regimes of turbulent thermal and vortical column, metal equilibrates with a volume of silicates and hence dilution is the key parameter controlling the efficiency. The efficiency decreases with the impactor size in both regimes (figures 3.11a-3.11c and 3.12a-3.12c), and it increases with decreasing angular velocities Ω in the vortical regime (see figure 3.13a when $\Omega < \Omega_c$). In the regime of iron rain involving a continuously-renewed volume of silicates, the decisive quantity affecting mass transfers is the equilibration length scale l_{eq} (equation (3.18)).

These results show that the depth of the magma ocean and how it compares with the three depths z_{col}, z_β and $z_\beta + l_{\mathrm{eq}}$ controls the efficiency of chemical equilibration.

The above conclusions are based on strong assumptions. When metal drops rain out of the vortical column, they may partly entrain some contaminated silicates. This ability of particles to drag the interstitial fluid that separates them has been investigated in the literature; it depends on the interparticle distance and how it compares with a critical distance of hydrodynamical interaction (Harada et al., 2012; Yamamoto et al., 2015) that is a function of the dynamics of the flow past the particles (Subramanian and Koch, 2008; Daniel et al., 2009; Guazzelli and Hinch, 2011). These effects lack understanding and have therefore been neglected in the present work. Additional experiments of suspensions should be led that control the interparticle distance, as well as the size and settling velocity of particles, exploring different ratios of the particle inertia over viscous dissipation – the so-called particle Reynolds number. Such experiments would improve our ability to account for a partial drag of silicates by the iron drops. This effect would lead to a smoother evolution of the efficiency $\mathcal{E}_i(z)$ at depths $z > z_\beta$. In addition, we have neglected the flow caused by the difference in composition between the silicates in the vortical column and the surrounding magma ocean. This could lead to the vertical displacement of the column within the ocean. Finally, we have assumed that the convective motions in the magma ocean are much weaker than the flows in the thermal and vortical column. However, convective motions will certainly affect the long-term fate of the vortical column.

The present work focuses on the dynamical regimes and the equilibration of a cloud of metal drops falling parallel to the rotation axis of the target planet. This corresponds to a scenario of an impact near the poles. Investigation of the effect of rotation at different latitudes as in Maas et al. (2021) would be beneficial. The misalignment between $\vec{g}$ and $\vec{\Omega}$ might affect the

turbulent stirring of metal drops, and their dispersion and equilibration in the mantle. To tackle the misalignment between $\vec{g}$ and $\vec{\Omega}$, experiments could be performed using an off-centered tank on a rotating table and the centrifugal force to mimic inclined gravity. However, the range of accessible angles could be limited, so numerical simulations would be well-suited to investigate this. Simulations could also incorporate the heating during the impact. If the metal cloud is warmer, we expect that an upward buoyancy force of thermal origin will reduce the cloud inertia and therefore favour a transition to the columnar regime at a lower depth.

Additional experiments at faster rotation rates or starting with releases of lower buoyancy would be beneficial to model small impactors on a fast-spinning planet whose dynamics is constrained by planetary rotation at the top of the magma ocean ($z_{\text{col}} = 0$). They could be complemented by new experiments investigating the role of planetary rotation during the phase of impact and crater collapse, and how dilution by entrainment of already rotating fluid plays any part in the cloud dynamics and onset of settling. Together, they could improve the modelling of the critical condition $\Omega \geq \Omega_c$ for the onset of vortical columns at the very surface of the planet. As regards the vortical regime, additional experiments at larger scale with larger initial cloud buoyancy or lower rotation rates would be beneficial to better constrain the process of detrainment and the subsequent raining out of metal drops, and how it may be influenced by Ekman pumping if the latter develops before raining out from the swirling motions.

3.8 Acknowledgements

This work was supported by the Programme National de Planétologie (PNP) of CNRS-INSU co-funded by CNES.

3.A Thermodynamical equilibrium and uniformity in the flow

As stated in section 3.6.1, the efficiency quantifies mass transfers under the assumptions that a thermodynamical equilibrium is reached by metal and silicates during the cloud fall, and that the cloud is uniform in concentration.

The first requirement translates as a condition $\tau_\chi \ll 2r/\dot{z}$ where τ_χ is the timescale of chemical transfers and $2r/\dot{z}$ is the advective timescale i.e. the typical timescale for the variation of the macroscopic cloud properties (such as its density and radius): this condition means that chemical transfers should complete long before the cloud properties vary to ensure a thermodynamical equilibrium is reached at any depth of the cloud fall. The timescale τ_χ is provided by Deguen et al. (2014) in their equation (22)

$$\tau_\chi \propto \frac{(2r)^2}{\kappa_c^s} Sc^{-1/2} Re^{-1/2} We^{-3/5}, \tag{3.21}$$

and we verify that the requirement $\tau_\chi \ll 2r/\dot{z}$ is met for all scenarios explored in figure 3.8a almost immediately (for the impactors that are influenced by rotation immediately in the

aftermath of the impact, we find $2r/\dot{z}\tau_\chi > 1$ as soon as $z \geq 0.9$ km i.e. $z/z_\beta \geq 2 \times 10^{-3}$; for the other impactors, we find $2r/\dot{z}\tau_\chi > 1$ as soon as $z/z_{\text{col}} \geq 5 \times 10^{-3}$).

The second requirement translates as a condition $\tau_K \ll \tau_\chi$ with τ_K a timescale of dissipation of heterogeneities within the cloud. This condition means that as chemical transfers proceed forward, heterogeneities are smoothed out by turbulence much faster, so that the cloud can be considered homogeneous during mass transfers. While the literature contains evidences of heterogeneities within turbulent thermals (Lherm, 2021), past studies in a variety of contexts have proved the robustness and accuracy of predictions based on the assumption of homogeneity within the turbulent thermal (Deguen et al., 2014; Landeau et al., 2021; Ayotte and Fernando, 1994; Helfrich, 1994; Fernando et al., 1998; Morton et al., 1956; Turner, 1986) and in particle clouds (Deguen et al., 2011; Kriaa et al., 2022; Landeau et al., 2014). This can be verified by computing the timescale of homogenisation based on local velocity gradients. Deguen et al. (2014) have shown that the turbulence that develops inside turbulent thermals can be modelled as a homogeneous isotropic turbulence at first order. Hence the timescale of local homogenisation is the Kolmogorov timescale based on the cloud radius and entrainment velocity

$$\tau_K = \sqrt{\frac{\nu r}{\alpha^3 \dot{z}^3}}, \tag{3.22}$$

which does verify the condition $\tau_K \ll \tau_\chi$ for all impactors and all depths in the general configuration of figure 3.8a ($\beta = 0.12$, $\Omega = 2\Omega_\oplus$, $g = g_\oplus$, $r_p = 10^{-3}$ m).

As regards the vortical regime, renewal of the metal volume fraction $\phi(z)$ within the frontal sphere happens on a timescale τ_β. We assume that turbulence is little altered in the frontal sphere whose Reynolds number remains constant, consequently the timescale of homogenisation τ_K is unaltered, and so is the timescale of chemical transfers τ_χ. Then, we verify that the condition $\tau_K \ll \tau_\chi$ is verified for all impactors at all depths. As for the condition $\tau_\chi \ll \tau_\beta$, it is verified by all vortical columns of figure 3.8a having $z_{\text{col}} > 0$. For the other clouds in the range $R/R_t \leq 4.99 \times 10^{-3}$, in the worst case we find $\tau_\beta/\tau_\chi > 1$ as soon as $z/z_\beta \geq 1 \times 10^{-4}$.

Finally, consider the regime of swarm with iron raining out of the vortical column. In this regime homogeneity is guaranteed: indeed, as a first approximation, metal drops fall individually and cross quiescent unpolluted fluid whose concentration all around each drop is still the initial silicate concentration of the magma ocean c_s^0. However, a thermodynamical equilibrium can only be reached after the drops have travelled a distance long enough to have completed mass transfers with the ambient, thus reaching the ideal equilibrium described by $\mathcal{M}_{\text{i,max}}$. We show in appendix 3.C how to quantify a transient mixing efficiency before this ultimate thermodynamical equilibrium is reached.

3.B Equilibration efficiency of a uniform mixture of metal and silicates

To quantify the mass transfer of an element i between metal and silicates, consider some mass of metal $m_m(z)$ and some mass of silicates $m_s(z)$ that are sufficiently uniformly mixed to be at thermodynamical equilibrium at a given depth z (right-hand side of equation (3.23)), and the initial state of both masses when metal is isolated with a concentration c_m^0, and when silicates

are isolated with a concentration c_s^0 (left-hand side of equation (3.23)). Mass conservation between these two states reads

$$m_m(z)c_m^0 + m_s(z)c_s^0 = m_m(z)c_m^{\mathrm{eq}}(z) + m_s(z)c_s^{\mathrm{eq}}(z). \tag{3.23}$$

In equation (3.23), the masses $m_m(z)$ and $m_s(z)$ are those involved in chemical transfers when either a turbulent thermal or a vortical column (i.e. the combination of a frontal sphere and its wake) is at depth z. The mass concentration $c_m^{\mathrm{eq}}(z)$ (respectively $c_s^{\mathrm{eq}}(z)$) is the concentration of i in the metal (respectively in silicates) when thermodynamical equilibrium is reached. The condition of thermodynamical equilibrium imposes that $c_s^{\mathrm{eq}}(z) = c_m^{\mathrm{eq}}(z)/D_i$. Using this constraint of equilibrium in equation (3.23) and isolating the equilibrium concentration of metal $c_m^{\mathrm{eq}}(z)$ yields

$$c_m^{\mathrm{eq}}(z) = \frac{m_m(z)c_m^0 + m_s(z)c_s^0}{m_m(z) + m_s(z)/D_i} \tag{3.24}$$

The equilibration efficiency quantifies the net mass transfer of element from the very initial state (at impact) to the state of equilibrium $c_m^{\mathrm{eq}}(z)$ so that

$$\mathcal{E}_i(z) = \frac{m_m(z)|c_m^{\mathrm{eq}}(z) - c_m^0|}{\mathcal{M}_{\mathrm{i,max}}}, \tag{3.25}$$

with $\mathcal{M}_{\mathrm{i,max}} = m_0|c_m^0 - D_i c_s^0|$. By subtracting c_m^0 from both sides in equation (3.24), and using equation (3.25), we readily obtain

$$\mathcal{E}_i(z) = \frac{m_m(z)m_s(z)}{m_0}\frac{1}{m_s(z) + D_i m_m(z)}. \tag{3.26}$$

This last equation can be rearranged to take the exact same form as the efficiency of a turbulent thermal expressed by Deguen et al. (2014),

$$\mathcal{E}_i(z) = \frac{k(z)}{1 + \frac{D_i}{\Delta(z)}}, \tag{3.27}$$

with $k(z) = m_m(z)/m_0$ and $\Delta(z) = m_s(z)/m_m(z)$ is the metal dilution. Importantly, equation (3.27) is valid for any uniform structure containing a mass $m_m(z)$ of metal and a mass $m_s(z)$ of silicates. Therefore, it applies for turbulent thermals with $\Delta(z) = \Delta_{\mathrm{th}}(z)$ and the equation (3.13) is recovered. It also applies for a vortical column with $\Delta(z) = \Delta_{\mathrm{col}}(z)$ and the equation (3.15) is recovered.

3.C Equilibration efficiency for a swarm in the regime of iron rain

Mass transfers in the regime of iron rain are characterised by an exponential evolution of the concentration in element i in depth, on a characteristic length scale l_{eq} provided in equation

(3.18) (see Lherm and Deguen, 2018). The mass concentration $c_m(z)$ in element i in the metal phase varies to reach the equilibrium concentration $D_i c_s^0$ and verifies

$$c_m(z) - D_i c_s^0 = [c_m(z_\beta) - D_i c_s^0] \exp\left(-\frac{z - z_\beta}{l_{\text{eq}}}\right), \tag{3.28}$$

which applies for $z \geq z_\beta$. Then it follows that

$$\begin{aligned}
\frac{m_0[c_m(z) - c_m^0]}{\mathcal{M}_{\text{i,max}}} =& \frac{m_0}{\mathcal{M}_{\text{i,max}}}[D_i c_s^0 - c_m^0] + \frac{m_0}{\mathcal{M}_{\text{i,max}}}[c_m(z) - D_i c_s^0] && (3.29)\\
=& \frac{m_0}{\mathcal{M}_{\text{i,max}}}[D_i c_s^0 - c_m^0] + \frac{m_0}{\mathcal{M}_{\text{i,max}}}[c_m(z_\beta) - D_i c_s^0] \exp\left(-\frac{z - z_\beta}{l_{\text{eq}}}\right) \\
=& \frac{m_0}{\mathcal{M}_{\text{i,max}}}[D_i c_s^0 - c_m^0]\left[1 - \exp\left(-\frac{z - z_\beta}{l_{\text{eq}}}\right)\right] + && (3.30)\\
& \frac{m_0}{\mathcal{M}_{\text{i,max}}}[c_m(z_\beta) - c_m^0] \exp\left(-\frac{z - z_\beta}{l_{\text{eq}}}\right)
\end{aligned}$$

From the definitions of $\mathcal{M}_{\text{i,max}}$ and of the equilibration efficiency in equation (3.17), the latter finally reads

$$\mathcal{E}_i(z) = 1 + [\mathcal{E}_i(z_\beta) - 1] \exp\left(-\frac{z - z_\beta}{l_{\text{eq}}}\right). \tag{3.31}$$

Under the present form, equation (3.31) applies for clouds that transition from the regime of vortical column to the swarm regime. Yet, it can be generalised: the position z_β can be replaced with $z = 0$ for a cloud behaving as a swarm immediately after impact, and it can be replaced with the depth of separation where $\mathcal{R}^*(z) = 1$ for a cloud transitioning from the thermal regime to the swarm regime without ever behaving as a vortical column.

Part II

Plumes of reactive particles

Chapitre 4

Plumes of settling and dissolving sugar grains

Summary

As an analog of snow-driven flows, we present experiments of settling and dissolving grains of sugar that are continuously sieved above water with various mass fluxes and sizes of sugar grains. Through drag and dissolution, particles force a central plume whose inner structure is analysed in a laser sheet thanks to PIV measurements and the use of home-made fluorescent sugar to track the negatively buoyant sugary water. The size of grains controls a wealth of behaviours, from a laminar plume that gains intensity over a long transient when forced by the rectilinear fall of large grains, to a turbulent lazy plume that emerges faster when forced by fast-dissolving small grains. This transition is determined by the enhanced forcing imposed by smaller grains, and their ability to nourish a Rayleigh-Taylor-like instability at the plume onset. In the quasi-steady state, the combination of settling and advection of sugar by the flow controls the dilution of the buoyant material, which in turn feedbacks on the flow to select the plume velocity. The coupling of this velocity with the Lagrangian evolution of a settling and dissolving grain sets the depth of complete dissolution in the plume.

4.1 Introduction

Our interest is in buoyancy-driven flows laden with reactive particles that initially force the flow by their sedimentation, but ultimately change phase by dissolution, thus imparting their buoyancy to the fluid. Our laboratory experiments consist of sugar grains that are continuously sieved above a water tank; as they settle and dissolve in a plume, they produce negatively buoyant sugary water that sinks in the tank, and we analyse both solid and fluid motions. What is the impact of this transition from a dispersed forcing to a continuous field of buoyancy in the fluid?

In a particle-laden flow, large particles of large inertia are insensitive to local modifications of the flow due to their considerable response time (Maxey, 1987; Ghosh et al., 2005; Yoshimoto

and Goto, 2007). This low-pass 'inertial filtering' results in a decoupling of particles from fluid motions. In addition, the present study focuses on flows driven by the sedimentation of buoyant particles, so the same particles have settling velocities that are much larger than the fluid velocities. As a result, they settle in the direction of gravity irrespective of fluid motions (e.g. Balachandar and Eaton, 2010, and see Chapter 1). Conversely, tiny particles of negligible inertia and settling velocity move like passive tracers (Maxey, 1987): they are fully coupled to the fluid motions and are advected by the flow like a scalar field (Balachandar and Eaton, 2010). Consequently, for an identical global buoyancy, settling-driven flows forced by particles of different sizes can be very different (see Chapters 1 and 2).

Beyond these limiting cases, the particles' inertia and settling velocity control their dispersion in the flow, with consequences on the heterogeneity of the buoyancy forcing. Dense particles of finite inertia preferentially concentrate on the periphery of eddies in zones of large strain rate (Maxey, 1987; Aliseda et al., 2002; Yoshimoto and Goto, 2007; Salazar et al., 2008; Toschi and Bodenschatz, 2009; Falkinhoff et al., 2020); due to settling, they preferentially fall on the eddy side of downward velocity (Maxey and Corrsin, 1986; Wang and Maxey, 1993; Nielsen, 1993; Elghobashi and Truesdell, 1993; Bosse et al., 2006; Good et al., 2014; Falkinhoff et al., 2020; Hassaini and Coletti, 2022); when they fall in an upwelling region, the latter delays their progression so particles sample these upwelling regions for a longer time, resulting in a 'loitering' that affects their dynamics (Nielsen, 1993). These examples of mechanisms of preferential sampling modify the distribution of particles in space and time, thus imprinting the influence of the particles' inertia and settling on the field of concentration (see Chapters 1 and 2).

For an identical buoyancy flux, the particulate nature of the buoyancy forcing has an impact on the flow. This has manifested as a modification of the entrainment rate of plumes and thermals for pointwise injections of buoyant particles (McConnochie et al., 2021; Kriaa et al., 2022, and Chapter 1). This has also been shown in experiments or simulations where particles are injected from, or settle over, a line source (when the flow is 2D) or a large surface area (when the flow is 3D). Compared to the injection of buoyant fluid (Friedl et al., 1999; Kaye and Hunt, 2009), the buoyancy flux is not the sole ingredient controlling a particle-driven flow: experiments of settling particles (Mizukami et al., 1992; Carey, 1997; Carazzo and Jellinek, 2012; Jacobs et al., 2015; Lemus et al., 2021; Magnani et al., 2021; Zürner et al., 2023) or rising bubbles (Kimura, 1988; Climent and Magnaudet, 1999) have shown that the settling velocity conditions the development of buoyancy-driven instabilities and controls the structure of the flow (Murai and Matsumoto, 1998; Iga and Kimura, 2007).

Finally, the heterogeneity of the particle concentration due to preferential sampling effects results in a heterogeneous concentration of solute during dissolution. Additionally, the dissolution rate depends on the grains' size (Ranz and Marshall, 1952; Kerr, 1995). Consequently, despite the transition of the flow from particle-driven to solute-driven, we show that the final dynamics of a solutal plume is still marked by the dynamics that particles had prior to their full dissolution.

We present the results of our experiments on sugary plumes in which we vary the mass rate and the size of the sugar grains at the source. Section 4.2 presents the experimental setup. Section 4.3 introduces three reference cases of sugar plumes that enable to identify in section 4.4 the essential ingredients that force the flow. Section 4.5 then focuses on the onset of the flow

below the water free surface and how it constrains the plume structure. Section 4.6 analyses the transient and the quasi-steady regimes of the sugary plumes, providing a description of the flow that enables to predict in section 4.7 the evolution of sugar grains before they fully dissolve. Section 4.8 offers some final remarks. Appendixes 4.A and 4.B give details about the experimental setup and processing techniques.

4.2 Experimental setup

Experiments are performed by continuously sieving sugar above a cylindrical water tank of height 38.5 cm and diameter 28.5 cm containing 24.5 L of initially fresh water ($\rho_0 = 1000$ kg.m^{-3}, $\nu = 10^{-6}$ m^2.s^{-1}). The tank is filled long before the experiments to ensure that water is at room temperature, i.e. 22°C on average. A sieve of radius $R_{\text{sieve}} = 8.25$ cm is placed above the water free surface, with a distance of 8.15 cm between the latter and the bottom of the sieve. The latter is held by a ring that is screwed to a magnetised rod which oscillates back and forth thanks to a motor which is controlled by a computer to adapt the amplitude, velocity, frequency or functional form of oscillation (sine wave or triangle).

When ordinary sugar falls in water, only small changes of refractive index can be seen after dissolution. To visualise sugary water, we decided to put fluorescent colouring in sugar by cooking our own. No matter whether dyed sugar or ordinary sugar is used, grains must be crushed to obtain very small sizes, which then imposes to sort all the grains by sieving. During this procedure, and most of all during an experiment, sieves tend to clog while they oscillate, which complexifies the calibration of the mass rate. All these aspects are detailed in Appendix 4.A. Important points are that a new calibration is performed for each experiment, and that the size of grains is constrained by the size of the sieves that are used to separate them; their average radii are listed in table 4.1.

Range of diameters (μm)	56-125	125-140	140-180	180-224	224-450	450-1000
Average radius r_p (μm)	45.25	66.25	80	101	168.5	362.5
Re_p	0.226	0.671	1.13	2.12	7.66	41.6

Table 4.1: *Average radius of sugar grains and particle Reynolds number $Re_p = r_p w_s/\nu$ based on their settling velocity w_s, depending on the range of diameters they belong to.*

The visualisations are performed in a vertical laser sheet (see figure 4.1a) with half-angle of divergence 30°, using a Powell lens and a laser of wavelength 532 nm with a power of 450 mW (Laser Quantum 532 nm CW laser 2 W). When ordinary sugar grains are sieved, they reflect and refract the laser beam so they appear in green. Consequently their motions are recorded by a PointGrey camera equipped with a green filter (band-pass filter from Edmund Optics, CWL 532 nm, FWHM 10 nm) with a frame rate of 50 fps.

Alternatively, when dyed sugar grains are used, they appear orange due to their fluorescence. Importantly, the presence of the coloured molecules *inside* the sugar ensures that throughout the whole process of dissolution, these molecules are released in water, that is why sugary water also appears in orange in the laser sheet. The motions of both dyed sugar grains and sugary

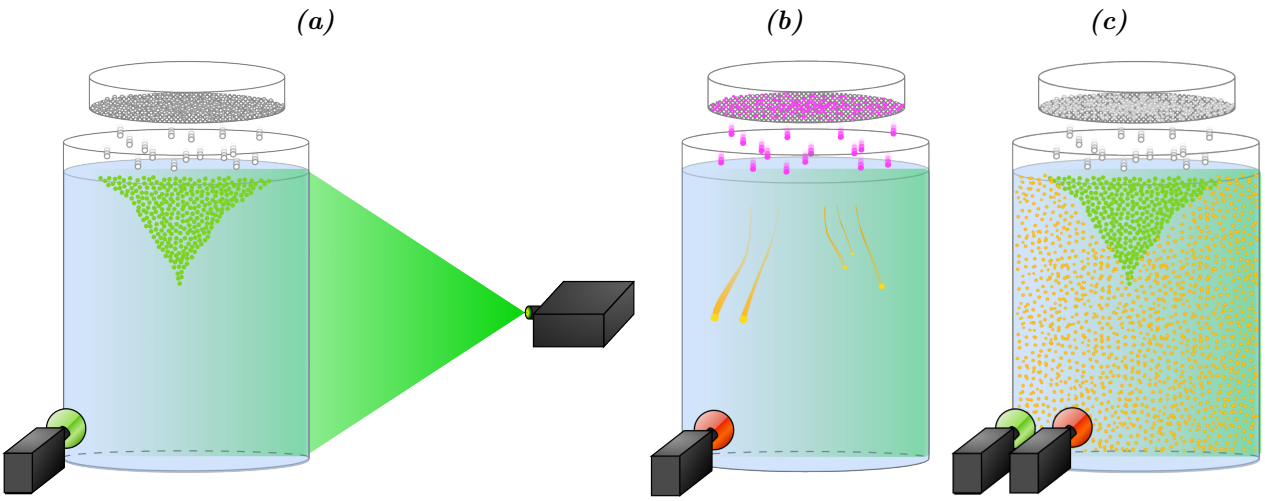

Figure 4.1: *Three configurations for recording experiments. (a) Ordinary sugar is sieved and recorded by the camera with a green filter. (b) Dyed sugar is sieved in the same laser sheet and recorded by the camera with an orange filter. (c) Ordinary sugar is sieved while the tank is seeded with orange PIV particles. The camera with green filter records the motions of sugar grains, while the camera with orange filter records the motions of orange tracers.*

water are recorded at 50 fps by another identical camera that is equipped with an orange filter (high-pass filter above 570 nm), see figure 4.1b.

Finally, to quantify the velocity field in water, the two cameras are synchronised, again at 50 fps. The first camera with a green filter records the motions of ordinary sugar grains, while the second camera with an orange filter records the motions of orange PIV particles (see figures 4.1c and 4.2).

4.3 Core physical ingredients: focus on three representative cases

4.3.1 Rectilinear precipitation of large sugar grains

Figure 4.3 shows snapshots of 363 μm-sized dyed sugar grains settling in quiescent water when sieving with a mass rate $\dot{m} = 0.052$ g/s, i.e. typically 163 sugar grains per second. Streaks of rhodamine evidence the vertical settling of these grains, which is the most characteristic feature of this category of experiments. At large times, weak horizontal deviations of these wakes of rhodamine can be seen at the top of the tank due to the formation of a local converging flow. Deviations of sugar grains are even weaker: they are almost insensitive to horizontal fluid velocities. This is because they partly decouple from fluid motions due to settling. Under the widely used assumption that the particle inertia can be neglected, and considering the motion of a sugar grain on a timescale much lower than the dissolution timescale, the momentum equation of a single supposedly spherical sugar grain of radius r_p reduces to a balance between

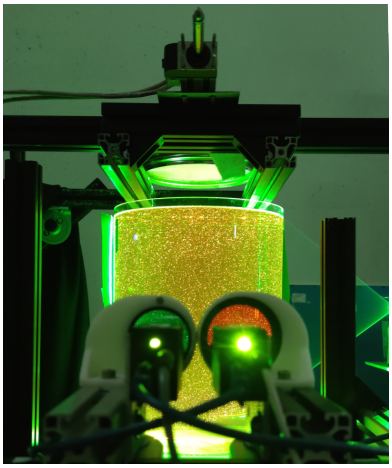

Figure 4.2: *Photograph of the experimental setup before an experiment corresponding to the sketch in figure 4.1c. The orange tracers are clearly visible in the water tank; they are recorded by the camera on the right-hand side that is equipped with an orange filter. The laser beam emitted by the laser is visible as a green triangle due to the presence of some dust in the room. The bright green circle above the tank is the bottom of the sieve that lies on two rods to oscillate horizontally.*

its buoyancy and drag:

$$\boldsymbol{v}_p(\boldsymbol{x}_p, t) = \boldsymbol{v}(\boldsymbol{x}_p, t) \underbrace{+ w_s(r_p)\boldsymbol{e}_z}_{\text{gravitational drift}}, \quad \text{with } \boldsymbol{e}_z = \boldsymbol{g}/g. \tag{4.1}$$

This equation means that the grain velocity $\boldsymbol{v}_p(\boldsymbol{x}_p, t)$ is equal to the local fluid velocity $\boldsymbol{v}(\boldsymbol{x}_p, t)$ with the addition of a *gravitational drift* along the direction of gravity at the terminal velocity $w_s(r_p)$. The latter is parameterised as (Crowe et al., 2011)

$$w_s = \frac{w_s^{\text{Stokes}}}{1 + 0.15 Re_p^{0.687}}, \tag{4.2}$$

where $Re_p = w_s r_p/\nu$ is the particle Reynolds number and

$$w_s^{\text{Stokes}} = \frac{2 g r_p^2 (\rho_p - \rho_0)}{9 \nu \rho_0} \tag{4.3}$$

is the Stokes velocity. In equation (4.3), g is gravity, ρ_p is the density of sugar, ρ_0 is the density of clear water and ν is its kinematic viscosity (we neglect the change in density and viscosity associated with dissolved sugar, see section 4.7.3 below for further discussions). The values of these quantities are listed in table 4.2. The vertical settling and the resistance of large grains to the horizontal convergence is a consequence of their large settling velocity that predominates over the fluid velocity.

Together with the continuous stochastic deposition of additional sugar wakes in the flow, the convergence ultimately leads to the overlap of these dyed wakes, which implies an enhancement of the local negative buoyancy which accelerates the downward fluid motions. The latter gain intensity during a transient which eventually leads to a quasi-steady flow – these two stages are separately analysed for all experiments in sections 4.6.2 and 4.6.3. Importantly, the last

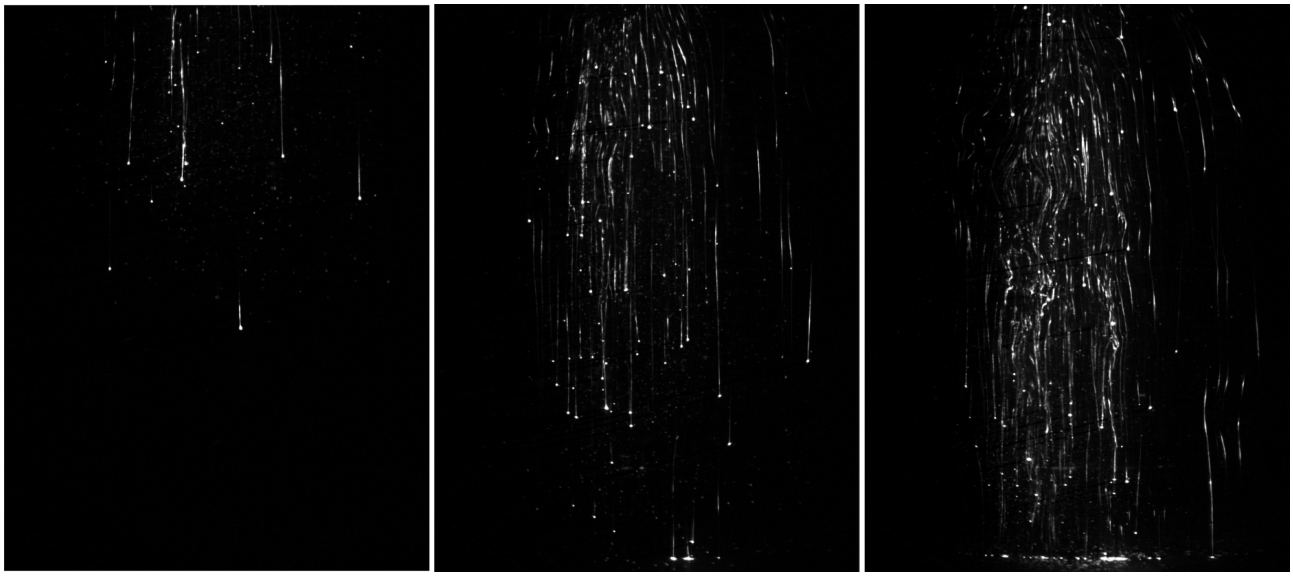

Figure 4.3: *Three snapshots of dyed sugar grains of mean initial radius* $r_p = 363$ μm *sieved with an average mass rate* $\dot{m} = 0.052$ g/s. *The total height is* 38 cm *and the time interval between snapshots is* 6 s.

snapshot in figure 4.3 still preserves a layered structure of vertical wakes, evidencing the laminar and essentially irrotational nature of the plume that develops.

Quantity	Notation	Value	Reference
Density of sucrose	ρ_p	1590 kg.m^{-3}	[1]
Density of saturated sugary water	ρ_{sat}	1450 kg.m^{-3}	[2]
Mass concentration at saturation	$\mathcal{C}_{\text{sat}}$	968 kg.m^{-3}	[2]
Diffusivity of sucrose in water	κ	0.5×10^{-9} m^2.s^{-1}	[3,4]
Density of clear water	ρ_0	1000 kg.m^{-3}	-
Gravity	g	9.81 m.s^{-2}	-
Kinematic viscosity of water	ν	10^{-6} m^2.s^{-1}	-

Table 4.2: *Main properties of sugar and sugary water. References correspond to: [1] Hancock and Zografi (1997); [2] Cohen et al. (2020); [3] Linder et al. (1976); [4] Price et al. (2016).*

4.3.2 Lazy plume of fast-dissolving small grains

Figure 4.4 shows snapshots of 45 μm-sized dyed sugar grains sieved with a mass rate $\dot{m} = 0.120$ g/s, i.e. about 1.9×10^5 grains per second. Photographs evidence a strikingly different onset of solutal convection compared to the previous section, with the development of sugar-laden mushrooms underlying the free surface. This localised interfacial instability is identified as a Rayleigh-Taylor-like instability forced by the excess density of the sugary layer located just below the free surface.

As the sugary mushrooms grow, they coalesce and gradually converge to form a plume, in a similar way as observed for 3D one-phase plumes (Friedl et al., 1999) and for 2D bubble plumes (Mudde, 2005). The constriction of the flow is characteristic of lazy plumes which have a deficit of momentum flux at the source compared to a pure plume of identical volume flux and buoyancy flux (Hunt and Kaye, 2005). This necking phenomenon enhances the local buoyancy by concentrating sugar grains and dissolved sugar, and it accelerates the flow by continuity, leading to an increase of the plume momentum flux and thus its transition to the state of a pure plume (Hunt and Kaye, 2005).

The lazy plume that develops is laden with convoluted patches of sugary water which are due to the presence of numerous eddies of varying sizes, evidencing the (moderately) turbulent nature of the flow. The rapid vortical onset of the flow stands in stark contrast with the delayed onset observed in the previous section for large grains (see figure 4.3). Also, in figure 4.4 no sugar grain is visible because grains are very small and their signal is lost in the brightness of the dyed sugary water. Yet, these grains dissolve at a finite depth which can be measured in the absence of rhodamine when using ordinary sugar, as we shall see later. As for all regimes, we observe that the flow eventually reaches a quasi-steady state with a central turbulent plume and upward recirculations on the sides.

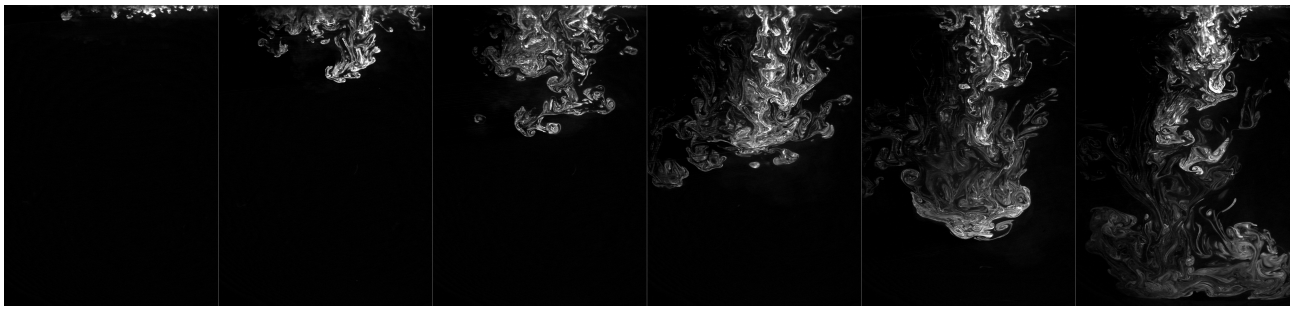

Figure 4.4: *Six snapshots of dyed sugar grains of mean initial radius* $r_p = 45$ μm *sieved with an average mass rate* $\dot{m} = 0.120$ g/s. *The total height is* 38 cm *and the time interval between snapshots is* 10 s.

4.3.3 Grains of intermediate size

Experiments with grains of intermediate size are more representative of the general evolution of the flow in experiments, and combine observations made with small and large grains. Snapshots in figure 4.5 for grains of radius $r_p = 101$ μm sieved with a mass rate $\dot{m} = 0.115$ g/s (i.e. typically 1.7×10^4 grains per second) show that grains initially just settle vertically in water (first snapshot): apart from variations of light intensity due to light scattering at the scale of sugar grains, the precipitation is uniform and its front is flat. Yet, ultimately a Rayleigh-Taylor-like instability emerges (second snapshot) whose mushrooms grow and coalesce (third snapshot) until converging to form a central downward plume (fourth and fifth snapshots). Lastly, the plume reaches quasi-steadiness at the centre of recirculation cells.

Interesting features emerge when looking at sugar grains which are sufficiently large and bright to be visible even in the plume of dyed sugar. Unlike the largest grains of section 4.3.1,

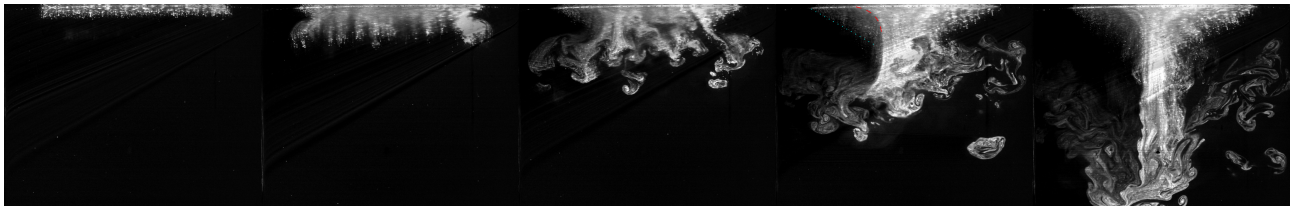

Figure 4.5: *Five snapshots of dyed sugar grains of mean initial radius* $r_p = 101$ μm *sieved with an average mass rate* $\dot{m} = 0.115$ g/s. *The total height is* 23 cm *and the time interval between snapshots is* 5.2 s.

the present grains are sufficiently small to be carried along by the lazy plume. Yet, they prove to have sufficient inertia and gravitational drift to have vertically-biased trajectories and to partly decouple from fluid motions by raining out of the region of flow convergence below the free surface: while the dissolved sugar converges with a convex profile *within* the plume (see the red dashed line in the fourth snapshot), large sugar grains converge along a cone *outside* of the solute (see the blue dotted line in the fourth snapshot of figure 4.5).

The visual texture of the plume is also intermediate between previous observations. It combines the smooth variations of light intensity due to dissolved sugar as well as some bright dots of large sugar grains which dissolve sufficiently deep to be visible at finite depth. Some regions are layered due to the vertical wakes of sugar grains, suggesting the flow is locally laminar. At the same time, the last snapshot in figure 4.5 shows shear instabilities that induce fluctuations at larger depths, possibly leading to turbulence if the flow is sufficiently vigorous.

All in all, figures 4.3 to 4.5 suggest that the Rayleigh-Taylor-like instability or the shear instabilities are responsible for the transition of the flow to turbulence. However, as the plume develops, it carries buoyant material downward and dilutes the incoming flux of sugar grains, thus reducing the local buoyancy and inertia that force the instabilities. This dilution explains why the transition to turbulence may initially take place at a shallow depth, and yet be delayed further downstream once downward fluid motions have developed.

4.4 Influence of the grain size on three local forcings

We just saw that large grains fall ahead of fluid motions and deposit their buoyancy along vertical paths that largely constrain the resulting laminar flow; conversely, small grains are rapidly invisible in the vortical turbulent flow they force – hence a transition from a particle-driven and settling-constrained flow to a fluid-like behaviour. As a first step to understand this transition, we present three ingredients that account for an enhanced local forcing of the flow when the size of grains decreases.

4.4.1 Collective drag

The first ingredient is the ability of particles to drag fluid downward when they settle. While an individual grain essentially drags fluid in its wake, a collection of multiple grains acts like a local negative buoyancy at a mesoscopic scale. This can be explicitly captured by averaging the

drag force of all grains in a unit volume, which yields the volumetric drag force (see Chapter 2)

$$\boldsymbol{f}_{\text{drag}}(\boldsymbol{x},t) = [\rho_p - \rho(\boldsymbol{x},t)]\phi(\boldsymbol{x},t)\boldsymbol{g} \ , \tag{4.4}$$

where $\phi(\boldsymbol{x},t)$ is the local volume fraction of grains, ρ_p is the density of a sugar grain and $\rho(\boldsymbol{x},t) \geq \rho_0$ is the local density of sugary water. Because equation (4.4) is derived by modelling particles as a continuum, any information about the radius of particles is lost: drag only depends on the volume fraction. Yet, a simple laboratory experiment immediately shows that the volume of fluid dragged by two settling particles and the velocity it acquires depend on their spacing: when they are too distant, the two particles only drag fluid in their respective isolated wake, whereas the interstitial fluid remains motionless. Similarly, experiments with particle clouds of identical volume fraction reveal that the larger the particles, the less efficient their forcing of fluid motions (see Chapter 1). The contrast between the actual influence of r_p on drag and the equation (4.4) is due to the mathematical requirement underlying this equation: the averaging procedure that leads to equation (4.4) is only appropriate when the number density $\sim \phi r_p^{-3}$ of particles is sufficiently large for the averaged quantity (here, drag) to be representative at the mesoscopic scale (Chou and Shao, 2016). A mathematically equivalent condition is that the interparticle distance

$$l_{\text{inter}} \propto r_p \phi^{-1/3} \tag{4.5}$$

of a uniform suspension should be sufficiently small for the hydrodynamic perturbations of neighbouring grains to overlap, enabling them to collectively drag the interstitial fluid, as concluded in past experimental (Harada et al., 2012) and numerical (Yamamoto et al., 2015) studies. These conclusions are further supported by several studies which show that despite their fundamentally long-range hydrodynamical interactions, the perturbations induced by particles with negligible (Subramanian and Koch, 2008; Guazzelli and Morris, 2011; Pignatel et al., 2011) or finite inertia (Koch, 1993; Daniel et al., 2009) extend only up to some typical length scales that are finite. Since the interparticle distance increases linearly with r_p, the downward fluid motions induced by the largest grains tend to remain localised behind each of them in wakes, as consistently observed with PIV particles during experiments; it is the cumulated influence of several wakes over time that leads to an eventual macroscopic flow. Conversely, for a given injection mass rate, small grains being closer to one another, they are expected to drag the fluid more efficiently. In reference to hydrodynamical interactions that lead grains to behave fluid-like (Harada et al., 2012), we refer to this behaviour as 'collectivity'. It is a key ingredient driving fluid motions and in particular the onset of a Rayleigh-Taylor-like instability, because the latter is fundamentally an instability of *fluids* and therefore its emergence requires the growing sugary layer to behave as such.

4.4.2 Gravitational drift

The second ingredient responsible for the discrepancy between the experiments with large grains and those with small grains is the gravitational drift in equation (4.1). As aforementioned, as soon as the interparticle distance is sufficiently small to model the drag of particles as a continuous forcing due to a field of volume fraction, grains of all sizes impose the same forcing. Suppose that particles are sufficiently small and concentrated for this continuum description to apply. Then, it means that the field $\phi(\boldsymbol{x},t)$ exerts an identical drag at a position $\boldsymbol{x}$ and *at*

a specific time t. Yet, due to the particle settling, the advection of the volume fraction $\phi(\boldsymbol{x}, t)$ reads

$$\partial_t \phi + \boldsymbol{v} \cdot \nabla \phi = -w_s \frac{\partial \phi}{\partial z}, \tag{4.6}$$

where κ and $\mathcal{C}$ are respectively the diffusivity and the mass concentration of sugar in water. The right-hand side of equation (4.6) is a term of gravitational drift due to equation (4.1) which causes a partial decoupling between the volume fraction and the fluid parcels moving with the fluid velocity $\boldsymbol{v}$. Thus, forcing of a quiescent fluid parcel at position $\boldsymbol{x}$ is expected to be less efficient when w_s increases due to a faster decoupling – see the numerical simulations of Chapter 2.

4.4.3 Dissolution

The third ingredient that strictly contributes to a transition from a particle-driven flow to a fluid-like flow is dissolution, which is faster for smaller grains. Dissolution is quantified by the diffusive mass flux from a supposedly spherical sugar grain to the fluid which reads

$$\Phi = -\kappa \boldsymbol{\nabla} \mathcal{C} \cdot \boldsymbol{n} \tag{4.7}$$

with $\boldsymbol{n}$ the normal to the grain-fluid interface pointing in the direction of the fluid. The concentration gradient scales like the ratio of the concentration contrast between the bulk fluid and the concentration at the interface, over the thickness of the diffusive boundary layer that develops at the surface of each grain. Settling causes a local advection around a grain with a slip velocity $-w_s(r_p)\boldsymbol{e}_z$ (equation (4.1)) that enhances the diffusive mass flux. To account for this effect, the boundary layer thickness must be parameterised. To do so, we first assume a linear relation between sugar concentration and density (Philippi et al., 2019; Pegler and Wykes, 2020; Cohen et al., 2020)

$$\mathcal{C}(\boldsymbol{x}, t) = \frac{\rho(\boldsymbol{x}, t) - \rho_0}{\rho_{\text{sat}} - \rho_0} \mathcal{C}_{\text{sat}}, \tag{4.8}$$

with $\rho(\boldsymbol{x}, t)$ the local fluid density, ρ_0 the fluid density in the absence of solute, and ρ_{sat} and $\mathcal{C}_{\text{sat}}$ respectively the density and concentration of water at saturation. Any latent heat absorption during dissolution is neglected as the past literature has shown it is negligible for the dissolution of sucrose in water (Pegler and Wykes, 2020). Then, assuming the grain remains spherical while it dissolves (which effectively assumes that the dissolution flux is uniform) and using equations (4.7) and (4.8), mass conservation reads $d(4\pi r_p^3 \rho_p/3)/dt = -4\pi r_p^2 \Phi$, or after simplications,

$$\underbrace{-\dot{r}_p}_{\text{recession speed}} = \overline{k} \frac{\mathcal{C}_{\text{sat}}}{\rho_p} \frac{\rho_i(t) - \rho(t)}{\rho_{\text{sat}} - \rho_0}, \tag{4.9}$$

where $\overline{k}$ is the coefficient of mass transfer averaged over the whole surface area of the sugar grain. Two parameterisations are considered depending on the particle Reynolds number $Re_p = r_p w_s/\nu$. When $Re_p \gg 1$, we apply the parameterisation by Ranz and Marshall (1952), while the

parameterisation by Levich (1962) applies when $Re_p \ll 1$ (Ulvrová et al., 2011). In practice, we impose a transition of $\overline{k}$ from the former law to the latter as follows

$$\overline{k} = \frac{\kappa}{2r_p} Sh, \text{ with } Sh = \begin{cases} 2 + 0.6 Sc^{1/3} Re_p^{1/2}, & \text{if } Re_p \geq 1 \\ 2 + 0.64 Sc^{1/3} Re_p^{1/3}, & \text{if } Re_p < 1 \end{cases} \tag{4.10}$$

where the Schmidt number $Sc = \kappa/\nu$ is the ratio of the diffusivity of sugar in water, over the kinematic viscosity of water. The mass transfer coefficient $\overline{k}$, whose dimensionless form is called the Sherwood number Sh, has the dimension of a velocity (in m/s) and parameterises the size of the diffusive boundary layer. In equation (4.10) the mass flux is driven both by advection, and by diffusion whose harmonic solution around a sphere in a steady regime yields the exact flux κ/r_p (Epstein and Plesset, 1950), hence an acceleration of mass transfers with the grain curvature (Pegler and Wykes, 2020). In addition, the last fraction on the right-hand side of equation (4.9) recovers the expected delay of dissolution when the density contrast between the ambient and the concentration at the grain interface is lowered (Liu et al., 1996). Note in particular that dissolution can no longer proceed when the ambient is saturated (i.e. $\rho(t) = \rho_{\text{sat}}$) since the inequality $\rho_{\text{sat}} \geq \rho_i(t) \geq \rho(t)$ then imposes that $\rho_i(t) = \rho_{\text{sat}}$ hence $\dot{r}_p = 0$.

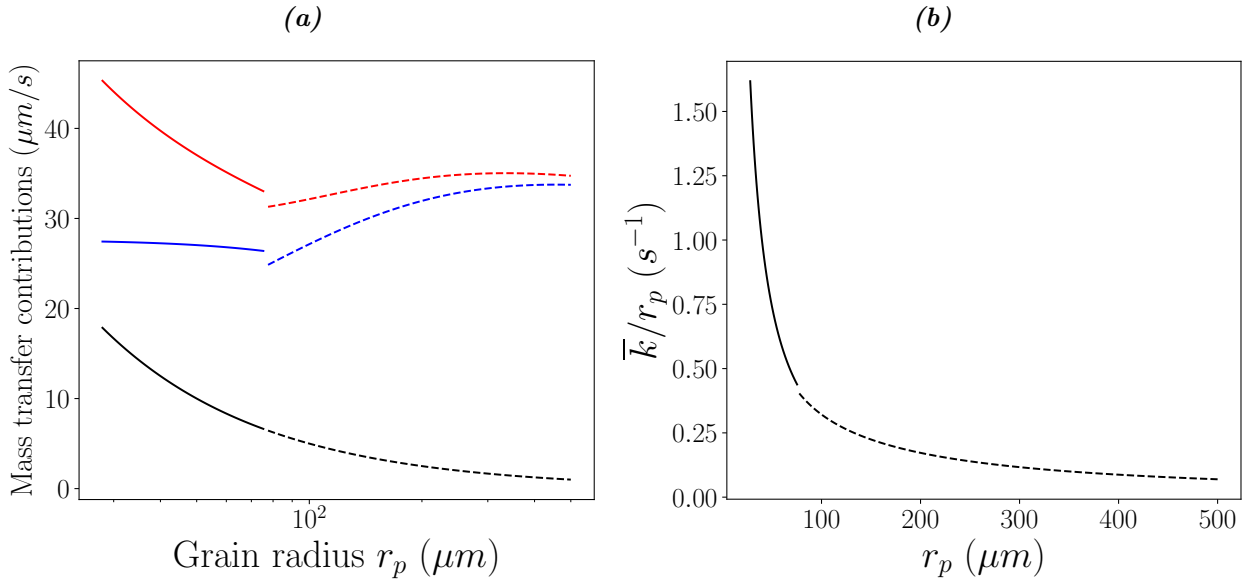

Figure 4.6: *(a) Contributions to the mass transfer coefficient $\overline{k}$ computed assuming the ambient fluid is clear ($\rho(t) = \rho_0$). The dark line shows the diffusive contribution κ/r_p, the blue line shows the advective contribution $\overline{k} - \kappa/r_p$, and the red line shows the full coefficient $\overline{k}$. (b) Evolution of the ratio $\overline{k}/r_p$ that controls the total mass transfer due to a collection of grains of radius r_p and uniform volume fraction. In both graphs, the lines are continuous when the parameterisation of Levich (1962) applies ($Re_p < 1$); they are dashed when the parameterisation of Ranz and Marshall (1952) applies ($Re_p \geq 1$).*

At this stage, determination of the recession speed of the grain-fluid interface only requires knowledge of the fluid density $\rho_i(t)$ at this interface. As widely assumed in the literature

(e.g. Pegler and Wykes, 2020), we consider that $\rho_i(t) = \rho_{\text{sat}}$ at all times. Finally, under the assumption that a sugar grain is falling in fresh water ($\rho = \rho_0$), the recession speed can be computed analytically: it now only depends on the mass transfer coefficient $\overline{k}$ whose evolution with r_p is shown by the red line in figure 4.6a. Although larger grains settle faster thus increasing the advective contribution to mass transfers in equation (4.10) (see the blue line in figure 4.6a), smaller grains have a larger curvature hence the diffusive flux around these grains is more intense (see the dark line in figure 4.6a). These two competing effects lead to a non-monotonic variation of the mass transfer coefficient as the size r_p increases. Consequently, the mass transfer coefficient is larger for smaller grains but its variations are limited.

Yet, the previous sections showed that smaller grains of sugar seem to impart their buoyancy to the fluid faster than larger grains. This faster transfer is actually due to the larger surface area of reaction that is in contact with water when r_p is lower. In fact, in a unit volume of fluid with volume fraction ϕ, the mass of sugar that dissolves per unit time is the integral of equation (4.9) over the surface area of one grain, multiplied by the number of grains in the unit volume. This total mass rate reads

$$\frac{dm_{\text{tot}}}{dt} \propto \underbrace{\frac{\phi}{\frac{4}{3}\pi r_p^3}}_{\text{number of grains per unit volume}} 4\pi r_p^2 \rho_p |\dot{r}_p| \propto \frac{\overline{k}}{r_p} , \tag{4.11}$$

which is valid under the assumption that saturation effects can be neglected (such effects likely depend on the radius r_p since smaller particles are closer to each other). According to this equation, the total mass flux dm_{tot}/dt increases as r_p is lowered (figure 4.6b) due to the surface-to-volume ratio being proportional to r_p^{-1}. The conclusion is consistent with observations: smaller sugar grains impart their buoyancy to water faster. This transfer is an actual transition from a particle-driven and settling-constrained flow to a buoyancy-driven fluid motion, favouring in particular the development of the Rayleigh-Taylor-like instability.

4.5 Onset of the flow: transition from grains to large scales

The previous section established that reducing the size of grains improves local forcings of fluid motions and favours a transition towards a more fluid-like behaviour. Now, what controls the plume formation, and why are some plumes turbulent and others laminar? The present section considers the combined action of the grain size r_p and the mass rate $\dot{m}$ on the densification of the cylindrical sugar-laden layer that develops at early times below the air-water interface, which is the key phenomenon driving the sugary plumes.

4.5.1 Regimes of onset

The initial Rayleigh-Taylor-driven growth is a common observation for the onset of turbulent plumes from a large area source of buoyancy. Figures 4.3, 4.4 and 4.5 in the previous section showed that the initiation of convection critically depends on the size of sugar grains for a fixed

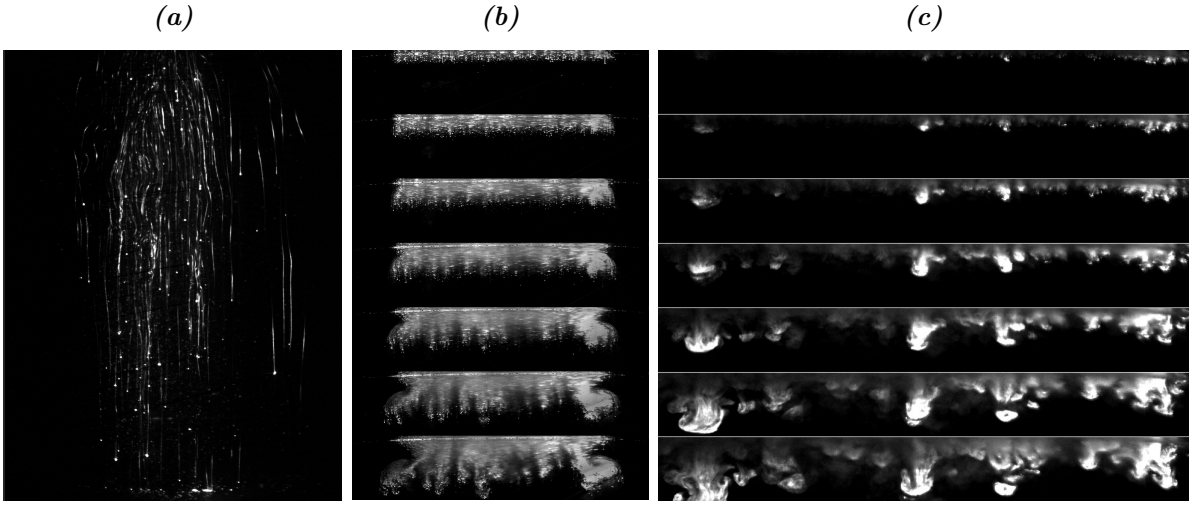

Figure 4.7: *Three regimes of onset of the flow. (a) Regime of pure sedimentation with no visible instability (r_p = 363 μm, $\dot{m}$ = 0.052 g/s; the snapshot is* 22 cm*-large along the horizontal). (b) Transition from an initial regime of pure settling to the development of the Rayleigh-Taylor-like instability (r_p = 101 μm, $\dot{m}$ = 0.115 g/s; the time lapse between snapshots is* 1.2 s *and the snapshots are* 23 cm*-large along the horizontal). (c) Immediate development of sugary mushrooms due to the Rayleigh-Taylor-like instability (r_p = 45 μm, $\dot{m}$ = 0.23 g/s; the time lapse between snapshots is* 0.59 s *and the snapshots are* 16 cm*-large along the horizontal).*

mass rate. A visual inspection of all experiments reveals that the onset of convection falls into one of three main groups, here ordered by decreasing radius:

(G1) grains settle vertically and no Rayleigh-Taylor-like instability is ever observed over the depth of our tank ($r_p \geq 169$ μm, see figure 4.7a); whether the instability could eventually emerge at larger length scales is an open question,

(G2) grains first settle vertically before Rayleigh-Taylor-like mushrooms appear ($80\mu m \leq r_p \leq 101$ μm, see figure 4.7b),

(G3) convection starts immediately with a Rayleigh-Taylor-like instability and no visible phase of grain settling ($r_p \leq 66$ μm, see figure 4.7c).

The key contribution to the transition (G1→G2→G3) is the densification of the initial sugar-laden layer at the top of the tank. At first order, this forcing does not require a distinction of the contributions of sedimentation on one hand and dissolution on the other hand: the Rayleigh-Taylor-like instability is driven by the density contrast across the lower interface of the sugary layer, here corresponding to the Atwood number

$$\mathcal{A} \equiv \frac{\rho_{\text{eff}} - \rho_0}{\rho_{\text{eff}} + \rho_0}, \tag{4.12}$$

where $\rho_{\text{eff}} > \rho_0$ is the effective density that accounts for the total mass of sugar in the top layer. A canonical linear Rayleigh-Taylor instability growing at an interface between two semi-infinite layers of different yet uniform densities, with gravity pointing in the direction of the

lightest layer, and damped by viscosity as in the present case, leads to the selection of a mode of maximum growth rate (Alqatari et al., 2020; Magnani et al., 2021)

$$\sigma_{\max} = \sqrt{\mathcal{A}g k_{\max} + (\nu k_{\max}^2)^2} - \nu k_{\max}^2 \ , \tag{4.13}$$

with wavenumber (Plesset and Whipple, 1974; Mikaelian, 1993; Magnani et al., 2021)

$$k_{\max} = \left(\frac{\mathcal{A}g}{8\nu^2} \right)^{1/3} \ . \tag{4.14}$$

As shown by equation (4.13), the larger the Atwood number i.e. the more concentrated the initial sugary layer, the faster the growth of the instability. The present context slightly differs from the canonical configuration. Because the sugary layer develops just below the water free surface, it may feel the influence of confinement. Alqatari et al. (2020) have shown that the most unstable mode is $k_{\max}$ only when the dense layer is thicker than $2\pi/k_{\max}$. Otherwise, the present confinement stabilises the system and modifies the wavelength of the instability which now scales like the thickness of the sugary layer. Another difference is that the present instability is forced by a dispersed phase rather than a dense fluid. Yet the forcing conditions and the phenomenology are similar, as previously observed in the literature (Kimura, 1988; Climent and Magnaudet, 1999; Mezui et al., 2022; Caballina et al., 2003; Mudde, 2005). An example can be found in the study by Kimura (1988) who injected bubbles at the bottom of a 2D cell ($40 \times 8 \times 2$ cm^3) in experiments. They observed that the positively buoyant bubble-laden layer near the bottom developed a Rayleigh-Taylor-like instability whose mushrooms grew all the faster as bubbles accumulated more in this unstable layer, which is consistent with an increase of the bubble volume fraction in this layer. A quantification of the instability onset from equations (4.12) -(4.14) is given in the next section.

Consider now the transition (G3→G2). Several studies in the literature have focused on the forcing of a Rayleigh-Taylor instability by settling particles in horizontally periodic numerical domains with a suspension of particles overlying a layer of clear fluid (Magnani et al., 2021; Chou and Shao, 2016). They showed that the initial growth rate of the instability is reduced by the settling of particles, all the more so as particles settle faster, in agreement with the linear stability analysis of Burns and Meiburg (2012) in two dimensions. These latter authors showed that during the growth of the particle-laden mushrooms, particles advect vorticity away from the interface which results in a smearing of the vorticity profile at the interface, thus damping the instability all the more efficiently as the settling velocity increases. These observations contribute to the transition (G3→G2) when r_p increases.

Finally, the transition (G2→G1) is due to the impossibility for excessively large grains to force the Rayleigh-Taylor-like instability because sugary mushrooms have not enough time to grow before sugar grains decouple from them. The instability therefore develops if the sugary mushrooms grow faster than particles rain out of them, a criterion that holds for particle-laden Rayleigh-Taylor-like instabilities (Carey, 1997; Jacobs et al., 2015; Lemus et al., 2021) and that is similar to the case of solutal convection (Berhanu et al., 2021) where the onset of convection happens when fluctuations grow faster than the unsteady base state. Thus, of two sugary layers of identical effective density hence identical growth rate $\sigma_{\max}$, the one with larger grains is less prone to destabilise.

4.5.2 Onset through a Rayleigh-Taylor-like instability

We now quantify the onset of the Rayleigh-Taylor-like instability. Despite the non-ideal experimental conditions of grains penetrating through the air-water interface with small yet visible perturbations of this interface during sieving, the core competition between the destabilising buoyancy and the stabilising viscosity captures the essence of the instability. Our first-order estimate is based on the maximum growth rate of the actual Rayleigh-Taylor instability in equation (4.13) with the wavenumber given by equation (4.14). The instability is expected to emerge (Carey, 1997; Jacobs et al., 2015; Lemus et al., 2021) provided that the inverse growth rate $\sigma_{\max}^{-1}$ is comparable to or lower than the settling time over the scale of mushrooms $2\pi/k_{\max}w_s$, i.e.

$$w_s \leq \frac{2\pi\sigma_{\max}}{k_{\max}} \ . \tag{4.15}$$

In the following, we simply call the case of equality the 'marginal stability'[1] at the onset of the flow, which we aim to characterise in the parameter space $(\dot{m}, r_p)$. The effective density of the sugary layer is given by assuming a uniform dilution of the total mass of sugar sieved since the start of the experiment in the sugary layer, whose surface area is πR_{sieve}^2 and whose depth corresponds at first order to the distance travelled by the first grains sieved with constant velocity w_s, so that

$$\rho_{\text{eff}} = \rho_0 + \frac{\dot{m}}{\pi R_{\text{sieve}}^2 w_s}, \tag{4.16}$$

which leads to the expression of the Atwood number

$$\mathcal{A} = \frac{\rho_{\text{eff}} - \rho_0}{\rho_{\text{eff}} + \rho_0} = \left[1 + \frac{2\rho_0 \pi R_{\text{sieve}}^2 w_s}{\dot{m}}\right]^{-1} . \tag{4.17}$$

Equation (4.17) shows that the larger the mass rate the denser the sugary layer and hence the more likely the emergence of an instability; this is due to an increase of the total mass contained in the sugary layer, irrespective of its volume. In addition to this effect, the same consequence holds when the settling velocity reduces, which is now due to a lower height and therefore lower volume of the sugary layer. Finally, a second effect of the settling velocity is that, for an identical Atwood number, a lower settling velocity further favours the growth of the instability because raining out of sugary mushrooms is slower, in agreement with the criterion in equation (4.15).

The solid dark line in figure 4.8 shows the curve of marginal stability in the parameter space $(\dot{m}, r_p)$. The region of instability is shaded below this line, whereas the region above is stable and will not lead to the formation of mushrooms according to equation (4.15). It can be compared with experimental measurements shown as coloured symbols: dark squares are experiments which never lead to the Rayleigh-Taylor-like instability (G1), green circles are experiments with a delayed onset of the instability after a phase of settling (G2), and red diamonds are experiments with immediate formation of mushrooms (G3). The curve of marginal stability

[1] The description is willingly kept simple for the sole onset of the flow. We expect the instability to emerge if it grows faster than the background density evolves due to sedimentation. Even when the criterion (4.15) is not verified, the fluid is unstable, but it evolves slower than the background of settling grains. Thus, the instability may emerge at later times but with a growth rate that is different from equation (4.13).

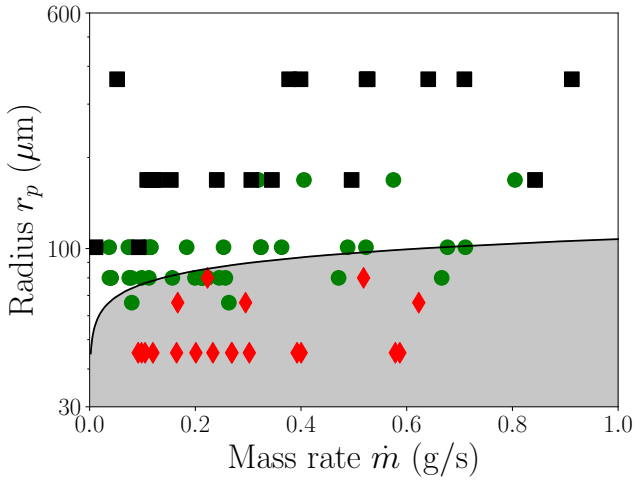

Figure 4.8: *Parameter space $(\dot{m}, r_p)$ grouping experiments according to the phenomenology observed at the onset of convection: ■ experiments of group G1 evidence no instability and particles only settle; ● experiments of group G2 evidence an initial vertical settling of grains before the onset of the Rayleigh-Taylor-like instability; ♦ experiments of group G3 evidence an immediate formation of sugary mushrooms. The solid dark line is the curve of marginal instability from equation (4.15).*

proves consistent: experiments of category (G3) lie in the shaded region. Some experiments of category (G2) lie in this same region near the marginal curve, suggesting that some reduction of the growth rate, either due to settling or to confinement (see the discussion in section 4.5.1), is already active in this region.

Most experiments of group (G2) lie above the marginal curve. Their delayed destabilisation is due to the fact that initially, grains settle too fast for the instability to grow as estimated with equations (4.15)-(4.17). But the estimate (4.17) neglects the fact that the continuous addition of new grains gradually increases the concentration of dissolved sugar since the latter barely moves before the instability onset. As a result, for a constant mass rate and hence a presumably constant volume fraction ϕ, the concentration of dissolved sugar increases in time, hence the effective density increases as well, favouring the emergence of the instability after a phase of settling.

4.5.3 Critical size decoupling from the starting plume

As previously observed in other contexts of two-phase (Caballina et al., 2003) and one-phase starting plumes (see figure 4 in Friedl et al., 1999), the acceleration of our sugary plumes eventually leads them to a phase of propagation with constant velocity. Balancing the leading contributions of inertia and buoyancy, the fluid velocity is expected to scale like the square root of buoyancy multiplied by the typical plume width, at first order given by the radius at injection R_{sieve}, as verified in the literature for bubble plumes (Caballina et al., 2003) and bubble columns (Mezui et al., 2022). From equation (4.16), this constant free-fall velocity reads

$$U_{\text{onset}} = \left[\frac{\rho_{\text{eff}} - \rho_0}{\rho_0} g R_{\text{sieve}}\right]^{1/2} = \left[\frac{\dot{m} g}{\pi R_{\text{sieve}} w_s \rho_0}\right]^{1/2}. \tag{4.18}$$

We are interested in comparing this reference velocity with the settling velocity of our sugar grains under the form of an initial Rouse number

$$\mathcal{R}_0 \equiv \frac{w_s}{U_{\text{onset}}} = \left[\frac{w_s^3 \pi R_{\text{sieve}} \rho_0}{\dot{m} g}\right]^{1/2} . \tag{4.19}$$

The Rouse number $\mathcal{R}_0$ characterises the coupling of sugar grains with the starting plume: grains accompany the starting plume while it sinks when $\mathcal{R}_0 < 1$, whereas grains verifying $\mathcal{R}_0 > 1$ fall ahead of the starting plume because they settle faster than its characteristic velocity. The iso-contour $\mathcal{R}_0 = 1$ is shown as a dashed line in figure 4.9 in the parameter space $(\dot{m}, r_p)$: grains in the range $r_p > 200$ μm are expected to fall ahead of the sugar plume, as consistently observed in our experiments.

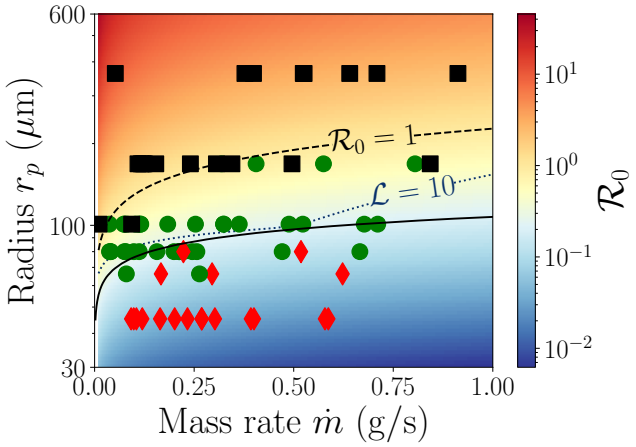

Figure 4.9: *Initial Rouse number in the parameter space $(\dot{m}, r_p)$. The dashed dark line indicates the transition between the grains that settle faster than the starting plume characteristic velocity ($\mathcal{R}_0 > 1$) and those that settle slower ($\mathcal{R}_0 < 1$). The dotted blue line delineates the region of collectivity ($\mathcal{L} < 10$ below) and the region where grains behave individually ($\mathcal{L} > 10$ above). The solid dark line is the curve of marginal stability of the Rayleigh-Taylor-like instability (see figure 4.8).*

Some nuances are neglected in this first order reasoning. As long as the plume has not finished accelerating, its downward velocity is still lower than the estimate U_{onset}, so the actual Rouse number is larger than the estimate $\mathcal{R}_0$. Therefore, grains even slightly smaller than predicted in figure 4.9 might decouple from the starting plume. Note however that grains that lie just above the isocontour $\mathcal{R}_0 = 1$ tend to fall ahead of the plume only temporarily: these grains decelerate due to dissolution while the plume is accelerating, hence the latter catches up with these grains, as already visible in the first three snapshots of figure 4.5.

4.5.4 Collective vs. individual forcing

So far equations (4.16) to (4.19) have been derived from a field theory which, as discussed in section 4.3.2, may poorly describe the behaviour of particles that behave individually when their interparticle distance is larger than a critical threshold. Arguments in section 4.4.1 showed that if particles have an individual behaviour, the Rayleigh-Taylor-like instability may not emerge

even if the effective density of the sugary layer is sufficiently large for a fully fluid sugary layer of identical Atwood number to be unstable to the Rayleigh-Taylor-like instability. Then, is the region of transition from red to dark symbols in figure 4.8 only due to an insufficient Atwood number of the sugary layer, or is it due to a transition from a collective to an individual behaviour of sugar grains that are too decoupled from the flow to produce a fluid-like instability? Answering this question requires to quantify the transition from collective to individual behaviour by defining the critical interparticle distance over which particles are capable of interacting. This critical distance $l_{\text{inter,c}}$ is sought in the structure of the flow produced in the vicinity of an individual particle settling in a quiescent fluid with velocity w_s, namely the radius of disturbance of the flow due to the presence of a particle having a differential motion compared to the fluid. This length scale is computed as the distance from the particle where advection and diffusion balance out; for low particulate Reynolds numbers it is the inertial screening length ν/w_s (Subramanian and Koch, 2008; Guazzelli and Morris, 2011; Pignatel et al., 2011) whereas for small yet finite particulate Reynolds numbers it corresponds to the particle radius r_p (Koch, 1993; Daniel et al., 2009). For our largest particle Reynolds numbers, particles may have laminar wakes whose typical size is also given by the particle size r_p. Therefore, the critical interparticle distance is estimated as

$$\forall r_p,\ l_{\text{inter,c}} = \max\left\{\frac{\nu}{w_s}, r_p\right\}, \tag{4.20}$$

and particles are expected to behave individually if their interparticle distance is larger than $l_{\text{inter,c}}$, typically by a factor $O(10)$ to be conservative. The estimate of this threshold has been validated in previous experiments (Tsuji et al., 1982) where spheres of large particle Reynolds numbers ($Re_p \sim 10^2 - 10^3$) could interact hydrodynamically up until $l_{\text{inter}} \sim 10 r_p$, in agreement with the estimate $10 l_{\text{inter,c}}$ for this regime of large particle Reynolds numbers.

Now through collectivity, the densification of the sugary layer is again a key phenomenon controlling the onset of convection. From the expression of the effective volume fraction

$$\phi_{\text{eff}} = \frac{\dot{m}}{\pi R_{\text{sieve}}^2 w_s \rho_p}, \tag{4.21}$$

equations (4.5) and (4.21) can be combined to estimate the interparticle distance. Then, the dimensionless interparticle distance

$$\mathcal{L} = \frac{l_{\text{inter}}}{l_{\text{inter,c}}}. \tag{4.22}$$

is calculated in the whole parameter space to quantify collective ($\mathcal{L} \ll 10$) and invidual ($\mathcal{L} \gg 10$) behaviours. Figure 4.9 shows that experiments of group (G2) lie in the region of transition, typically in the range $\mathcal{L} \simeq 5 - 15$ which includes the curve of marginal stability for the Rayleigh-Taylor instability. Therefore, the transition from (G1) to (G3) and the transition from individuality to collectivity overlap in the parameter space, which makes us unable to disentangle them as the radius is decreased for a fixed mass flux.

Of course the previous computation of $\mathcal{L}$ is a crude estimate, especially as it neglects the fact that sugar grains are always dissolving in the sugary layer, hence their interparticle distance may vary little but their critical length scale of interaction $l_{\text{inter,c}}$ is expected to vary as their

size decreases, in a non-monotonic way (with decreasing r_p, the distance $l_{\text{inter,c}}$ decreases as long as $Re_p > 1$ and then increases if $Re_p < 1$). Accounting for this evolution in time and space then requires to model grains that are sieved at different times, which cross different solute concentrations along their fall, experience different fluid velocities as the plume builds up velocity during the transient, and therefore reach a certain depth with different sizes and relative motion. This is beyond the scope of this Chapter, and additional discussions can be found in Chapter 5 and in the Conclusion and future lines of work; the present calculations essentially guide the interpretations of measurements in the next sections.

4.5.5 Transition to large scales

Figure 4.9 shows that green circles (i.e. experiments for which the Rayleigh-Taylor-like instability emerges after a phase of settling) are delineated by the solid dark curve of marginal stability for the Rayleigh-Taylor-like instability, and by the dashed curve of equation $\mathcal{R}_0 = 1$. They also lie in the region of transition from individual to collective behaviour[2]. Beyond confirming the role of the local forcings in the transition from particle-driven to fluid-like behaviour, it highlights their role in the transition from small to large hydrodynamical structures, in two different ways.

Consider first a fixed mass rate while the size of grains is reduced. The action of drag is longer-lasting because grains drift slower. Additionnally, reducing the size of grains reduces the inter-grain distance, hence their efficiency to drag the interstitial fluid is enhanced by collectivity. That is why reducing the grain size favours a transition from a localised grain-scale forcing to a volumetric forcing, as shown in figure 4.10a. This space-time diagram is a stack of the horizontal profiles of light intensity recorded at the front of the sugary layer when being tracked in time and depth (see explanations in appendix 4.B.1). The top of the graph shows tiny grain-scale filaments that coalesce and eventually organise as one large macroscale. This coarsening is initially due to the fact that many length scales are unstable when the sugary layer grows, including large ones of small growth rate whose emergence is therefore delayed; eventually, the coarsening is due to the formation of the lazy plume in which small grains are advected.

Consider now some large grains ($\mathcal{R}_0 > 1$) sieved with a low mass rate. The first grains settle vertically in almost perfectly still water (see how localised the sugary wakes are in figures 4.10b-4.10c). From an Eulerian viewpoint in the fluid, the forcing imposed by their drag is only temporary and random in space. The forcing imposed by their sugary wake is also random in space, but it lasts in time. As sugary lamellae diffuse towards one another, their buoyancy decreases (thus reducing the buoyancy forcing) but the inter-lamellae spacing decreases (thus favouring a forcing at a larger scale). That is why after a long delay, slow fluid motions set in even when grains are large and the mass rate is low – and also because new wakes are stochastically deposited as long as sieving keeps going. If the mass rate is enhanced, the number of lamellae deposited per unit time increases, thus reducing the inter-lamellae spacing and the delay before the interstitial fluid starts moving. This transition from an isolated to a volumetric

[2]The fact that all transitions are close in the parameter space $(\dot{m}, r_p)$ is due to the values of the experimental parameters g, R_{sieve}, ν and r_p and $\dot{m}$. For example, figure 4.9 shows that larger mass fluxes would separate the solid dark line of stability from the dotted blue line of isovalue $\mathcal{L} = 10$.

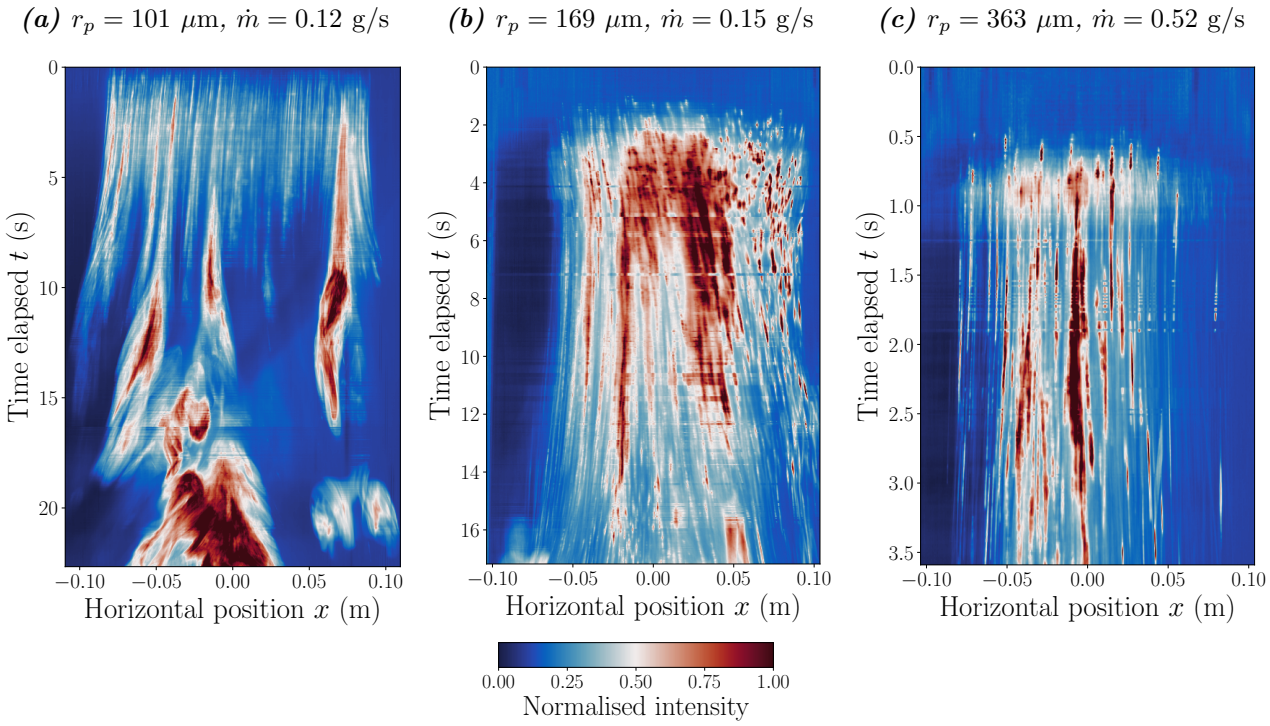

Figure 4.10: *When tracking the front position of a plume of dyed sugar during the transient, at any time, the profile of light intensity can be extracted at the plume front. The figures (a) to (c) are space-time diagrams that stack such horizontal profiles in time from the start of an experiment (at the top of the diagrams) to the end of the transient (at the bottom of the diagrams). Blue regions are devoid of sugar, while red regions are concentrated in solid or dissolved sugar. See Appendix 4.B.1 for details about the processing. Radii and mass rates are specified above each diagram.*

forcing favours again a transition from the small grain scale to larger hydrodynamical structures. In our experiments, this macroscopic motion happens after a long time lag, after several grains have hit the bottom of the tank (see figure 4.3), so we effectively observe a transition in time from small-scale wakes that are distributed in the tank but which move individually, to a large-scale plume formed by the combination of lamellae. Note that dissolution is not key to this transition, which we recover when sieving glass spheres instead of sugar grains, and which has previously been observed in bubble-laden flows (Mazzitelli and Lohse, 2009).

4.6 Characterisation of the flow

4.6.1 Overview with dyed sugar

To provide a synthetic view of the characteristic features of the flow when varying parameters $(\dot{m}, r_p)$, figure 4.11 presents space-time diagrams of the light intensity recorded during the fall of dyed sugar. These profiles are obtained by a horizontal average of the light intensity captured by the camera at different times, before stacking them as Hovmoller diagrams. For sufficiently small sizes of grains, all diagrams evidence a concave downward sinking of the

buoyant material due to the growth of the sugary layer, whose front position is anticipated to increase quadratically in time for the non-linear growth of a Rayleigh-Taylor instability (Magnani et al., 2021; Boffetta and Mazzino, 2017). Then, the concavity evens out around a depth $z = 0.1$ m and leads to a downward fall with apparent constant velocity. For a given size of small grains, increasing the mass rate shortens the time required for the front of the buoyant material to reach the bottom of tank (compare the abscissas of figures 4.11b and 4.11c). By contrast, the transient plunging of sugar in experiments having $r_p = 363$ μm shows no sharp front (figure 4.12a). This observation is due to the fact that sugar does not accumulate in the top sugary layer when sugar grains are too large. Consequently, large grains fall in isolation, no bright concentrated region falls as a whole, so no sharp front of well-defined trajectory is visible in the space-time diagrams.

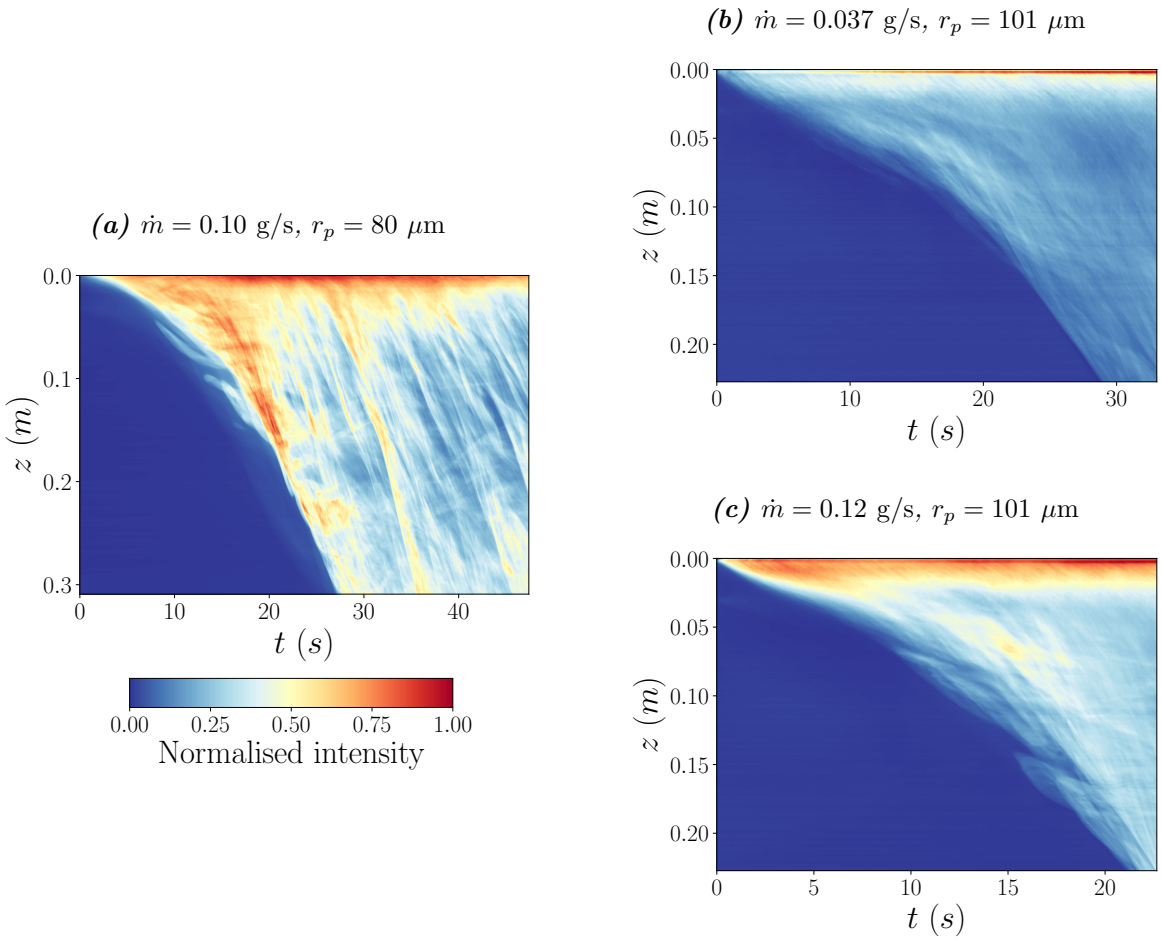

Figure 4.11: *Space-time diagrams of the horizontally averaged light intensity recorded during the fall of small grains of dyed sugar. The mass rate and grain size are specified above each diagram. Note the difference of ordinates for each diagram. The colorbar is common for all graphs.*

The texture of the space-time diagrams provides additional information. In figure 4.11a for $r_p = 80$ μm, one can follow the detachment and downward sinking of some successive turbulent puffs of buoyant material (grains or solute) which accelerate at depths $z \leq 0.1$ m and are

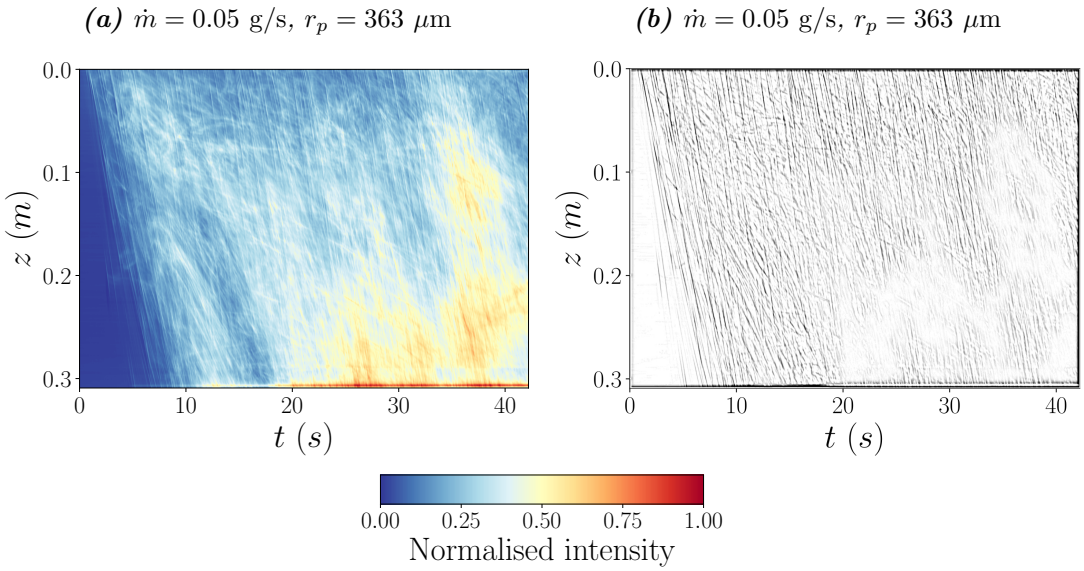

Figure 4.12: *(a) Space-time diagram of the horizontally averaged light intensity recorded during the fall of large grains of dyed sugar. The mass rate and grain size are specified above the diagram. The small-scale structures of this diagram are highlighted in (b) (see the text for processing details).*

advected with constant velocity at larger depths. Conversely for $r_p = 101$ μm (figures 4.11b and 4.11c), the diagrams are smooth with no puffs since the plumes are more laminar.

Because large grains decouple from fluid motions, different structures must be distinguished in figure 4.12a. To highlight the trajectories of solid grains, a Gaussian filter of 2-pixels-wide standard deviation has been applied three times to figure 4.12a, and then subtracted to get figure 4.12b. The dark steep stripes reveal the rapid fall of large grains. Their straightness implies that dissolution little affects their settling velocity over the distance ~ 0.3 m, and the constant slope of the stripes from the start to the end of the experiment shows that fluid motions have little influence on the grains (see section 4.5.3). Figure 4.12a also contains blurred shapes of vertical extension ~ 0.1 m that fall in the tank at much lower velocity than the large grains. These large-scale structures correspond to collections of wakes of sugar that gradually fall coherently due to the continuous drag and deposition of new wakes by the falling grains. These fluid motions are slow and delayed compared to the fast fall of sugar grains.

These observations prefigure a net contrast between the fluid velocities and the fall velocity of sugar grains when r_p is large. The following sections present results from experiments performed with ordinary white sugar detected by the camera with a green filter, while the fluid motions are quantified by PIV thanks to the camera with an orange filter (see the setup in figures 4.1c and 4.2). The downward propagation of fluid motions during the transient is first described before analysing the quasi-steady regime that ensues.

4.6.2 Top-down propagation of fluid motions in the transient

This section focuses on the emergence of the flow during the transient: except when $r_p = 363$ μm, it is characterised by the propagation of fluid motions that emerge below the free surface and which propagate downward in the tank. We distinguish the propagation of these

fluid motions from the sinking of sugar grains or solute. Note our convention of notations: v is reserved for a fluid velocity measured from PIV, whether it be horizontal v_x or vertical v_z; a time derivative $\dot{z}$ of the z-position is reserved for Lagrangian velocities when tracking the propagation of a structure, whether it be solid grains, dissolved sugar, or a region of fluid motions.

Figure 4.13 shows the time evolution of vertical profiles of the horizontally averaged vertical velocity magnitude $\langle|v_z|\rangle_x$ for three different radii. When sieving starts at $t = 0$, dark blue levels are due to the absence of any initial fluid motion; after a certain delay, fluid motions appear at the top of the tank, they gradually intensify, and sink downward until reaching the bottom of the field of view. Due to the non-penetration of the fluid at the top free surface and the bottom wall, vertical velocities vanish near these boundaries.

Figures 4.13a to 4.13c immediately reveal the decrease of the typical fluid velocities during the transient and in the quasi-steady regime when r_p increases. This observation is consistent with the dilution of the buoyant material when w_s increases (equations (4.16) and (4.18)), with the lower efficiency of the three local forcings as r_p increases (section 4.4) and with the favoured decoupling of larger grains from the starting plume (section 4.5.3). Time fluctuations in figure 4.13a are due to the turbulent nature of the plume when $r_p = 45$ μm, by contrast with the more laminar plumes when $r_p \geq 169$ μm in figures 4.13b and 4.13c.

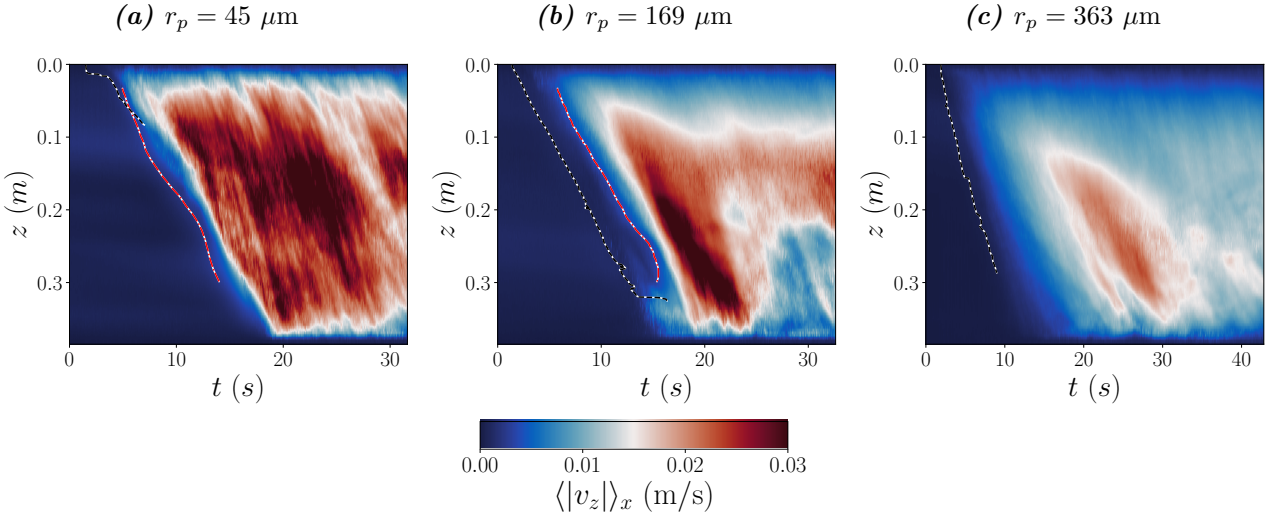

Figure 4.13: *Space-time diagrams of vertical profiles of the horizontally averaged magnitude of the vertical fluid velocity $\langle|v_z|\rangle_x$. From left to right, the three panels show the influence of increasing the particle size in three experiments of comparable mass rates, namely (a) $\dot{m} = 0.59$ g/s, (b) $\dot{m} = 0.57$ g/s, (c) $\dot{m} = 0.64$ g/s. The colorbar is common for the three graphs. The black and white dotted curves show the maximum depth where solid grains are still visible. The red and white dotted lines show the convergence of isocontours of the space-time diagrams.*

The influence of the mass rate on the transient sinking of the flow is visible in figure 4.14 for $r_p = 101$ μm and $r_p = 169$ μm. Both cases confirm that the flow is more vigorous and the transient shorter as the mass rate increases. All six diagrams evidence that a vigorous transient almost systematically develops (see the large fluid velocities in figures 4.14a to 4.14f

respectively before t is equal to 35s, 30s, 25s, 35s, 30s, 30s), and then relaxes to a somewhat quieter quasi-steady regime.

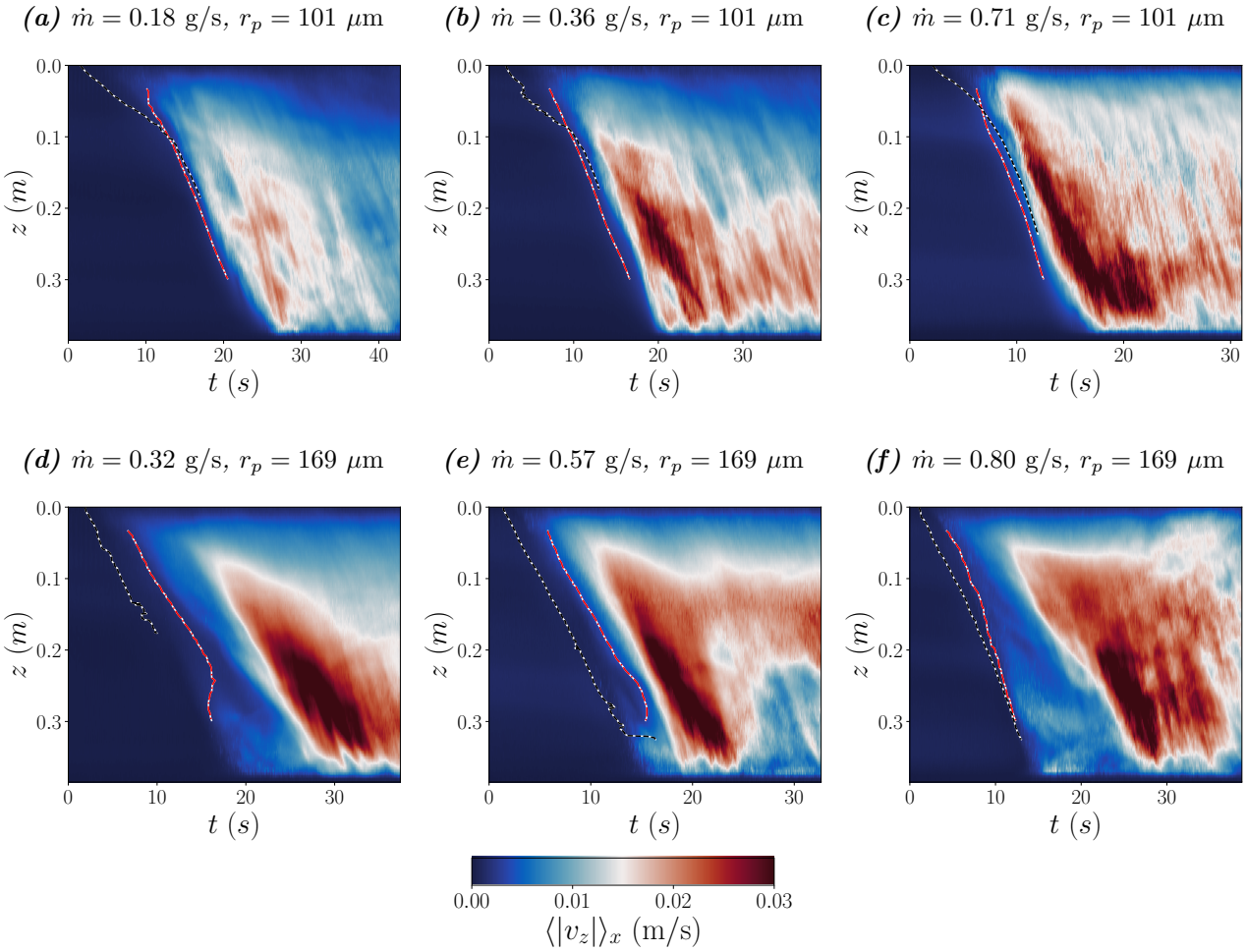

Figure 4.14: *Space-time diagrams of vertical profiles of the horizontally-averaged magnitude of the vertical fluid velocity $\langle |v_z| \rangle_x$. Experiments in figures (a) to (c) correspond to increasing mass rates for $r_p = 101$ μm. Experiments in figures (d) to (e) correspond to increasing mass rates for $r_p = 169$ μm. The colorbar is common for all diagrams. See the caption of figure 4.13 for the dashed curves.*

4.6.2.1 Propagation of the plume front

The existence of a violent transient before a quasi-steady regime has already been observed in experiments of inert particles continuously sieved in water (Zürner et al., 2023), and it is reminiscent of *downbursts* in atmospheric flows (e.g. Srivastava, 1985, 1987). These studies observed that the fluid motions initially developped through the propagation of a front. This observation is recovered in the present experiments for sufficiently small grains (figures 4.11, 4.13a and 4.14a-4.14c). However, fluid motions propagate less and less as a front as the grains decouple more from the starting plume due to a large Rouse number $\mathcal{R}_0 \gg 1$ (figures 4.12 and 4.14d-4.14f).

To be quantitative, we define the front of the downward-propagating fluid motions as the curve along which different iso-contours of velocity converge in the space-time diagrams of $\langle |v_z| \rangle_x$ (see Appendix 4.B.2 for more details), as shown by the red and white dash-dotted lines in figures 4.13 and 4.14. We want to compare this front position to the maximum depth sugar where grains complete their dissolution. To this end, the same procedure is implemented on Hovmoller diagrams of the light intensity visualised when filming the sugar grains (photographs taken by the camera of green filter). The resulting black and white dotted curves in figures 4.13 and 4.14 correspond to the front of the *precipitation layer* which is the zone where sugar grains are still visible before complete dissolution.

In figures 4.14a-4.14c, the little time lag between the front of the precipitation layer (black and white dashed line) and the front of fluid motions (red and white dash-dotted line) is due to small grains falling together with the plume front. Conversely, a time lag appears when sieving large grains: grains fall before the emergence of fluid motions (see figures 4.14d-4.14f). This time lag is a measure of the delayed onset of fluid motions that require an accumulation of stochastic forcings of several grains and the deposition of several sugary wakes before a plume develops. This delay is maximum for the largest grains, and no front of fluid motions can be defined due to the absence of a proper convergence of the iso-contours.

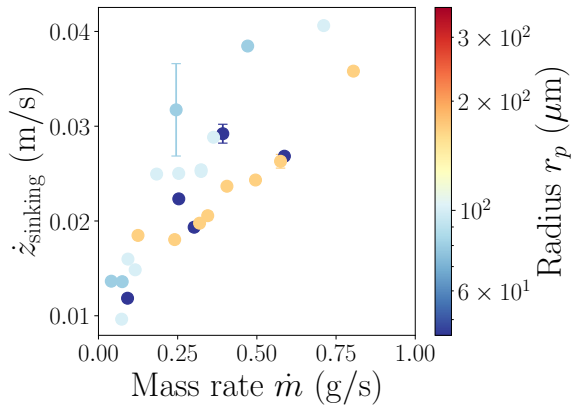

Figure 4.15: *Average sinking velocity of the front of the starting plume for all experiments where a front of fluid motions can be defined ($r_p \leq 169$ μm).*

The red and white curves have been computed for all experiments and we observe that the sinking front always propagates with an approximately constant velocity after a few centimeters below the region of flow convergence and acceleration near the free surface (see figures 4.36a-4.36c in Appendix 4.B.2). An affine law is fitted on each of these trajectories; its slope provides the constant propagation velocity $\dot{z}_{\text{sinking}}$ of the front in figure 4.15. The latter confirms that the sinking is faster when the mass rate increases, and shows little influence of the particle size.

4.6.2.2 Time before the quasi-steady regime

Figure 4.15 suggests that the duration of the transient is essentially controlled by the mass rate. To confirm it, we search for a definition of the time t_{QS} elapsed before the quasi-steady regime is reached. The quasi-steadiness of the velocity field can be assessed from the PDF of the vertical fluid velocities as shown in figure 4.16. The ultimately invariant shape of the PDF

is one possible criterion for the time of quasi-steadiness (see the horizontal dashed line). Yet, a close inspection of experiments shows that this criterion is accurate only at large mass rates, probably because the PDF integrates so much information in the laser sheet that it can reach steadiness before the front of the sugary plume hits the bottom of the tank. Conversely when the mass rate is low, the time when the plume reaches the bottom wall is a good estimate of the end of the transient, as assessed from the evolution of the average kinetic energy within the plume (not shown here). This time is defined with no ambiguity by visualising large sugar grains hitting the bottom wall, or by visualising changes in the refractive index due to the presence of density gradients once the front of the plume reaches the reflection of the laser sheet on the bottom wall. Then, we adopt a conservative definition of t_{QS}: it is the maximum between the time of quasi-steadiness of the PDF of vertical fluid velocities, and the time for the plume to hit the bottom wall.

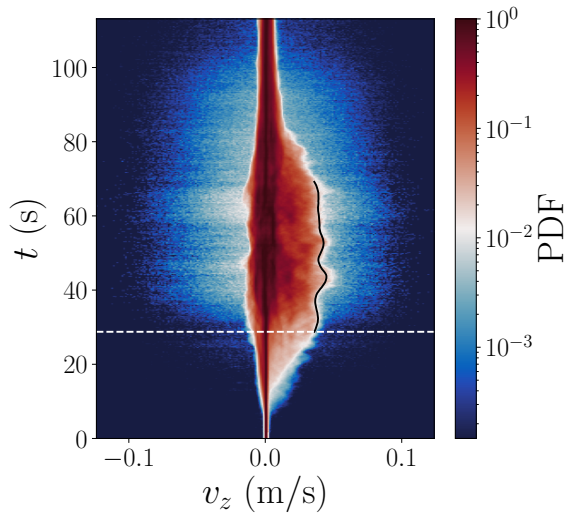

Figure 4.16: *Probability Density Function (PDF) of vertical fluid velocities v_z in the laser sheet, at each time from the start of an experiment (bottom of the diagram) to the end (top of the diagram). For this example, $r_p = 45$ μm and $\dot{m} = 0.09$ g/s. The horizontal dashed line corresponds to the time when the PDF reaches quasi-steadiness (for details about the dark line and about processing, see Appendix 4.B.3).*

Figure 4.17a confirms that the duration of the transient is essentially controlled by the mass rate. However, larger grains lead to a larger time lag between their fall and the downward propagation of the starting plume. This is shown in figure 4.17b which compares t_{QS} with the characteristic time of sedimentation over the height of the tank. When grains are large ($r_p \geq 169$ μm), steadiness is reached *after* the first grains have hit the bottom of the tank. Conversely, the plume enables small grains to reach the bottom of the tank before the sedimentation timescale since $t_{\mathrm{QS}} < H_{\mathrm{tank}}/w_s$.

The relevance of the timescale t_{QS} is also confirmed by figure 4.17c since the time elapsed before the vertical kinetic energy becomes maximum (at the end of the violent transient) is approximately equal to t_{QS} with an additional shift of about 3 s, leading to a maximum discrepancy of 40% between the two timescales. The maximum vertical kinetic energy $E_{\mathrm{kz,max}} = \max(E_{\mathrm{kz}})$ is shown in figure 4.17d where we observe that this energy expectedly increases with the mass

rate. More importantly, we note that the intensity of the 'downburst-like' transient is considerably reduced for the largest grains, confirming their slow and inefficient forcing of fluid motions.

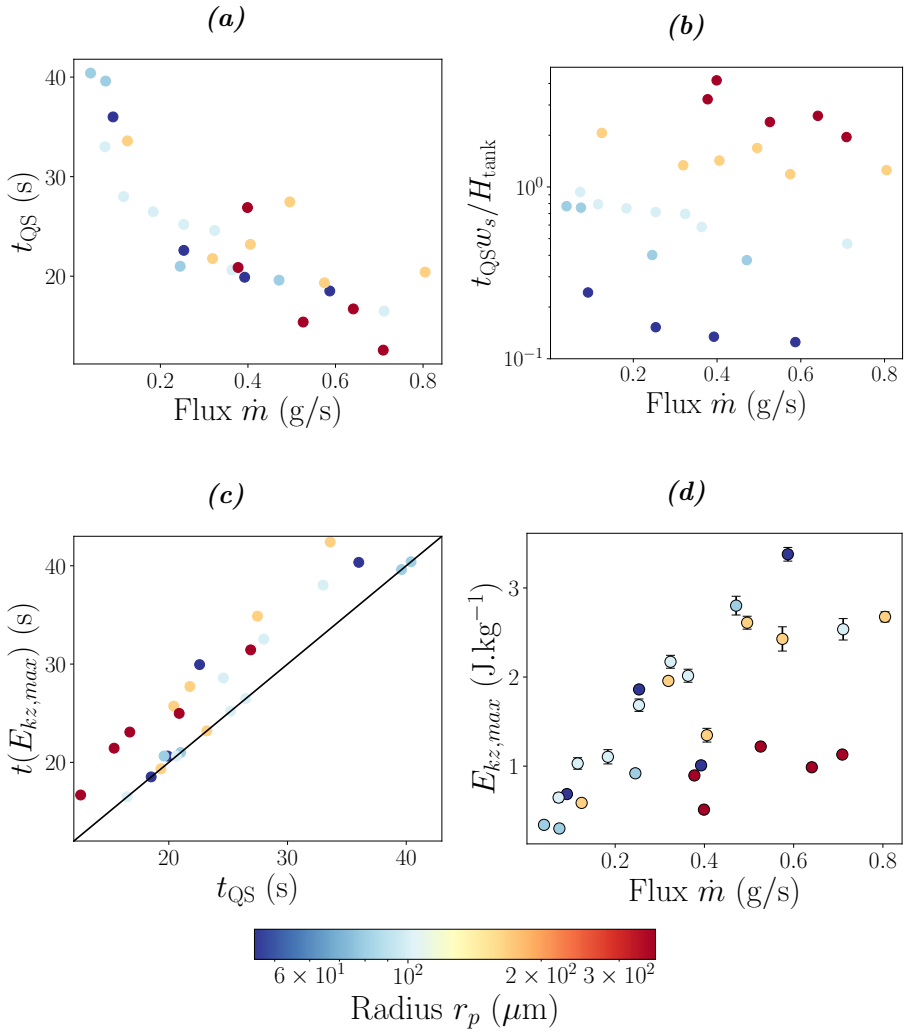

Figure 4.17: *Characterisation of the end of the transient. (a) Time elapsed before the quasi-steady regime is reached, and (b) is normalised using the sedimentation timescale H_{tank}/w_s over the height of the tank H_{tank}. (c) Comparison of the timescale t_{QS} with the time elapsed before the vertical kinetic energy is maximum. The solid dark line is the first bisector. (d) Maximum vertical kinetic energy. The colorbar is common for all figures.*

4.6.3 Quasi-steady flow

This section focuses on the quasi-steady flow. Quantities are now time-independent because data are averaged in time. We focus on the flow inside the central plume, whose typical structure is shown with an example in figure 4.18a. The plume is the region that concentrates downward fluid velocities near the centre of the tank. To get rid of the influence of the upward

recirculations, the plume centreline $x_{\mathrm{c,plume}}(z)$ is defined at all heights as the centroid of the downward fluid velocities $\tilde{v}_z = \max(v_z, 0)$ along the horizontal direction (see the thick white line in figure 4.18a). Then, the plume radius is defined as a weighted standard deviation with respect to the plume centreline

$$\sigma_{\mathrm{x,plume}}(z) = \gamma \sqrt{\frac{\int \tilde{v}_z (x - x_{\mathrm{c,plume}})^2 dx}{\int \tilde{v}_z dx}}, \tag{4.23}$$

with γ a constant of order unity. In our experiments we empirically set $\gamma = 3/2$ as a compromise for the plume radius to include most of the downward fluid motions without extending as far as the regions of recirculations (see the black and white dashed lines in figure 4.18a). The plume is defined at all heights as the region where $|x - x_{\mathrm{c,plume}}| \leq \sigma_{\mathrm{x,plume}}(z)$. Note that in all our experiments, we have found that the plume width barely varies with depth: it slightly fluctuates around a constant value, as visible in figure 4.18b.

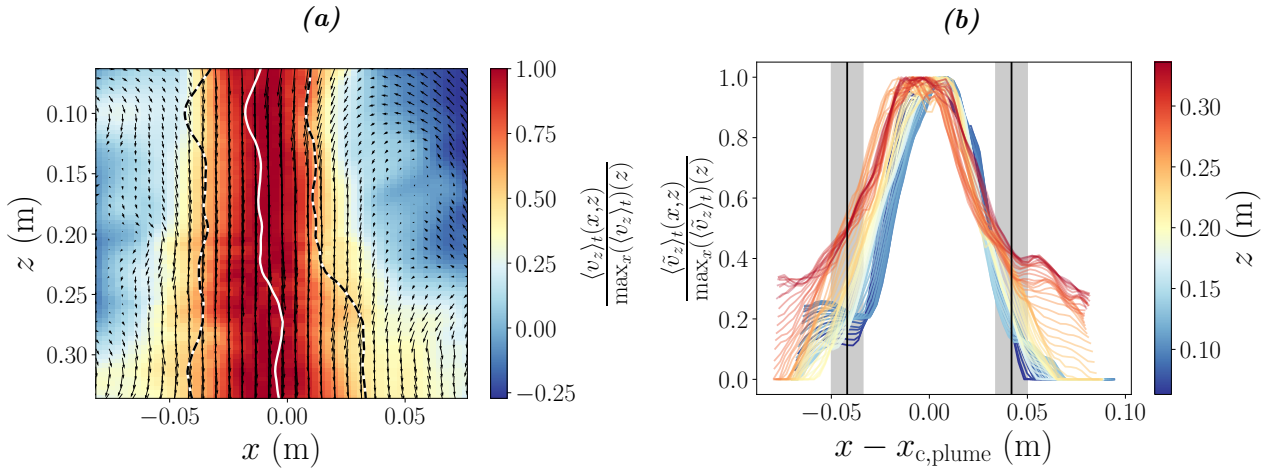

Figure 4.18: *Plume structure for an experiment of properties $r_p = 45$ µm, $\dot{m} = 0.09$ g/s. (a) Time-averaged plume structure during the quasi-steady regime. The time-averaged vertical fluid velocities $\langle v_z \rangle_t$ are normalised by the maximum fluid velocity at every height z. The top convergence and bottom divergence have been cropped to focus on the region of the plume that is least influenced by the boundaries. (b) Superimposition of the profiles of normalised time-averaged positive vertical velocity $\tilde{v}_z = \max(v_z, 0)$ at each depth. The solid dark lines show the average edges $\langle x - x_{\mathrm{c,plume}} \pm \sigma_{\mathrm{x,plume}} \rangle_z$ of the plume, and shaded regions extend at a distance of 1 standard deviation on each side of these averages.*

The vertical velocity is averaged over the whole plume and results are shown for all experiments in figure 4.19. Scattering is due to turbulence in the flow and to the sensitivity of the plume to the recirculations that tend to constrain the plume orientation and deflect it from the vertical. Nevertheless, measurements show clear trends: fluid motions are more vigorous when the mass rate is larger, and conversely tend to weaken as the grain size increases. This is consistent with previous sections (e.g. figure 4.13), and in particular with the analysis of the onset of the flow. However, the velocity U_{onset} (4.18) is not an appropriate estimate for

the plume velocity because it depends excessively on the grain size: $U_{\text{onset}} \propto w_s^{-1/2}$ which gets infinitely large for vanishingly small grains. This inconsistency originates from the assumption that the cylindrical sugar-laden layer dilutes in a volume growing with a velocity w_s, which only holds *before* fluid motions appear. Afterwards, fluid motions dilute grains and dissolved sugar by advecting them away from the free surface; this reduces both the plume buoyancy and the fluid inertia, which we assume to be in balance in the quasi-steady regime.

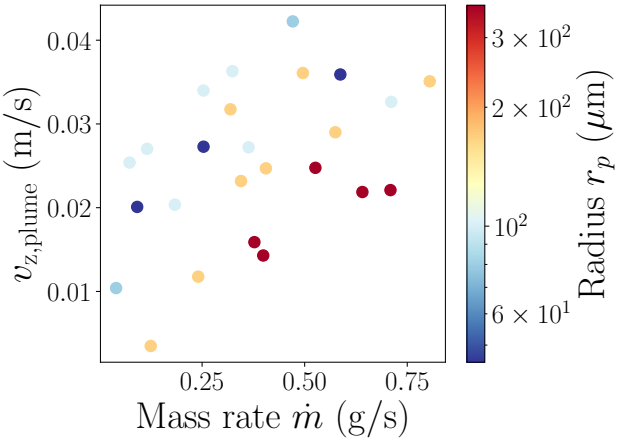

Figure 4.19: *Average vertical velocity in the plume.*

To refine our estimate of the plume velocity, let us denote U_{plume} the constant velocity that is expected in the plume by balancing the fluid inertia and the plume effective buoyancy. Assume that the radius of the plume is constant and equal to R_{sieve} as a first order estimate. During any time lapse Δt, the mass $\dot{m}\Delta t$ that is sieved dilutes in a volume of plume $\pi R_{\text{sieve}}^2 (U_{\text{plume}} + w_s)\Delta t$ due to the combined transport of sugar by the settling of grains and the advection by the flow. Note that we neglect the side fluxes associated with the global recirculation. Therefore, the effective density is now expected to scale as

$$\rho_{\text{eff,QS}} = \rho_0 + \frac{\dot{m}}{\pi R_{\text{sieve}}^2 (U_{\text{plume}} + w_s)} \ . \tag{4.24}$$

Following the reasoning of section 4.5.3, equation (4.18) now reads

$$U_{\text{plume}} = \left[\frac{\rho_{\text{eff,QS}} - \rho_0}{\rho_0} g R_{\text{sieve}} \right]^{1/2} = \left[\frac{\dot{m} g}{\pi R_{\text{sieve}} (U_{\text{plume}} + w_s) \rho_0} \right]^{1/2} \ . \tag{4.25}$$

Terms can be recast in the previous equation and we have to solve for $U_{\text{plume}}(\dot{m}, w_s)$ in the following cubic equation

$$U_{\text{plume}}^3 + U_{\text{plume}}^2 w_s = \frac{\dot{m} g}{\pi R_{\text{sieve}} \rho_0} \ . \tag{4.26}$$

The two asymptotes are informative. When the settling velocity is very large compared to the plume velocity, only the term of leading order $U_{\text{plume}}^2 w_s$ is considered on the left-hand

side of equation (4.26) so we recover the expression of U_{onset} in equation (4.18). In the limit of vanishing settling velocities, grains are so small that they behave as tracers, so the fluid velocity U_{tracers} should be independent of w_s; it is indeed the case when simplifying equation (4.26) for $w_s \ll U_{\text{plume}}$, which yields

$$U_{\text{tracers}} = \left(\frac{\dot{m} g}{\pi R_{\text{sieve}} \rho_0} \right)^{1/3} . \tag{4.27}$$

Equation (4.27) is the typical velocity that can be expected from the sole knowledge of the plume buoyancy flux and the typical radius at the section of injection (Friedl et al., 1999; Caballina et al., 2003). Since U_{tracers} is independent of the particle size, it solves the problem of the divergence of U_{onset} in the limit of vanishing settling velocities.

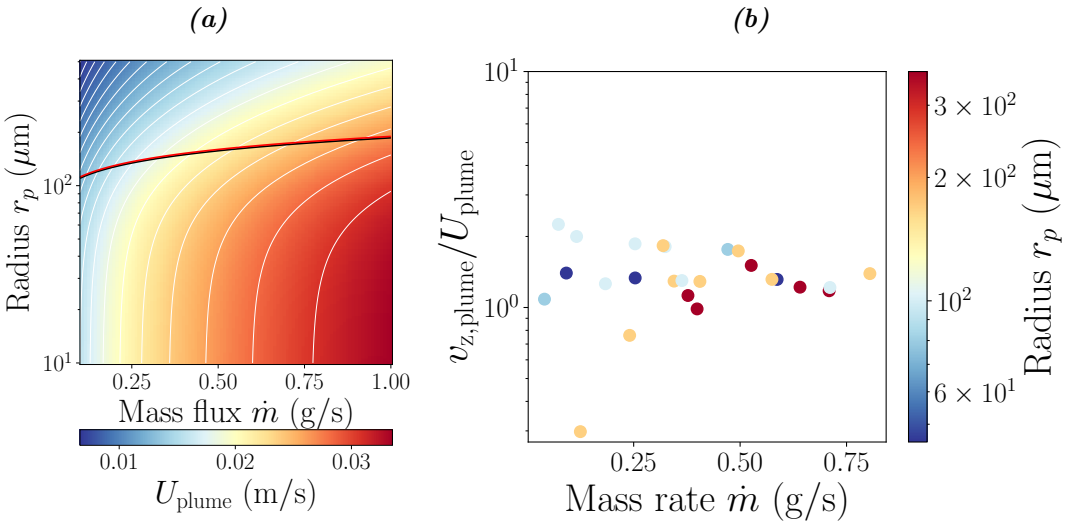

Figure 4.20: *(a) Evolution of the characteristic plume velocity U_{plume} in the parameter space. White lines are logarithmically equispaced isocontours. The red line corresponds to the isovalue $w_s/U_{\text{plume}} = 1$, and the dark line corresponds to the isovalue $w_s/U_{\text{onset}} = 1$. (b) Measurements of the average plume velocity normalised by U_{plume}.*

For all experiments, the exact real root of equation (4.26) is found using the library Numpy in Python, and results are shown in figure 4.20a. The values of U_{plume} are consistent with the fluid velocities measured in experiments and evidence the expected trends: they increase as sugar grains are smaller and as the mass flux increases. The velocity U_{plume} depends less and less on r_p as the grain size vanishes, as expected from the expression of U_{tracers} in equation (4.27). Although U_{onset} is generally different from U_{plume}, the isovalues $w_s/U_{\text{plume}} = 1$ (red solid line) and $w_s/U_{\text{onset}} = 1$ (dark solid line) are very close; this means the critical grain size decoupling from the fluid motions during the quasi-steady regime is extremely close to the critical size that decouples from the starting plume as estimated in section 4.5.3 with U_{onset} instead of U_{plume}.

The accuracy of the prediction U_{plume} is confirmed by rescaling the measurements of the plume velocities in figure 4.20b. All data points lie near unity, with only a few measurements

that depart from unity by a factor ~ 2. This good agreement raises a question: In the quasi-steady regime, once the flow has developed in the plume, could it be that the specificities of small versus large grains average out, since we observe that they have little influence on the average plume velocity? Indeed, fluid velocities are essentially controlled by the balance between the inertia and the buoyancy which dilutes in the downward stream. The question remains open, but note that this last observation may only hold for the *average* downward plume velocity, since previous sections showed that discrepancies between small and large grains do remain in the quasi-steady regime, in particular the turbulent nature of the flow when r_p is small, compared to the laminar nature of the flow when r_p is large.

4.7 Precipitation layer: coupling between grains and the flow

The present section focuses on the motion of the solid grains to analyse their coupling with the fluid motions, firstly during the transient growth of the precipitation layer (abbreviated PL in subscripts, corresponding to the region of the flow where solid grains are present), and secondly in the quasi-steady regime. The experimental data analysed in this section are obtained with ordinary white sugar (setups in figures 4.1a and 4.1c).

4.7.1 Transient sinking of sugar grains

(a) $\dot{m} = 0.20$ g/s

(b) $\dot{m} = 0.59$ g/s

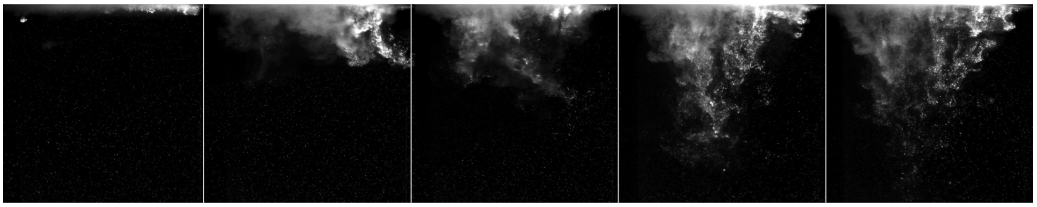

Figure 4.21: *Snapshots of the precipitation layer with an identical grain size* $r_p = 45$ μm. *The mass rate increases from (a) to (b) (see captions above each subfigure). Intervals between snapshots are (a)* $\Delta t = 4$ s, *(b)* $\Delta t = 3$ s, *and the width of every snapshot is (a)* 16 cm *and (b)* 18 cm.

The evolution of the precipitation layer for small ($r_p = 45$ μm), medium ($r_p = 101$ μm) and large ($r_p = 169$ μm) grains is illustrated respectively in figures 4.21, 4.22 and 4.23. The successive snapshots in figure 4.21 show that during the transient, the first sugar grains that fall in the tank propagate downward in quiescent water (first snapshot of figures 4.21a-4.21b).

(a) $\dot{m} = 0.10$ g/s

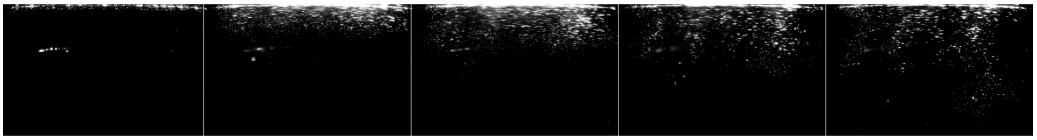

(b) $\dot{m} = 0.71$ g/s

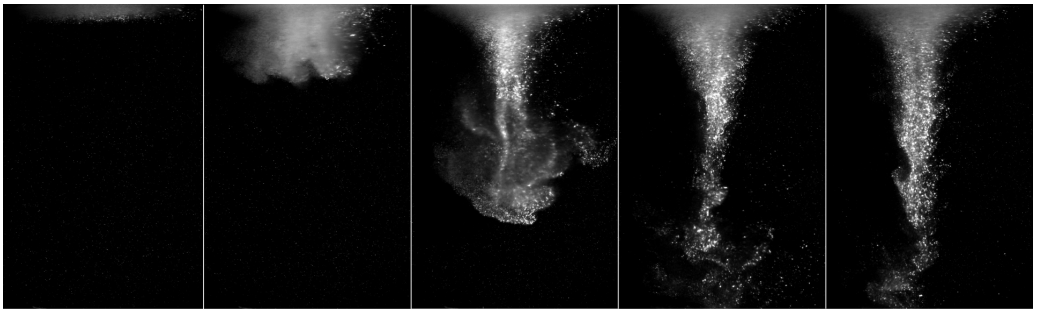

Figure 4.22: *Snapshots of the precipitation with an identical grain size* $r_p = 101$ μm. *The mass rate increases from (a) to (b) (see captions above each subfigure). Intervals between snapshots are (a)* $\Delta t = 3$ s, *(b)* $\Delta t = 4$ s, *and the width of every snapshot is* 17 cm *for (a) and (b).*

(a) $\dot{m} = 0.21$ g/s

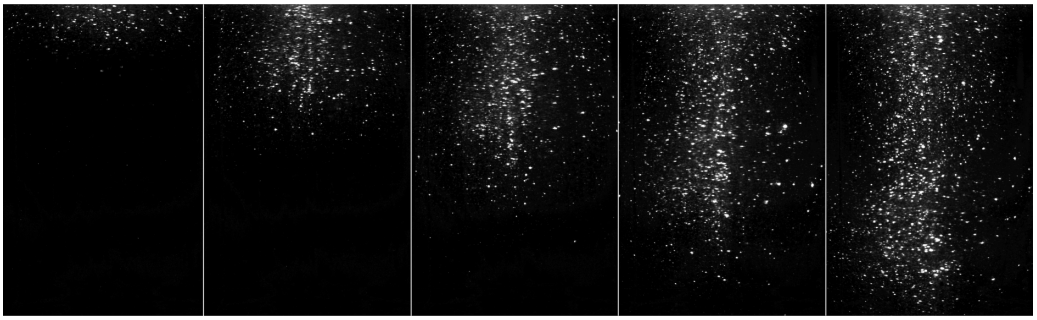

(b) $\dot{m} = 0.84$ g/s

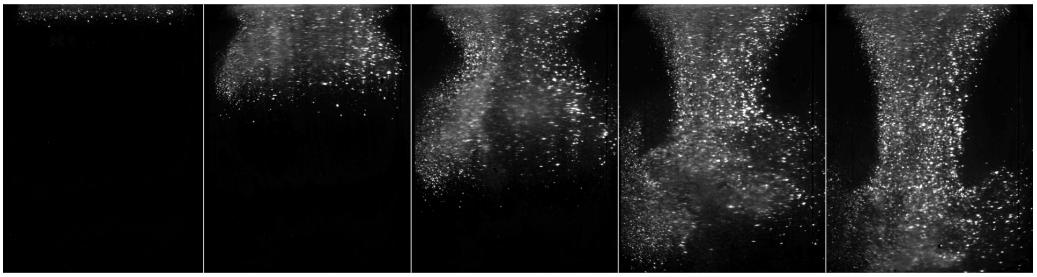

Figure 4.23: *Snapshots of the precipitation with an identical grain size* $r_p = 169$ μm. *The mass rate increases from (a) to (b) (see captions above each subfigure). Intervals between snapshots are (a)* $\Delta t = 3.5$ s, *(b)* $\Delta t = 4$ s, *and the width of every snapshot is* 16 cm *for (a) and (b).*

As they accelerate to reach their terminal velocity, they also dissolve; every new grain that is sieved falls in the wake of some previous ones until the influence of the sugary layer is sufficient to push the underlying fluid downward and towards the sides. This forces a recirculation on the periphery that leads to the roll-up of the precipitation layer (second snapshot of figure 4.21b). Then, a constriction propagates radially inward, favouring the downward acceleration of fluid motions. The latter carry sugar grains towards larger depths until the fluid motions reach a quasi-steady state: the precipitation layer has reached its equilibrium depth, which is a growing function of $\dot{m}$ (see figures 4.21 to 4.23).

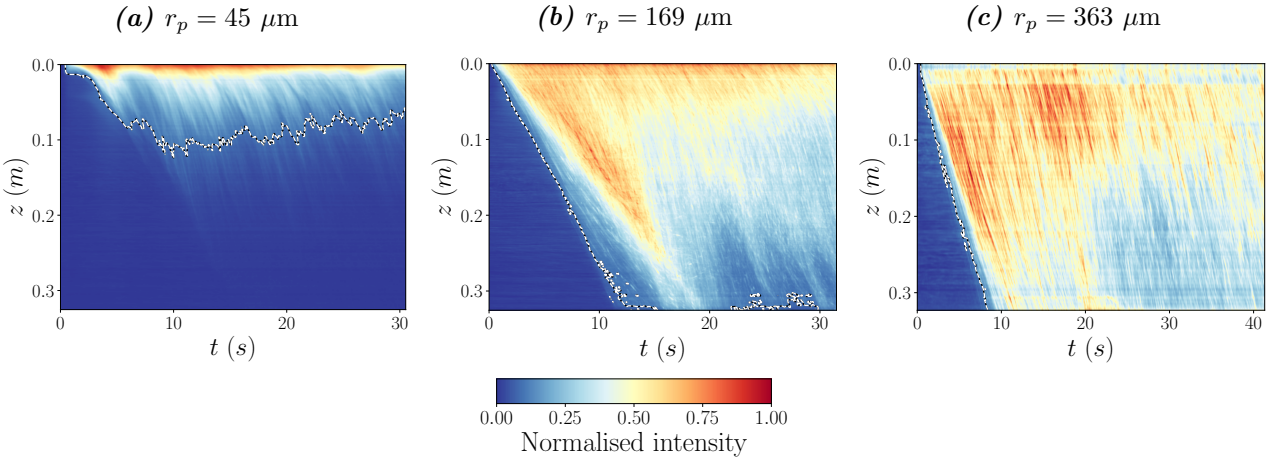

Figure 4.24: *Space-time diagrams of the horizontally-averaged light intensity from low values in blue to large values in red. From left to right, the three panels show the influence of increasing the particle size in three experiments of comparable mass rates, namely (a)* $\dot{m} = 0.59$ g/s, *(b)* $\dot{m} = 0.57$ g/s, *(c)* $\dot{m} = 0.64$ g/s. *The black and white dotted curves show the bottom of the precipitation layer.*

How fast does the precipitation layer form? To quantify the sinking velocity of the precipitation layer, the light intensity of each photograph is averaged horizontally and the resulting vertical profiles are stacked in time to build space-time diagrams.

First, the influence of the grain size for a comparable mass rate is shown in figure 4.24. When laden with small grains ($r_p = 45$ μm in figure 4.24a), the precipitation layer initially accelerates before sinking with a constant velocity; the subsequent quasi-steady regime shows oscillations due to successive turbulent puffs of grains that never reach the bottom of the tank. When grains are sufficiently large to decouple from the starting plume ($r_p = 169$ μm in figure 4.24b and $r_p = 363$ μm in figure 4.24c), they fall ahead of the plume cap hence no clear phase of acceleration appears. Such large grains fall with an approximately constant velocity, down to the bottom of the tank when the mass rate is large, as seen in figures 4.24b-4.24c for $\dot{m} \simeq 0.6$ g/s. Again, oscillations in light intensity mark the existence of puffs of sugar grains in the quasi-steady regime.

Second, the influence of the mass rate is shown in figures 4.25a-4.25c for $r_p = 101$ μm and in figures 4.25d-4.25f for $r_p = 169$ μm. The larger the mass rate, the larger the volume fraction in the precipitation layer hence the larger the horizontally-averaged light intensity. Also, a larger mass rate leads to a larger effective buoyancy in the plume, hence a shorter transient and a flow that is more vigorous and more fluctuating.

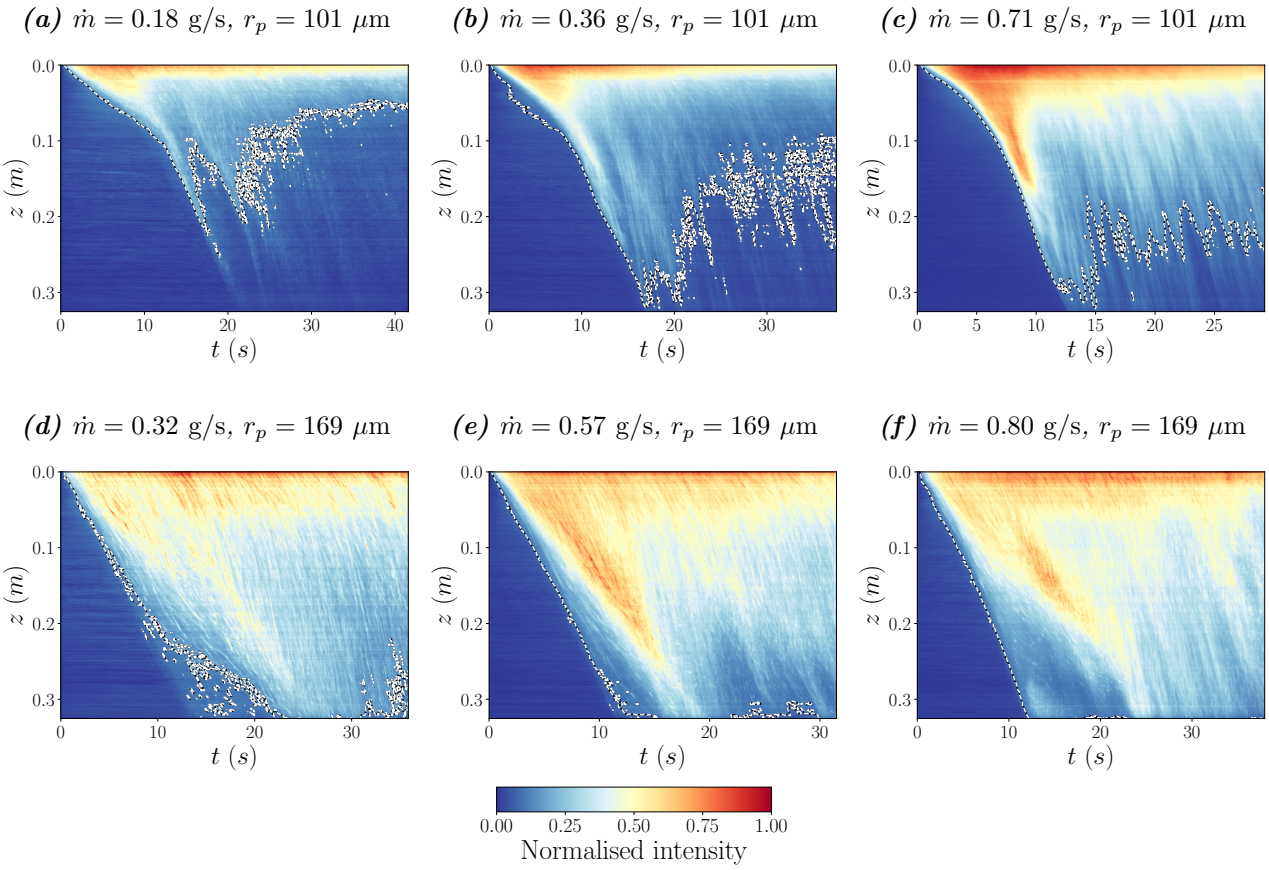

Figure 4.25: *Space-time diagrams of horizontally-averaged light intensity from low values in blue to large values in red. Radii (r_p) and mass rates ($\dot{m}$) are specified above each diagram. The black and white dotted curves show the bottom of the precipitation layer.*

The convergence of iso-contours of light intensity in the space-time diagrams enables to define the front of the precipitation layer, as shown by a black-and-white dashed line in figures 4.24 and 4.25. In the present section, we focus on the sinking of the precipitation layer in the transient, which ends when the front position of the precipitation layer no longer increases in time but only fluctuates around a constant value. Figures 4.25a-4.25c show that the precipitation layer sinks with a low initial velocity in the first ten centimetres before accelerating. In the second phase the slope of the black-and-white dashed line is comparable to that of the puffs of grains in the quasi-steady regime, suggesting that this slope is characteristic of the fluid motions in the plume once quasi-steadiness is reached. Since our interest is presently on the transient, we analyse the initial low sinking velocity *before* the change of slope.

This sinking velocity of the precipitation layer is denoted $\dot{z}_{\mathrm{PL}}$. It is measured by fitting a linear law on the dashed curve for each experiment, and results are shown in figure 4.26a. The sinking velocity of sufficiently small grains ($r_p < 169$ μm) increases essentially with the mass rate with little influence of the grain size. Conversely, for a fixed mass rate the radius r_p noticeably modifies the sinking velocity when $r_p \geq 169$ μm, with sudden jumps when r_p varies from 101 μm to 169 μm, and then from 169 μm to 363 μm. These jumps are due to

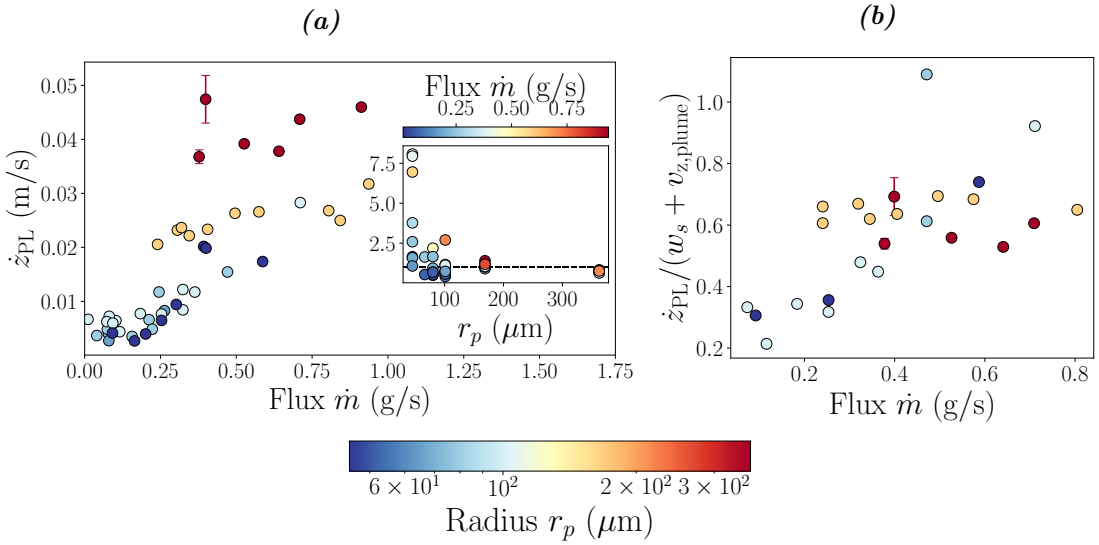

Figure 4.26: *(a) Sinking velocity $\dot{z}_{PL}$ of the precipitation layer as detected from Hovmoller diagrams. The same data are rescaled in the inset whose ordinate is the ratio $\dot{z}_{PL}/w_s$: for $r_p \geq 169$ μm, data collapse on the dashed black curve of equation $\dot{z}_{PL}/w_s = 1$. (b) Comparison of the sinking velocity $\dot{z}_{PL}$ with the sum of the settling velocity w_s and the measured fluid velocity within the plume during the quasi-steady regime $v_{z,plume}$. The colorbar for radii applies for both figures.*

the gravitational decoupling between the starting plume and these large sugar grains whose settling velocity is much larger than the fluid velocities. This is shown by the inset of figure 4.26a whose ordinate is the rescaled velocity $\dot{z}_{PL}/w_s$: unlike smaller grains, those in the range $r_p \geq 169$ μm verify $\dot{z}_{PL}/w_s \simeq 1$.

This last conclusion means that the influence of the plume velocities is almost negligible for large grains ($r_p \geq 169$ μm). Yet, the fluid velocities are *not perfectly* negligible. Figure 4.26a shows that the larger the mass rate, the larger the plume velocity $v_{z,plume}$, the faster the grains fall since their velocity reads $v_p = v_{z,plume} + w_s$ (see equation (4.1)). This is confirmed in figure 4.26b which shows the normalised velocity $\dot{z}_{sinking}/(v_{z,plume} + w_s)$ for all experiments that included PIV measurements. As expected, the rescaled velocities are of order unity and major jumps due to the particle size have now disappeared. We still observe a departure from unity by a factor $\sim 1/2$. A key aspect that likely contributes to this departure is the fact that during the transient, the plume velocity is still developping, so the use of the steady-state velocity $v_{z,plume}$ in the normalisation is an anticipation that overestimates the role of advection in carrying grains faster downstream.

A slight increase of the normalised velocity $\dot{z}_{PL}/(v_{z,plume} + w_s)$ is still observable as the mass flux increases, especially for small grains. This remaining trend can originate from different physical aspects that have been neglected so far, which we discuss in section 4.7.3.

4.7.2 Equilibrium depth

As mentioned in the previous section, the transient is considered to cease when the front position of the precipitation layer no longer increases and instead fluctuates around a constant

value. This front position is therefore averaged over the whole quasi-steady regime, and the resulting measurements of the equilibrium depth z_{PL}^{∞} are shown in figure 4.27. Grains with a size $r_p = 363$ μm always hit the bottom of the tank before full dissolution. Consequently, measurements for this size are irrelevant and not shown.

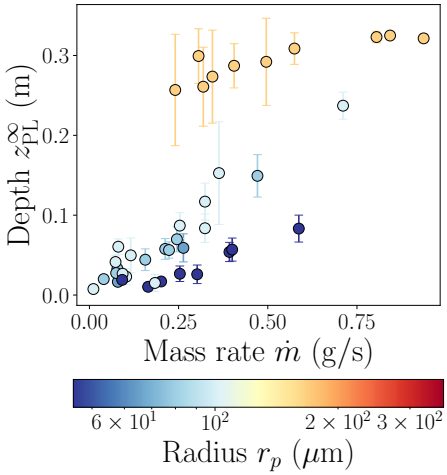

Figure 4.27: *Equilibrium depth of the precipitation layer for all experiments performed with ordinary white sugar.*

For $r_p < 363$ μm, figure 4.27 shows that for a fixed mass flux, the larger the grains the deeper the equilibrium depth. This can be captured from simple arguments. Consider the fall of a supposedly spherical and isolated grain of initial size r_{p0} in clear motionless water. Let us assume that at any time, the buoyancy and drag of the grain are in balance so that the grain falls at its terminal velocity $w_s(t) = w_s(r_p(t))$. The time evolution of the grain can be solved numerically by integrating the two following equations

$$\begin{cases} \dot{r}_p &= -\overline{k}(t)\frac{\mathcal{C}_{\mathrm{sat}}}{\rho_p}, & \text{(4.28a)} \\ \dot{z}_p &= w_s(r_p(t)), & \text{(4.28b)} \end{cases}$$

where z_p is the time-dependent vertical position of the grain centre of mass, and equation (4.28a) follows from the mass balance in equation (4.9) after assuming that the concentration at the grain interface is the saturation concentration so that $\rho_i = \rho_{\mathrm{sat}}$ (see section 4.4.3 for additional details). These equations show that during an infinitesimal timestep dt the size of the grain reduces because of dissolution (equation (4.28a)), thus resulting in a reduction of the grain terminal velocity (equation (4.28b)).

Appendix 4.C gives analytical solutions for the time $t_{\max}$ and depth $z_{\max}$ of complete dissolution when $Re_p \ll 1$ or $Re_p \gg 1$, where Re_p is based on the initial grain radius. In general, solutions of equations (4.28a)-(4.28b) are obtained by numerical integration with the initial conditions $(r_p, z_p) = (r_{p0}, 0)$ at $t = 0$. Measurements of the equilibrium depth of the precipitation layer z_{PL}^{∞} are compared with the numerical solutions $z_{\max}$ in figure 4.28a. Almost all data points lie above unity, meaning sugar grains fall deeper than the depth $z_{\max}$. Additionally the smaller the grains, the farther away they fall compared to $z_{\max}$, even more so as the mass rate

increases. These observations are due to the downward fluid motions that carry sugar grains deep in the tank and enhance their maximum depth of dissolution. This effect is even more pronounced for smaller grains due to the large contrast between their small settling velocity and the large fluid velocity.

To account for this effect, we need to take into account the advection by the plume velocity. According to equation (4.1), this advection can be taken into account by adding a constant plume velocity on the right-hand side of equation (4.28b). Therefore, any grain is expected to travel a distance which is the sum of the advection by the plume, and the distance $z_{\max}$ of complete dissolution which the grain travels by gravitational drift with respect to the fluid. Figure 4.28b compares the measurements z_{PL}^{∞} with the prediction $z_{\max} + U_{\mathrm{plume}} t_{\max}$, and show that the latter is reasonable since the results rescale around unity. Note, however, a remaining trend of increase of the rescaled depth $z_{\mathrm{PL}}^{\infty}/(z_{\max} + U_{\mathrm{plume}} t_{\max})$ with $\dot{m}$ for small grains $r_p < 169$ μm. This suggests that some remaining physics has not been accounted for, as already evoked when discussing figure 4.26b. This additional physics is discussed in the next section.

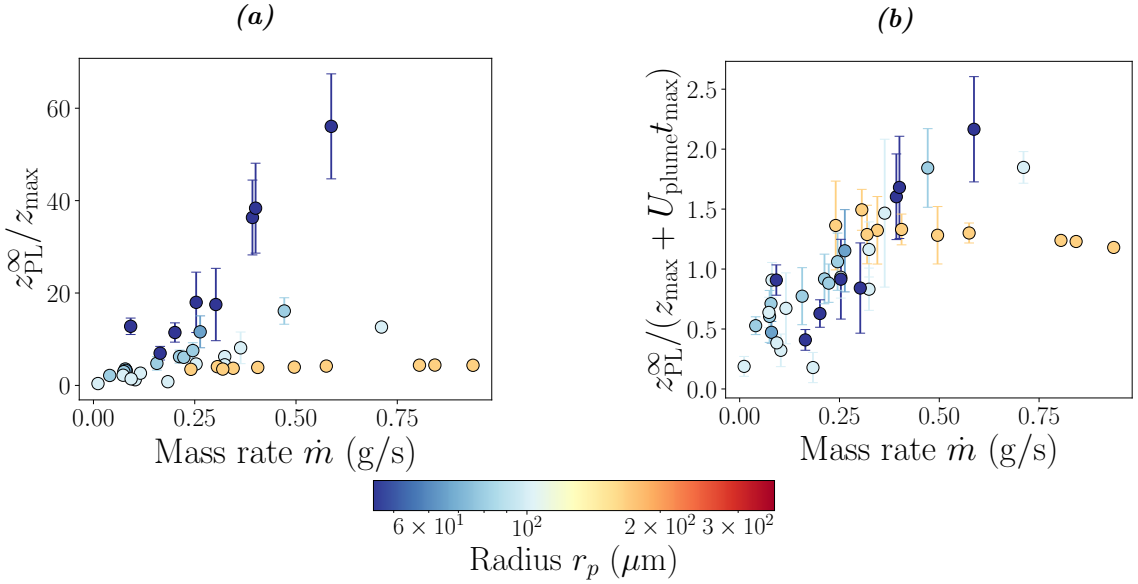

Figure 4.28: *(a) Comparison between the measured equilibrium depth of the precipitation layer z_{PL}^{∞} and the numerical value $z_{\max}$ of the maximum distance travelled by an isolated grain settling in clear still water. (b) Comparison between z_{PL}^{∞} and the prediction $z_{\max} + U_{\mathrm{plume}} t_{\max}$. The colorbar is common for all graphs; the size r_p is implicitly the initial grain radius r_{p0} that is used to compute $z_{\max}$ and $t_{\max}$.*

4.7.3 Processes at the grain scale

The remaining increase of the sinking velocity $\dot{z}_{\mathrm{sinking}}/(v_{\mathrm{z,plume}} + w_s)$ (figure 4.26b) and of the equilibrium depth $z_{\mathrm{PL}}^{\infty}/(z_{\max} + U_{\mathrm{plume}} t_{\max})$ (figure 4.28b) with the mass rate $\dot{m}$ could be due to processes that we have observed at the scale of individual sugar grains. Because we lack technical means to perform quantitative measurements, we present observations whose

interpretations are for now essentially speculations and which require analyses beyond the scope of the present study to arrive to a conclusion.

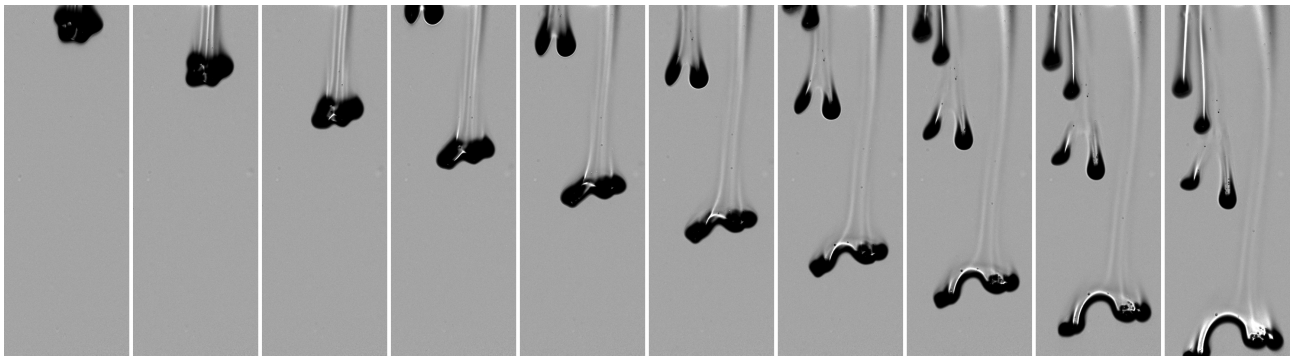

Figure 4.29: *Free-fall of a few sugar grains dropped with a spoon in distilled water at room temperature. The horizontal width of every snapshot is* 835 μm *and the delay between two snapshots is* 66.7 ms.

For very large mass rates, small sugar grains with a low Rouse number follow the vigorous eddies of the turbulent flow. For a sufficiently vigorous turbulence, if their Rouse number is not too small they may preferentially concentrate in certain regions, favouring clustering (e.g. Yoshimoto and Goto, 2007; Salazar et al., 2008) which may enhance the downward fall of the grains (e.g. Aliseda et al., 2002; Ghosh et al., 2005; Brandt and Coletti, 2022). Indeed, clustering has been observed in experiments even in the absence of turbulence when we dropped only a few grains in still water (figure 4.29); it remains an open question to determine whether the corrugated surface of the grains and their dissolution favour some kind of sticking between them. Another aspect of importance is the concentration in dissolved sugar which is maximum for the smallest grains and the largest mass rates, because both elements increase the total dissolution rate $dm_{\text{tot}}/dt \propto \dot{m}\overline{k}/r_p$ (see equation (4.11) and the increase of the effective density at the plume source with increasing $\dot{m}$ and decreasing w_s in equation (4.16)). This increases the plume concentration (or equivalently its density $\rho(z)$) that surrounds sugar grains; therefore it slows down their dissolution since $\dot{r}_p \propto (\rho_{\text{sat}} - \rho)$ (see equation (4.9) with $\rho_i = \rho_{\text{sat}}$).

Another key effect is that, because sugary water is negatively buoyant, the dissolved sugar at the edge of a grain and in its wake tends to accompany it during its fall. This is confirmed by sub-millimiter observations of isolated grains of sugar dissolving in still water which show that the capsule of dissolved sugar falls even after the solid grain has fully dissolved, see figure 4.30. This capsule of buoyant fluid has its own inertia and is forced by its own buoyancy, hence it favours a faster fall of the solid grain in its interior during dissolution. These interpretations and observations are consistent with the work of Kerr (1995) who analysed the dissolution of spherical particles of NaCl in water. The larger concentration of solute in this capsule delays dissolution by an effect of saturation, and the larger fluid viscosity inside the capsule might also reduce the contribution of advection to mass transfers. For large mass fluxes $\dot{m}$ and low radii r_p, the plume has a large concentration of solute that lowers the density contrast $(\rho_{\text{sat}} - \rho)$. This likely reduces the diffusive flux that dilutes the capsule, enhancing its persistence and therefore its ability to shelter the grain and carry it over large distances.

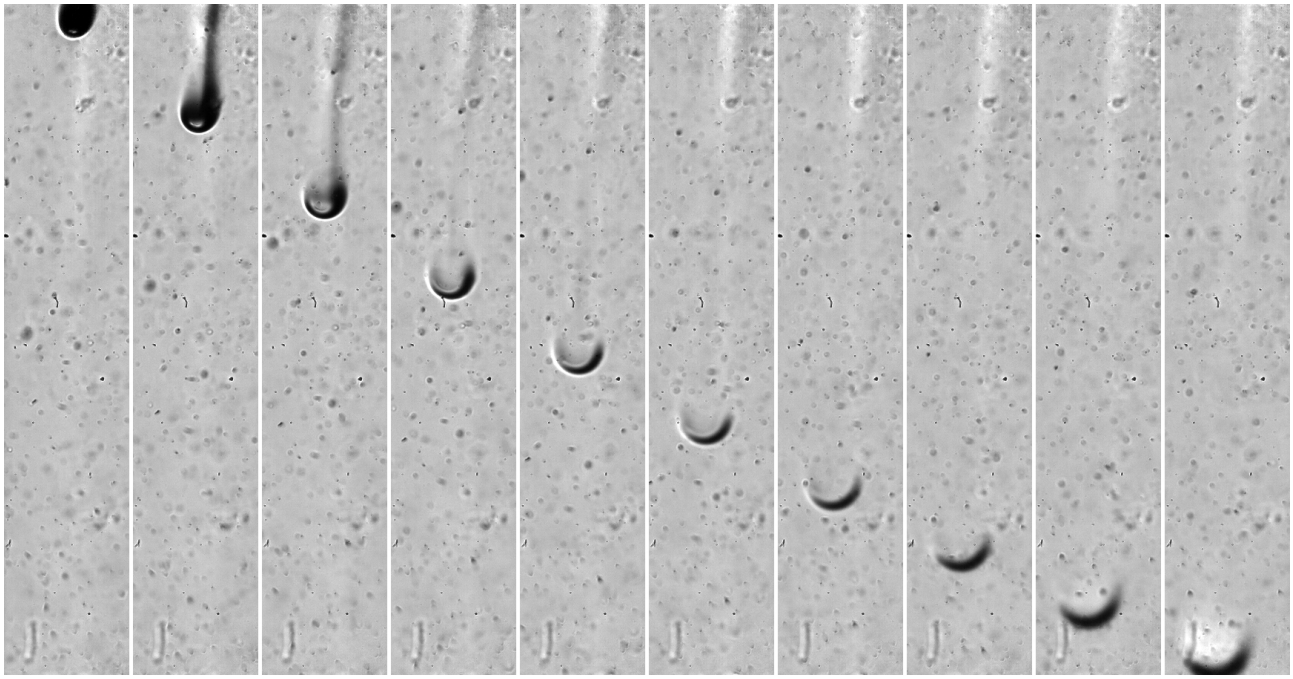

Figure 4.30: *Fall of the residual capsule produced by the dissolution of a sugar grain falling in hot water at* 42.1°C. *The many small grey dots correspond to impurities in water. The horizontal width of every snapshot is* 415 μm *and the delay between two snapshots is* 200 ms.

4.8 Final remarks

The key observation of this study is probably the paramount influence of the size of sugar grains on the flow they force. The inefficient forcing of laminar plumes by large grains (section 4.3.1) is an undeniable evidence that for a given input of potential energy, the size r_p controls the macroscopic evolution of the whole system of sugar grains, solute and fluid motions, even at large times when the flow reaches quasi steadiness. The experience gained from the experiments and simulations of the previous Chapters 1 and 2 has been crucial to shed light on the enhanced efficiency of small grains to force the flow through drag. All this proves that, as long as grains have not fully dissolved, the particulate nature of the buoyant material strongly constrains the forcing and the concentration of solute in the plume. Even more striking, we observed that the particulate nature of the forcing imprints a persistent trace on the flow even below the precipitation layer, since its structure is directly conditioned by the initial size of grains. It remains to be verified with sugar grains smaller than 45 μm if this influence of r_p ultimately disappears when the size of grains is reduced typically down to 10 μm or less (see the isocontours in figure 4.20a).

The average plume velocity U_{plume} in the quasi-steady regime is only a function of the effective volume fraction of sugar, which corresponds to the ratio $(\rho_{\text{eff,QS}}-\rho_0)/\rho_p = \dot{m}/\pi R_{\text{sieve}}^2(U_{\text{plume}}+w_s)\rho_p$ (see equations (4.24)-(4.25)). This expression suggests that the average quasi-steady plume velocity only depends on w_s, by an effect of dilution that modifies the effective volume fraction. Because w_s and r_p could be decoupled, additional experiments where the size of grains and the settling velocity could be modified independently could confirm this conclusion and

provide additional insight on the forcing of the flow by the grains.

This last effective volume fraction $(\rho_{\text{eff,QS}} - \rho_0)/\rho_p$ was derived for the quasi-steady regime; the one derived for the onset of the flow is $\phi_{\text{eff}} \propto \dot{m}/w_s$ (equation (4.21)). Both of them depend on w_s, whereas the time t_{QS} to reach the quasi-steady regime is *only* a function of the mass rate (figure 4.17a). An important consequence is that the time t_{QS} shows no correlation with these volume fractions. What exactly controls the duration of the transient? The influence of dissolution could play a role in setting the fluid in motion. Accounting for it during the transient would require a time-dependent and possibly depth-dependent volume fraction, which then calls for a more sophisticated modeling of the plume from the very start, including effects of constriction that may explain some of the remaining increase observed in figure 4.28b. But even in the absence of dissolution, sieving inert particles leads to a delayed onset of the steady regime. What controls the gradual emergence of larger and larger length scales in the experiments with the largest sugar grains? This emergence is likely controlled by the spacing between grains (how much do they influence one another?), by the time lapse between the fall of two grains at the same location (does the motion induced by the drag of the first grain vanish before the second grain falls?), by the amount of solute deposited by grains, and by how much the sugary wakes diffuse towards one another to combine and thus distribute the forcing in an effectively larger volume. See further discussion in the Conclusion and future lines of work.

A knotty question is: What is exactly the influence of dissolution in our experiments? This question is especially motivated by the striking similarity between our flows and *downbursts* – violent downward currents of air generated below clouds by precipitation and latent heat absorption due to melting or sublimation of ice, or due to the evaporation of raindrops. These flows also combine sedimentation and phase change, they propagate as fronts, are all the more vigorous as particles are smaller, and intensify when the mass flux of hydrometeors increases (Kamburova and Ludlam, 1966; Harris, 1977; Srivastava, 1985, 1987). These studies insist on the role of phase change in driving the flow (Srivastava, 1985, 1987). They showed that the fall of ice crystals induces more vigorous downward motions than the fall of water drops; this was interpreted as being due to the slow settling of ice particles that absorb latent heat in a shallow region, whereas fast-falling drops absorb latent heat in a deeper region, thus leading to a comparatively lower temperature anomaly Srivastava (1987). We have performed experiments by sieving glass spheres that have several similarities with our experiments on sugary plumes – hence, how much does dissolution play a part? Can we discriminate between the roles of hydrodynamics and phase change in out experiments?

Some first remarks can be made from our experiments. Grains shrink as they sink, hence their dynamics changes: the particle Reynolds number and the Rouse number keep decreasing so the flow is necessarily more and more fluid-like, less and less settling-constrained as we consider a slice of plume that is deeper. Such a transition cannot exist if all particles are inert. This difference might go unnoticed without an accurate quantitative comparison because of the finite depth of our water tank. In a deep ambient, however, inert particles will never lose their minimum settling velocity w_s with respect to the fluid in their vicinity, and settling will always constrain the flow to be vertically biased due to finite-Rouse-number effects; conversely, all sugar grains will inevitably dissolve, guaranteeing a transition to a fluid-like behaviour. Large particles will remain insensitive to minute perturbations at large depths whereas the solute

produced by large grains will mix with the ambient and diffuse, so that a difference between inert and reactive particles is anticipated to be visible at a large scale. This calls for future experiments in a larger tank, with reference experiments using inert particles that have the same size and density as sugar grains to quantitatively compare the trajectories of particles and the fluid velocities.

4.9 Acknowledgments

We would like to thank Emmanuel Villermaux for fruitful discussions on the physics that governs mass transfers at the grain scale. We also thank Lucas Rotilly and Emmanuel Villermaux for giving us access to their optical apparatus to visualise grains on a submillimeter scale. We also thank Eric Bertrand and William Le Coz for providing the motor and its attachment system to sieve sugar automatically in experiments.

4.A Experimental setup and calibration

4.A.1 Cooking fluorescent sugar

To visualise the motions of the negatively buoyant sugary water, we home-cook our sugar by adding rhodamine B in sucrose.

We prepare the sugar in a chemistry room under an extractor fan. A precise mass of sugar is mixed with a precise small amount of water in a frying pan at room temperature. Both are stirred until the sugary water is homogeneous. Then, heating is turned on while the sugary water is regularly stirred. The presence of water favours a homogeneous heating of the mixture. After approximately 20 min, water starts boiling. Due to regular stirring, this phase can last up to 10 min before all the water has evaporated. Then, heat can rise up in the absence of water and reach a temperature of about 155°C. At that moment, the sugar turns brown. A precise mass of rhodamine is then added with no delay and vigorously stirred to reach homogeneity as fast as possible in about 30 s. The dyed sugar is then quickly spread on parchment paper where it cools until reaching ambient temperature. It was found that rather than letting the sugar spill as a sheet on the baking paper, spreading it with a spatula leads to the rapid growth of large air bubbles in the sugar over a duration of a few seconds. This foamy form of sugar seemed to cool faster, and most of all was simpler to crush and blend with a mixer to reduce sugar to tiny grains no larger than 1 mm in diameter.

4.A.2 Sorting sizes of grains and clogging

Whether experiments be performed with dyed sugar or ordinary sucrose with no colouring, the stage of blending leads to an extremely polydisperse collection of sugar grains that require sorting. This is performed by automatically sieving sugar grains with sieves having different mesh sizes, in a closed cardboard box to avoid unwanted propagation of the very small sugar grains in the air due to vigorous sieving. Sieving starts with the sieve of largest mesh (1000 μm), down

to the sieve of mesh size 56 μm. Some grains are shown in figure 4.31a, and all the different ranges of sizes are summed up in table 4.1. Each of them is characterised by an average radius r_p which is computed as the arithmetic mean of the minimum and maximum radii of this range.

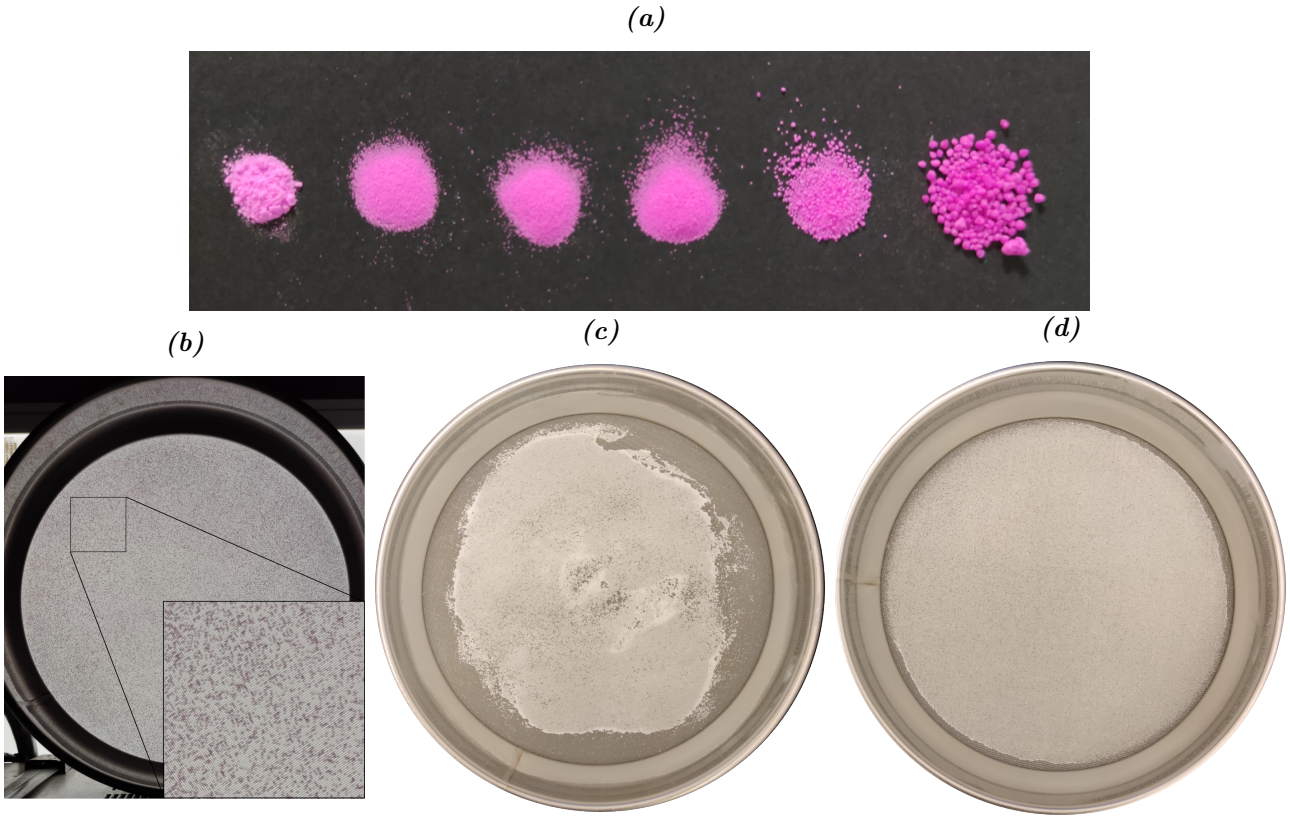

Figure 4.31: *(a) Some sugar grains of diameters in the ranges (from left to right):* ≤ 125, $125-140$, $140-180$, $180-224$, $224-1000$, ≥ 1000 *(in microns). (b) Clogging of a sieve by medium dyed sugar grains. (c) Clogging of a sieve by small grains of ordinary sugar after a few experiments is essentially concentrated in the centre of the sieve, while after many experiments (d) the whole sieve is clogged. No specific trend is observed as to where clogging starts, it depends on humidity, the total mass of grains, their size and the sieve used.*

Sieving of large grains is fast because very small grains quickly fall through the much larger mesh so little clogging is observed. As the process goes on, the difference between the mesh size and the diameter of any grain that should fall through the mesh gets smaller and smaller. Consequently more and more clogging is observed as illustrated in figures 4.31b-4.31d.

Such clogging is expected because it is inherently due to the filtering process that sorts the grains of sugar. Unfortunately, clogging also happens when sieving sugar during experiments, despite the use of a sieve whose mesh is immediately larger than the grain size (e.g. when using the sieve of size 224 μm with grains in the range $180-224$ μm) or even larger (e.g. when using the same sieve for grains in the range $140-180$ μm). This means that although grains passed through this very mesh during the sorting procedure, clogging is still possible. We believe it is

due to several grains falling through the same hole at the same time and ending up one leaning against the other. With their own weight and the pressure exerted by the overlying grains, the hole can remain jammed until a vibration of the sieve manages to separate these two grains. Experience shows that the most efficient way to unclog a sieve so is by hitting it shortly with a tool, enabling all grains to jump vertically in the sieve which is then unclogged.

Another complexity that is specific for sugar is its interaction with moisture in the ambient. Experience shows that the pattern of clogging in figure 4.31c is partly due to humidity: when this sieve is hit by a tool, the white region at the center preserves this convoluted shape, suggesting that humidity fixed some of the sugar on the metal mesh. This inference was confirmed by experiments performed on different days with varying ambient humidity: the more humid the air, the faster clogging of the sieves.

These observations raise the question of the best way of sieving sugar grains. Although vertical oscillations would limit the problem of clogging, they introduce another undesired phenomenon of heterogeneous migration of sugar grains. This phenomenon sometimes recalls the classical accumulation of grains in the antinodes of stationary Chladni-like vibration modes, and some other times it evidences an unsteady dynamic migration in the sieve. Due to the complexity to control such motions, horizontal sieving was preferred. To limit the influence of clogging and to avoid again some effects of migrations of grains, sieving should be with a sufficient amplitude (typically above 1 mm) to guarantee that grains either roll over the mesh or slide against it, which seems to favour a homogeneous sieving. At the same time, the amplitude should not be too large (typically below 1 cm) to guarantee that the sugar grains, after falling in the air, land on the water free surface in a circular region. This is also to mitigate the fact that excessive amplitudes lead to a heterogeneous sieving because in that case, most grains are expelled when the motion of the sieve reaches an extremum along the horizontal, so few grains are sieved at the center.

Since the mass rate of sieved sugar depended on the total mass of grains in the sieve, and most of all because ambient humidity could not be controlled, no calibration of the mass rate was observed to be reliable from one day to another. Consequently, the next section describes the calibration procedure that is implemented for every experiment.

4.A.3 In-situ calibration

Since the mass rate continuously decreases in time, any representative measurement of the mass rate should be obtained on a sufficiently small timescale for the mass rate to be considered approximately constant during the time of sieving.

Calibration is performed right above the water tank. A rigid A2 sheet of paper is placed horizontally between the top of the tank and the bottom of the sieve (see figure 4.32) to make sure that no sugar is lost in water during the calibration. Then, all the sugar grains of a given range are poured on top of the sieve and gently spread to get an approximately uniform covering of the sieve. The few sugar grains that fell through the sieve in the meantime are collected with the paper sheet, which is then rolled as a funnel to pour them back into the sieve; the aim here is to guarantee that the total mass of sugar that oscillates remains constant.

The oscillations are parameterised depending on the mass rate that is aimed for: the larger the velocities of the sieve, the larger the mass rate. Since the fall of sugar grains is correlated

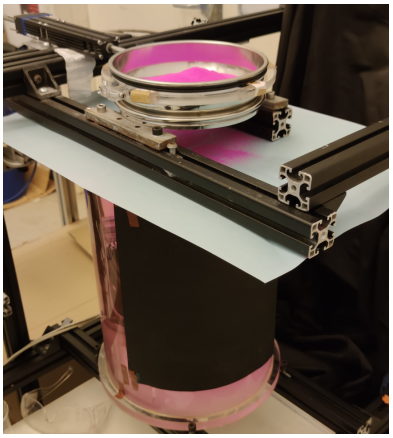

Figure 4.32: *During calibration, sugar is collected on a horizontal rigid A2 paper sheet before being poured on a scale to get a measure of the mass rate.*

to the period of oscillation, the latter should never be too large to guarantee that it can be neglected compared to the characteristic timescales of the flow, so that the mass rate of sugar grains contacting the water free surface can be considered continuous.

Once parameters are chosen, sieving is first performed over a duration of 5 s as controlled by a timer. The sugar that has been sieved is collected and weighed. This provides an estimate of the mass rate during the first 5 s of sieving: see the first data point in the calibration curve of figure 4.33. The procedure can be repeated through several successive 5 s-long iterations. The resulting calibration curve (figure 4.33)shows a decrease of the mass rate over the total cumulative duration of sieving. Experience shows that the decay scales as a power law $\dot{m} \propto t^{-\alpha}$ with $\alpha \geq 1$ a coefficient that varies from an experiment to another due to the size of grains, their total mass, the parameters of oscillations and the humidity. An approximately constant mass rate can be obtained when $\alpha > 1$ if the calibration is iterated many times, since then the slope of the power law becomes small, see figure 4.33. For small mass rates such a long calibration is not an issue. However when the targeted mass rate is large, it should be anticipated that the initial mass rate should be extremely larger than the targeted value to make up for clogging over the course of the calibration.

Once the mass rate gets close to the targeted value, the A2 paper sheet is removed from above the tank and an experiment can be performed. Depending on the wish to analyse the transient or the quasi-steady regime, the typical duration of sieving during an experiment varies from 10s to at most 2min. As soon as an experiment is finished, the calibration procedure starts again with successive iterations. The final curve of calibration is therefore a decreasing mass rate as a function of the total time of sieving since the very start of the calibration, with a 10s-long to 2min-long blank corresponding to the experiment. Experience shows that the mass rates measured before and after the experiment almost always align along a power law $\dot{m} \propto t^{-\alpha}$ where the value of $\alpha \geq 1$ is now definitive based on all the measurements performed before and after the experiment. The power law that is fitted on the measurements enables to compute a mean mass rate for each experiment.

Figure 4.34 shows the mean mass rate and grain radius of all experiments. The vertical error bars range from the minimum to the maximum size of grains in a given set of table 4.1.

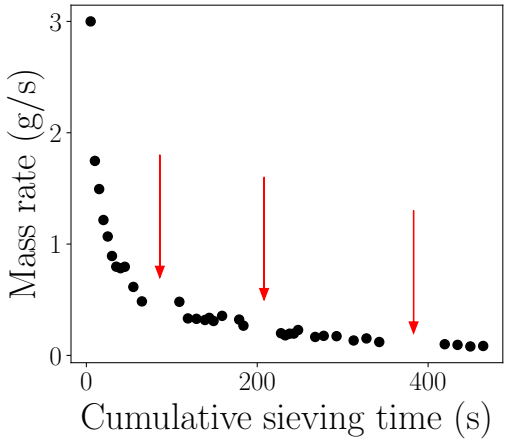

Figure 4.33: *Calibration curve for three successive experiments (shown by the red arrows). The curve shows the mass rate measured on a scale during iterative runs of* 5 s *as a function of the cumulative time of sieving. The large gaps where the red arrows are located correspond to the duration of sieving during experiments (of order* $\sim$ 30 s*), not to the duration of an experiment (*$\sim$ 5 min*) nor the delay between two experiments (*$\sim$ 30 min*).*

Horizontal error bars range from the maximum mass rate at the start of an experiment, to the minimum mass rate at the end of an experiment.

Different colors appear for the following reason. When starting a calibration, the mass rate decreases as a power law. If this power law remains the same even after an experiment (see the three examples of figure 4.33), the power law is used to compute the mean mass rates, and data points are shown in red. However, in many cases the power law transitions to a different law after some time. In that case, we fit experimental data with the law that best fits the 5 measured mass rates before the experiment, and the 5 measurements after the experiment. When this law is linear, data points appear in blue. For two experiments, this law is exponential; the corresponding points are in magenta. When the calibration could not be fitted by any law because of noise, or when the sieve was accidentally unclogged a few measurements after the experiment, the mass rate was calculated as the mean between the last measurement before the experiment, and the first measurement after the experiment. Corresponding data points are shown in dark in figure 4.34. Finally, some experiments were too complex to calibrate with a curve; after verifying that sieving was uniform and the mass rate was approximately constant, the mean mass rate was measured by computing the difference between the total mass of sugar in the sieve before and after the experiment; these data points are shown in green.

4.B Processing methods

4.B.1 Profiles of intensity along the trajectory of the plume front

This processing is only applied for experiments with dyed sugar. The successive steps are:

1. Detect the front position of the starting plume in space-time diagrams as those in figures 4.11 and 4.12 (see Appendix 4.B.2 for this method); this provides measurements of the

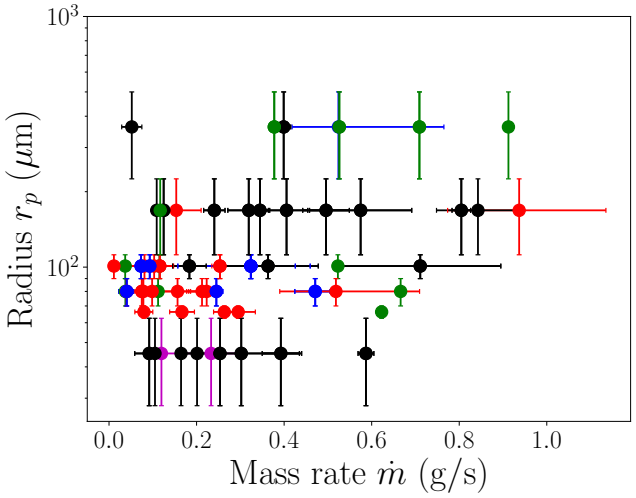

Figure 4.34: *Average radius and mass rate of all experiments. For the colors of the different experiments, and for a description of the range spanned by the errorbars, please refer to the text.*

front position in time.

2. Fit a parabola on these measurements.
3. The measurements on which the parabola is fitted integrate contributions from several large grains or several sugary mushrooms, depending on the experiment considered. Not all of them have the same size and depth. To capture all of them on the intensity profile, the light intensity is integrated in a window spanning through the whole width of the photographs and with a vertical extent that is adapted to best capture all structures: the window extends 1 cm above the plume front and 1.5 cm below. This larger extension below the front enables to capture occasional large grains that settle ahead of others for short amounts of times. In this window, the light intensity is averaged along the vertical direction z.

The final results are the space-time diagrams in figure 4.10.

4.B.2 Convergence of isocontours in space-time diagrams

Space-time diagrams show a transition between regions of large light intensity (where sugar grains reflect the laser sheet, or where dyed sugar is present) and dark regions. The aim is to find this transition. Space-time diagrams of the smallest or the largest grain sizes are so different that an automatic algorithm of detection of contours can work for the former, not for the latter. To apply a same processing for all experiments, the following method was implemented.

On a given space-time diagram, a total of 50 equispaced isocontours are considered. Each isocontour delineates a different region of the space-time diagram: the contour of lowest intensity encircles the largest region, and the larger the isocontour intensity, the smaller this region. For very low intensities, changing isocontour results in a considerable change of the total surface area that is encircled. At larger intensities however, increasing the isocontour value from one to the next leads to very little modification of the region that is encircled. Consistently, the

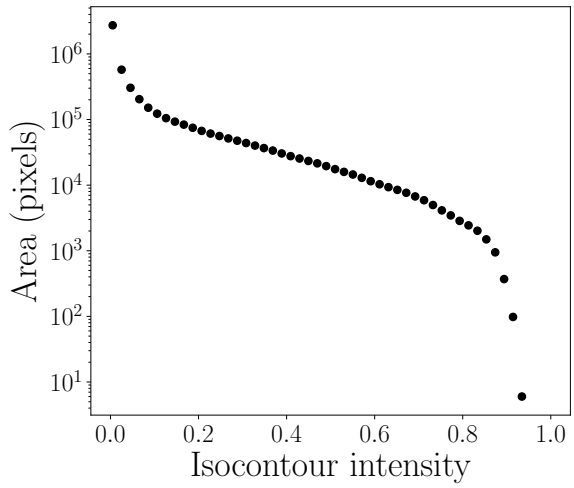

Figure 4.35: *Processing of the experiment whose space-time diagram is shown in figure 4.25a. Evolution of the surface area encircled by an isocontour as a function of the intensity of the corresponding isocontour. The isocontour intensity is normalised by the difference between the maximum and minimum values in the space-time diagram.*

surface area of the encircled region – calculated as the number of pixels in this region – transitions from a regime where it depends hugely on the isocontour intensity, to a regime where it depends little on this intensity: this transition is visible at an abscissa ~ 0.12 in figure 4.35. The isocontour we seek for, separating dark regions from regions of large light intensity, is given by the abscissa where the change of slope operates, because isocontours with an intensity equal or slightly larger than this value converge on the space-time diagram.

This technique has notably been applied to detect the downward propagation of fluid motions in experiments (e.g. in figures 4.13-4.14). This has enabled to extract the propagation of fluid motions in figure 4.36. In the range $z \in [5\text{ cm}, 33\text{ cm}]$, the trajectories of the sinking fronts are essentially linear, so each of these profiles has been fitted with a first-order polynomial to extract its slope, that corresponds to a velocity point in figure 4.15.

4.B.3 Quasi-steadiness of the PDF of vertical velocity

From a statistical viewpoint, the PDF in figure 4.16 shows that the downward fluid velocities gain in intensity during the transient, possibly reach a maximum at the end of the transient, then plateau in the quasi-steady regime, before eventually vanishing after sieving is stopped. Therefore, apart from the violent end of the transient, the permanent regime corresponds to a time window where the downward velocities are maximum. Consequently, a time of steadiness is defined from the PDF of the vertical velocity like so:

1. Detect numbers above 10 on the side of positive (downward) velocity v_z in the PDF.
2. At each time i.e. for a fixed ordinate, extract the maximum value of v_z that verifies the previous condition. The final result is a velocity curve $\max(v_z(t))$ as a function of time.
3. Time-average the velocity curve with a moving average to reduce noise. This smoothed

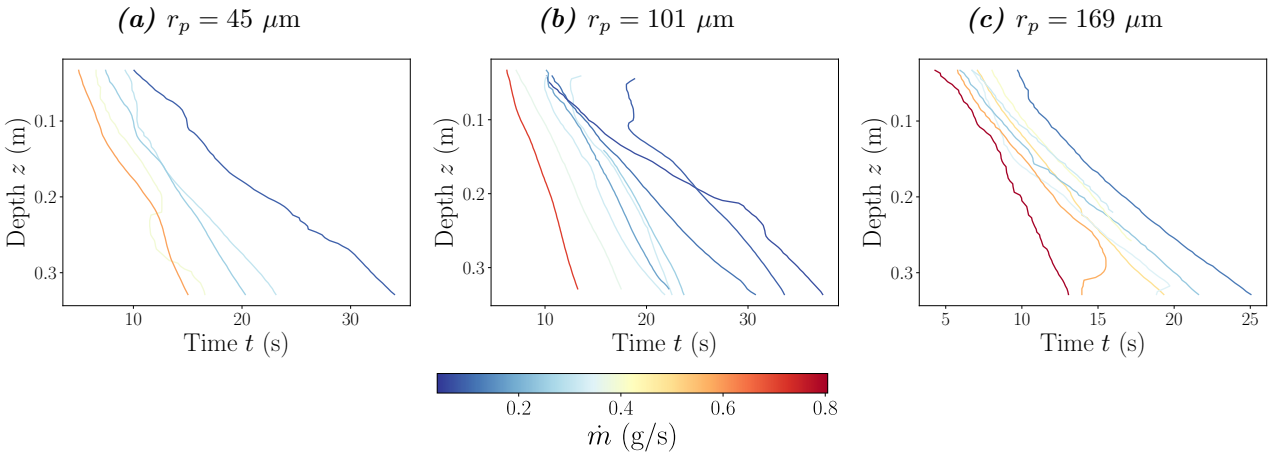

Figure 4.36: *Downward propagation of fluid motions as detected from the convergence of isocontours in space-time diagrams like those in figures 4.13-4.14. Each panel evidences a faster propagation when increasing the mass rate for a fixed particle size. The time origin $t = 0$ corresponds to the start of sieving.*

curve which we here denote $\langle \max(v_z(t)) \rangle_t$ corresponds to the dark curve overlayed on the PDF in figure 4.16 near the value $v_z = 0.04$ m/s.

4. The maximum of $\langle \max(v_z(t)) \rangle_t$ corresponds to the peak velocity at the end of the transient. To get rid of it, we define the start of the permanent regime as the earliest time when the dark curve $\langle \max(v_z(t)) \rangle_t$ is equal to or larger than 80% of this peak value. This time is shown by the white dashed line in figure 4.16, and the curve $\langle \max(v_z(t)) \rangle_t$ is shown only above the threshold of 80% of the peak value.

4.C Time and depth of complete dissolution

The time and depth of complete dissolution of an isolated spherical grain settling in still water are found by integrating equations (4.28a)-(4.28b) numerically. Analytical solutions are available for the two limiting cases $Re_p \ll 1$ and $Re_p \gg 1$.

For grains of vanishingly small particle Reynolds number $Re_p \ll 1$, the terminal velocity can be simplified as the Stokes velocity and the advective contribution to the mass flux in equation (4.10) can be neglected, so that the coefficient of mass transfer simply reads $\overline{k} = \kappa / r_p$ in the limit $Re_p \ll 1$. In that case the integration of equation (4.28a) is straightforward and shows that the radius of the grain varies as

$$r_p^2(t) \underset{Re_p \ll 1}{=} r_{p0}^2 - \frac{2\mathcal{C}_{\text{sat}}\kappa}{\rho_p} t, \tag{4.29}$$

which corresponds to the well-known 'd^2-law' which originates from the r_p^{-1} dependency of the diffusive mass flux around a sphere (Epstein and Plesset, 1950). Isolating for t in equation (4.29) and taking $r_p = 0$ immediately leads to the time of complete dissolution

$$t_{\max} \underset{Re_p \ll 1}{=} \frac{\rho_p}{2\mathcal{C}_{\text{sat}}\kappa} r_{p0}^2 \propto r_{p0}^2. \tag{4.30}$$

This last expression shows that larger grains have a larger 'lifetime' for two reasons: first because they have more material to dissolve, and second because their dissolution rate $|\dot{r}_p|$ is lower. Indeed, $t_{\max} \propto r_{p0}/|\dot{r}_p|(t=0)$ which is the typical lifetime of a grain estimated by assuming its whole volume dissolves with the initial recession velocity $|\dot{r}_p|(t=0)$. This contributes to smaller grains reaching lower depths during their shorter lifetime. This conclusion is exacerbated by the slower settling velocity of smaller grains. To show it, we use the expression of the Stokes velocity in equation (4.3) and inject equation (4.29) into equation (4.28b). This enables to compute the distance $z_p(t)$ travelled at time t by a grain initially at position $z_p(t=0)=0$:

$$z_p(t) \underset{Re_p \ll 1}{=} w_s^{\text{Stokes}}(r_{p0}) t \left(1 - \frac{\mathcal{C}_{\text{sat}}}{\rho_p} \frac{t}{r_{p0}^2/\kappa}\right). \tag{4.31}$$

Equation (4.31) shows that in the diffusive regime ($Re_p \ll 1$) grains initially fall with an approximately constant Stokes velocity based on their initial radius r_{p0}, but they gradually decelerate and disappear at a finite depth when $t = t_{\max}$. This maximum depth is obtained by substituting t in equation (4.31) with $t_{\max}$ in equation (4.30):

$$z_{\max} \underset{Re_p \ll 1}{=} \frac{\rho_p}{4\mathcal{C}_{\text{sat}}\kappa} w_s^{\text{Stokes}}(r_{p0}) r_{p0}^2 \propto r_{p0}^4. \tag{4.32}$$

All in all, equation (4.32) confirms that smaller grains complete their dissolution at shallower depths, because they have less material, because their dissolution rate is larger, and because they fall slower.

For grains of very large particle Reynolds number, the terminal velocity can be simplified as the Newton velocity

$$w_s^{\text{Newton}} = \sqrt{\frac{8g(\rho_p - \rho_0)}{3C_d\rho_0} r_p}\,, \tag{4.33}$$

and the diffusive contribution to the mass flux in equation (4.10) can be neglected, so that the coefficient of mass transfer reads $\overline{k} = 0.3\kappa r_p^{-1} Re_p^{1/2} Sc^{1/3}$. During dissolution, the particle Reynolds number continuously decreases so that a gradual transition from the Newton regime to the Stokes regime is inevitable; a numerical integration of equations (4.28a)-(4.28b) shows that all grains verifying $Re_p(t=0) \gtrsim 5$ spend the majority of their lifetime having $Re_p(t) > 1$ hence the gradual transition to the Stokes regime will prove of negligible influence on the calculations made for those large grains. Under these assumptions, the integration of equation (4.28a) is straightforward and shows that the radius of the grain varies as

$$r_p^{5/4}(t) \underset{Re_p \gg 1}{=} r_{p0}^{5/4} - \underbrace{\frac{3\mathcal{C}_{\text{sat}}\kappa^{1/2}Sc^{-1/6}}{8\rho_p}\left(\frac{8g(\rho_p-\rho_0)}{3C_d\rho_0}\right)^{1/4}}_{\Pi} t. \tag{4.34}$$

Isolating for t in equation (4.34) and taking $r_p = 0$ immediately leads to

$$t_{\max} \underset{Re_p \gg 1}{=} \frac{r_{p0}^{5/4}}{\Pi} \propto r_{p0}^{5/4}. \tag{4.35}$$

This last expression shows again that larger grains have a larger lifetime; since they also fall faster, larger grains complete their dissolution at a larger depth. To show it, we use the expression of the Newton velocity in equation (4.33) and inject equation (4.34) into equation (4.28b). This enables to compute the distance $z_p(t)$ travelled at time t by a grain initially at position $z_p(t=0)=0$:

$$z_p(t) \underset{Re_p \gg 1}{=} w_s^{\text{Newton}}(r_{p0}) \frac{5 r_{p0}^{5/4}}{7\Pi} \left[1 - \left(1 - \frac{\Pi}{r_{p0}^{5/4}} t \right)^{7/5} \right]. \tag{4.36}$$

Equation (4.36) shows that grains initially fall with the Newton velocity $w_s^{\text{Newton}}(r_{p0})$ before decelerating and disappearing at a finite depth when $t = t_{\max}$. Substituting t in equation (4.36) with $t_{\max}$ in equation (4.35) yields

$$z_{\max} \underset{Re_p \gg 1}{=} w_s^{\text{Newton}}(r_{p0}) \frac{5 r_{p0}^{5/4}}{7\Pi} \propto r_{p0}^{7/4}. \tag{4.37}$$

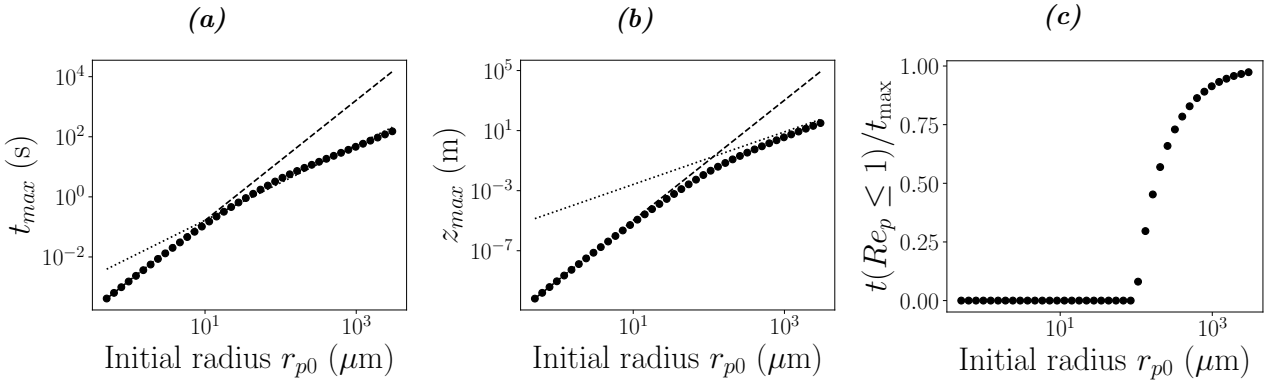

Figure 4.37: *(a) Time before full dissolution of a grain of initial size r_{p0} in clear water. (b) Distance travelled by a grain settling in clear still water up until its full dissolution. (c) Fraction of the 'lifetime' of a grain that the latter spends with a particle Reynolds number above unity.*

The asymptotes of the Stokes regime and Newton regime are compared with numerical solutions of equations (4.28a)-(4.28b). Time integration is performed with a simple forward Euler method as long as the radius $r_p(t)$ is strictly positive i.e. until the grain has fully dissolved, at which point the time $t_{\max}$ and position $z_{\max}$ of complete dissolution are computed. Figure 4.37a shows numerical values of $t_{\max}$ as circles; they consistently transition from the asymptote of the Stokes regime (4.30) for small initial radii to the asymptote of the Newton regime (4.35) for large initial radii. Similarly, the numerical values of $z_{\max}$ consistently transition from the former asymptote to the latter in figure 4.37b. The good agreement between the asymptote of the Newton regime and the numerical values confirms that grains verifying $Re_p(t=0) \gg 1$ spend a negligible amount of time in the Stokes regime, as quantitatively assessed in figure 4.37c where all grains above $r_{p0} = 200$ μm (corresponding to $Re_p(t=0) > 5$) spend the majority of their lifetime with a particle Reynolds number above unity.

Chapitre 5

Ganymede's iron snow: focus on the remelting of snow flakes

Summary

Observations of Ganymede's surface and measurements of its mass, low axial moment of inertia, and equatorial magnetic field, suggest that this moon is composed of three layers: an icy shell, a rocky mantle and a metal core. Ganymede's magnetic dipole is so intense that it likely originates from a dynamo located in its iron-rich core. The latter is subadiabatic so the fluid motions feeding the dynamo likely originate from heterogeneities of composition. Here, we suppose the core bulk composition is on the iron-rich side of the eutectic in the binary phase diagram of Fe-FeS. Consequently, the core evolves according to the scenario of *iron snow* (see Introduction). Past studies (Rückriemen et al., 2015, 2018) shed light on this phenomenon from the sole consideration of the thermal evolution of Ganymede, without considering the specific influence of the particulate nature of the buoyancy forcing when snow flakes settle and then melt. We use the results of Chapter 4 to model the settling and remelting of snow flakes in plumes at the bottom of the snow zone. We align with previous studies to determine the boundary conditions of our model. We then analyse the role of the particulate nature of the buoyant material by varying the size of snow flakes, the radius of the plumes, and the mass flux of snow flakes coming from the snow zone. Snow flakes of radius $r_p \lesssim 10$ μm have little influence on the plume velocity and follow the fluid motions. Larger flakes modify the plume velocity, but decouple from the plume when $r_p > 100$ μm. Varying r_p from 10 μm to 1 m leads to orders-of-magnitude differences on the plume velocity, the volume fraction of grains and the concentration of molten snow. Since remelting accelerates as the flakes shrink, most of the molten snow is produced when they complete their remelting, down to 29 km below the snow zone for 1 m-large snow flakes, which represents 33% of the size of our snow zone.

5.1 Crystallisation of Ganymede's core in the literature

5.1.1 Structure of Ganymede

5.1.1.1 A three-layered icy moon

Ganymede is the largest of the four natural Galilean satellites of Jupiter, which are, in order of distance from Jupiter: Io, Europa, Ganymede and Callisto. A lot of information about these satellites comes from the Galileo mission that made its first pass close to Ganymede in January 1996 (Kivelson et al., 2002).

By measuring Ganymede's mass and average radius 2631.2 ± 1.7 km, the average density of the moon was found to be equal to 1942.0 ± 4.8 kg/m^3 (Schubert et al., 2004). Like Europa and Callisto, Ganymede shows the presence of water ice at its surface, as observed by spectroscopy from the Earth (Calvin et al., 1995). This evidence and the low bulk density of Ganymede suggest that the moon has experienced a differentiation between ice on one hand, and metal and rocks on the other hand (Schubert et al., 1981, 2004) with approximately 60% of the mass which corresponds to rocks and the rest to ice (Anderson et al., 1996).

Further information on the interior of the moon is obtained by analysing its gravity field. After decomposition of the gravitational potential in spherical harmonics, Doppler radio tracking measurements enabled to determine Ganymede's gravitational quadrupole. Under the assumptions of hydrostatic equilibrium and sphericity of the moon, knowledge of the quadrupole and of Ganymede's mass M_G enabled to determine its dimensionless moment of inertia $C/(M_G R_G^2)$ with R_G its radius. For a homogeneous sphere the value of the dimensionless moment of inertia is 2/5; a lower (respectively larger) value indicates that mass is more concentrated at the centre (respectively at the periphery) of the planet (Schubert et al., 2004). Ganymede's dimensionless moment of inertia was found the lowest of all satellites and rocky planets in the solar system (Anderson et al., 1996), equal to 0.3115 ± 0.0028 (Schubert et al., 2004). Compared to the reference 2/5 of a homogeneous body, this very low value (Anderson et al., 1996) was interpreted as a sign of further differentiation in three layers (from the centre to the periphery: metal, rock and ice, see Kuskov and Kronrod (2001); Sohl et al. (2002)) which might have been favoured by past tidal heating (Turcotte and Schubert, 2002) and by radiogenic heating that could have melted the metal and rocks of Ganymede (Schubert et al., 2004).

An additional strong argument in favour of a deep layer of partially or fully molten metal in Ganymede comes from its magnetic field. The Galileo mission revealed an intense dipolar magnetic field in its vicinity (Kivelson et al., 1996), with a slight 4° tilt with respect to the rotation axis (Kivelson et al., 2002), and of strength 719 nT at the equator. This value is much larger than the locally uniform jovian field of strength 100 nT; additionally, this local magnetic field is clearly delimited by a magnetopause and it converges towards the centre of Ganymede, strongly suggesting that it originates from Ganymede's interior (Kivelson et al., 1996). We discuss the properties and possible origins of this magnetic field in the next section.

5.1.1.2 Origin of Ganymede's magnetic field

A priori, three mechanisms could account for the generation of Ganymede's intrinsic magnetic field.

The first mechanism is *remanent magnetisation* or *remanence*. It would impose constraints on the location of the source: the source cannot be too deep since its temperature cannot exceed the Curie temperature, and it must be located in the rocky layer of the moon. Under these considerations, Schubert et al. (1996) showed that a 300 km-deep layer of rocks could be ferromagnetic in Ganymede at the top of the rocky layer. The question is then: could this layer produce a magnetic field as intense as that of Ganymede ? Although this possibility cannot be ruled out (Kivelson et al., 1996), it remains unlikely due to the implausibly large amounts of magnetite required (Scott et al., 2002), and due to the large external field required for the remanent magnetisation to be sufficiently intense (Schubert et al., 1996; Kivelson et al., 1996), much above the present-day jovian magnetic field. A paleomagnetic field originating from a primordial deep dynamo in Ganymede could have led to a sufficient remanence, but this paleomagnetic field should have been 15 times larger than the present-day jovian field or even larger (Crary and Bagenal, 1998; Schubert et al., 2004). As a consequence, remanence is considered unlikely for the generation of Ganymede's magnetic field.

The second mechanism of magnetic field production is *magnetic induction*. This corresponds to the induction of a perturbative magnetic field due to the movement of an electrically conducting fluid that is embedded in an external magnetic field – here, the one of Jupiter. This scenario only requires the presence of such a fluid layer in Ganymede because, unlike dynamo, induction is subject to no threshold on the magnetic Reynolds number for the perturbative magnetic field to be generated (see the Introduction). Essentially two electrically-conducting fluid layers may exist in Ganymede: deep in the satellite in the partially or fully molten metal core, and likely in a sub-surface ocean of salty water. Nonetheless, authors have argued that the magnetic fields that can be produced at a global scale by induction cannot exceed much the external field that feeds them (Schubert et al., 1996, 2004; Kivelson et al., 2002). Therefore, although the next paragraphs will show that induction can be the origin of the quadrupole component of Ganymede's magnetic field, this mechanism is considered inappropriate to explain the 719 nT dipole which is too large compared to the 100 nT jovian field in the vicinity of Ganymede.

The third mechanism is *dynamo*, which is the preferred candidate to explain the origin of Ganymede's dipole at least. Again, this dynamo may originate from any of the two electrically-conducting fluid layers mentioned above. Taking the typical electrical conductivity of salt water and considering a typical thickness of several hundreds of kilometers for the subsurface ocean, Schubert et al. (1996) showed that, for a dynamo to meet the requirement $Re_m > 10$ in a salty subsurface ocean, the values of flow velocity would need to reach the order of 1 m.s^{-1}. This was deemed implausibly large by comparison with the typical velocity 10^{-4} m.s^{-1} in the Earth core. Although this comparison does not rule out the possible existence of these motions, it was concluded that the dynamo most likely originates from a layer of liquid metal in the core of the satellite, again supporting the differentiation of Ganymede in three layers, and it imposes that at least a fraction of the metal core should still be molten today.

5.1.1.3 Structure and composition of Ganymede

To determine the structure of a satellite made of three supposedly uniform layers with spherical symmetry, there exist five unknowns: the density of each layer (ρ_c for the core, ρ_{mant} for the

mantle, ρ_{ice} for the outer icy shell, part of which can be liquid), the radius r_c separating the core and the mantle, and the radius r_{mant} separating the mantle from the icy shell. The satellite's structure should comply with three geodetic constraints (Schubert et al., 2004; Hauck II et al., 2006; Sohl et al., 2002)

1. the average density $\overline{\rho}_G = 3M_G/4\pi R_G^3 = 1942$ kg/m^3,
2. the radius $R_G = 2631$ km,
3. the dimensionless axial moment of inertia $C/M_G R_G^2 = 0.3115$.

The radius R_G imposes the available range of values for r_c and r_{mant}. Then, the definition of the satellite's density provides a first equation relating the size and density of each spherical shell as (Schubert et al., 2004)

$$\overline{\rho}_G = \rho_{\text{ice}} + (\rho_c - \rho_{\text{mant}}) \left(\frac{r_c}{R_G}\right)^3 + (\rho_{\text{mant}} - \rho_{\text{ice}}) \left(\frac{r_{\text{mant}}}{R_G}\right)^3 . \tag{5.1}$$

An additional similar equation can be obtained from the definition of the axial moment of inertia (Schubert et al., 2004; Kuskov and Kronrod, 2001) which yields

$$\overline{\rho}_G \frac{C}{M_G R_G^2} = \frac{2}{5} \left[\rho_{\text{ice}} + (\rho_c - \rho_{\text{mant}}) \left(\frac{r_c}{R_G}\right)^5 + (\rho_{\text{mant}} - \rho_{\text{ice}}) \left(\frac{r_{\text{mant}}}{R_G}\right)^5 \right] . \tag{5.2}$$

These two equations and the three constraints hereabove are insufficient to determine a unique structure for Ganymede due to large uncertainties on the five unknowns (Anderson et al., 1996). If only one or two of the five unknowns are fixed to values that are deemed relevant from the literature, a number of models can be obtained, which must be sorted owing to their compatibility with the geodetic constraints and other cosmochemical considerations (see the discussion of figure 13.4 in Schubert et al. (2004)). If three unknowns are fixed, then the whole structure of the planet is determined from equations (5.1)-(5.2). The typical structures presented by Sohl et al. (2002) have a fixed ice density in the range $950 - 1300$ kg/m^3, a mantle whose density is chosen close to that of olivine ($\rho_{\text{mant}} = 3222$ kg/m^3) because this mineral is dominant in the upper mantle of the Earth (Schubert et al., 2004), and a core density varying typically between 5000 kg/m^3 (eutectic composition) and 8000 kg/m^3 (pure iron). They obtain typically $r_c/R_G \in [1/3, 1/4]$ and $r_{\text{mant}} \sim 0.65 R_G$ (see three examples in figure 5.1). Of course, such results are essentially guiding values since they depend on the initial choice of the ice and mantle compositions (Schubert et al., 2004), and results are highly sensitive due to the high powers on the radii in equations (5.1)-(5.2).

A close inspection of the core composition is required to discuss the possibility of a dynamo. Little is known with exactitude about this composition because of the scarcity of available measurements. Due to the constraints on Ganymede's moment of inertia and on the origin of its magnetic field in a deep electrical conductor, the presence of an iron-rich core in Ganymede is not debated. The presence of lighter elements and their proportion is, however, more complex to settle. A common starting guess for the bulk composition of a body is that of the protosolar nebula, i.e. the solar composition, because it is preserved in bodies that have not experienced

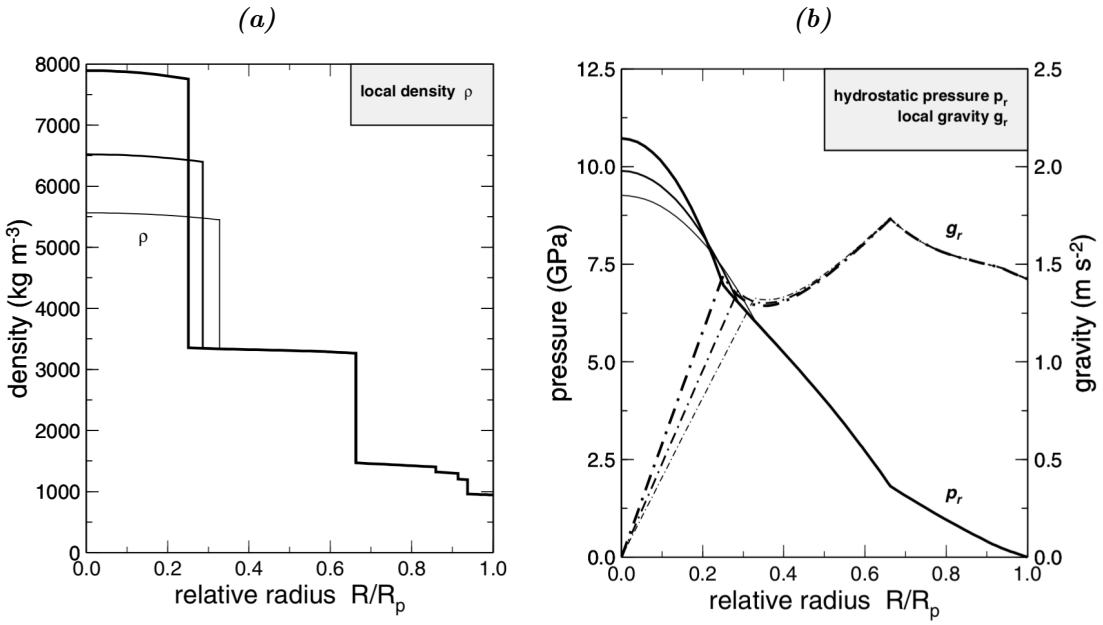

Figure 5.1: *Profiles of (a) density, (b) pressure and gravity for three possible structures of Ganymede: a pure iron core (bold curve), a pure iron sulphide core (thin line) and a 50-50*wt% *composition (semibold line). Figures (a) and (b) respectively correspond to figures 9 and 10 of Sohl et al. (2002) whose notation R_p corresponds to Ganymede's radius which is denoted R_G in this manuscript.*

mineral alteration or metamorphism (Robert and Bousquet, 2013). Sulfur being abundant in the protosolar nebula (Canup and Righter, 2000) and siderophilic, it has been considered a good candidate for a lighter element in iron-rich planetary cores (Breuer et al., 2015) amongst which Ganymede (Hauck II et al., 2006) (see figure 1 in Hirose et al., 2013). Although many more light elements could be plausible candidates (Hirose et al., 2013), Breuer et al. (2015) remarked that most experimental and theoretical studies on the thermochemistry at the core pressures and temperatures have focused on the iron-and-sulfur system. Such a simple system has also been commonly considered a good approximation of the core chemistry given the few constraints available to refine the composition.

The question is then: What is the proportion of sulfur in Ganymede's core? The answer to this question is decisive for the whole scenario of core crystallisation which is discussed in the next section.

5.1.2 Regimes of crystallisation in an Fe-FeS core

5.1.2.1 Thermochemistry of the Fe-FeS system

At the typical pressures of Ganymede's core, the iron-sulfur system is eutectic as shown by the binary phase diagrams in figure 5.2a which correspond to figure 2 in Fei et al. (1997). The liquidus that separates the region of fully liquid state (very top of each diagram) from the regions containing both solid and liquid (circular sectors labelled Fe+L and FeS+L) admits a minimum at the eutectic composition $x_{S,e}$ which is paramount for the core crystallisation. To understand

why, consider a sample of liquid that is initially at a very large temperature with a composition lying on the iron-rich side of the eutectic ($x_S < x_{S,e}$, situation of the star A in figure 5.2b). Keeping the pressure constant, as the sample is cooled down it gradually approaches the liquidus where the first crystal of solid appears (star B). For the present binary diagram with $x_S < x_{S,e}$, this crystal is made of pure iron Fe(s) (grey circle), while the composition of the liquid follows the liquidus (yellow circle). As the sample is cooled further down, it now lies in a region where the solid and liquid coexist (star C). Again the composition of any new solid crystal is pure iron Fe(s); as for the liquid, its composition is given by the abscissa of the intersection between the liquidus and the sample temperature along the horizontal (see the horizontal dotted line). Therefore, as the sample cools down, the liquid gets richer in light element because of depletion of iron which goes into the solid phase due to solidification. When the sample temperature reaches the eutectic temperature, the composition of the last drop of liquid is the eutectic composition. Further down, two solids are present: pure iron on one hand whose first crystal appeared when the sample temperature first contacted the liquidus, and FeS(s) whose first crystal appears once the sample temperature reaches the eutectic temperature.

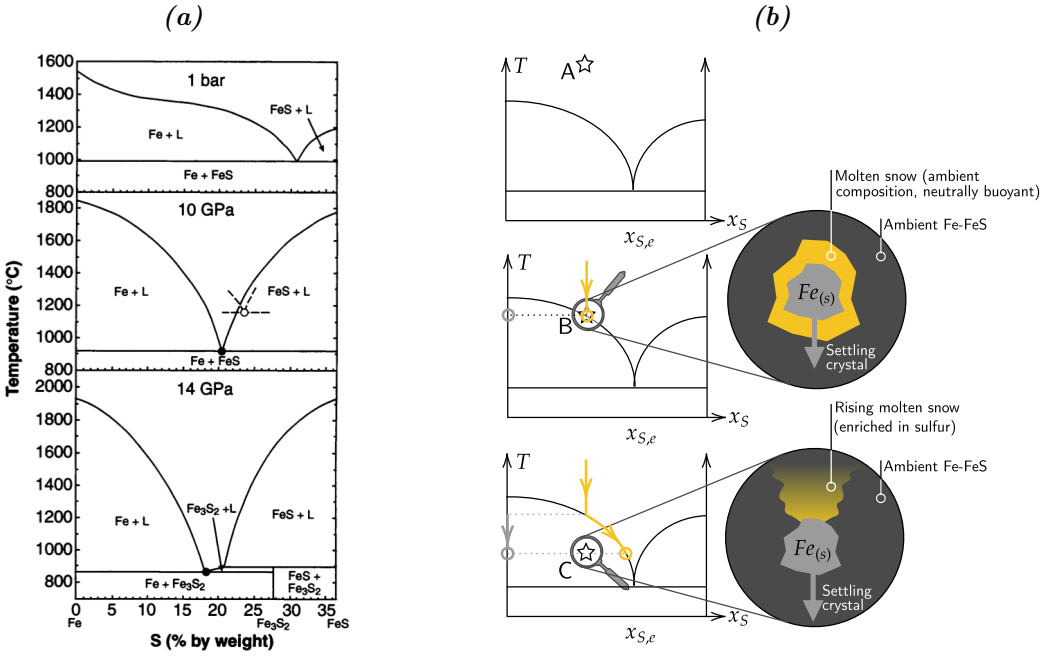

Figure 5.2: *(a) Binary phase diagrams of the Fe-FeS system at pressures of* 1 GPa, 10 GPa *and* 14 GPa. *These diagrams are extracted from figure 2 in Fei et al. (1997). (b) Evolution of a system that is cooled from situation A to situation C on the iron-rich side of the eutectic, with sketches of the solid-melt separation.*

Consider now a sample at a very large temperature with a composition lying on the sulfur-rich side of the eutectic. As the system cools down, the first crystal of solid that appears is FeS(s) when the sample temperature contacts the liquidus; then FeS(s) keeps crystallising while the residual liquid gets richer in iron. Once the eutectic temperature is reached, the first crystal of Fe(s) appears, and for a sub-eutectic temperature, the two solids Fe(s) and FeS(s) are present.

Finally, consider a sample that is initially at a very large temperature with a eutectic composition. As the sample cools down, no solidication happens before the eutectic composition is reached. At that point, both Fe(s) and FeS(s) crystallise while the residual liquid keeps a eutectic composition. Indeed, the composition for which an initially hot and fully liquid mixture of Fe-FeS solidifies the latest is the eutectic composition; additionally, solidification of a eutectic mixture leaves the liquid composition (and density) unmodified.

5.1.2.2 Iron snow or iron sulphide crystallisation?

In the light of these elements, the comparison between the core composition and the eutectic composition appears decisive. If the core is on the iron-rich side of the eutectic, and if there exists a region of the core with super-eutectic temperature yet sufficiently cold for crystals to form, then crystals are made of pure iron Fe(s) whereas the liquid contains sulfur. Consequently, the crystals are denser than the fluid, so they settle towards the centre of the core: this is the phenomenon of iron snow. Since the residual liquid is itself enriched in sulfur, it is lighter than the ambient and it rises towards the CMB.

Alternatively, if the core crystallises on the sulfur-rich side of the eutectic, the crystals that appear are FeS(s), whose concentration in sulfur is at most $x_S = 36.5\text{wt}\%$. Whether the density of these crystals is lighter or denser than the ambient fluid depends on the composition of the liquid and is uncertain (Rückriemen et al., 2018); several studies assume that the crystals are lighter than the ambient (Breuer et al., 2015). In that case the crystals rise towards the CMB; since the residual liquid is more concentrated in iron than the ambient, it is denser so it sinks towards the centre of the core.

These considerations evidence the key role of the proportion of sulfur in Ganymede's core. Unfortunately, the latter is very poorly constrained. In models of the structure of Ganymede, varying the amount of sulfur in the core implies a variation of the core radius r_c, but due to the wide range of compatible values for r_c, the range of acceptable values for the sulfur concentration remains large. Other considerations like the link between this concentration and the heat flux coming out from the core hardly provide more constraint. By analysing the reaction of water with material of chondritic chemistry at 1.5GPa and temperatures in the range $300-800°\text{C}$, Scott et al. (2002) tried to reproduce the conditions of accretion and differentation, during which silicates were expected to react with aqueous material in Ganymede. Pyrrhotite, a mineral composed of iron and sulfur, was the sole dense iron-rich phase they obtained, which led them to conclude that the core of Ganymede is likely on the sulfur-rich side of the eutectic. Yet, Breuer et al. (2015) remark that this suggestion based on the chemistry of type I carbonaceous chondrite (CI) cannot be validated since the oxidation state of Ganymede remains unknown. In addition, the pressures considered are those expected at the base of the icy layer (Scott et al., 2002), much lower than those deep in Ganymede; hence depending on the history of metal-silicate mixing, equilibration might have been very different as metal sank down towards larger pressures and temperatures – see chapter 3.

For simplicity and brevity, the rest of this presentation focuses on the configuration of iron snow. Most of the physics that is described and analysed in the next sections can be adapted to other geophysical flows that involve crystallisation, sedimentation and melting, including FeS(s) formation in planetary cores.

5.1.2.3 Iron snow: top-down crystallisation above convection

Under the assumption that the core composition is on the iron-rich side of the eutectic, the next key aspect is to determine where crystallisation happens. The familiar situation that happens on Earth corresponds to iron crystals forming at the centre of the core: the solid crystals form a solid inner core that grows while the light residual liquid rises towards the CMB, possibly driving a compositional convection. However, thermochemistry tells us that in Ganymede's core, a sub-eutectic sulfur concentration x_S leads to core crystallisation close to the CMB. This conclusion is not trivial. It is the result of several laboratory studies that analysed the different phases in the Fe-S system at high pressure and temperature (e.g. Fei et al., 1995, 1997, 2000), sometimes overlapping with the relevant values expected in Ganymede's core.

Schematically, Ganymede was very hot after differentiation with a temperature above the core liquidus at all depths; since then, it has cooled down with a very slow rate 0.01 K/Myr (Hauck II et al., 2006). Therefore, the location where crystallisation starts corresponds to the depth where the liquidus and the core temperature first cross. Little is known about the thermal state of Ganymede's core; if it is vigorously convecting, the temperature profile might be adiabatic, otherwise it should be subadiabatic, and no result enables to quantify to what extent. An adiabatic profile is commonly adopted and conveniently assumed to enable modelling of the core temperature (Rückriemen et al., 2015, 2018). The adiabat depends on the thermal conductivity, the thermal expansivity and the specific heat capacity of the liquid metal, the former two being very poorly constrained (Breuer et al., 2015; Rückriemen et al., 2015, 2018).

The liquidus temperature depends both on pressure and composition. Often, the evolution of the eutectic temperature is analysed as a reference, since the liquidus temperature of other compositions can then be obtained by interpolation between the eutectic and the pure-iron end member when experimental data are unavailable. For example, Hauck II et al. (2006) used a linear interpolation (see their figure 3) which likely underestimates the liquidus temperature since the latter is usually a concave function of sulfur composition – see figure 5.2a. Rivoldini and collaborators (Rivoldini et al., 2011; Dumberry and Rivoldini, 2015) obtained a decreasing eutectic temperature as a function of pressure down to 14 GPa (figure 2 in Rivoldini et al., 2011) i.e. for the whole range $6 - 10$ GPa expected in Ganymede's core (Rückriemen et al. (2015), see figure 5.1b). This trend is also the one visible in the three binary diagrams of figure 5.2a. However, more measurements from additional studies show that at pressures $6 - 10$ GPa the eutectic temperature is non-monotonic with pressure, as shown in figure 5.3a extracted from Chudinovskikh and Boehler (2007). Buono and Walker (2011) fitted the eutectic temperature as a function of pressure (in the range $1 - 10$ GPa) and sulfur concentration, and the resulting correlation was used by Rückriemen et al. (2015, 2018) for their models. All these studies lead to the same conclusion: either because the liquidus temperature decreases in depth or because it increases with a steeper gradient than the core temperature, core crystallisation is expected to start at the CMB in Ganymede. This start of crystallisation is illustrated by some of the results of Rückriemen et al. (2018) in figure 5.3b: the liquidus (dashed line) and adiabat (solid line) initially cross at the CMB, as shown for four values of the sulfur concentration.

As crystals grow, the fluid released is more concentrated in sulfur. Since the snow zone is more and more depleted in iron, its average sulfur concentration increases. As visible in

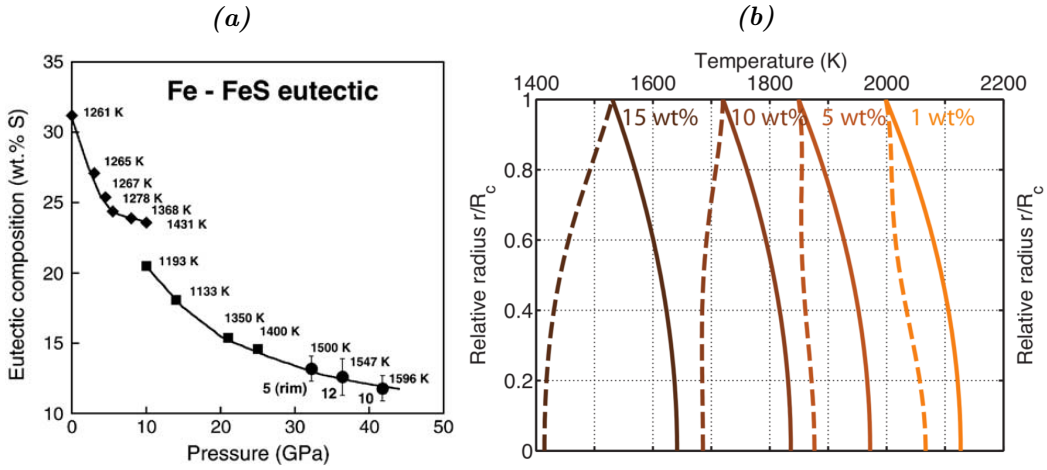

Figure 5.3: *(a) Evolution of the eutectic composition and temperature of the system Fe-FeS as a function of pressure. Figure extracted from Chudinovskikh and Boehler (2007). (b) Evolution of the liquidus (dashed lines) and adiabat (solid line) in Ganymede's core (the ordinate is the dimensionless radial coordinate starting from the core centre $r = 0$ to the CMB when $r = R_c$) for four different sulfur compositions $x_S \in \{1, 5, 10, 15\}$ wt%. Figure extracted from Rückriemen et al. (2018).*

figure 5.2b, it means the liquidus temperature in the snow zone should be lower than in the absence of crystallisation. Therefore, as the core temperature keeps decreasing due to secular cooling, the liquidus follows the core temperature due to the local enrichment in sulfur. If the system evolves on the edge of a thermodynamic equilibrium, crystallisation keeps going while the liquidus and core temperature are colinear (see figure 5 in Rückriemen et al., 2015). If supercooling is taken into account, the core temperature can be lower than the liquidus; this out-of-equilibrium configuration is disregarded in this presentation.

Consider now the bottom of the snow zone at the crossing point of the liquidus and the core temperature. Just below the snow zone, the core temperature is still above the liquidus, that is why iron flakes remelt. During remelting, the fluid is enriched in iron so the liquidus temperature is now larger than in the absence of remelting. Again, this reduces the gap between the local core temperature and the liquidus. The liquidus ultimately increases up to the local core temperature, guaranteeing the downward progression of the snow zone due to the gradual shift of the liquidus.

Note however that the dense molten snow produced by the remelting snow flakes cannot accumulate at the lower boundary of the snow zone because this fluid is more concentrated in iron than the underlying fluid, hence it is denser. As a consequence, this dense molten snow should sink in the deeper core. This sinking has been assumed to feed a compositional convection at the core scale (Christensen, 2015; Rückriemen et al., 2015, 2018).

Since a dynamo action requires motions of the electrically conducting liquid metal, both the fall of snow flakes (Hauck II et al., 2006) and the compositional convection (Christensen, 2015; Rückriemen et al., 2015, 2018) have been considered as plausible candidates nourishing the dynamo. Neglecting the stratification of the snow zone, and disregarding crystallisation, the previous Chapters can provide insights on the flows that can be forced by settling particles

in this layer, whether they settle as transient particle clouds (see Chapters 1 and 2) or quasi-steady plumes (see Chapter 4). We choose in this chapter to focus on the remelting of snow flakes, so the next section presents key results of numerical models from the literature that do not resolve the snow zone and only consider the compositional convection as the source of the magnetic field.

5.1.3 Iron snow from reference models of Ganymede's thermal evolution

Our calculations on the evolution of snow flakes in Ganymede are based on the results of the model of Rückriemen et al. (2015, 2018), so we recall the main elements of their model.

Rückriemen et al. (2015) model the thermal evolution of Ganymede's core in a 1D model along the radial coordinate, while varying three control parameters that are poorly constrained by the literature: the thermal conductivity of the core, the heat flux going out of the CMB, and the initial bulk sulfur concentration in the core. The snow zone is assumed both thermally and compositionally stratified, therefore its evolution is solved with a heat conduction equation, from the CMB down to the depth where the core temperature crosses the liquidus. The boundary conditions are the imposed heat flux at the CMB, and the temperature at the bottom of the snow zone.

To determine this latter temperature, the conservation of energy is solved in the deeper convective core. Because convection is assumed sufficiently vigorous, the temperature profile is imposed as adiabatic in this region, with a continuous temperature at the bottom of the snow zone. Rückriemen et al. (2015) assume that the snow zone prescribes the thermal evolution of the deeper core. Therefore, they assume that if the convective heat flux right below the snow zone is larger than the conductive heat flux right above this interface, then this excess heat remains in the convective zone, advected downward by convective motions.

The equations of evolution of temperature in both layers depend on the rate of solidification in the snow zone, because solidification releases latent heat in the snow zone, whereas remelting (which is also related to the rate of solidification) absorbs latent heat in the convective zone. The system is assumed to evolve in a limit of small supercooling, so that the mass fraction of iron at a given time and depth in the snow zone is given by the lever rule applied to the binary phase diagram. The time evolution of this mass fraction gives the rate of crystallisation.

They estimate that crystallisation, settling and remelting all last much shorter than the 1 Myr-timestep they use in their numerical model, so they assume that the integral of the rate of solidification in the snow zone is equal to the total rate of remelting during each timestep. The conversion of the mass flux of molten snow into heat is calculated with parameters at the bottom of the snow zone because remelting is supposed so fast that snow flakes remelt very close to this interface. Estimates about the crystallisation and settling of snow flakes are based on the assumption that crystals would have a typical size $r_p = 10$ μm, that they would settle as spheres with the Stokes velocity, and that supercooling could be of order 0.01 K below the liquidus in the snow zone.

Finally, they consider that dynamo is possible if the magnetic Reynolds number Re_m is larger than 100. The number Re_m is proportional to the root-mean-square velocity, which Rückriemen et al. (2015) estimate from a scaling law of Aubert et al. (2009). The latter

depends on the rotation rate of the planet, the size and density of the convective zone, and the total dissipation of the dynamo, which is equal to the product of the total mass anomaly flux multiplied by the average difference of the gravitational potential.

The next sections present a model that draws some first conclusions on the remelting of snow flakes in an iron-rich core with a snow zone spanning through 10% of the core thickness and which delivers a mass flux of order 1000 kg.s^{-1}, these values corresponding to typical results of Rückriemen et al. (2015).

Quantity	Notation	Value	Reference
Radius of Ganymede	R_G	2631.2 ± 1.7 km	[1]
Mass of Ganymede	M_G	1481.7×10^{20} kg	[2]
Axial moment of inertia	$C/M_G R_G^2$	0.3115 ± 0.0028	[1]
Angular velocity of Ganymede	Ω_G	1.02×10^{-5} rad.s^{-1}	[3]
Average density of Ganymede	$\overline{\rho}_G$	1942.0 ± 4.8 kg.m^{-3}	[1]
Core thermal expansivity	α_c	9×10^{-5} K^{-1}	[4]
Core specific heat capacity	$c_{p,c}$	800 J.K^{-1}.kg^{-1}	[4]
Magnetic diffusivity	η_m	1 m^2.s^{-1}	[5,6]
Kinematic viscosity of the bulk core	ν_c	2.22×10^{-6} m^2.s^{-1}	[7]
Specific entropy of fusion of pure iron	ΔS_{fus}	136 J.kg^{-1}.K^{-1}	[4]
Latent heat of fusion of pure iron	$\mathcal{L}_{\text{fus}}$	$\Delta S_{\text{fus}} \times T_{\text{Liq}}(z)$ J.kg^{-1}	[4]
Heat conductivity of pure solid iron	k_{Fe}	55 W.m^{-1}.K^{-1}	[5]
Thermal diffusivity of liquid iron	κ_{th}	10^{-6} m^2.s^{-1}	[5]

Table 5.1: *Values adopted to model the structure of Ganymede with concentric uniform spherical shells, and the remelting of snow flakes. References correspond to: [1] Schubert et al. (2004); [2] Sohl et al. (2002); [3] Olson et al. (2017); [4] Rückriemen et al. (2018); [5] Rückriemen et al. (2015); [6] Pozzo et al. (2014); [7] Dobson et al. (2000).*

5.2 A simple three-layers model of Ganymede

To model plumes of snow flakes in Ganymede's core, we need to know the core size, as well as its profiles of density, pressure, temperature and gravity along the radial direction r. We therefore propose a simple model of Ganymede based on those of Sohl et al. (2002). Our present aim is only to get relevant orders of magnitude of all thermodynamical properties to get first-order estimates about the remelting of iron snow flakes.

The starting point is the equations for the mean density (5.1) and axial moment of inertia (5.2) of Ganymede. Isolating for $\rho_c - \rho_{\text{mant}}$ in equation (5.1) on one hand, and subtracting equation (5.2) from equation (5.1) on the other hand, after substitution of $\rho_c - \rho_{\text{mant}}$ the core

radius reads

$$\left(\frac{r_c}{R_G}\right)^2 = \frac{\frac{5C}{2M_G R_G^2}\overline{\rho}_G - \rho_{\text{ice}} - (\rho_{\text{mant}} - \rho_{\text{ice}})\left(\frac{r_{\text{mant}}}{R_G}\right)^5}{\overline{\rho}_G - \rho_{\text{ice}} - (\rho_{\text{mant}} - \rho_{\text{ice}})\left(\frac{r_{\text{mant}}}{R_G}\right)^3}\,, \tag{5.3}$$

from which the core density is immediately obtained from equation (5.1)

$$\rho_c = \rho_{\text{mant}} + \left[\overline{\rho}_G - \rho_{\text{ice}} - (\rho_{\text{mant}} - \rho_{\text{ice}})\left(\frac{r_{\text{mant}}}{R_G}\right)^3\right]\left(\frac{R_G}{r_c}\right)^3\,. \tag{5.4}$$

The gravity field inside Ganymede is readily obtained from Gauss's theorem and reads

$$\frac{3g(r)}{4\pi G} = \begin{cases} \rho_c r, & \text{if } r < r_c \\ \Pi_{\text{mant}} r^{-2} + \rho_{\text{mant}} r, & \text{if } r_c \leq r < r_{\text{mant}} \\ \Pi_{\text{ice}} r^{-2} + \rho_{\text{ice}} r, & \text{if } r_{\text{mant}} \leq r \leq R_G \end{cases} \tag{5.5}$$

with

$$\Pi_{\text{mant}} = r_c^3(\rho_c - \rho_{\text{mant}}); \quad \Pi_{\text{ice}} = (\rho_c r_c^3 + \rho_{\text{mant}} r_{\text{mant}}^3 - \rho_{\text{mant}} r_c^3 - \rho_{\text{ice}} r_{\text{mant}}^3)\,. \tag{5.6}$$

Lastly, the pressure field is computed under the assumption of hydrostatic equilibrium:

$$\frac{3P(r)}{4\pi G} = \begin{cases} \frac{3P(r_c)}{4\pi G} + \rho_c^2(r_c^2 - r^2)/2, & \text{if } r < r_c \\ \frac{3P(r_{\text{mant}})}{4\pi G} + \Pi_{\text{mant}}\rho_{\text{mant}}(r^{-1} - r_{\text{mant}}^{-1}) + \rho_{\text{mant}}^2(r_{\text{mant}}^2 - r^2)/2, & \text{if } r_c \leq r < r_{\text{mant}} \\ \Pi_{\text{ice}}\rho_{\text{ice}}(r^{-1} - R_G^{-1}) + \rho_{\text{ice}}^2(R_G^2 - r^2)/2. & \text{if } r_{\text{mant}} \leq r \leq R_G \end{cases} \tag{5.7}$$

Typical values adopted for the calculations are reported in table 5.1. Notations are illustrated in figure 5.4, which shows an intermediate *precipitation layer* (abbreviated PL) between the snow zone and the convective zone: this is the zone where snow flakes have started remelting but not yet finished. The presence of such a zone is neglected in previous models based on instantaneous melting.

Equations (5.3) to (5.7) enable to relate pressure, density and the radial position; the core temperature is the final requirement to have a full description of the core. Rückriemen et al. (2018) have shown that thermal convection may have happened in the early history of Ganymede. If vigorous enough, this convection might have led to an adiabatic temperature profile in Ganymede's core. This phase of thermal convection was short-lived according to their model, lasting about a few Myr as shown by their figure 7d. As discussed in their section 5.2, the time lapse between the end of thermal convection and the onset of iron snow controls how subadiabatic the core heat flux might be when core crystallisation starts. Due to the lack of data and to keep all considerations simple, we align with the model of Rückriemen et al. (2018) and adopt an adiabatic temperature profile in Ganymede's core as a first estimate. Therefore we model the core with the following adiabatic temperature profile

$$T(r) = T_{\text{PL}} \exp\left[-\frac{\alpha_c}{c_{p,c}}\frac{2}{3}\pi G\rho_c(r^2 - r_{\text{PL}}^2)\right] \tag{5.8}$$

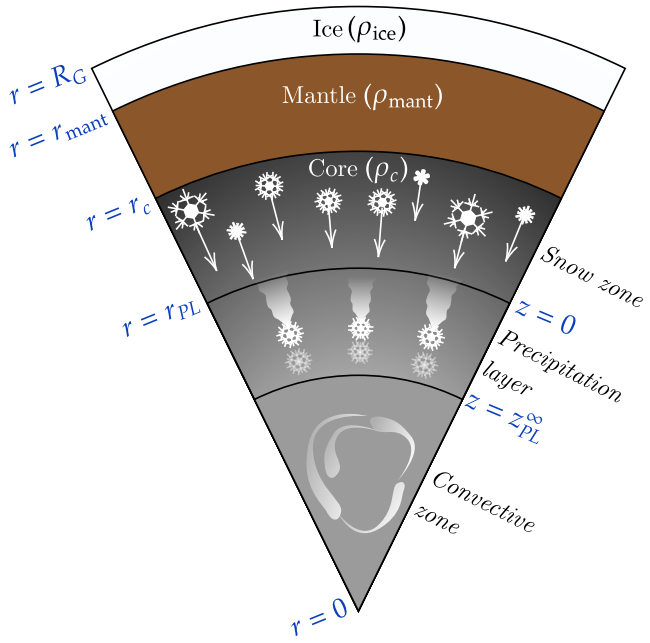

Figure 5.4: *Structure of Ganymede with the constant densities of the three main layers (proportions are not respected). On the left-hand side, radii indicate interfaces between different regions. On the right-hand side the vertical coordinate z is used to describe profiles in the precipitation layer.*

where T_{PL} is the temperature at the bottom of the snow zone i.e. at the top of the precipitation layer, α_c is the core thermal expansivity, $c_{p,c}$ is the core specific heat capacity, $G = 6.67 \times 10^{-11}$ N.m^2.kg^{-2}, ρ_c is the uniform core density and r_{PL} is the radial position of the top of the precipitation layer (see figure 5.4). We also adopt the same model of liquidus T_{Liq} as Rückriemen et al. (2018) which originates from the study of Buono and Walker (2011) (see their equation 29); its evolution with pressure and sulfur composition is shown in figure 5.5. In reference to the nominal case in Rückriemen et al. (2018), the value of sulfur mass fraction 10.93 wt% is adopted to compute the liquidus.

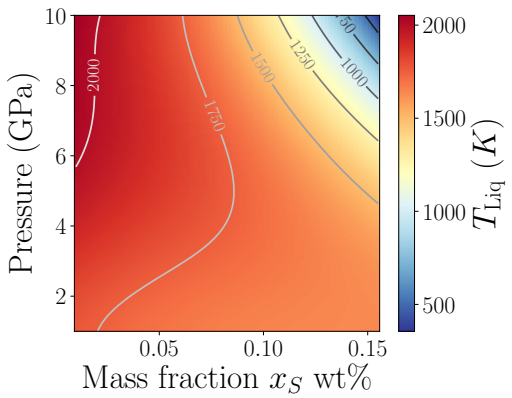

Figure 5.5: *Evolution of the liquidus temperature T_{Liq} with pressure and the sulfur mass fraction x_S.*

Quantity	Notation	Value	Reference
Sulfur mass fraction	x_S	10.93 wt%	[1]
Ice density	ρ_{ice}	1215 kg.m^{-3}	[1]
Mantle density	ρ_{mant}	3300 kg.m^{-3}	[1]
CMB position	r_{mant}	1770 km	[1]
Core density	ρ_c	5843 kg.m^{-3}	Equation (5.4)
Core radius	r_c	871 km	Equation (5.3)
Top of the precipitation layer	r_{PL}	$0.9r_c$	[2]
Total mass rate in the core	-	10^3 kg.s^{-1}	[2]
Mass flux	$\dot{m}''$	1.29×10^{-10} kg.m^{-2}.s^{-1}	deduced from [2]
Density of solid iron	ρ_{Fe}	$\rho_c + 1000$ kg.m^{-3}	[2]

Table 5.2: *Nominal values for the structure of Ganymede and the scenario of core crystallisation. References correspond to: [1] Rückriemen et al. (2018); [2] Rückriemen et al. (2015).*

The core density depends severely on small variations of the ice density, the mantle density or the radius r_{mant} due to the high powers in equations (5.3)-(5.4). Rather than tuning the values of ρ_{ice}, ρ_{mant} and r_{mant}, we decided to impose these three quantities with values taken from the literature, namely $\rho_{\text{ice}} = 1215$ kg.m^{-3}, $\rho_{\text{mant}} = 3300$ kg.m^{-3}, $r_{\text{mant}} = 1770$ km and $x_S = 10.93$ wt% (see references in table 5.2). Figure 5.6a shows the final nominal structure, which is very similar to those obtained by Sohl et al. (2002) visible in figure 5.1. The core radius is $r_c = 871$ km and the core density is $\rho_c = 5843$ kg.m^{-3} which fits in the range of core densities obtained in the literature (e.g. Rückriemen et al. (2018); Sohl et al. (2002); Breuer et al. (2015); Zhan and Schubert (2012)). Figure 5.6b shows the evolution of the core adiabat (dashed dark line) and the core liquidus (dashed blue line) as a function of the radial coordinate. The curves have been calculated under the assumption that crystallisation is just starting at the CMB i.e. $r_{\text{PL}} = r_c$, which is why they cross at the very top of the iron core. It is important to note that the temperature contrast $T(z) - T_{\text{Liq}}(z)$ increases with depth: this means that an isolated snow flake should remelt faster and faster as it sinks deeper in the precipitation layer.

Having an estimate of the gravity field and the temperature contrast $T(z) - T_{\text{Liq}}(z)$ was the motivation for the present simple model, since they govern the settling and remelting of snow flakes. This ensures that the results obtained in the next sections are representative of the conditions in Ganymede's core. Yet, some subtle effects have not been included. For example, the liquidus and adiabat depend on the sulfur mass fraction, which we take into account: additional curves in figure 5.6b show that an increase of the sulfur mass fraction increases the temperature contrast at all depths. However, we did not take into account the fact that x_S and ρ_c are coupled: cores that are more sulfur-rich have a lower density. A consequence is that these cores are larger to verify the geodetic constraints. More sophisticated parameterisations exist that account for such effects (Rückriemen et al., 2015, 2018); these elements are beyond the scope of this chapter, and the reader is referred to those studies for more details.

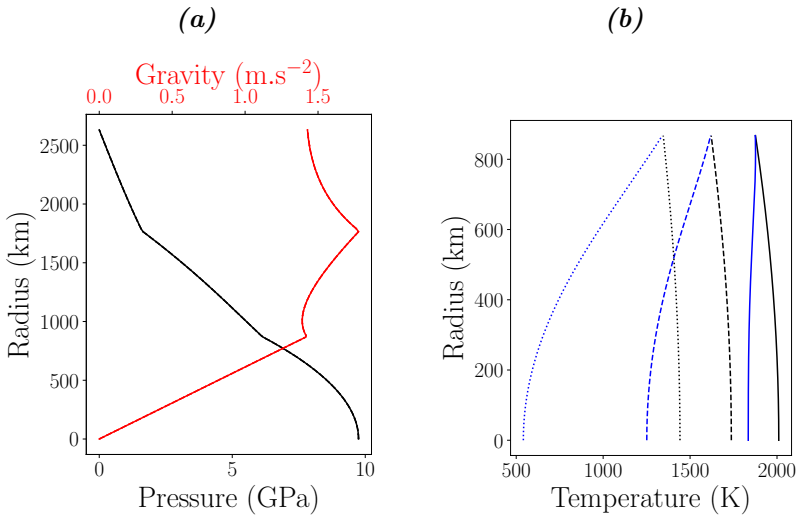

Figure 5.6: *(a) Nominal structure of Ganymede when imposing* $\rho_{\text{ice}} = 1215$ kg.m^{-3}, $r_{\text{mant}} = 1770$ km *and* $x_S = 10.93$ wt%. *With the present model, varying the sulfur mass fraction does not modify the core density hence the gravity and pressure fields remain the same. Varying* x_S *modifies the core liquidus (blue lines) and the core adiabat (dark lines), as shown for* $r \leq r_c$ *in (b) as a function of the radial position* r. *Lines correspond to* $x_S = 5$ wt% (——), $x_S = 10.93$ wt% (- - -), $x_S = 15$ wt% (·····).

5.3 Modelling steady precipitation-driven plumes

To model plumes that are forced by the precipitation of snow flakes, we start from the results obtained in experiments of settling and dissolving grains of sugar in Chapter 4. The sugary plumes reached a quasi-steady regime characterised by a constant velocity for a constant plume radius R_{plume}. Essential elements of the model are recalled here (see section 4.6.3 for more details). The characteristic plume velocity U_{plume} is obtained by balancing the plume inertia with its buoyancy, leading to the following cubic equation

$$U_{\text{plume}}^3 + U_{\text{plume}}^2 w_s = \frac{\dot{m}'' R_{\text{plume}} g}{\rho_c} \ , \tag{5.9}$$

where $\dot{m}''$ is the mass of snow flakes injected in the plume from the bottom of the snow zone per unit time (hence the dot) and per unit surface area (hence the double prime). The exact real root of equation (5.9) is found for any value of $\dot{m}''$, R_{plume} and w_s using the library Numpy in Python. Note that the plume velocity depends both on the mass flux and on the plume radius, but only through the product $\dot{m}'' R_{\text{plume}}$. Therefore, as a single snow flake falls, its evolution in depth and time only depends on the latter product. However, when it comes to quantifying the concentration of grains through a volume fraction ϕ, or the mass concentration $\mathcal{C}$ of molten snow in the plume, the respective roles of $\dot{m}''$ and R_{plume} will prove different.

Iron is present not only in snow flakes and in molten snow, but also in the ambient liquid. For the sake of brevity we call 'iron' only this iron that specifically originates from the iron flakes formed in the snow zone, and that gradually becomes liquid due to phase change in the precipitation layer. The ambient is simply referred to as liquid metal. The coordinate z is used to denote depth from the source of the plume $z = 0$ to increasing depths towards the centre of

the core (see figure 5.4). At the source, all the iron is in solid form with a volume fraction that reads

$$\phi(z=0) = \frac{\dot{m}''}{\rho_{Fe}(U_{\text{plume}} + w_s)} \ , \tag{5.10}$$

with ρ_{Fe} the density of a snow flake.

The nominal conditions of precipitation are chosen such that the total mass of iron flakes melting per unit time is equal to 1000 kg/s while the top of the precipitation layer is at a radius $r_{\text{PL}} = 0.9 r_c$. These values are chosen from results of the model of Rückriemen et al. (2015) (see their figure 6). For the nominal structure of Ganymede, the value $r_c = 871$ km implies that the total mass rate converts into a mass flux per unit surface area $\dot{m}'' = 1.29 \times 10^{-10}$ kg.m^{-2}.s^{-1}. All the nominal values are listed in table 5.2. Unless specified, the default values of $\dot{m}''$ and r_{PL} are the nominal values.

The plume velocity U_{plume} and the volume fraction of iron flakes at the plume source $\phi(z=0)$ are shown in figures 5.7a and 5.7b respectively. In figure 5.7a, the plume velocity increases when snow flakes get smaller and when the plume radius R_{plume} increases, as expected from equation (5.9). At vanishingly small sizes of snow flakes, the plume velocity is independent of their radius r_p because each snow flake moves as a tracer, hence the plume velocity is only constrained by the size of the plume (and the incoming mass flux). However as soon as r_p reaches about 30 μm, the size of snow flakes already alters the flow. The influence of the size r_p is also visible in figure 5.7b where an increase of the radius r_p quickly leads to a decrease of the flake volume fraction $\phi(z=0)$. More striking is the decorrelation of the volume fraction $\phi(z=0)$ from the plume velocity when the size of flakes is above the thin solid line of equation $U_{\text{plume}} = w_s$. This is due to the decoupling of these flakes that fall faster than the plume velocity, as can be seen in equation (5.10) (see section 4.5.3).

Chapter 4 established a link between the presence of turbulence in the plume, and the development of a Rayleigh-Taylor-like instability due to sufficient plume buoyancy (section 4.5.2). At the plume source, the plume density excess is quantified by the source Atwood number

$$\mathcal{A} = \frac{\phi(z=0)\rho_{Fe}}{2\rho_c + \phi(z=0)\rho_{Fe}} = \left[1 + \frac{2\rho_c(U_{\text{plume}} + w_s)}{\dot{m}''}\right]^{-1} \ , \tag{5.11}$$

where ρ_{Fe} and ρ_c are respectively the density of a snow flake and the density of the ambient, and w_s is the settling velocity of a snow flake. The Atwood number controls the maximum growth rate $\sigma_{\max}$ of the Rayleigh-Taylor-like instability

$$\sigma_{\max} = \sqrt{\mathcal{A} g k_{\max} + (\nu_c k_{\max}^2)^2} - \nu_c k_{\max}^2, \quad \text{where} \quad k_{\max} = \left(\frac{\mathcal{A} g}{8\nu_c^2}\right)^{1/3} \ . \tag{5.12}$$

The condition for the onset of the inverse growth rate $\sigma_{\max}$ should be larger than the turnover time $2\pi/k_{\max} w_s$, i.e.

$$w_s \leq \frac{2\pi\sigma_{\max}}{k_{\max}} \ . \tag{5.13}$$

This condition is evaluated at the plume source with $g(z=0)$ in equation (5.12) and the curve of marginal stability is shown as a dashed line in figures 5.7a-5.7e. The dotted line shows when

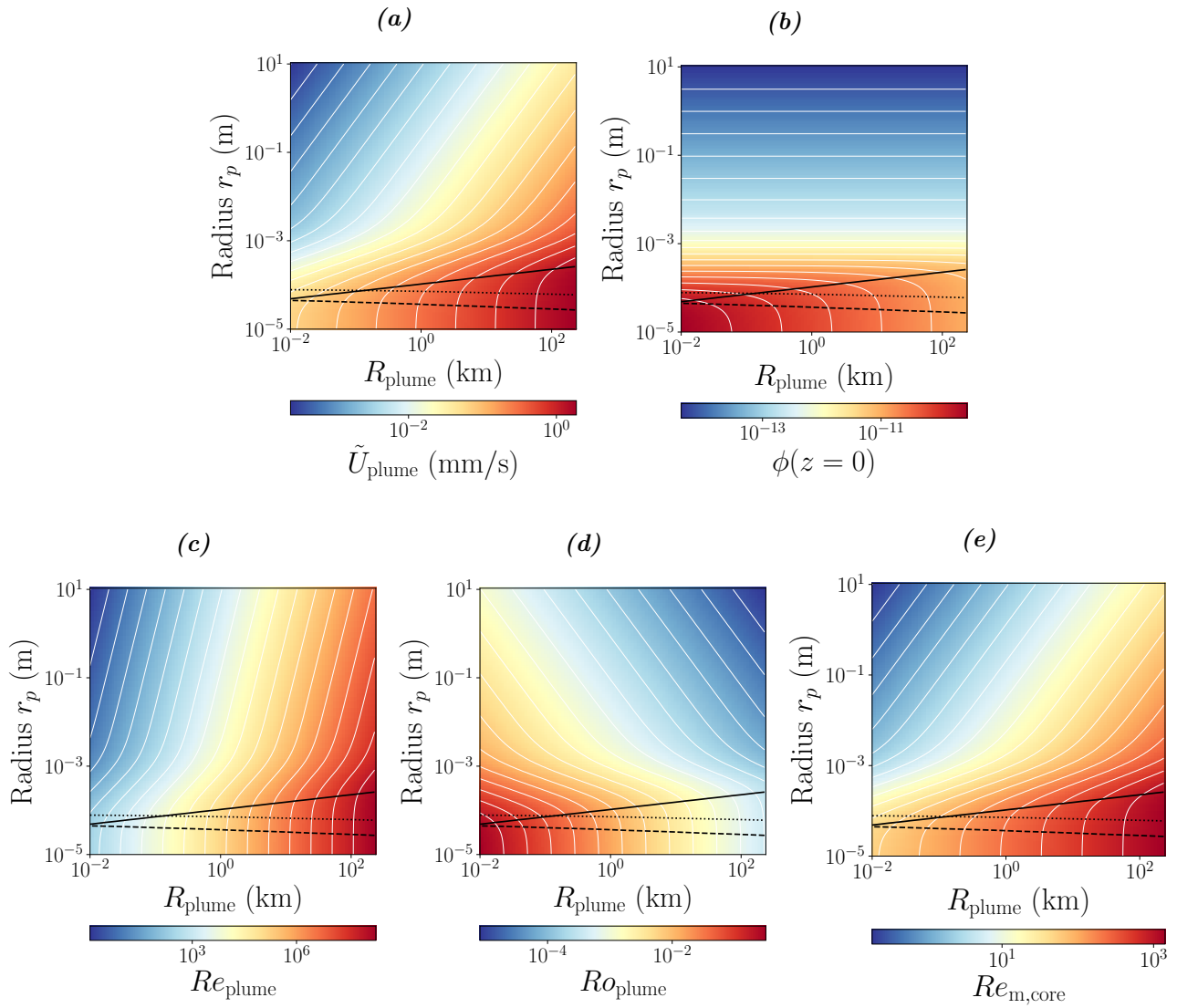

Figure 5.7: *Source conditions of several plumes for the nominal parameters. (a) Plume velocity, (b) volume fraction of snow flakes, (c) plume Reynolds number, (d) plume Rossby number, (e) magnetic Reynolds number based on the radius of the precipitation layer r_{PL}. In each diagram white lines are logarithmically equispaced isocontours, the thin solid line corresponds to $U_{\text{plume}} = w_s$, the dashed line corresponds to the threshold of Rayleigh-Taylor-like instability, and the dotted line corresponds to the transition from collectivity (below this line) to individual settling (above this line).*

the interparticle distance between snow flakes $l_{\text{inter}} = r_p\phi(z=0)^{-1/3}$ is equal to 10 times the characteristic distance of hydrodynamical interaction between grains $l_{\text{inter,c}} = \max\{\nu_c/w_s, r_p\}$ (section 4.5.4). Below the dotted line, snow flakes behave collectively, while above this line they behave individually. Because all the thresholds in solid, dashed or dotted lines are around $r_p \simeq 100$ μm, we can conclude that when snow flakes are larger than this typical radius, they force a laminar plume ($w_s > 2\pi\sigma_{\max}/k_{\max}$: no onset of the Rayleigh-Taylor-like instability, see section 4.5.2), likely with delay due to their individual behaviour ($l_{\text{inter}} > l_{\text{inter,c}}$, see section 4.5.4), and with a non-negligible decoupling from the flow ($w_s > U_{\text{plume}}$, see section 4.5.3).

Larger plume velocities and plume radii both enhance the plume inertia. The latter is compared to molecular diffusion with a Reynolds number Re_{plume}, and to the magnitude of the Coriolis force with a Rossby number Ro_{plume}. We assume that the velocity components that are orthogonal to Ganymede's rotation axis scale like αU_{plume} with $\alpha \leq 1$, so that the Coriolis force is proportional to $\alpha\Omega_G U_{\text{plume}}$. The definitions of Re_{plume} and Ro_{plume} are

$$Re_{\text{plume}} = \frac{U_{\text{plume}} R_{\text{plume}}}{\nu_c}; \quad Ro_{\text{plume}} = \frac{U_{\text{plume}}}{2\Omega_G R_{\text{plume}}\alpha}, \tag{5.14}$$

where ν_c is the kinematic viscosity of iron and Ω_G the angular velocity of Ganymede, see table 5.1. In the following we discard the coefficient α by assuming $\alpha = 1$, which effectively means that the Rossby number Ro_{plume} is computed as a lower bound. These two numbers are shown in figures 5.7c and 5.7d respectively. Despite low plume velocities of order $10^{-5} - 10^{-4}$ m/s, the large radius and low viscosity of the liquid metal enable the plume Reynolds number to reach large values that may favour a transition of the flow to turbulence. However, the large plume inertia is mostly due to its large radius since the plume velocities are low. As a result, plumes are characterised by low Rossby numbers (see figure 5.7d). Although Ro_{plume} is calculated as a lower bound, plumes are likely subject to planetary rotation. The influence of rotation is nevertheless neglected for now; it will be discussed in the final discussion.

Finally, the assembly of plumes in the whole core below the precipitation layer will collaborate to generate dynamo-capable motions at the core scale. We can thus define a magnetic Reynolds number based on the magnetic diffusivity η_m (see table 5.1) and depth r_{PL} of the convective zone plus precipitation layer

$$Re_{\text{m,core}} = \frac{U_{\text{plume}} r_{\text{PL}}}{\eta_m}, \tag{5.15}$$

whose values are shown in figure 5.7e. The large values of $Re_{\text{m,core}}$ compared to ~ 10 are consistent with the fact that the nominal scenario ($\dot{m}'' = 1.29 \times 10^{-10} kg.m^{-2}.s^{-1}$, $r_{\text{PL}} = 0.9 r_c$) corresponds to a simulation that successfully evidenced dynamo action from the iron-snow-induced compositional convection in Ganymede's deeper core (see figure 6 in Rückriemen et al., 2015). Note however that the correspondence between the present model and that of Rückriemen et al. (2015) is not straightforward. These authors model the melting of the snow flakes as an instantaneous process at the position $z_{\text{PL}} = 0$, which formally corresponds to the limit of small particle radius $r_p \to 0$. Hence their model lies in that region where the plume velocity is independent of the size of flakes. Additionally, their model supposes that the influx of buoyancy is uniform at depth z_{PL}, while the present model introduces the typical

length scale R_{plume} of heterogeneity that controls the flow velocity. How their estimate of the flow velocity compares with the present plume velocity U_{plume} is therefore uncertain. As numerous elements could cause heterogeneities (see the final discussion) and therefore lead to the formation of several plumes of finite size R_{plume}, the maps in figure 5.7 show that orders-of-magnitude differences can be obtained for the same nominal scenario when considering the influence of r_p and R_{plume}.

5.4 Remelting in monodisperse plumes

5.4.1 Melting of a single iron flake

For simplicity, snow flakes are assumed spherical, with a uniform density ρ_{Fe} and a radius r_p. Following Rückriemen et al. (2015) and Hauck II et al. (2006), we define the density of snow flakes as $\rho_{Fe} = \rho_c + 1000$ kg.m^{-3} (table 5.2). The melting rate of snow flakes is governed by the Stefan condition (Batchelor et al., 2000; Huguet et al., 2020) which reads

$$\mathcal{L}_{\text{fus}}\rho_{Fe}\dot{r}_p = \underbrace{k_{Fe}\frac{T_{\text{Liq}}(z)-T_0}{r_p}}_{\text{inner gradient}} - \rho_c c_{p,c}\underbrace{\overline{k}(T(z)-T_{\text{Liq}}(z))}_{\text{outer gradient}}, \tag{5.16}$$

where $\mathcal{L}_{\text{fus}} = \Delta S_{\text{fus}} \times T_{\text{Liq}}(z)$ is the latent heat of fusion of pure iron that varies with the liquidus temperature, $\Delta S_{\text{fus}} = 136$ J.kg^{-1}.K^{-1} is the specific entropy of fusion of pure iron, and k_{Fe} is the heat conductivity of pure solid iron (see reference values in table 5.1). The quantity $\dot{r}_p$ is the Lagrangian time derivative of the particle radius; its absolute value $|\dot{r}_p|$ is the melting rate.

The first term on the right-hand side is the heat flux at the solid-liquid interface on the solid side. For simplicity, the temperature profile inside snow flakes is always assumed linear, varying from the melt temperature $T_{\text{Liq}}(z)$ at the interface to the temperature T_0 at the centre of the snow flake. Although this is just an approximation of the inner heat flux at the surface of a snow flake, this assumption has proven reasonable in experiments of large melting and dissolving spheres settling in a warm ambient (Huguet et al., 2020). Two end-members can be considered for T_0: either diffusion is very fast in snow flakes so that $T_0 \simeq T_{\text{Liq}}(z)$ at all depths, in which case this term vanishes; or the temperature T_0 is a constant. The experiments of Huguet et al. (2020) proved to be reasonably described by this second end member, where T_0 was the initial temperature of their particles. The inner gradient proves of little consequence since it is much lower than the outer gradient. For the sake of brevity, only results for the first end member $T_0 \simeq T_{\text{Liq}}(z)$ are presented.

The second term on the right-hand side of equation (5.16) is the outer heat flux at the surface of the snow flake. It is parameterised as for the dissolution of sugar (section 4.4.3): this heat flux is driven by the temperature contrast between the ambient $T(z)$ and the liquidus $T_{\text{Liq}}(z)$, and by both diffusion and advection. Due to the analogy between heat and mass transfers (Clift et al., 2005; Bird et al., 2006), like Huguet et al. (2020) we use the parameterisation of Zhang and Xu (2003) that is valid over a wide range of particle Reynolds number

$$\overline{k} = \frac{\kappa_{th}}{2r_p}Nu, \text{ with } Nu = 1 + (1 + Re_p Pr)^{1/3}\left(1 + \frac{0.096Re_p^{1/3}}{1 + 7Re_p^{-2}}\right) \tag{5.17}$$

In equation (5.17) the quantities κ_{th} and Pr respectively correspond to the thermal diffusivity of liquid iron, and the Prandtl number of liquid iron $Pr = \nu_c/\kappa_{th}$. The particle Reynolds number is defined as $Re_p = 2r_p w_s/\nu_c$ where r_p is the flake's radius, w_s its settling velocity, and ν_c the kinematic viscosity of the core. The Nusselt number Nu quantifies the enhancement of heat transfers due to convection, compared to the reference of purely conductive transfers. Figure 5.8 shows the diffusive and advective contributions to the heat transfer coefficient. Importantly, note that this coefficient always decreases with r_p so that smaller flakes melt faster if all other parameters are considered constant.

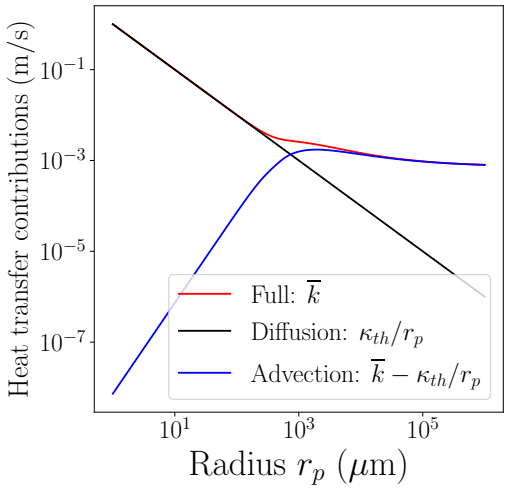

Figure 5.8: *Contributions to the heat transfer coefficient $\overline{k}$ as parameterised by equation (5.17).*

5.4.2 Modelling a plume of snow flakes

Snow flakes are considered to settle and remelt in a plume of constant width and velocity, based on the model of steady precipitation-driven plume of section 5.3. The radius of snow flakes decreases in depth because they remelt; under the assumption that the flow is steady, all snow flakes experience the same history of melting from the source to the finite depth of melting, so that all snow flakes at a given depth have the same radius $r_p(z)$.

Due to gravitational drift, snow flakes fall with a velocity $U_{\text{plume}} + w_s(z)$ that varies in depth due to the reduction of $r_p(z)$. Using the model of Samuel (2012), the settling velocity reads

$$w_s(z) = \frac{20\nu_c}{r_p(z)} \left[\sqrt{1 + \frac{(\rho_{Fe} - \rho_c) g r_p(z)^3}{45 \rho_c \nu_c^2}} - 1 \right] . \tag{5.18}$$

This expression ensures a transition from the Newton regime to the Stokes regime as the particle Reynolds number decreases. Note that the density contrast $\rho_{Fe} - \rho_c$ is fixed because we neglect any feedback from the varying plume density.

Melting leads to a reduction of the volume of snow flakes, as quantified by their volume fraction $\phi(z)$, and it is responsible for the presence of molten iron snow in the plume, whose mass concentration $\mathcal{C}(z)$ is related to the plume density through a constitutive equation which

we assume is known. Therefore, $\rho(z)$ is completely determined by the knowledge of $\mathcal{C}(z)$, so that the evolution of snow flakes is described by three unknowns: the radius $r_p(z)$, the volume fraction $\phi(z)$ and the mass concentration $\mathcal{C}(z)$.

The profile $r_p(z)$ is obtained by Lagrangian integration of the equation of motion of a single grain

$$\dot{z}_p = U_{\text{plume}} + w_s(z) \tag{5.19}$$

with the equation (5.17) of heat transfer. The volume fraction and the mass concentration must verify the conservation of the total mass of iron – both in solid and molten form. In the absence of any source term and since the flow is steady, conservation of mass reduces to a balance between the flux of iron coming in a slice of plume from the top, and the flux of iron going out through the bottom of this slice. This balance reads

$$\frac{\partial}{\partial z}\left[\{\underbrace{\phi\rho_{Fe}(U_{\text{plume}}+w_s)}_{\text{flux of solid}}+\underbrace{(1-\phi)\mathcal{C}U_{\text{plume}}}_{\text{flux of solute}}\}\right]=0\ . \tag{5.20}$$

The mass transferred from the solid phase to the molten phase is given by the spherical shell of iron $4\pi r_p^2|\dot{r}_p|dt\rho_{Fe}$ that melts around each snow flake during a time increment dt, and that must be integrated over the surface of the total number of snow flakes in the slice $\pi R^2_{\text{plume}}dz\phi/(4\pi r_p^3/3)$. Under the assumption of steady flow, the total mass of *molten* iron in a plume slice remains constant, so this source term balances the fluxes of *molten* iron coming in from the top and out through the bottom. After simplification by R^2_{plume}, our last equation reads

$$\frac{\partial}{\partial z}\left[(1-\phi)\mathcal{C}U_{\text{plume}}\right]=\underbrace{\frac{3\phi\rho_{Fe}|\dot{r}_p|}{r_p}}_{\text{total melting rate}}\ , \tag{5.21}$$

where $|\dot{r}_p|$ is given at all depths by equation (5.16). In the following, the right-hand side of equation (5.21) is called the total melting rate, because it originates from the integration of the melting rate $|\dot{r}_p|$ over the surface area of all snow flakes in a unit volume, so it quantifies the rate of phase change for an entire section of the plume.

Combining equations (5.20) and (5.21) yields

$$\frac{\partial}{\partial z}\left[\phi(U_{\text{plume}}+w_s)\right]=-\frac{3\phi|\dot{r}_p|}{r_p} \tag{5.22}$$

that is integrated numerically with a forward Euler method to determine $\phi(z)$ since $r_p(z)$ and the associated field of settling velocity are directly determined by Lagrangian integration of the equation of melting along the trajectory of a snow flake. Then, equation (5.20) directly yields the mass concentration as

$$\mathcal{C}(z)=\frac{[\phi\rho_{Fe}(U_{\text{plume}}+w_s)]_z^0}{(1-\phi(z))U_{\text{plume}}}\ , \tag{5.23}$$

where we define the notation $[Q]_z^0 = Q(0) - Q(z)$. The previous equations can be integrated with the following boundary conditions at the plume source

$$r_p(z=0) = r_{p0} \ , \tag{5.24}$$
$$w_s(z=0) = w_s(r_{p0}) \ , \tag{5.25}$$
$$\phi(z=0) = \frac{\dot{m}''}{\rho_{Fe}(U_{\text{plume}} + w_s(z=0))} \ . \tag{5.26}$$

Note that the initial size of snow flakes is now denoted r_{p0} to clearly distinguish it from their size at depth $z > 0$. Unless specified, the parameters used to obtain the results presented in the next sections all correspond to the nominal configuration of Ganymede (table 5.2).

5.4.3 Settling and melting at the individual scale

This section focuses on settling and remelting from the point of view of an individual snow flake of initial size r_{p0} that is transported by a plume of radius $R_{\text{plume}} = 10$ m.

Figure 5.9a shows the trajectory of snow flakes of radius between 10 μm and 1 m, up until they completely remelt: flakes that are initially larger fall faster. Anticipating this observation is not immediate because the increase of $w_s(z=0)$ with r_{p0} competes with the decrease of the plume velocity U_{plume} with r_{p0} (figure 5.7a). With the present parameters, this competition leads to an increase of the initial fall velocity $U_{\text{plume}} + w_s(z=0)$ with r_{p0} (figure 5.9b). This trend is preserved at all depths despite the shrinking of snow flakes due to melting (figure 5.9c) because $w_s(z)$ is a growing function of $r_p(z)$. Finally, snow flakes complete melting at a time $t_{\max}$ and a depth z_{PL}^{∞}. The inset of figure 5.9d shows that the depth of remelting increases monotonically with r_{p0}, which is due both to the monotonic increase of $U_{\text{plume}} + w_s(z)$ and to the monotonic decrease of $|\dot{r}_p|(z)$ with r_{p0} (figure 5.9e).

Figure 5.9d shows that the time of complete remelting $t_{\max}$ varies non-monotonically with the initial flake size. Since curves do not cross in figure 5.9c, and since the heat transfer coefficient $\overline{k}(z)$ decreases monotonically with $r_p(z)$, the intermediate decrease of $t_{\max}$ is of thermal origin, driven by the increase of the temperature contrast $T(z)/T_{\text{Liq}}(z) - 1$ with depth (see figure 5.6b) to which the melting rate $|\dot{r}_p|(z)$ is proportional (the presence of $T_{\text{Liq}}(z)$ at the denominator is due to the term of latent heat of fusion in equation (5.16)). In figure 5.9e, all curves of melting rate increase with depth both due to the shrinking of snow flakes and due to the temperature increase; time integration of the melting rate all along these curves determines the lifetime $t_{\max}$ of a snow flake.

Apart from this observation about $t_{\max}$, all observations are monotonic in z and $r_p(z)$ (see how curves are sorted in figure 5.9c). This monotony considerably simplifies interpretations; it is due to the monotonic variations of $w_s(z)$ and $|\dot{r}_p|(z)$ with $r_p(z)$, which is itself a monotonic function of z. However, it should be borne in mind that the monotonous variations we observe are conditioned by the initial increase of $U_{\text{plume}} + w_s(z=0)$ with r_{p0}; for another configuration of Ganymede, this velocity could be a decreasing function of r_{p0}, which could reverse some trends.

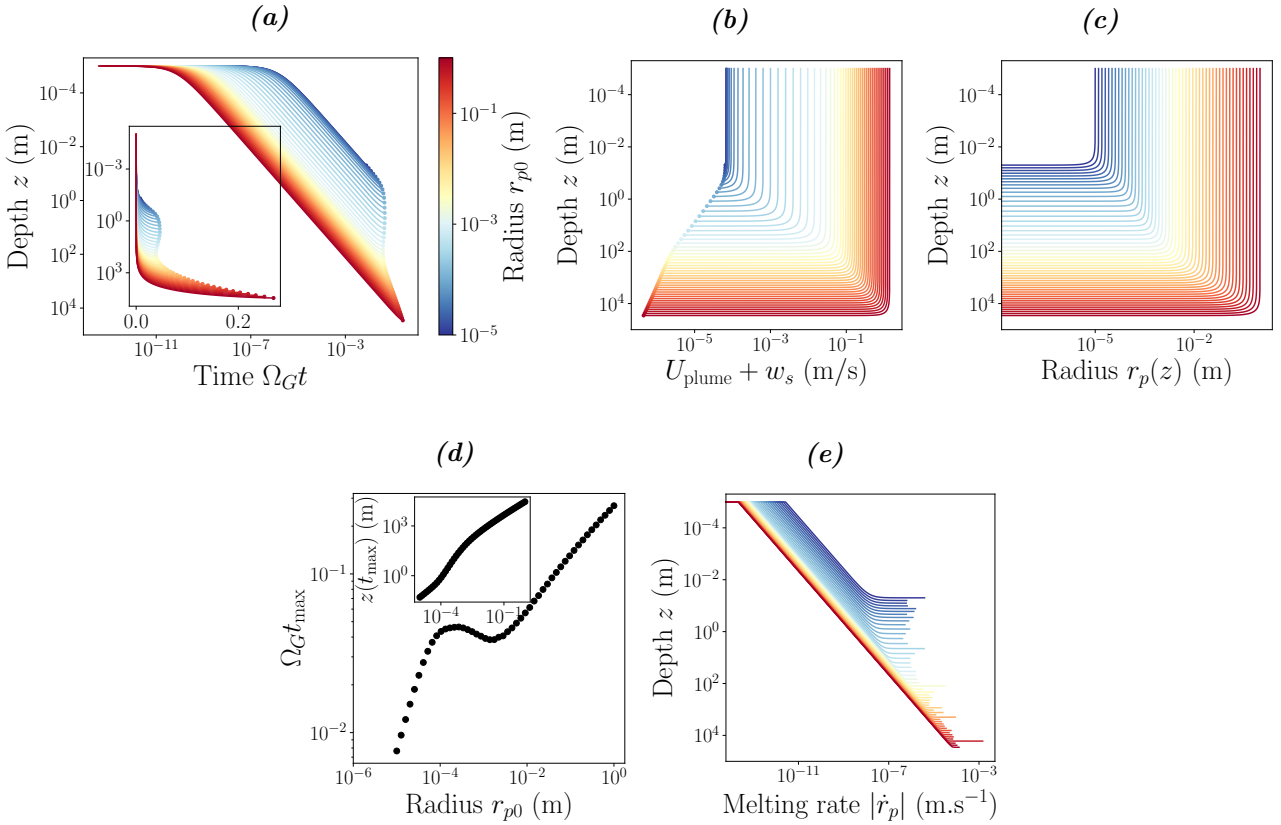

Figure 5.9: *Evolution of a monodisperse plume for various initial flake sizes r_{p0} shown as a colorscale given in (a) and valid for all subfigures. Diagrams show the evolution of various quantities from the top of the precipitation layer to the maximum depth where grains have completely remelted, hence the interruption of each curve at its maximum depth. (a) Trajectory of grains in depth with time in logarithmic scale; the inset is the same graph with time in linear scale. (b) Fall velocity of a flake advected by the plume. (c) Decrease of the flake radius due to melting. (d) Time $t_{\max}$ of completion of melting as a function of the initial flake radius r_{p0}; the inset shows the depth where melting completes as a function of r_{p0}. (e) Melting rate of a grain.*

5.4.4 Mesoscopic description in plumes

We begin by analysing how profiles of volume fraction and concentration vary in depth, before analysing the role of the initial flake size r_{p0}. All the parameters of this section are those of the previous section 5.4.3.

During their fall, snow flakes both slow down and shrink. The former effect contributes to a compaction of snow flakes that favours an increase of the volume fraction ϕ with depth (see the term $U_{\text{plume}} + w_s$ in equation (5.22)), whereas remelting reduces the volume occupied by the solid phase in a given slice of plume, all the faster as $r_p(z)$ reduces, favouring a decrease of the volume fraction with depth (see the numerator and denominator of the right-hand side of equation (5.22)). This second contribution predominates since the volume fraction decreases with depth for all initial radii r_{p0} in figure 5.10a.

The concentration of molten snow increases with depth (figure 5.10b), which is a result of

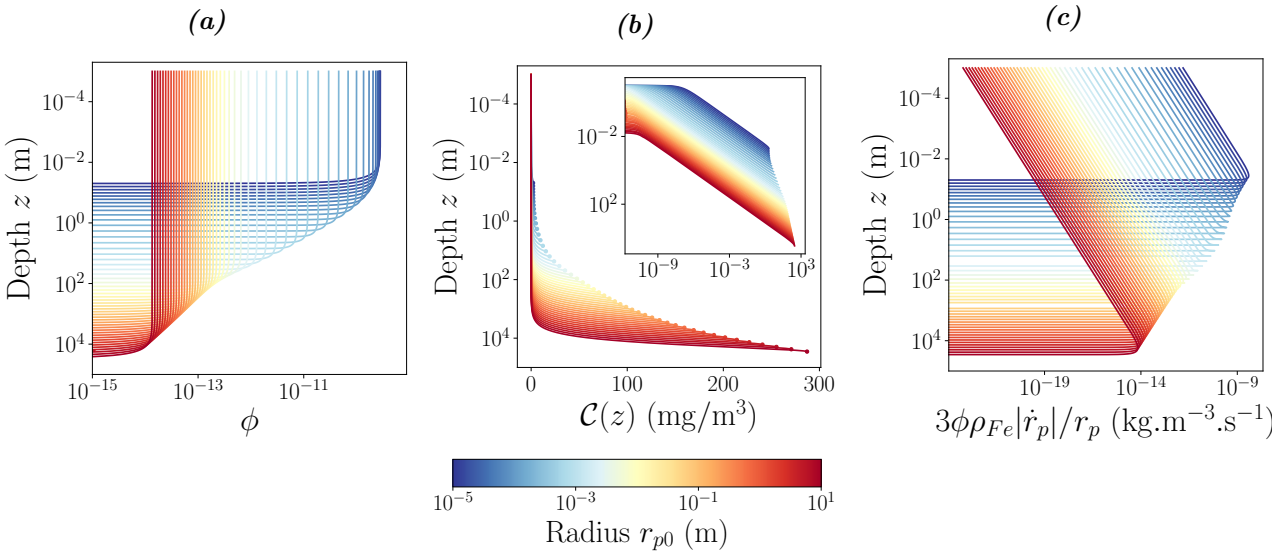

Figure 5.10: *Evolution of (a) the volume fraction of snow flakes, (b) the mass concentration of molten snow (the abscissa is in linear scale in the main graph, in logarithmic scale in the inset), and (c) the total melting rate, for various initial flake radii r_{p0}.*

a competition between two ingredients. The decrease of the solid volume fraction $\phi(z)$ dilutes the molten snow (left-hand side of equation (5.21)) whereas the combined decrease of $\phi(z)$ and $r_p(z)$ enhances the total melting rate $3\phi\rho_p|\dot{r}_p|/r_p$ (figure 5.10c) that is the source term for $\mathcal{C}(z)$ (right-hand side of equation (5.21)). This latter enhancement predominates over dilution for the present set of parameters.

The influence of the initial flake size is shown by the different colours of curves in figure 5.10. The volume fraction of smaller flakes is initially larger as previously seen in figure 5.7b. However, their volume fraction decreases the fastest because the heat transfer coefficient $\overline{k}$ is a decreasing function of $r_p(z)$, and due to the larger surface area of the interface between snow flakes and the ambient (figure 5.10c). As a consequence, and because they settle slower, smaller flakes melt at shallower depths so at any given depth the concentration $\mathcal{C}(z)$ is larger for smaller flakes (see the inset of figure 5.10b). However, most of the remelting of snow flakes happens at the end of their trajectory (see the main graph of figure 5.10b) because this is where they become very small hence the coefficient of heat transfer $\overline{k}$ becomes very large (see figure 5.8). Therefore, it is not surprising to observe that all plumes transition from particle-laden to solute-laden near the depth of complete remelting z_{PL}^{∞}, but the plumes with the smallest flakes dilute less so their concentration is several orders of magnitude larger than in plumes laden with large snow flakes. What is surprising, however, is that the maximum concentration ever reached in the plume is a growing function of r_{p0}. Since the total melting rate is lower for larger flakes, this observation is due to larger flakes falling deeper where the temperature contrast $T(z)/T_{\mathrm{Liq}}(z) - 1$ is larger, thus accelerating melting.

The plume velocity contributes to diluting the molten snow, while the mass rate controls the total surface area dissolving in a plume slice, so both should play a role in determining the

profiles of volume fraction and concentration. Their effects are therefore discussed in the next two sections.

5.4.5 Influence of the plume radius

The influence of the plume radius R_{plume} is shown in figure 5.11. The initial size of flakes is now fixed to the value $r_{p0} = 10$ μm that is usually considered in the literature (Rückriemen et al., 2015, 2018). Figure 5.11a shows that snow flakes complete their remelting at a larger depth and fall faster when R_{plume} increases due to the larger plume velocity (see also the inset of figure 5.11c). At a fixed depth z, when R_{plume} increases the snow flakes have spent less time remelting hence their size $r_p(z)$ is larger so the melting rate $|\dot{r}_p|(z)$ is lower (figure 5.11b). Considering now the remelting of snow flakes up until completion, when the plume radius increases snow flakes travel deeper in the core where the liquid is warmer, thus their total time of remelting $t_{\max}$ decreases (figure 5.11c).

The volume fraction decreases with depth as in the previous section (figure 5.11d). The larger the plume radius, the deeper flakes are advected, the deeper they remelt hence the deeper the volume fraction vanishes. Importantly, the initial volume fraction is lower when the plume radius is larger due to the dilution of snow flakes by the flow. In addition, we just saw that $|\dot{r}_p|(z)$ (respectively $r_p(z)$) decreases (respectively increases) with R_{plume}. Consequently, the evolution of all three quantities $r_p(z)$, $\phi(z)$ and $|\dot{r}_p|(z)$ concurs to the decrease of the total melting rate $3\phi\rho_{Fe}|\dot{r}_p|/r_p$ when R_{plume} increases (figure 5.11e). As a consequence, the mass concentration of molten snow decreases with increasing plume radius (figure 5.11f).

5.4.6 Influence of the mass flux

The influence of the mass flux is shown in figures 5.12a-5.12f. A quick comparison of the Lagrangian evolution of snow flakes between figures 5.11a-5.11c and figures 5.12a-5.12c shows that increasing R_{plume} or $\dot{m}''$ has a similar influence on the evolution of snow flakes: they fall faster, remelt deeper where the ambient is warmer, hence they complete remelting in a shorter amount of time. This is expected since the trajectories of snow flakes are only influenced by the plume velocity that depends on the product $\dot{m}''R_{\text{plume}}$. However, the picture is different concerning concentrations in the plume. For a fixed plume size, a larger volume of snow flakes is injected at the plume source when $\dot{m}''$ is increased, favouring a larger initial volume fraction $\phi(z = 0)$; conversely, increasing $\dot{m}''$ also increases the plume velocity U_{plume} that dilutes snow flakes, favouring a lower initial volume fraction. The former effect proves to overcome the latter, as visible in figure 5.12d. Then, the volume fraction decreases with depth, vanishing all the deeper as $\dot{m}''$ increases due to larger plume velocities.

The variation of the total melting rate (figure 5.12e) essentially decreases with depth because it is proportional to $\phi(z)$, (although it varies non-monotonically, with a noticeable competing influence of $r_p(z)$ and $|\dot{r}_p|(z)$ at shallow depths). Consequently, larger mass fluxes lead to larger total melting rates at a given depth (figure 5.12e) and therefore to larger mass concentrations of molten snow $\mathcal{C}(z)$ (figure 5.12f).

The last two sections have shown that the plume radius is an inhibitor of remelting due to

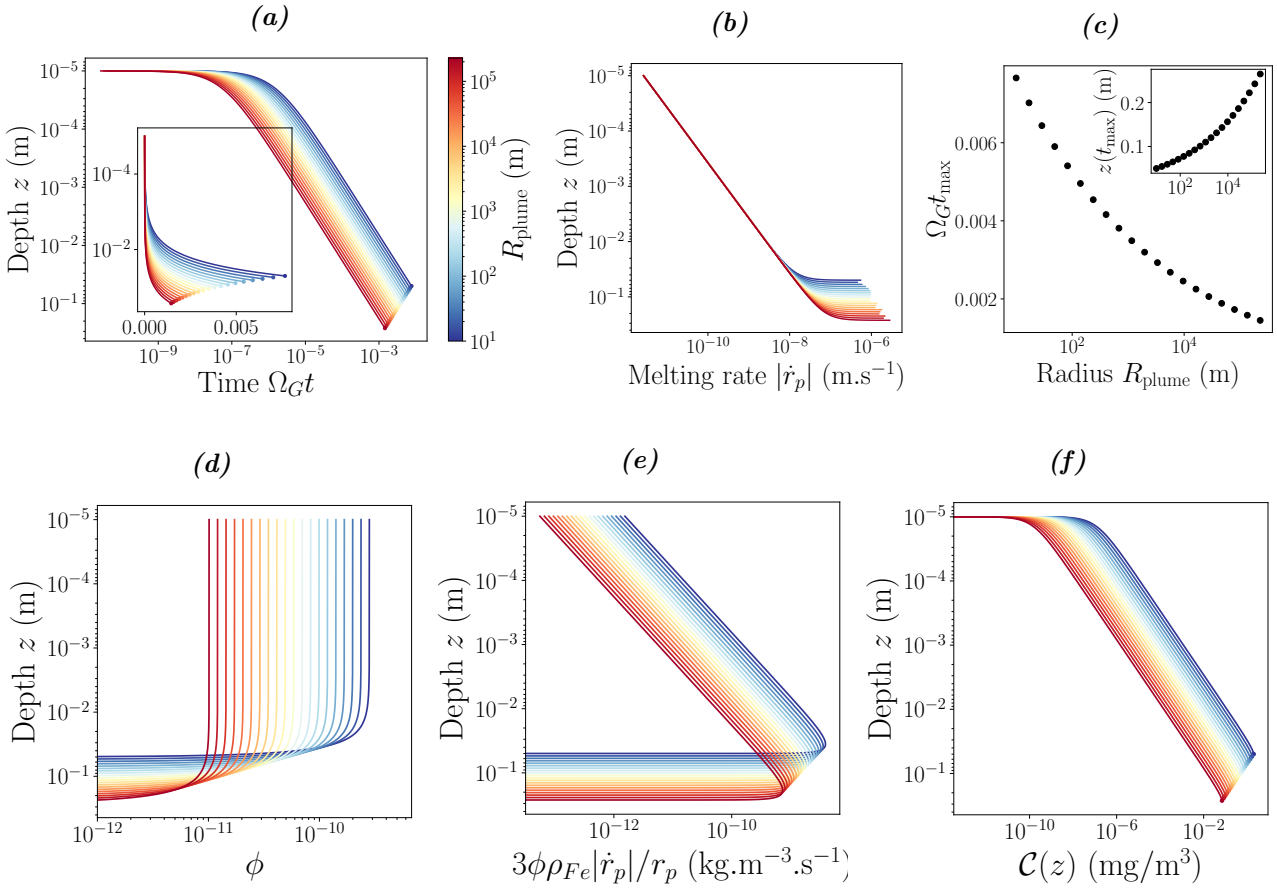

Figure 5.11: *Influence of the plume radius on snow flakes with initial radius $r_{p0} = 10$ μm. The plume radius is shown as a colorscale provided in (a) and used in all other subplots. (a) Trajectory of snow flakes with a time scale that is logarithmic in the main diagram, linear in the inset. (b) Melting rate at the solid-liquid interface. (c) Time of completion of melting as a function of R_{plume}; the inset shows the depth where melting completes as a function of R_{plume}. (d) Volume fraction of snow flakes. (e) Total melting rate. (f) Mass concentration of molten snow.*

deeper advection of snow flakes and dilution of the buoyant material, whereas the mass rate increases the concentration of the plume in snow flakes even more than it accelerates dilution, so that the total melting rate gets enhanced and the concentrations of molten snow are higher. Note however that these two effects have weaker influences than the size of grains on the profiles of concentration and volume fraction. These results confirm the key role of the flake size in precipitation below the snow zone.

5.5 Discussion

The present model of plume was willingly adapted to the results obtained by Rückriemen et al. (2015, 2018) to align with their assumptions and assess the consequences of the remelting of snow flakes in a plume. We now propose a revision of some assumptions and draw some key

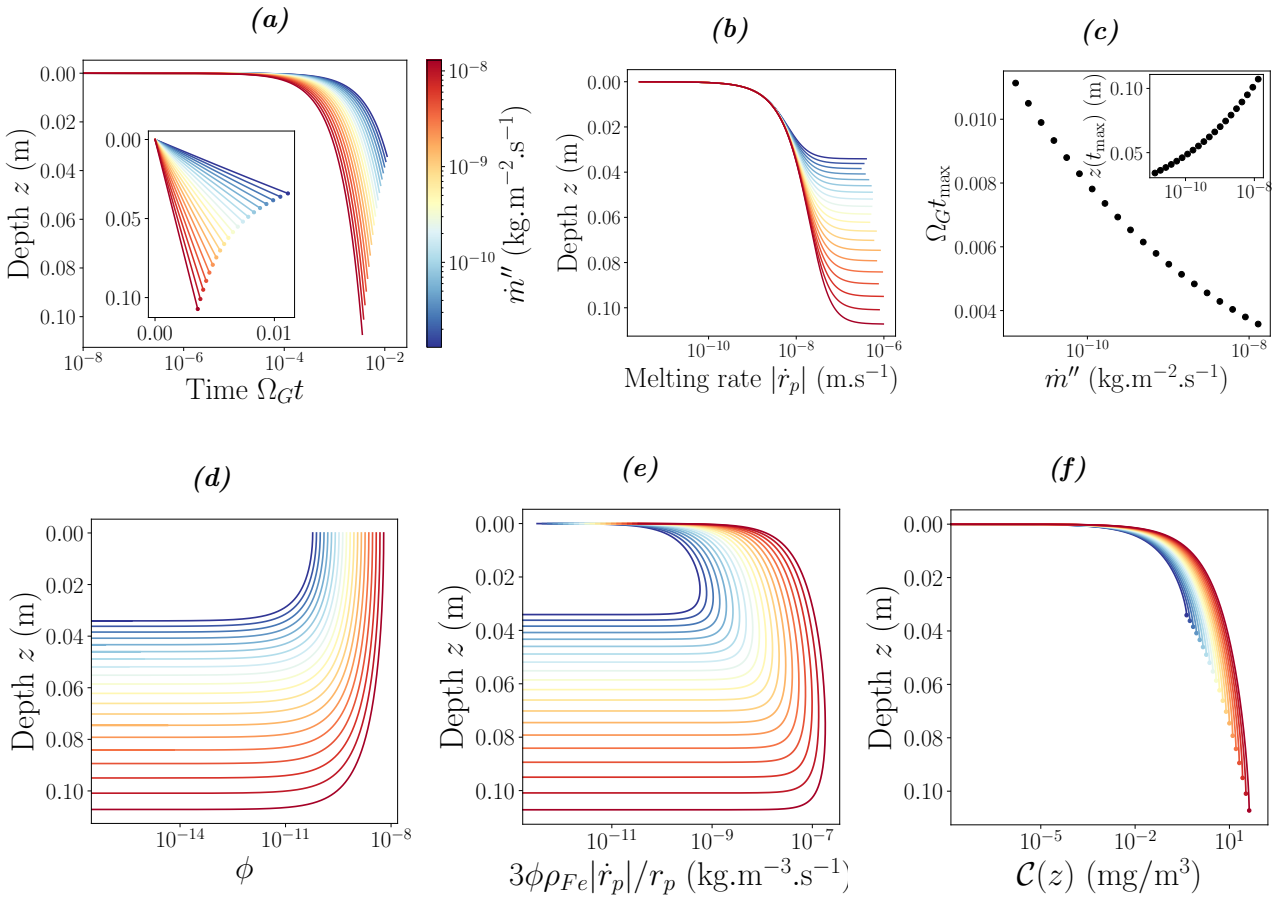

Figure 5.12: *Influence of the mass flux (colorscale shown in (a)) on snow flakes with initial radius $r_p = 10$ μm falling in a 10 m-large plume. (a) Trajectory of snow flakes with a time scale that is logarithmic in the main diagram, linear in the inset. (b) Melting rate at the solid-liquid interface. (c) Time of completion of melting as a function of $\dot{m}''$; the inset shows the depth where melting completes as a function of $\dot{m}''$. (d) Volume fraction of snow flakes. (e) Total melting rate. (f) Mass concentration of molten snow.*

conclusions.

5.5.1 Depth of injection of molten snow

The model of Rückriemen et al. (2015, 2018) is one-dimensional so the snow zone and the remelting of snow flakes are homogeneous in space. Additionally, they estimate that remelting takes much shorter than their 1 Myr-timestep and therefore model remelting as an instantaneous process. Due to the assumption of fast remelting, they also assume that all crystals melt at a negligible distance from the bottom of the snow zone. This distance of remelting can be quantified with the present model depending on the size of crystals and on the plume velocity. Results are shown in figure 5.13a for various plume radii, in the nominal configuration $\dot{m}'' = 1.29 \times 10^{-10}$ kg.m^{-2}.s^{-1}. The largest snow flakes ($r_p = 1$ m) reach a maximum depth

of 29 km, which represents 3.3% of the thickness of the convective zone (r_{PL}) and 33% of the depth of the snow zone ($r_c - r_{\mathrm{PL}}$). The graphs of the last three sections have shown that this is a non-negligible distance over which snow flakes and molten snow are diluted: neglecting the whole phenomenon of phase change could lead to orders-of-magnitude errors on the concentration of molten snow hence on the material properties of the fluid, and on the velocities that are expected in the convective zone.

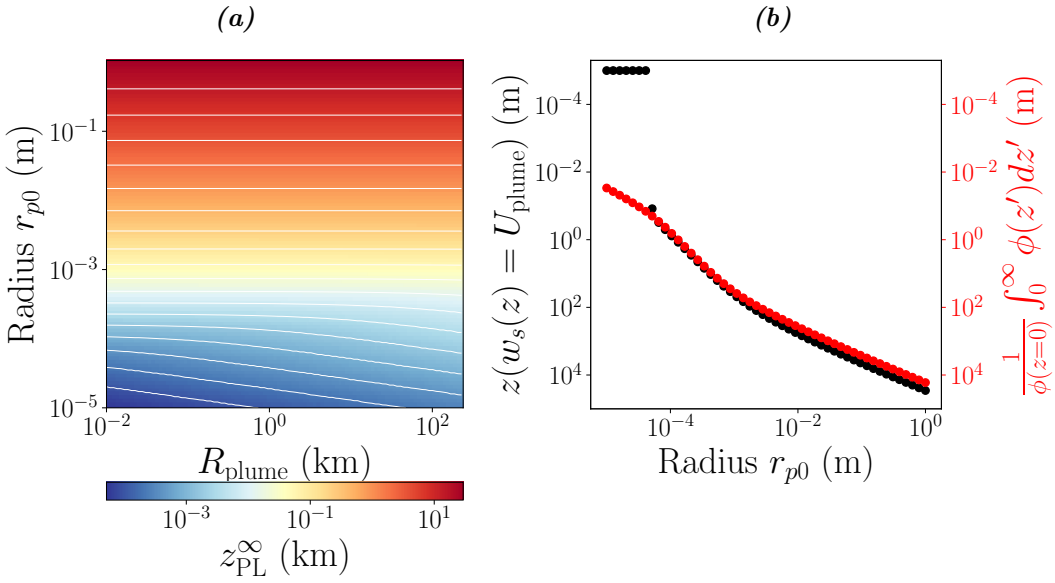

Figure 5.13: *(a) Maximum depth of remelting for various monodisperse plumes of varying plume radius R_{plume} and initial flake size r_{p0}. (b) Results of section 5.4.3 for the nominal configuration and $R_{\mathrm{plume}} = 10$ m, showing in dark (•) the depth of decoupling of snow flakes from the plume as a function of their initial radius r_{p0}, and in red (•) the depth where the volume fraction of snow flakes vanishes.*

The results of figure 5.13a only show where snow flakes complete their remelting; it does not clearly show that the molten snow is produced at such large depths, and the depth z_{PL}^{∞} could be of little importance. Let us show it is not.

Snow flakes remelt over large distances, but the profiles of concentration, volume fraction and melting rates have shown that phase change usually takes place over a short distance at the end of the trajectory of snow flakes, when their size decreases sufficiently for the melting rates to be the largest. It means molten snow is not uniformly produced up until snow flakes disappear, and it is effectively injected at the depth where most of the phase change occurs. Then, what is the effective depth of injection of molten snow – hereafter referred to as the 'injection depth'? This can be quantified by computing where the amount of solute $(1-\phi)\mathcal{C}$ suddenly increases in depth. Alternatively, a simpler definition is the depth where the volume fraction of snow flakes vanishes. Mathematically, this depth is the integral of the volume fraction in z, normalised by the initial volume fraction, as shown with red circles in figure 5.13b for the results of section 5.4.3 (nominal configuration with $R_{\mathrm{plume}} = 10$ m). Expectedly, flakes of larger initial size inject

molten snow deeper in the core because they remelt deeper. The correlation between figures 5.13a and 5.13b confirms that, because molten snow is mostly generated at the end of the flakes' trajectory, the depth z_{PL}^{∞} is an important quantifier of where the compositional convection is the most actively nourished by molten snow.

When molten snow and snow flakes fall, they nourish compositional convection which can be highly heterogeneous and constrained by rotation as we saw in section 5.3. How does it affect the settling of snow flakes and therefore their remelting? To answer this question, dark circles in figure 5.13b show the depth where the settling velocity of snow flakes becomes equal to the plume velocity. Above this depth, the settling velocity is larger than the plume velocity so snow flakes are decoupled from fluid motions. If the Rouse number is below unity much above the injection depth, it means snow flakes were following fluid motions before remelting. Conversely, if the unit Rouse number is reached close to the injection depth, it means snow flakes were decoupled from fluid motions while they were settling in the plume, and they just reached the threshold $w_s(z) = U_{\mathrm{plume}}$ at the final stage of their remelting when they shrank fast. Results show that below $r_{p0} = 50$ μm, snow flakes are sufficiently small to follow fluid motions when they reach the depth of injection of molten snow, whereas those in the range $r_{p0} > 50$ μm were decoupled from fluid motions. This observation is crucial: however complex the fluid motions might be in the zone of compositional convection, since their characteristic velocity is at most U_{plume}, snow flakes in the range $r_{p0} > 50$ μm might be able to cross through these motions, and thus actually remelt at the injection depth, without being carried away by the flow. How much they would deviate from the direction of gravity while crossing through Taylor-column-like structures depends on how much w_s is large compared to U_{plume}. What would happen to the molten snow remains an open question. Another unknown is the influence of the time lag required for large snow flakes to force the flow through drag, as observed in our experiments of sugary plumes (see figure 4.17b in section 4.6.3 of Chapter 4 for example), and how it compares with characteristic timescales of the convective motions.

5.5.2 Sizes of crystals

The result $z_{\mathrm{PL}}^{\infty}/r_{\mathrm{PL}} \simeq 3.3\%$ in the previous section holds for 1 m-large snow flakes i.e. the largest size investigated in this chapter. The burning question is: What size of crystals is expected in Ganymede's core? Let us assume like previous authors (Rückriemen et al., 2015, 2018) that crystallisation happens in the bulk of the snow zone. As in Rückriemen et al. (2015, 2018), nucleation is assumed to happen with an arbitrary supercooling of 0.01 K, although data are severely lacking on this matter. Knowing the size r_{p0} of snow flakes at the top of the precipitation layer, the equations of settling and phase change can be integrated backward in time in order to determine at what radial position such crystals must have formed in the snow zone. Implicitly, this integration relies on the assumption that melting and solidification are symmetric. This is just an approximation: curvature breaks this symmetry (Langer, 1980), and the realistic formation of crystals of complex geometries involves processes like some microscopic rearrangements of atoms (Kurz and Fisher, 1998; Houze Jr, 2014) that are irreversible. Yet, under the simplistic assumption that snow flakes are spherical, we believe that such a calculation can give some insight for the following discussion. Equations are integrated up until the radius $r_p(z)$ vanishes to zero, and this defines the radial position of nucleation r_{nuc}. Results are shown

with a dark curve in figure 5.14a. All snow flakes with a size below $r_p = 2.6$ cm must have nucleated somewhere between the top (r_c) and the bottom ($r_{\rm PL}$) of the snow zone. According to this calculation, larger snow flakes cannot have grown by individual crystallisation from an initial size $r_p = 0$ and reached the precipitation layer with $r_{p0} \geq 2.6$ cm: indeed, even if they formed at the CMB, they would need to start settling with an initial size $r_p(r = r_c) > 0.27$ cm that is shown by the red curve in figure 5.14a.

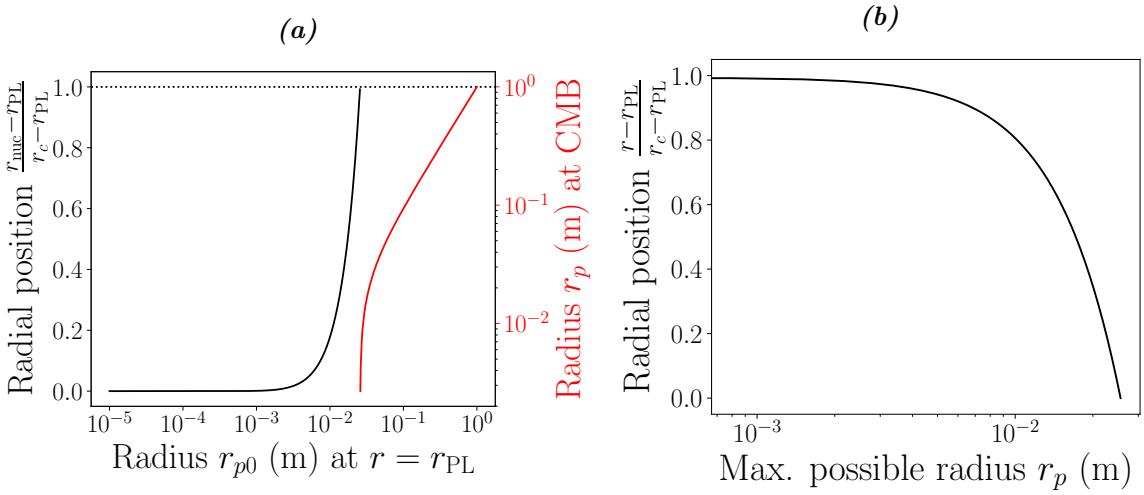

Figure 5.14: *(a) The solid dark line shows where a snow flake of given size r_{p0} at the bottom of the snow zone (0 in ordinate) must have nucleated to have grown to such a size while settling. Above a critical size, the snow flake cannot have nucleated in the snow zone; therefore the red line shows the size that the nucleus should have at the top of the snow zone for this crystal to reach a size r_{p0} at the bottom of the snow zone. (b) Maximum size that a single snow flake can have at a given radial position in the snow zone when nucleating from $r_p = 0$.*

This observation implies that crystals of size $r_{p0} > 2.6$ cm cannot form by individual crystallisation in the bulk of a 87 km-thick snow zone with 0.01 K supercooling and with $\rho_{Fe} = \rho_c + 1000$ kg.m^{-3}. Yet, the presence of such crystals cannot be excluded. First, because the present estimate is conservative since we have neglected the fact that supercooling usually leads crystals to start solidifying from a non-zero initial size (e.g. Houze Jr, 2014; Huguet et al., 2018b). Second, because some assumptions have been made that are very strong: (i) the snow zone is motionless; (ii) crystallisation happens in the bulk with supercooling; (iii) crystallisation is uniform and statistically steady; (iv) crystals do not interact; (v) crystals are monodisperse. These assumptions are commented below.

(i) The snow zone is motionless. The stable chemical and thermal stratification of the snow zone is the main ingredient that favours little motion in the snow zone appart from inertia-gravity waves. Experiments with glass spheres during this PhD and in preceding experiments of Valentin Dorel and Ludovic Huguet in IRPHE (summer 2020) have shown that particles can 'swim' in inertial and internal waves when their settling velocity couples adequately with the phase or the group velocity of these waves. This might induce heterogeneities and maybe additional motions in the snow zone. The strength of the stratification depends on its ability

to resist these motions and the convective overshoots at its lower end – Christensen (2015) calculated that overshoots would typically be 2.5 km-high in Ganymede's core –, on how subadiabatic the snow zone is, and on the rate of crystallisation since the release of light sulfur-rich fluid strengthens the stratification.

(ii) Crystallisation happens in the bulk with supercooling. The existence of fluid motions in the snow zone could favour a mode of bulk crystallisation due to local perturbations that would trigger crystallisation in the supercooled metastable liquid. Due to the unreasonable degrees of supercooling that are required for crystallisation without condensation nuclei (the so-called *homogeneous nucleation*), the presence of such nuclei is paramount for crystallisation to be volumetric (Houze Jr, 2014). It is unclear what these condensation nuclei could be in a planetary core, what their concentration could be, and whether they would have an appropriate wettability and crystal lattice to enable pure iron to crystallise on their surface (Houze Jr, 2014). The possibility of volumetric crystallisation remains to be proven. Another option is the crystallisation of snow flakes at the CMB, which is discussed along with the assumption (v).

(iii) Crystallisation is uniform and statistically steady. The fluid motions mentioned when discussing (i) favour the formation of heterogeneities that make a uniform crystallisation unlikely. Crystallisation has little chance to be steady because a supercooled system is metastable: the assumption of a constant supercooling cannot hold if the kinetics of crystallisation is faster than the secular cooling of Ganymede (0.01 K/Myr). If crystallisation is assumed to be steady in the bulk, some resulting open questions are: Are condensation nuclei continuously renewed? If so, how are they, where do they originate from?

(iv) Crystals do not interact. Although flake-flake interactions have been disregarded in the literature, they are extremely likely. The various particle-laden flows investigated in this manuscript provide numerous illustrations of particle-particle interactions at several different particle Reynolds numbers even just through hydrodynamics, even in a quiescent fluid – for example with drafting-kissing-tumbling interactions when two particles settle one in front of the other. The presence of velocity gradients generates relative velocities between snow flakes hence it further favours flake-flake interactions (Ghosh et al., 2005). These remarks are important because mechanisms of stochastic collection have proven decisive for the growth of hydrometeors in the Earth atmosphere (Falkovich et al., 2002; Houze Jr, 2014). We have seen that the volume fraction of snow flakes is $\phi(z = 0) \sim 10^{-10}$ at the top of the precipitation layer, which is detrimental for crystal-crystal interactions, but these values are obtained if crystallisation is uniform and steady. If instead the mass flux $\dot{m}'' = 1.29 \times 10^{-10}$ kg.m^{-2}.s^{-1} is a time average of episodic and heterogeneous puffs of concentrated snow flakes, and since debris of large snow flakes are likely condensation sites for others (Rees Jones and Wells, 2018), collisions and collection of snow flakes might be possible. Then, these snow flakes would grow much larger than estimated until now (e.g. Houze Jr, 2014).

(v) Crystals are monodisperse. Lastly, a crucial point is that the distribution of snow flakes *cannot* be monodisperse if crystallisation is possible in the bulk. This conclusion can be drawn from figure 5.14a. Consider an arbitrary radius $r_{p0} < 2.6$ cm at the bottom of the snow zone, and assume the distribution is monodisperse: then, the solid dark line shows the position where every single crystal must nucleate. A consequence of this unrealistic scenario would be that crystallisation is absent in the upper part of the snow zone, although it is the region evacuating heat out of the core. Instead, figure 5.14a should be read as such: the solid

dark line shows the fraction of the snow zone (below the line) where crystals of size $\leq r_{p0}$ originate from. Importantly, crystals of size $r_{p0} < 10^{-3}$ m only form very near the bottom of the snow zone and therefore account for just a tiny fraction (in volume of the snow zone) of the crystallisation inside the snow zone.

Under the assumption of bulk uniform crystallisation, nucleation happens anywhere in the snow zone, so at a given depth many crystal sizes are found, with the largest crystals originating from the CMB. The latter set an upper bound for the radius of crystals at a given depth. This upper bound is shown in figure 5.14b: this size is nil at the CMB where the largest crystals nucleate, and it grows up to $r_p \simeq 0.5$ cm within 10% of the thickness of the snow zone. This dark curve gives a hint of how polydisperse the snow zone is for a bulk uniform steady crystallisation with no flake-flake interactions. Adding interactions should exacerbate this conclusion. Similarly, the solid-liquid interface of the CMB is a wide nucleation site that is not subject to the constraint of settling during crystallisation. There, crystals might grow much larger than the present estimates before detaching from the CMB, beyond kilometers Huguet et al. (2018a,b); Neufeld et al. (2019). The detachment of such huge blocks would be another source of substantial fluid motions and heterogeneities in the snow zone. Coming back to (iv), even in the absence of heterogeneities and fluid motions, polydispersity is a source of differential settling between fast-falling large flakes and slowly-falling small flakes, favouring mechanisms of collection that positively feedback on polydispersity and differential settling.

5.5.3 Implications of polydispersity for remelting

There are two main reasons for remelting snow flakes to be polydisperse at a given depth. The first one is discussed above: crystallisation of snow flakes at different depths necessarily leads to a polydisperse distribution at the top of the precipitation layer.

The second reason is due to the coupling between remelting flakes and the plume, that has been neglected so far. To illustrate this point, let us simplify the problem: consider a monodisperse distribution that starts remelting at depth $z = 0$ in a motionless ambient. Consider a series of successive timesteps dt. During the first timestep, snow flakes settle and remelt. Because the fluid is motionless, they have left solute behind them, so that the fluid is now denser with $\mathcal{C}(z = 0^+) > 0$. During the second timestep, new snow flakes settle in the dense fluid with a lower density ratio $\rho_{Fe}/\rho(z = 0^+) - 1$ and a lower melting rate $|\dot{r}_p|(z = 0^+)$ because both quantities decrease with the plume concentration. These two effects compete in determining how snow flakes evolve: snow flakes are larger than in the absence of feedback from the concentration, thus increasing their settling velocity, but the reduced density ratio conversely slows them down. If flakes fall faster, they catch up some smaller grains at larger depth: the distribution becomes polydisperse. Similarly, if snow flakes fall slower, they might be caught up by the flakes of the next timestep.

Since the distribution of snow flakes is necessarily polydisperse, a key question is: How reliable are results of monodisperse models to represent iron snow ? The results of monodisperse plumes provide the fundamental elements to understand polydisperse distributions, but summing these results over several sizes of snow flakes is not possible. Indeed, the field of concentration $\mathcal{C}(z)$ is determined by all sizes of flakes, and it feedbacks on all of them. Similarly, the plume velocity U_{plume} depends on the radius of snow flakes, and it feedbacks on all of them.

Consequently, a simple summation on r_p is only valid when disregarding flake-flake interactions, the plume velocity and the feedback of the fluid on snow flakes. Further insight would require a dedicated method that can resolve the system's polydispersity, which is beyond the scope of the present work. Preliminary considerations and work on this aspect are briefly presented in the Conclusion and future lines of work.

5.6 Final remarks and open questions

The present estimates on the distance of remelting of snow flakes are based on the assumptions that they are monodisperse and that they fall in a plume.

To gain insight on the role of polydispersity, new experiments of sugary plumes could be designed with a larger number of sieves to precisely control the polydispersity of sugar grains at the source. Key questions are: Is the mean radius sufficient to predict the evolution of snow flakes? Of the flow? If not, how many new moments of the distribution should be known? The shape of the distribution could be willingly modified to vary from Gaussian to bimodal, as can spontaneously emerge by processes of stochastic collection in clouds (e.g. Houze Jr, 2014).

Even if we assume that snow flakes instantly remelt with a uniform flux at the bottom of the snow zone, the molten snow would nourish a Rayleigh-Taylor instability that is a source of heterogeneity parallel to the lower interface of the snow zone, and that nourishes a compositional convection that is at best *statistically* homogeneous along this direction. Along with other sources of heterogeneity, like the existence of typically 2.5 km-high convective overshoots at the bottom of the snow zone (Christensen, 2015), these elements favour the formation of plumes, but what controls their dynamics? Better constraints on the plume formation could be obtained by additional experiments of sugary plumes in a larger tank (see the final remarks in section 4.8). The influence of the source radius could be quantified by changing the size of the sieve, ideally reaching very large surface areas. A key question here is: When the surface area of the source is very large, does the flow evolve to a unique large length scale, or does it destabilise and generate several plumes ? If several plumes develop, what sets their length scale? Experiments of Iga and Kimura (2007) with a uniform flux of bubbles injected at the bottom of a square 24 cm $\times$ 24 cm water tank have shown that the bubble-driven convection leads to irregular 3D patterns that do not reach a steady state. Although experiments with a very large sieve over a very wide tank would be beneficial, such experiments would be very challenging due to their daunting complexity and the difficulty to control perturbations of the water free surface when sugar grains land on water.

The influence of planetary rotation should also be investigated, as suggested by the low plume Rossby numbers in figure 5.7d. Previous authors Tao et al. (2013) have shown that background rotation can delay the onset of a Rayleigh-Taylor instability. Then, how does rotation constrain the size of plumes ? The answer might depend on the latitude. Indeed, plumes near the pole would be parallel to the rotation axis, so that the Coriolis force would have a low magnitude due to small horizontal velocities. Conversely, near the equator the plumes would be orthogonal to the rotation axis so we expect the Coriolis force to have a major influence on their dynamics – in fact preventing them from falling – as quantified by the conservative estimate Ro_{plume} (5.14). If the length scale of deflection of these plumes is

controlled by a balance between their inertia and the Coriolis force, equatorial plumes are expected to deflect at a distance in the range $10^{-4} - 10^{-1} R_{\text{plume}}$. Polar plumes can easily be studied in experiments, but plumes at lower latitudes would require an off-centered tank to modify the angle between gravity and the rotation axis. Of course, insight can be gained from numerical simulations. If snow flakes are considered to melt instantly, or if they are monodisperse and not too decoupled from the flow (see the Conclusion and future lines of work), an equilibrium-Eulerian approach as in chapter 2 can be used. Otherwise, finer models might be required like Lagrangian point-particle approaches, or for a small number of particles, simulations that fully resolve the flow, even at the particle scale (Balachandar and Eaton, 2010).

Conclusion and future lines of work

6.1 Main results

This PhD was motivated by particle-driven flows in two contexts: the iron snow driven by the cooling of small planetary cores, and the metal-silicate mixing following a planetary impact. After past studies that were led in the team (Wacheul and Le Bars, 2018; Qaddah et al., 2019; Huguet et al., 2020), the new ingredients of interest for this PhD were the influence of the collective behaviour of particles on their dynamics, on the flow they can force, and how planetary rotation affects them. The main results are summarised here.

1. An instantaneous localised release of glass spheres settling in water initially grows linearly with depth; after a short acceleration phase, the cloud decelerates; when the cloud velocity becomes lower than the settling velocity of an individual particle, the glass spheres rain out of the cloud. The initial growth of the cloud fits in the theory of one-phase turbulent thermals, according to which clouds of identical initial size and buoyancy should evolve identically. Yet, we showed that varying the radius of the glass spheres modifies the growth rate of particle clouds – the so-called entrainment rate α. Particle-laden thermals grow faster than their one-phase salty counterparts, with an optimum for a given size of particles, quantified by the dimensionless settling velocity of particles – the so-called Rouse number $\mathcal{R}$ – which equals $\mathcal{R} \sim 0.3$ at the maximum growth rate.

2. The observation of an enhanced growth rate of particle clouds compared to their salty counterparts proved consistent with classical interpretations based on the well-known phenomenology of particle-laden turbulent flows. Yet, a closer investigation with 3D two-way coupled Eulerian simulations shows that turbulence is not key to this phenomenon. Laminar simulations recover this maximum entrainment in buoyant vortex rings, which is controlled by how particles arrange in the vortex, disrupt its structure and weaken its circulation, thus enhancing the cloud growth.

3. The presence of a background solid-body rotation modifies the clouds' evolution in experiments. As they decelerate and grow, they lose inertia and are increasingly influenced by rotation. The clouds' growth ceases as soon as the Coriolis force becomes comparable to their inertia i.e. when the Rossby number equals unity. The clouds subsequently propagate downward with constant radius and velocity while detraining particles in a regime of vortical column that is aligned with the rotation axis.

4. After a planetary impact, the metal of the impactor falls down a magma ocean in the form of a turbulent thermal made of silicates and iron drops. Compared to past studies that neglect the influence of planetary rotation, the volume of silicates entrained by this cloud is reduced in the vortical regime. This reduces the dilution of metal drops in silicates, and therefore lowers the efficiency of chemical equilibration. If the magma ocean is deep enough, iron drops may rain out of the column and complete their equilibration through the so-called regime of 'iron rain'. The depth of the magma ocean controls the final efficiency of chemical equilibration.

5. The continuous sieving of sugar grains above water forces buoyant plumes that reach a quasi-steady state. Very small grains dissolve close to the surface in a short amount of time, and nourish a turbulent plume. For such grains, no specific influence of the sugar grains is detected. As the grain size increases, particulate effects set in: grains decouple from fluid motions and have vertically-biased trajectories. This leads to a dilution of buoyancy that nourishes a slower and increasingly laminar flow. The largest grains rain vertically and quickly hit the bottom of the tank, but it takes much longer for a large-scale laminar flow to emerge. The steady flow is controlled by the interplay between buoyancy and inertia, while the evolution of a grain is controlled by its dissolution and settling with respect to the downward stream.

6. These latter results were applied to draw preliminary conclusions on the remelting of snow flakes in Ganymede. So far, the literature proposed 10μm as an estimate of the size of snow flakes. We find that snow flakes of that size or smaller have little influence on the convective velocities in the deeper core. Conversely, larger flakes modify these convective velocities, but as soon as their size exceeds $\sim 50-100\mu$m, they decouple from the flow so that most of their evolution is controlled by their settling. Since the remelting of a snow flake accelerates as the snow flake shrinks, most remelting happens at the end of the flake's trajectory. Snow flakes below $\sim 50-100\mu$m follow the flow, so the fluid motions control the depth where molten snow is produced. Conversely, grains larger than $\sim 50-100\mu$m decouple from fluid motions and may therefore manage to cross through flow structures to inject molten snow down to 29 km below the snow zone when snow flakes are 1 m-large.

6.2 A few prospects and open questions

In the conclusion of each chapter can be found guidelines for future investigations that are specifically in the continuity of this chapter. My choice here is to present some main ideas that could guide new projects to improve our understanding about the global challenges of this work.

6.2.1 Background rotation and tilted gravity

The results of Chapter 5 show that rotation can largely affect some plumes of melting snow flakes in Ganymede, with a likely dependence on the latitude. This calls for experiments of

sugary plumes on a spin table with various angles between gravity and the rotation axis by varying the distance between the tank and the centre of the spin table – see an illustration in figure 6.15. The mass rate and size of grains could be varied, along with the angular velocity of the table and the distance between its centre and the position of the tank. Note that the angular velocity would set the magnitude of the Coriolis force, whereas the position of the tank would set the centrifugal force which controls the average direction of gravity where the tank is located. The homogeneity of the direction of effective gravity on the scale of the experiment would be controlled by the size of the tank. The magnitude of the centrifugal force could not be tuned without modifying the effective direction of gravity. Numerical simulations could offer more flexibility on this aspect, but their cost could be detrimental – see the following elements of discussion.

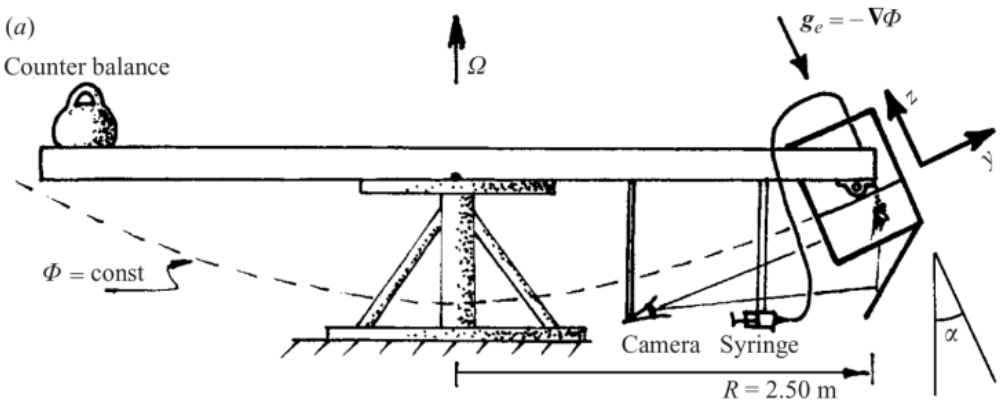

Figure 6.15: *Figure extracted from fig. 1 in Sheremet (2004). A tank is attached to the rightmost tip of a spin table that rotates around the vertical axis. The combination of gravity along the vertical and the centrifugal force along the horizontal results in an effective gravity that is inclined with an angle α with respect to the vertical. See Sheremet (2004) for additional details.*

6.2.2 Persistent challenges for numerical simulations

The numerical modelling of the reactive particle-laden flows of the present work is extremely challenging because of their multiscale and multiphysics nature. Experiments are a solution only up to their own limitations, some of which are the visualisation and flow-sensing techniques, the size of the experimental setup, the vertical gravity, the non-spherical geometry, the limited range of available particle sizes, densities, shapes, melting-or-dissolution rates, the limited number of fluids that can transport them, etc. Numerical simulations and experiments should therefore work hand in hand to gain understanding on these flows. This requires to solve persistent challenges for numerical modelling.

A first key ingredient that makes the cost of numerical simulations prohibitive is the contrast between the macroscale ($\sim 10^6$ m) and the particle scale ($\sim 10^{-6}$ m). This ingredient is problematic because the flows of interest are nourished by a buoyancy flux that explicitly depends on particulate properties like their size, density, and actually more when particles are not assumed spherical: porosity, anisotropy, surface roughness are some of many factors that

affect the orientation and settling velocity of complex particles (Heymsfield and Westbrook, 2010; Voth and Soldati, 2017; Sheikh et al., 2020; Li et al., 2021).

The dependence of the buoyancy flux on the particulate properties is true for inert particles due to the need to describe, at the very least, their sedimentation. It is even more true for reactive particles due to the need to account for the transfer of buoyancy from the particulate phase to the fluid through phase change, with a melting rate that is an explicit function of the particle size. This diversity of length scales is accompanied by a wide range of timescales to be solved, especially in the geophysical context. For example, the remelting of snow flakes in Ganymede must be analysed at the scale of seconds, but the fluid motions they nourish are analysed over billions of years in Rückriemen et al. (2015, 2018).

A second problematic ingredient is the dilution of particles. The agreement between the simulations in Chapter 2 and the experiments of Chapter 1 has shown the adequacy of the Eulerian two-way coupled formalism to model our particle-laden clouds with volume fractions of order $\phi \sim 10^{-3} - 10^{-4}$. However, according to the most recent models of iron snow (Rückriemen et al., 2015, 2018), snow flakes are expected to settle in a very dilute regime ($\phi \sim 10^{-10}$) for which an Eulerian description of particles as a field continuous field of concentration is expected to be inaccurate in the context of particle-driven flows due to the insufficient number of particles per unit volume to model them as a continuum (Chou and Shao, 2016). But this last conclusion is usually drawn on systems that exhibit no such huge separation of timescales as mentioned above. The experiments of sugary plumes have shown that the largest sugar grains were much too distant to collectively drag the interstitial fluid from the very start of the transient, but after some time, the cumulative drag and deposition of solute by many successive grains did produce a flow at a large scale. It means the continuum approach might be inaccurate at small timescales, but it might capture the forcing by particles when used on timescales that are larger than the sedimentation time, when averaging the forcing not only over the number of particles present in a unit volume at a given moment, but also over time. This is especially important as this regime is very likely for iron snow. In addition, Rückriemen et al. (2015) legitimately pointed out that a billions-of-years-long model of thermal evolution of Ganymede cannot resolve the timescales of crystallisation, settling and melting of the snow flakes.

All this suggests new approaches using multiscale numerical methods. The fluid motions could be solved on a large timescale, which would appear as a steady input from the point of view of the fast dynamics of snow flakes. The evolution of the flakes, on the opposite, would be solved on a short timescale, which should provide an output that is finally used to update the slowly-evolving fluid motions. However, these methods face their own challenges in terms of numerical cost, of how different the fast and slow timescales should be, and how the coupling should be performed to guarantee convergence (Kevrekidis and Samaey, 2009; Tong et al., 2019). Thus, such approaches would need to be benchmarked. This could be performed with experiments that would be sufficiently long and with a large separation of scales between the particle scale and the macroscale of the flow.

A third issue for numerical simulations is polydispersity. Consider a monodisperse particle-laden flow. In addition to the usual Navier-Stokes equations, the Eulerian formalism in Chapter 2 requires to solve a modified advection-diffusion equation for particles whose dynamics is simple enough because of their low inertia and settling velocity. Now, if particles get larger, their feedback on the fluid gets more complex; solving for their own momentum equation becomes

mandatory, thus largely increasing the numerical cost. But things get even worse if particles of different sizes are present: each new size settles with its own velocity, so the cost increases dramatically with polydispersity. Chapter 4 showed that a given mass rate of our smallest sugar grains produces a very different flow compared to that forced by the same mass rate of our largest grains. Thus, it can be expected that the transient formation of a polydisperse plume, and possibly its permanent regime (if it exists), depend on the size distribution of the grains that are sieved.

To what extent? How important is polydispersity? What is the minimum physics for numerical solutions to accurately model particle-driven flows ? Is it possible to circumvent the issue of dilution by averaging the particulate forcing in time? How can the flow and the evolution of particles be solved on different timescales while remaining coupled? The following discussion proposes ideas that are aimed at both gaining insight into the physics of particle-laden flows, and offering benchmarks to choose, validate and control numerical models.

6.2.3 Influence of the particle scale on the macroscale

Plumes of inert particles

Can our approach of modelling particles as a settling volume fraction be suitable for both the transient and the permanent regimes, or possibly just for the latter?

This question is raised because of two observations. First, experiments of sugary plumes have shown that the transient depends crucially on the particle size and not just on a volume fraction; yet, all experiments eventually show a steady plume whose average velocity is controlled only by the effective volume fraction of grains. Second, in Equilibrium-Eulerian simulations like those of Chapter 2, the particles decouple from the ambient due to the drift term that is proportional to the vertical gradient of concentration $\partial\mathcal{C}/\partial z$ in equation (2.9); this gradient is non-zero during the transient, but in the permanent regime it might reduce and possibly become negligible before other terms. Of course, if the transient cannot be captured by the Eulerian approach, one may wonder whether it can converge to a reliable permanent regime (assuming one exists).

In the context of a presumably quasi-steady iron snow, it would be beneficial to perform new Equilibrium-Eulerian simulations and new experiments of sedimentation of *inert* particles in a large tank. In experiments, particles should be sieved with a constant mass rate to impose their volume fraction, since it drives the flow in the simulations. To improve the steadiness of the mass flux and hopefully avoid an *in-situ* calibration for every experiment, the mechanism of sieving should be modified to allow for vigorous vertical shaking of a large mass of particles in a sieve with a lid (see figure 6.16).

Starting with monodisperse particles, the permanent regime of such inert plumes has already been studied experimentally by Zürner et al. (2023). Their experiments could be used as benchmarks to be compared with Equilibrium-Eulerian simulations. Analysing the transient formation of such plumes could also shed light on the transition of the flow from the particle scale to a larger scale. Then, new experiments could be performed with a bidisperse distribution of particles to enable their comparison with new simulations that would track two fields of concentration, one for each size of particles. Finally, additional experiments of polydisperse plumes could show whether polydispersity strongly alters the flow, how it affects the relative motions of particles, and if it modifies the ability of the plume to reach steadiness.

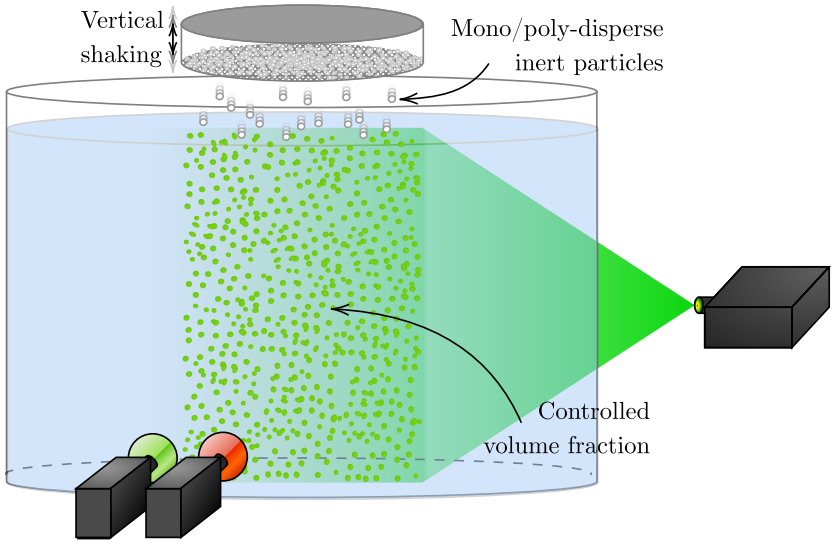

Figure 6.16: *Plume of inert particles, injected by vertical shaking of a closed sieve above a large-scale water tank. Fluid velocities could be measured by seeding the tank with orange PIV particles (not shown for the sake of visibility).*

Moving forward on these issues would enable to use numerical simulations and experiments jointly to answer the burning questions: *Does the large-scale flow (the macrophysics) fundamentally depend on the physics at the particle scale (the microphysics)?* Two quantities are included in the Eulerian simulations: the volume fraction ϕ (it is proportional to the mass concentration $\mathcal{C}$) and the settling velocity w_s. *Are these quantities sufficient to predict the flow?* Our experiments of sugary plumes do not enable us to answer this question: when varying the size of grains, we also varied their settling velocity, which in turn modified the effective volume fraction. To reach a conclusion, these new experiments should vary particle properties like their size, density, and interparticle distance while keeping ϕ and w_s constant. Note that the interparticle distance cannot be finely imposed in plumes; the next experiments propose a method to accurately impose its value when studying the interaction of a few particles.

Controlled interactions between particles or solute lamellae

What is the fundamental process of the transition of the flow from the particle scale to a larger scale?

To get further insight beyond global statistics, fine analyses could be performed at the particle scale. Figure 6.17a illustrates a first setup to conduct experiments with dyed sugar grains that deposit lamellae in water before they hit the bottom of a tank and sit there (step A). Since lamellae are negatively buoyant, they are expected to eventually fall in the liquid; of course, the motion of an isolated lamella should be investigated first. In the case of several lamellae, if they are not too buoyant, they may diffuse towards one another (step B) before falling under their own buoyancy. This diffusion reduces the inter-lamellae spacing and therefore favours their collective drag of the interstitial fluid, favouring the emergence of larger scales in the field of buoyancy. Finally, if lamellae diffuse sufficiently fast compared to the emergence of

fluid motions, step C shows that they will overlap. In that case, they form a macro-object whose buoyancy is reduced because of diffusion (see the attenuation of orange colouring in the sketch) but whose length scale is increased. These successive steps control an eventual transition of the field of buoyancy from the particle scale to a macroscopic scale, that is expected to eventually force a flow at a macroscopic scale as well. The size of each lamella, its concentration, the fluid viscosity, the diffusivity of the solute and the spacing between lamellae are expected to control the transition from the scale of isolated lamellae to a macroscale.

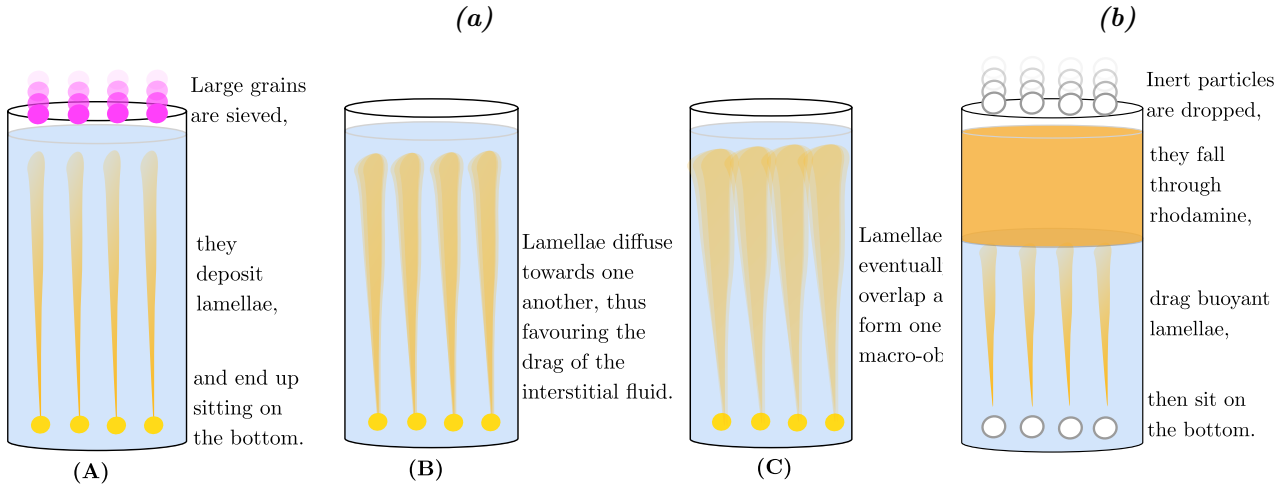

Figure 6.17: *(a) First setup: interaction of sugary lamellae in water after their deposition by settling sugar grains. (b) Second setup: interaction of lamellae that have been dragged down during the fall of inert particles from a top layer of fresh water containing rhodamine down to a bottom layer of salty transparent water.*

Preliminary experiments have been performed with a second setup shown in figure 6.17b. A beaker contained a two-layered system with salt-water at the bottom and fresh water containing a uniform concentration of rhodamine B on top. The density jump was meant to have a sharp interface between transparent salt-water and dyed fresh water. A LED panel was placed behind the beaker. After placing a sieve filled with glass spheres above the beaker, the sieve was gently hit. A few particles settled in the dyed water and eventually crossed the density jump, dragging rhodamine in their wake as lamellae that could interact, in a similar way as in the first setup of figure 6.17a.

These experiments investigate the interaction of lamellae that move due to their buoyancy. The experiments of the first setup should also be performed in a third configuration where particles are inert to avoid any density variation in the fluid. The aim now is to analyse how the wakes of particles can move the inter-wake fluid just through hydrodynamics. To do so, PIV measurements could be used with a small-scale resolution to record localised and slow fluid motions.

All these experiments should first be performed by releasing only two particles before increasing their number. The interparticle distance should be carefully controlled by replacing the sieve with another dedicated system. Additionally, the trajectories of particles ought to

be controlled. Depending on their particle Reynolds number and on the density profile, they may experience undesired complex behaviours (Camassa et al., 2022; Magnaudet and Mercier, 2020) when crossing a density interface like the one in figure 6.17b, especially if they are not spherical (Mrokowska, 2018). Consequently, a complementary setup would consist in placing a row of telescopic teeth underwater (see figure 6.18 for an illustration). The teeth would be fixed at the bottom of the tank, and they would initially be extended (situation A in figure 6.18) before quickly retracting at the start of an experiment (situation B in figure 6.18). The interaction between the teeth's wakes could be quantified by PIV measurements (as in the third setup); alternatively, retracting the teeth accross an interface between dyed water and transparent water would enable to analyse the interaction of lamellae through Laser-Induced Fluorescence (see the configuration B that is sketched in figure 6.18).

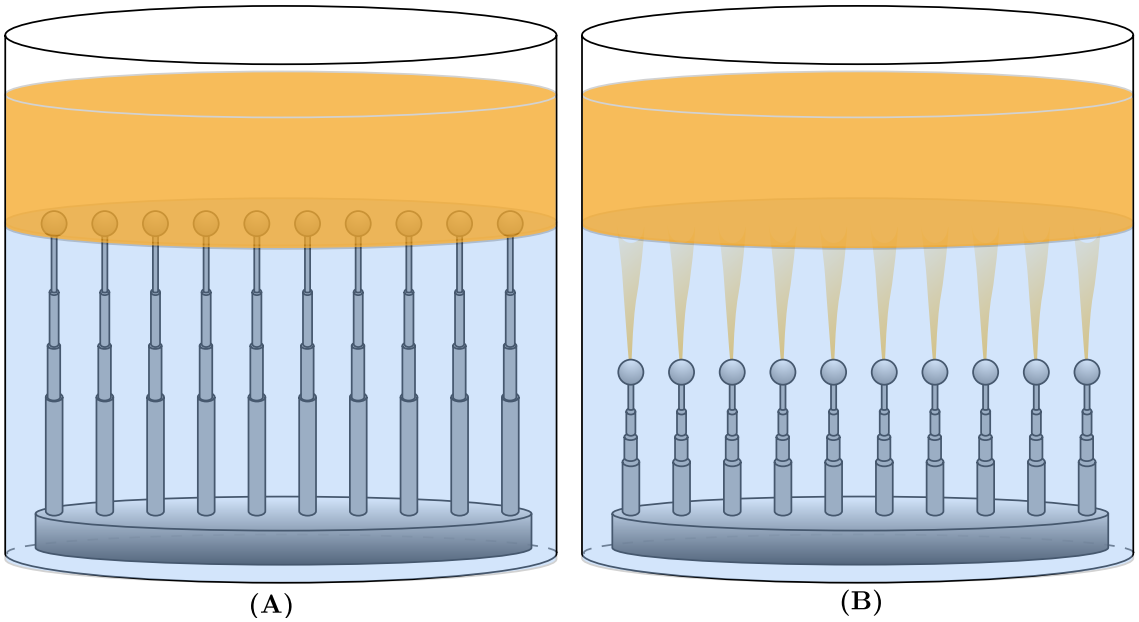

Figure 6.18: *A row of telescopic teeth is fixed at the bottom of a water tank. The teeth are initially extended high in the tank (A), before retracting them to analyse the interaction between their wakes (B). In the present sketch, the teeth drag dyed water downward, enabling to analyse the wakes' interactions with LIF.*

A last question is: *In the regime of dilute large sugar grains falling far from one another, how much are the eventual laminar plumes driven by the cumulative influence of successive wakes and lamellae, rather than by their interactions at a fixed time?*

To begin with, a single particle, reactive or inert, can be dropped in still water at a fixed location. Then, this can be reproduced iteratively with a fixed period T_{iter} between two iterations. With inert particles, if T_{iter} is much larger than the timescale of viscous dissipation of the wakes, all iterations are expected to be identical. With sugar grains, the deposition of a buoyant lamella will necessarily lead to the emergence of a downward motion so successive iterations are not identical. This experiment can finally be extended by dropping 2 or more particles, distributed on a chosen surface area with a controlled interparticle distance, so as

to get closer to the experimental conditions of the sugary plumes of the new experiments of plumes driven by inert particles (figure 6.16).

6.2.4 Accounting for polydispersity

How reliable are results of monodisperse experiments or simulations? What is the impact of polydispersity on the generation of fluid motions by particles? How could it be quantified?

To get some first insight on the consequences of polydispersity, a formalism of 'bin equations' could be used (Houze Jr, 2014). We here describe equations modelling the time-evolution of a distribution of sugar grains of various sizes. Assuming horizontal uniformity, the grains are described in a phase space (r_p, z, t) by a number density $\mathcal{N}(r_p, z, t)$ in units of number of grains per unit volume and per unit size of grains. Only the situation of a motionless and initially clear ambient is considered. Sugar grains enter the domain from the top, as they do at the start of our experiments. They evolve towards larger depths z because they settle with a velocity w_s, and they evolve towards smaller radii r_p because they dissolve with a velocity $|\dot{r}_p|$. These fluxes are responsible for time variations of the distribution $\mathcal{N}(r_p, z, t)$, and the mass concentration of solute $\mathcal{C}(z, t)$ is nourished by the dissolution at the surface of all grains of all possible sizes. These considerations translate mathematically as

$$\frac{\partial \mathcal{N}}{\partial t} = -\frac{\partial \mathcal{N} w_s}{\partial z} + \frac{\partial \mathcal{N}|\dot{r}_p|}{\partial r_p} \ , \tag{6.27}$$

$$\frac{\partial \mathcal{C}}{\partial t}(z,t) = \int_{\mathbf{R}^+} 4\pi r_p^2 |\dot{r}_p|(r_p, z, t)\mathcal{N}(r_p, z, t)\rho_p dr_p \ . \tag{6.28}$$

Equation (6.27) is the conservation of the number of grains, and equation (6.28) is the mass transfer from solids to solute. These equations are accompanied by boundary and initial conditions

$$\mathcal{C}(z, t = 0) = 0 \ , \tag{6.29}$$

$$\frac{\partial \mathcal{N} w_s}{\partial z}(r_p, z = 0, t) = j_{\mathcal{N},0}(r_p) \ , \tag{6.30}$$

$$\frac{\partial \mathcal{N}|\dot{r}_p|}{\partial r_p}(r_p = r_{p,\max}, z, t) = 0 \ , \tag{6.31}$$

where $j_{\mathcal{N},0}(r_p)$ is the flux of grains imposed at the plume source, and $r_{p,\max} \equiv \text{argmax}(\mathcal{N}_0)$ is the size of the largest grain in $j_{\mathcal{N},0}(r_p)$ which is always finite. Equation (6.29) imposes that the ambient is initially clear of solute, equation (6.30) controls the distribution of grains coming in through the plume, and equation (6.31) guarantees that no grain enter the phase space from the boundary $r_p = r_{p,\max}$. Figure 6.19a illustrates the time evolution of several possible sizes with a sketch.

Preliminary results have evidenced some core qualitative effects of polydispersity. The evolution of an initially Gaussian injection of average grain radius $r_p = 80$ μm is shown in figure 6.19b. The distribution evolves towards larger depths and smaller radii respectively

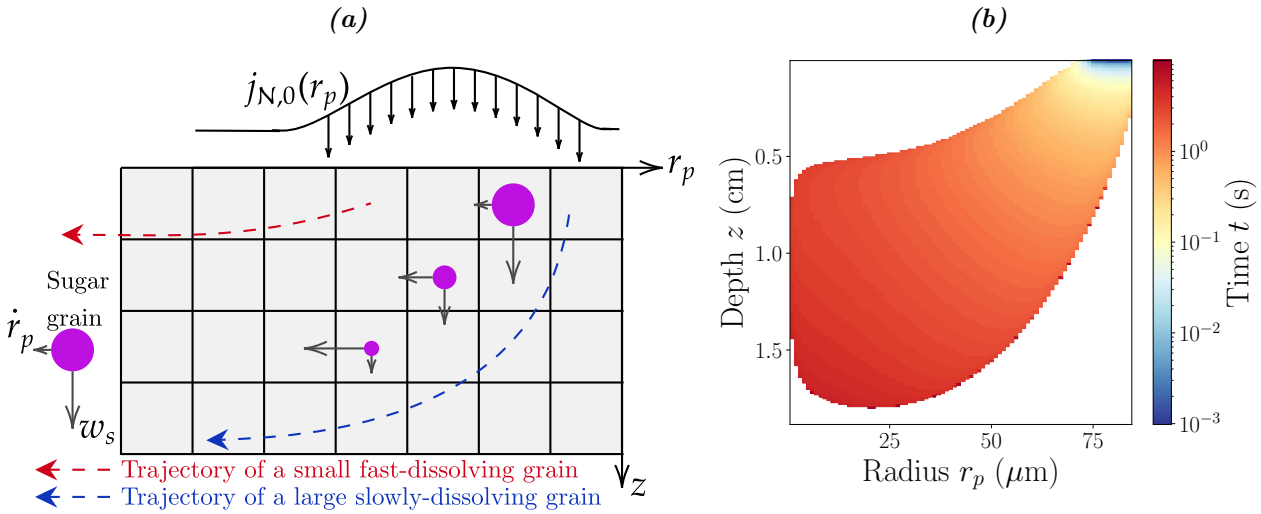

Figure 6.19: *(a) Evolution of a polydisperse system fed by a flux $j_{\mathcal{N},0}(r_p)$ at the top of the domain, whose grains evolve towards larger depths and lower radii due to phase change. (b) Time evolution of the isovalue $\mathcal{N}(r_p, z, t) = 10^{11}$ in the phase space (r_p, z), for a Gaussian injection of average radius 80 μm, standard deviation 3 μm and mass rate $\dot{m} = 0.1$ g/s at the source (the resolution is 1 μm in r_p and 10^{-2} cm in z, the timestep is $dt = 9.8 \times 10^{-4}$ s).*

due to settling and dissolution. We found (not shown here) that the moments of order ≤ 2 of the distribution $\mathcal{N}$ get closer and closer to a steady state. Yet, no permanent regime is reached. This is expected: no flow is presently modeled since no advection terms are present in equations (6.27)-(6.28), hence the concentration of sugar in the domain necessarily increases monotonically. This delays dissolution by an effect of saturation, and modifies the settling velocity of the grains because it modifies the ambient density and therefore the grains' buoyancy. These effects can compensate; their interplay can be a source of polydispersity at a given depth, depending on the concentration of solute and how the settling velocity $w_s(r_p)$ and the dissolution rate $|\dot{r}_p|(r_p)$ vary with r_p. Additional simulations (not shown here) with different initial distributions of identical average radius and variance led to different results. For the same average and variance, an enrichment of the distribution in larger grains enables sugar to dissolve deeper due to the larger settling velocity and slower dissolution of these large grains. Consequently, the concentration profile $\mathcal{C}(z, t)$ reaches deeper in the tank, which means the precipitation layer is deeper. Although qualitative and preliminary, these observations suggest that the mean size and variance at the source might be insufficient to accurately predict the development of the sugar-laden layer at the top of the computational domain. Higher-order moments of the distributions might be required for an improved modeling. We expect this conclusion to be exacerbated if instead of being unimodal at the source, the distribution is for example bimodal. In that case, depending on the amplitude of each of the two modes, the average radius may not be representative of the evolution of $\mathcal{N}$ in time and depth.

If the distributions cannot be resolved due to a large numerical cost, a key question is: *What closure should be proposed when integrating the equations (6.27)-(6.28) to formulate a so-called 'bulk model' based on a finite number of moments (Houze Jr, 2014)?*

Future work could quantify, for example, how much the depth of the sugary layer depends on the low-order moments of the initial distribution. Idealised experiments could control the initial distribution of sugar grains at the source and estimate its evolution with depth thanks to dedicated visualisations of grains in a narrow tank to prevent too many grains from masking the field of view if they fall in the foreground. The comparison of experiments and simulations would ideally help improving our understanding of the role of polydispersity in precipitation-driven flows, and how finely it should be modelled.

6.2.5 Quantifying the role of phase change

Reactive versus inert plumes

Are the fluid motions forced by reactive plumes due to the hydrodynamical forcing by particles, or due to the solute produced by phase change ? How much does the latter contribute to the forcing?

Because of the complexity of these structures, an unambiguous answer requires new experiments. The aim is to use a combination of (i) a fluid of predilection, (ii) some inert particles, (iii) some other particles of identical size and density that dissolve or melt in the chosen fluid. This would guarantee that the hydrodynamics of all particles are identical as long as phase change does not occur. Any difference between an inert and a reactive plume would thus be due to phase change. Note however that the role of phase change is twofold: by reducing the size of grains, it lowers their inertia and decoupling from the fluid motions; by reinjecting buoyancy in a dissolved form, it guarantees a transition of the flow to a fluid-like behaviour, and it modifies the ability of buoyancy to diffuse in the flow, with a transition from the hydrodynamical diffusion of sugar grains to the mass diffusivity of sugary water.

Melting/dissolution at the particle scale

How does the capsule of buoyant solute that accompanies dissolving sugar grains along their fall modify their settling velocity and dissolution rate? What is the maximum distance travelled by this capsule? How much does it contribute to forcing the flow, both before and after a grain has fully dissolved?

Here, insight could be gained by considering different reactive particles that melt or dissolve in a liquid, some with a negatively buoyant solute, some with a positively buoyant solute, and finally others with a neutrally buoyant solute. The concentration of the ambient could be varied to modify the rate of phase change, and the size of grains could be varied to modify the particles' Reynolds number. The procedure of cooking dyed sugar could be calibrated to quantitatively measure the concentration of the sugar grains. When dye cannot be introduced in the particles, Schlieren could be used to track changes of refractive index. Numerical simulations of a single particle could be especially valuable on these aspects to control the buoyancy of the solute and to track concentrations in the ambient.

A fundamental question for all parameterisations is: *How different are the settling and dissolution/melting of a spherical particle versus an actual crystal? How reliable are results based on the assumption that particles are spherical?*

Several references show that crystallisation can develop instabilities that lead to an anistropic growth of the crystal which results in distinct patterns, as typically observed for snow flakes (e.g. Langer, 1980; Houze Jr, 2014; Kurz and Fisher, 1998). For our experiments with sugar, we observed that particles are not spherical but have a smooth surface and an aspect ratio of order unity. This likely explains the reasonable agreement between our measurements and theoretical considerations that assumed the sugar grains spherical. For crystals however, a tree-like structure would make them porous. Just due to geometry, this could lead to a discrepancy between their assumed size and mass. In addition, despite an apparent large size, they may retain fluid – either their own melt/solute, or the ambient liquid – and therefore have a modified buoyancy compared to predictions based on the assumption of particles being spherical, as illustrated by the example of marine snow in the Introduction.

Phase change in planetary cores

What is the regime of crystallisation in planetary cores? Can crystals form in the bulk? How supercooled should the core be for their nucleation?

The questions about crystallisation in planetary cores remain numerous. Past studies in multiple contexts have shown that homogeneous nucleation is extremely unlikely due to the considerable amounts of supercooling it demands (Houze Jr, 2014; Huguet et al., 2018b), and that conversely, heterogeneous nucleation on nuclei is much more likely. According to Avrami (1939), 'the existence of [condensation nuclei] is so well established that to ignore it in a theory of the kinetics of phase transformation is to open the way to gross discrepancy with the experimental data'. Yet, due to the huge dependence of the rate of nucleation on temperature (Huguet et al., 2018b), large rates of supercooling might still be required for crystallisation, especially if the nuclei have a poor wettability and an inadequate crystalline structure (Houze Jr, 2014; Huguet et al., 2018b). The CMB offers a large surface area on which to nucleate, but is it an adequate nucleation site for iron snow flakes? Experiments of crystallisation in a supercooled liquid could help gaining insight on these issues. When the bulk is supercooled, if a solid surface is present, do crystals always nucleate on this surface? If not, what are the requirements for bulk crystallisation, in terms of surface condition of the substrate, amount of supercooling, purity of the fluid...? Once crystallisation starts, is it catastrophic or slow, localised or widespread? During crystallisation, how does the degree of supercooling evolve?

If results do exist in the literature on crystallisation at the particle scale, a lot remains to be known, and little exists on these challenging and exciting questions to model crystallisation of a large-scale system.

New horizons

The present work can be opened to broader horizons, starting with atmospheric flows. Through condensate loading and evaporative cooling (Zuidema et al., 2017), precipitation-induced downdrafts are known to carry cold air below the cloud level, forming regions of low temperature named *cold pools* (Tompkins, 2001) that play a key role in the organisation of clouds as aggregates (Muller et al., 2022), which 'remains one of the largest sources of uncertainty in climate models and thus for reliable projections of climate change' (Beniston, 2013). Indeed, when the

downdrafts reach the ground, they create diverging currents named *gust fronts*. These currents redistribute moisture as they spread (Lochbihler et al., 2021), lift the surrounding air and favour the formation of secondary updrafts (Zuidema et al., 2017; Tompkins, 2001), contributing to convective self-aggregation and organisation (Lochbihler et al., 2021; Muller et al., 2022).

The study of reactive particle-laden flows is also crucial for many phenomena that develop on Earth – from the formation and dynamics of aerosols (Spada et al., 2013; Veron, 2015) that remains a source of uncertainty in climate modelling (Beniston, 2013; Veron, 2015), to the formation of frazil ice by katabatic winds (Thompson et al., 2020), the transport of microplastics in river sediments (He et al., 2021), the formation of patterns by erosion or dissolution in the environment (Philippi et al., 2019; Cohen et al., 2020), the deposition of volcanic ash-fall layers following an explosive volcanic eruption (Carey, 1997), etc.

Beyond our planet, the flows investigated in this work open a window on a wealth of phenomena that remain to be investigated. The phenomenon of iron snow is one of several possible scenarios for the crystallisation of Ganymede's core, that remain to be explored with the assistance of upcoming measurements by the space mission JUICE. Other planets are thought to be concerned by such phenomena of precipitation by chemical separation, like the Moon in the past and Mars in the future (Breuer et al., 2015), Mercury at present (Dumberry and Rivoldini, 2015) as could be confirmed with new measurements by the ongoing BepiColombo mission, or Jupiter through the phenomenon of helium rain (Brygoo et al., 2021). At larger scales than planets, further understanding of particle-laden flows could help modelling the coupling between gas, dust and turbulence in protoplanetary disks, and how it contributes to early stages of planetary accretion Chambers (2010).

Bibliographie

Y. Abe and T. Matsui. The formation of an impact-generated H2O atmosphere and its implications for the early thermal history of the Earth. *Journal of Geophysical Research: Solid Earth*, 90(S02):C545–C559, 1985.

A. Abramian, O. Devauchelle, G. Seizilles, and E. Lajeunesse. Boltzmann Distribution of Sediment Transport. *Physical Review Letters*, 123(1):014501, July 2019.

A. Aliseda, A. Cartellier, F. Hainaux, and J. C. Lasheras. Effect of preferential concentration on the settling velocity of heavy particles in homogeneous isotropic turbulence. *Journal of Fluid Mechanics*, 468:77–105, Oct. 2002.

S. Alqatari, T. E. Videbæk, S. R. Nagel, A. E. Hosoi, and I. Bischofberger. Confinement-induced stabilization of the Rayleigh-Taylor instability and transition to the unconfined limit. *Science Advances*, 6(47):eabd6605, Nov. 2020.

J. D. Anderson, E. L. Lau, W. L. Sjogren, G. Schubert, and W. B. Moore. Gravitational constraints on the internal structure of Ganymede. *Nature*, 384(6609):541–543, Dec. 1996.

B. Andreotti, Y. Forterre, and O. Pouliquen. *Les milieux granulaires - Entre fluide et solide*. EDP Sciences, Dec. 2012. ISBN 978-2-7598-0925-7.

J. Aubert, S. Labrosse, and C. Poitou. Modelling the palaeo-evolution of the geodynamo. *Geophysical Journal International*, 179(3):1414–1428, Dec. 2009.

M. Avrami. Kinetics of Phase Change. I General Theory. *The Journal of Chemical Physics*, 7 (12):1103–1112, Dec. 1939.

B. A. Ayotte and H. J. S. Fernando. The Motion of a Turbulent Thermal in the Presence of Background Rotation. *Journal of the Atmospheric Sciences*, 51(13):1989–1994, July 1994.

J. Badro, J. Aubert, K. Hirose, R. Nomura, I. Blanchard, S. Borensztajn, and J. Siebert. Magnesium Partitioning Between Earth's Mantle and Core and its Potential to Drive an Early Exsolution Geodynamo. *Geophysical Research Letters*, 45(24):13,240–13,248, 2018.

P. G. Baines. Mixing in flows down gentle slopes into stratified environments. *Journal of Fluid Mechanics*, 443:237–270, Sept. 2001.

S. Balachandar and J. K. Eaton. Turbulent Dispersed Multiphase Flow. *Annual Review of Fluid Mechanics*, 42(1):111–133, 2010.

G. K. Batchelor, H. K. Moffatt, and M. G. Worster, editors. *Perspectives in Fluid Dynamics: A Collective Introduction to Current Research*. Cambridge University Press, Cambridge, 2000. ISBN 978-0-521-78061-2.

J. Bec, L. Biferale, G. Boffetta, A. Celani, M. Cencini, A. Lanotte, S. Musacchio, and F. Toschi. Acceleration statistics of heavy particles in turbulence. *Journal of Fluid Mechanics*, 550:349–358, Mar. 2006.

J. B. Bell, P. Colella, and H. M. Glaz. A second-order projection method for the incompressible navier-stokes equations. *Journal of Computational Physics*, 85(2):257–283, Dec. 1989.

M. Beniston. Grand challenges in climate research. *Frontiers in Environmental Science*, 1, 2013.

D. Bercovici and Y. Ricard. Plate tectonics, damage and inheritance. *Nature*, 508(7497): 513–516, Apr. 2014.

M. Berhanu, J. Philippi, S. Courrech du Pont, and J. Derr. Solutal convection instability caused by dissolution. *Physics of Fluids*, 33(7):076604, July 2021.

T. Berk and F. Coletti. Dynamics of small heavy particles in homogeneous turbulence: A Lagrangian experimental study. *Journal of Fluid Mechanics*, 917:A47, June 2021.

R. B. Bird, W. E. Stewart, and E. N. Lightfoot. *Transport Phenomena*. John Wiley & Sons, Dec. 2006. ISBN 978-0-470-11539-8.

G. Boffetta and A. Mazzino. Incompressible Rayleigh–Taylor Turbulence. *Annual Review of Fluid Mechanics*, 49(1):119–143, 2017.

G. Boffetta, A. Celani, F. D. Lillo, and S. Musacchio. The Eulerian description of dilute collisionless suspension. *Europhysics Letters*, 78(1):14001, Mar. 2007.

D. Bond and H. Johari. Effects of initial geometry on the development of thermals. *Experiments in Fluids*, 39(3):591–601, Sept. 2005.

D. Bond and H. Johari. Impact of buoyancy on vortex ring development in the near field. *Experiments in Fluids*, 48(5):737–745, May 2010.

T. Bosse, L. Kleiser, and E. Meiburg. Small particles in homogeneous turbulence: Settling velocity enhancement by two-way coupling. *Physics of Fluids*, 18(2):027102, Feb. 2006.

L. Brandt and F. Coletti. Particle-Laden Turbulence: Progress and Perspectives. *Annual Review of Fluid Mechanics*, 54(1):159–189, 2022.

D. Breuer, T. Rückriemen, and T. Spohn. Iron snow, crystal floats, and inner-core growth: Modes of core solidification and implications for dynamos in terrestrial planets and moons. *Progress in Earth and Planetary Science*, 2(1):39, Nov. 2015.

W. Brian Tonks and H. Jay Melosh. Core formation by giant impacts. *Icarus*, 100(2):326–346, Dec. 1992.

S. Brygoo, P. Loubeyre, M. Millot, J. R. Rygg, P. M. Celliers, J. H. Eggert, R. Jeanloz, and G. W. Collins. Evidence of hydrogen-helium immiscibility at Jupiter-interior conditions. *Nature*, 593(7860):517–521, May 2021.

A. S. Buono and D. Walker. The Fe-rich liquidus in the Fe–FeS system from 1bar to 10GPa. *Geochimica et Cosmochimica Acta*, 75(8):2072–2087, Apr. 2011.

P. Burns and E. Meiburg. Sediment-laden fresh water above salt water: Linear stability analysis. *Journal of Fluid Mechanics*, 691:279–314, Jan. 2012.

J. W. M. Bush, H. A. Stone, and J. Bloxham. Axial drop motion in rotating fluids. *Journal of Fluid Mechanics*, 282:247–278, Jan. 1995.

J. W. M. Bush, B. A. Thurber, and F. Blanchette. Particle clouds in homogeneous and stratified environments. *Journal of Fluid Mechanics*, 489:29–54, July 2003.

O. Caballina, E. Climent, and J. Dušek. Two-way coupling simulations of instabilities in a plane bubble plume. *Physics of Fluids*, 15(6):1535–1544, May 2003.

W. M. Calvin, R. N. Clark, R. H. Brown, and J. R. Spencer. Spectra of the icy Galilean satellites from 0.2 to 5μm: A compilation, new observations, and a recent summary. *Journal of Geophysical Research: Planets*, 100(E9):19041–19048, 1995.

R. Camassa, L. Ding, R. M. McLaughlin, R. Overman, R. Parker, and A. Vaidya. Critical Density Triplets for the Arrestment of a Sphere Falling in a Sharply Stratified Fluid. In F. Carapau and A. Vaidya, editors, *Recent Advances in Mechanics and Fluid-Structure Interaction with Applications: The Bong Jae Chung Memorial Volume*, Advances in Mathematical Fluid Mechanics, pages 69–91. Springer International Publishing, Cham, 2022. ISBN 978-3-031-14324-3.

R. M. Canup. Forming a Moon with an Earth-like Composition via a Giant Impact. *Science*, 338(6110):1052–1055, Nov. 2012.

R. M. Canup and E. Asphaug. Origin of the Moon in a giant impact near the end of the Earth's formation. *Nature*, 412(6848):708–712, Aug. 2001.

R. M. Canup and K. Righter, editors. *Origin of the Earth and Moon*. University of Arizona Press, 2000. ISBN 978-0-8165-2073-2.

G. Carazzo and A. M. Jellinek. A new view of the dynamics, stability and longevity of volcanic clouds. *Earth and Planetary Science Letters*, 325–326:39–51, Apr. 2012.

S. Carey. Influence of convective sedimentation on the formation of widespread tephra fall layers in the deep sea. *Geology*, 25(9):839–842, Sept. 1997.

P. Carlotti and G. R. Hunt. An entrainment model for lazy turbulent plumes. *Journal of Fluid Mechanics*, 811:682–700, Jan. 2017.

J. E. Chambers. Planetary accretion in the inner Solar System. *Earth and Planetary Science Letters*, 223(3):241–252, July 2004.

J. E. Chambers. Planetesimal formation by turbulent concentration. *Icarus*, 208(2):505–517, Aug. 2010.

Y.-J. Chou and Y.-C. Shao. Numerical study of particle-induced Rayleigh-Taylor instability: Effects of particle settling and entrainment. *Physics of Fluids*, 28(4):043302, Apr. 2016.

U. R. Christensen. Iron snow dynamo models for Ganymede. *Icarus*, 247:248–259, Feb. 2015.

L. Chudinovskikh and R. Boehler. Eutectic melting in the system Fe–S to 44 GPa. *Earth and Planetary Science Letters*, 257(1):97–103, May 2007.

R. Clift, J. R. Grace, and M. E. Weber. *Bubbles, Drops, and Particles*. Courier Corporation, Jan. 2005. ISBN 978-0-486-44580-9.

E. Climent and J. Magnaudet. Large-Scale Simulations of Bubble-Induced Convection in a Liquid Layer. *Physical Review Letters*, 82(24):4827–4830, June 1999.

C. Cohen, M. Berhanu, J. Derr, and S. Courrech du Pont. Buoyancy-driven dissolution of inclined blocks: Erosion rate and pattern formation. *Physical Review Fluids*, 5(5):053802, May 2020.

F. J. Crary and F. Bagenal. Remanent ferromagnetism and the interior structure of Ganymede. *Journal of Geophysical Research: Planets*, 103(E11):25757–25773, 1998.

C. T. Crowe, J. D. Schwarzkopf, M. Sommerfeld, and Y. Tsuji. *Multiphase Flows with Droplets and Particles*. CRC Press, Boca Raton, second edition, Sept. 2011. ISBN 978-0-429-10639-2.

M. Ćuk and S. T. Stewart. Making the Moon from a Fast-Spinning Earth: A Giant Impact Followed by Resonant Despinning. *Science*, 338(6110):1047–1052, Nov. 2012.

H. Daher, B. K. Arbic, J. G. Williams, J. K. Ansong, D. H. Boggs, M. Müller, M. Schindelegger, J. Austermann, B. D. Cornuelle, E. B. Crawford, O. B. Fringer, H. C. P. Lau, S. J. Lock, A. C. Maloof, D. Menemenlis, J. X. Mitrovica, J. A. M. Green, and M. Huber. Long-Term Earth-Moon Evolution With High-Level Orbit and Ocean Tide Models. *Journal of Geophysical Research: Planets*, 126(12):e2021JE006875, 2021.

T. W. Dahl and D. J. Stevenson. Turbulent mixing of metal and silicate during planet accretion — And interpretation of the Hf–W chronometer. *Earth and Planetary Science Letters*, 295 (1):177–186, June 2010.

W. B. Daniel, R. E. Ecke, G. Subramanian, and D. L. Koch. Clusters of sedimenting high-Reynolds-number particles. *Journal of Fluid Mechanics*, 625:371–385, Apr. 2009.

R. H. Davis. Hydrodynamic diffusion of suspended particles: A symposium. *Journal of Fluid Mechanics*, 310:325–335, Mar. 1996.

J. de Leeuw, M. P. Lamb, G. Parker, A. J. Moodie, D. Haught, J. G. Venditti, and J. A. Nittrouer. Entrainment and suspension of sand and gravel. *Earth Surface Dynamics*, 8(2): 485–504, June 2020.

W. C. de Rooy and A. P. Siebesma. A Simple Parameterization for Detrainment in Shallow Cumulus. *Monthly Weather Review*, 136(2):560–576, Feb. 2008.

W. C. de Rooy, P. Bechtold, K. Fröhlich, C. Hohenegger, H. Jonker, D. Mironov, A. Pier Siebesma, J. Teixeira, and J.-I. Yano. Entrainment and detrainment in cumulus convection: An overview. *Quarterly Journal of the Royal Meteorological Society*, 139(670): 1–19, 2013.

R. Deguen, P. Olson, and P. Cardin. Experiments on turbulent metal-silicate mixing in a magma ocean. *Earth and Planetary Science Letters*, 310(3):303–313, Oct. 2011.

R. Deguen, M. Landeau, and P. Olson. Turbulent metal–silicate mixing, fragmentation, and equilibration in magma oceans. *Earth and Planetary Science Letters*, 391:274–287, Apr. 2014.

N. Didden. On the formation of vortex rings: Rolling-up and production of circulation. *Zeitschrift für angewandte Mathematik und Physik ZAMP*, 30(1):101–116, Jan. 1979.

D. P. Dobson, W. A. Crichton, L. Vočadlo, A. P. Jones, Y. Wang, T. Uchida, M. Rivers, S. Sutton, and J. P. Brodholt. In situ measurement of viscosity of liquids in the Fe-FeS system at high pressures and temperatures. *American Mineralogist*, 85(11-12):1838–1842, Nov. 2000.

K. H. Dodds, J. F. J. Bryson, J. A. Neufeld, and R. J. Harrison. The Thermal Evolution of Planetesimals During Accretion and Differentiation: Consequences for Dynamo Generation by Thermally-Driven Convection. *Journal of Geophysical Research: Planets*, 126(3): e2020JE006704, 2021.

M. Dumberry and A. Rivoldini. Mercury's inner core size and core-crystallization regime. *Icarus*, 248:254–268, Mar. 2015.

S. Elghobashi. On predicting particle-laden turbulent flows. *Applied Scientific Research*, 52(4): 309–329, June 1994.

S. Elghobashi and G. C. Truesdell. On the two-way interaction between homogeneous turbulence and dispersed solid particles. I: Turbulence modification. *Physics of Fluids A: Fluid Dynamics*, 5(7):1790–1801, July 1993.

P. S. Epstein and M. S. Plesset. On the Stability of Gas Bubbles in Liquid-Gas Solutions. *The Journal of Chemical Physics*, 18(11):1505–1509, July 1950.

M. P. Escudier and T. Maxworthy. On the motion of turbulent thermals. *Journal of Fluid Mechanics*, 61(3):541–552, Nov. 1973.

A. Fabregat Tomàs, A. C. Poje, T. M. Özgökmen, and W. K. Dewar. Numerical simulations of rotating bubble plumes in stratified environments. *Journal of Geophysical Research: Oceans*, 122(8):6795–6813, 2017.

F. Falkinhoff, M. Obligado, M. Bourgoin, and P. D. Mininni. Preferential Concentration of Free-Falling Heavy Particles in Turbulence. *Physical Review Letters*, 125(6):064504, Aug. 2020.

G. Falkovich, A. Fouxon, and M. G. Stepanov. Acceleration of rain initiation by cloud turbulence. *Nature*, 419(6903):151–154, Sept. 2002.

Y. Fei, C. T. Prewitt, H.-k. Mao, and C. M. Bertka. Structure and Density of FeS at High Pressure and High Temperature and the Internal Structure of Mars. *Science*, 268(5219): 1892–1894, June 1995.

Y. Fei, C. M. Bertka, and L. W. Finger. High-Pressure Iron-Sulfur Compound, Fe3S2, and Melting Relations in the Fe-FeS System. *Science*, 275(5306):1621–1623, Mar. 1997.

Y. Fei, J. Li, C. M. Bertka, and C. T. Prewitt. Structure type and bulk modulus of Fe3S, a new iron-sulfur compound. *American Mineralogist*, 85(11-12):1830–1833, Nov. 2000.

H. J. S. Fernando, R.-r. Chen, and B. A. Ayotte. Development of a point plume in the presence of background rotation. *Physics of Fluids*, 10(9):2369–2383, Sept. 1998.

R. A. Fischer, Y. Nakajima, A. J. Campbell, D. J. Frost, D. Harries, F. Langenhorst, N. Miyajima, K. Pollok, and D. C. Rubie. High pressure metal–silicate partitioning of Ni, Co, V, Cr, Si, and O. *Geochimica et Cosmochimica Acta*, 167:177–194, Oct. 2015.

D. G. Fox. Forced plume in a stratified fluid. *Journal of Geophysical Research (1896-1977)*, 75 (33):6818–6835, 1970.

D. Frank, J. R. Landel, S. B. Dalziel, and P. F. Linden. Anticyclonic precession of a plume in a rotating environment. *Geophysical Research Letters*, 44(18):9400–9407, 2017.

D. Frank, J. R. Landel, S. B. Dalziel, and P. F. Linden. Effects of background rotation on the dynamics of multiphase plumes. *Journal of Fluid Mechanics*, 915:A2, May 2021.

M. J. Friedl, C. Haertel, and T. K. Fannelop. An experimental study of starting plumes over area sources. *Il nuovo cimento C*, 22 C(6):835–846, 1999.

H. M. Fritz, F. Mohammed, and J. Yoo. Lituya Bay Landslide Impact Generated Mega-Tsunami 50th Anniversary. In P. R. Cummins, K. Satake, and L. S. L. Kong, editors, *Tsunami Science Four Years after the 2004 Indian Ocean Tsunami: Part II: Observation and Data Analysis*, pages 153–175. Birkhäuser, Basel, 2009. ISBN 978-3-0346-0064-4.

M. Gharib, E. Rambod, and K. Shariff. A universal time scale for vortex ring formation. *Journal of Fluid Mechanics*, 360:121–140, Apr. 1998.

S. Ghosh, J. Dávila, J. Hunt, A. Srdic, H. Fernando, and P. Jonas. How turbulence enhances coalescence of settling particles with applications to rain in clouds. *Proceedings of the Royal Society A: Mathematical, Physical and Engineering Sciences*, 461(2062):3059–3088, Aug. 2005.

G. H. Good, P. J. Ireland, G. P. Bewley, E. Bodenschatz, L. R. Collins, and Z. Warhaft. Settling regimes of inertial particles in isotropic turbulence. *Journal of Fluid Mechanics*, 759, Nov. 2014.

J. C. Goodman, G. C. Collins, J. Marshall, and R. T. Pierrehumbert. Hydrothermal plume dynamics on Europa: Implications for chaos formation. *Journal of Geophysical Research: Planets*, 109(E3), 2004.

S. Goto and J. C. Vassilicos. Sweep-Stick Mechanism of Heavy Particle Clustering in Fluid Turbulence. *Physical Review Letters*, 100(5):054503, Feb. 2008.

H. P. Greenspan. The theory of rotating fluids. Technical report, Massachusetts Inst of Tech Cambridge Dept of Mathematics, Sept. 1968.

É. Guazzelli and J. Hinch. Fluctuations and Instability in Sedimentation. *Annual Review of Fluid Mechanics*, 43(1):97–116, 2011.

É. Guazzelli and J. F. Morris. *A Physical Introduction to Suspension Dynamics*. Cambridge Texts in Applied Mathematics. Cambridge University Press, Cambridge, 2011. ISBN 978-0-521-19319-1.

J. M. Ham and G. M. Homsy. Hindered settling and hydrodynamic dispersion in quiescent sedimenting suspensions. *International Journal of Multiphase Flow*, 14(5):533–546, Sept. 1988.

B. C. Hancock and G. Zografi. Characteristics and significance of the amorphous state in pharmaceutical systems. *Journal of Pharmaceutical Sciences*, 86(1):1–12, 1997.

S. Harada, T. Mitsui, and K. Sato. Particle-like and fluid-like settling of a stratified suspension. *The European Physical Journal E*, 35(1):1, Jan. 2012.

F. I. Harris. The Effects of Evaporation at the Base of Ice Precipitation Layers: Theory and Radar Observations. *Journal of the Atmospheric Sciences*, 34(4):651–672, Apr. 1977.

R. Hassaini and F. Coletti. Scale-to-scale turbulence modification by small settling particles. *Journal of Fluid Mechanics*, 949:A30, Oct. 2022.

S. A. Hauck II, J. M. Aurnou, and A. J. Dombard. Sulfur's impact on core evolution and magnetic field generation on Ganymede. *Journal of Geophysical Research: Planets*, 111(E9), 2006.

B. He, M. Smith, P. Egodawatta, G. A. Ayoko, L. Rintoul, and A. Goonetilleke. Dispersal and transport of microplastics in river sediments. *Environmental Pollution*, 279:116884, June 2021.

K. R. Helfrich. Thermals with background rotation and stratification. *Journal of Fluid Mechanics*, 259:265–280, Jan. 1994.

A. J. Heymsfield and C. D. Westbrook. Advances in the Estimation of Ice Particle Fall Speeds Using Laboratory and Field Measurements. *Journal of the Atmospheric Sciences*, 67(8): 2469–2482, Aug. 2010.

K. Hirose, S. Labrosse, and J. Hernlund. Composition and State of the Core. *Annual Review of Earth and Planetary Sciences*, 41(1):657–691, 2013.

R. A. Houze Jr. *Cloud Dynamics*. Academic Press, July 2014. ISBN 978-0-08-092146-4.

L. Huguet, S. A. Hauck, J. A. Van Orman, and Z. Jing. Implications of the Homogeneous Nucleation Barrier for Top-Down Crystallization in Mercury's Core. 2047:6101, May 2018a.

L. Huguet, J. A. Van Orman, S. A. Hauck, and M. A. Willard. Earth's inner core nucleation paradox. *Earth and Planetary Science Letters*, 487:9–20, Apr. 2018b.

L. Huguet, V. Barge-Zwick, and M. Le Bars. Dynamics of a reactive spherical particle falling in a linearly stratified fluid. *Physical Review Fluids*, 5(11):114803, Nov. 2020.

G. R. Hunt and N. B. Kaye. Lazy plumes. *Journal of Fluid Mechanics*, 533:329–338, June 2005.

H. Ichikawa, S. Labrosse, and K. Kurita. Direct numerical simulation of an iron rain in the magma ocean. *Journal of Geophysical Research: Solid Earth*, 115(B1), 2010.

K. Iga and R. Kimura. Convection driven by collective buoyancy of microbubbles. *Fluid Dynamics Research*, 39(1):68–97, Jan. 2007.

C. T. Jacobs, T. J. Goldin, G. S. Collins, M. D. Piggott, S. C. Kramer, H. J. Melosh, C. R. G. Wilson, and P. A. Allison. An improved quantitative measure of the tendency for volcanic ash plumes to form in water: Implications for the deposition of marine ash beds. *Journal of Volcanology and Geothermal Research*, 290:114–124, Jan. 2015.

P. L. Kamburova and F. H. Ludlam. Rainfall evaporation in thunderstorm downdraughts. *Quarterly Journal of the Royal Meteorological Society*, 92(394):510–518, 1966.

B. B. Karki and L. P. Stixrude. Viscosity of MgSiO3 liquid at Earth's mantle conditions: Implications for an early magma ocean. *Science (New York, N.Y.)*, 328(5979):740–742, May 2010.

N. B. Kaye and G. R. Hunt. An experimental study of large area source turbulent plumes. *International Journal of Heat and Fluid Flow*, 30(6):1099–1105, Dec. 2009.

R. C. Kerr. Convective crystal dissolution. *Contributions to Mineralogy and Petrology*, 121(3): 237–246, Sept. 1995.

I. G. Kevrekidis and G. Samaey. Equation-Free Multiscale Computation: Algorithms and Applications. *Annual Review of Physical Chemistry*, 60(1):321–344, 2009.

R. Kimura. Cell formation in the convective mixed layer. *Fluid Dynamics Research*, 3(1): 395–399, Sept. 1988.

T. Kiørboe. Formation and fate of marine snow: Small-scale processes with large- scale implications. *Scientia Marina*, 65(S2):57–71, Dec. 2001.

M. G. Kivelson, K. K. Khurana, C. T. Russell, R. J. Walker, J. Warnecke, F. V. Coroniti, C. Polanskey, D. J. Southwood, and G. Schubert. Discovery of Ganymede's magnetic field by the Galileo spacecraft. *Nature*, 384(6609):537–541, Dec. 1996.

M. G. Kivelson, K. K. Khurana, and M. Volwerk. The Permanent and Inductive Magnetic Moments of Ganymede. *Icarus*, 157(2):507–522, June 2002.

T. Kleine, C. Münker, K. Mezger, and H. Palme. Rapid accretion and early core formation on asteroids and the terrestrial planets from Hf-W chronometry. *Nature*, 418(6901):952–955, Aug. 2002.

D. L. Koch. Hydrodynamic diffusion in dilute sedimenting suspensions at moderate Reynolds numbers. *Physics of Fluids A: Fluid Dynamics*, 5(5):1141–1155, May 1993.

D. L. Koch. Hydrodynamic diffusion in a suspension of sedimenting point particles with periodic boundary conditions. *Physics of Fluids*, 6(9):2894–2900, Sept. 1994.

M. Kono. 5.01 - Geomagnetism: An Introduction and Overview. In *Treatise on Geophysics (First Edition)*, volume 5. 2010.

Q. Kriaa, E. Subra, B. Favier, and M. Le Bars. Effects of particle size and background rotation on the settling of particle clouds. *Physical Review Fluids*, 7(12):124302, Dec. 2022.

E. Kruger. *Dynamics of Downdraughts and Cold Pools: An Experimental and Numerical Study*. PhD thesis, University of Cambridge, Dec. 2020.

W. Kurz and D. Fisher. *Fundamentals of Solidification*. Trans Tech Publications Ltd, Feb. 1998. ISBN 978-3-0357-3239-9.

O. L. Kuskov and V. A. Kronrod. L- and LL-Chondritic Models of the Chemical Composition of Io. *Solar System Research*, 35(3):198–208, May 2001.

S. Labrosse. Thermal evolution of the core with a high thermal conductivity. *Physics of the Earth and Planetary Interiors*, 247:36–55, Oct. 2015.

A. J. C. Ladd. Dynamical simulations of sedimenting spheres. *Physics of Fluids A: Fluid Dynamics*, 5(2):299–310, Feb. 1993.

A. C. H. Lai, B. Zhao, A. W.-K. Law, and E. E. Adams. Two-phase modeling of sediment clouds. *Environmental Fluid Mechanics*, 13(5):435–463, Oct. 2013.

A. C. H. Lai, R.-Q. Wang, A. W.-K. Law, and E. E. Adams. Modeling and experiments of polydisperse particle clouds. *Environmental Fluid Mechanics*, 16(4):875–898, Aug. 2016.

J. R. Lake. The effect of drop size and velocity on the performance of agricultural sprays. *Pesticide Science*, 8(5):515–520, Oct. 1977.

M. Landeau, R. Deguen, and P. Olson. Experiments on the fragmentation of a buoyant liquid volume in another liquid. *Journal of Fluid Mechanics*, 749:478–518, June 2014.

M. Landeau, R. Deguen, D. Phillips, J. A. Neufeld, V. Lherm, and S. B. Dalziel. Metal-silicate mixing by large Earth-forming impacts. *Earth and Planetary Science Letters*, 564:116888, June 2021.

M. Landeau, A. Fournier, H.-C. Nataf, D. Cébron, and N. Schaeffer. Sustaining Earth's magnetic dynamo. *Nature Reviews Earth & Environment*, 3(4):255–269, Apr. 2022.

J. S. Langer. Instabilities and pattern formation in crystal growth. *Reviews of Modern Physics*, 52(1):1–28, Jan. 1980.

D. Lecoanet and N. Jeevanjee. Entrainment in Resolved, Dry Thermals. *Journal of the Atmospheric Sciences*, 76(12):3785–3801, Dec. 2019.

S. Lee, Y. Jang, C. Choi, and T. Lee. Combined effect of sedimentation velocity fluctuation and self-sharpening on interface broadening. *Physics of Fluids A: Fluid Dynamics*, 4(12): 2601–2606, Dec. 1992.

J. Lemus, A. Fries, P. A. Jarvis, C. Bonadonna, B. Chopard, and J. Lätt. Modelling Settling-Driven Gravitational Instabilities at the Base of Volcanic Clouds Using the Lattice Boltzmann Method. *Frontiers in Earth Science*, 9, 2021.

V. G. Levich. *Physicochemical Hydrodynamics*. Prentice-Hall International Series in the Physical and Chemical Engineering Sciences. Prentice-Hall, Englewood Cliffs, N.J., 1962. ISBN 978-0-13-674440-5.

V. Lherm. *Thermal and chemical partitioning dynamics during the differentiation of terrestrial planets*. PhD thesis, Université de Lyon, July 2021.

V. Lherm and R. Deguen. Small-scale metal/silicate equilibration during core formation: The Influence of stretching enhanced diffusion on mixing. *Journal of Geophysical Research: Solid Earth*, 123(12):10,496–10,516, 2018.

V. Lherm, R. Deguen, T. Alboussière, and M. Landeau. Rayleigh–Taylor instability in impact cratering experiments. *Journal of Fluid Mechanics*, 937:A20, Apr. 2022.

J. Li, A. Abraham, M. Guala, and J. Hong. Evidence of preferential sweeping during snow settling in atmospheric turbulence. *Journal of Fluid Mechanics*, 928, Dec. 2021.

P. F. Linden. The Fluid Mechanics of Natural Ventilation. *Annual Review of Fluid Mechanics*, 31(1):201–238, 1999.

P. W. Linder, L. R. Nassimbeni, A. Polson, and A. L. Rodgers. The diffusion coefficient of sucrose in water. A physical chemistry experiment. *Journal of Chemical Education*, 53(5): 330, May 1976.

Y. Liu, L. Ning, and R. E. Ecke. Dynamics of surface patterning in salt-crystal dissolution. *Physical Review E*, 53(6):R5572–R5575, June 1996.

K. Lochbihler, G. Lenderink, and A. P. Siebesma. Cold pool dynamics shape the response of extreme rainfall events to climate change. *Journal of Advances in Modeling Earth Systems*, 13(2):e2020MS002306, 2021.

G. Lujanienė, S. Byčenkienė, P. P. Povinec, and M. Gera. Radionuclides from the Fukushima accident in the air over Lithuania: Measurement and modelling approaches. *Journal of Environmental Radioactivity*, 114:71–80, Dec. 2012.

C. Maas, L. Manske, K. Wünnemann, and U. Hansen. On the fate of impact-delivered metal in a terrestrial magma ocean. *Earth and Planetary Science Letters*, 554:116680, Jan. 2021.

M. Magnani, S. Musacchio, and G. Boffetta. Inertial effects in dusty Rayleigh–Taylor turbulence. *Journal of Fluid Mechanics*, 926, Nov. 2021.

J. Magnaudet and M. J. Mercier. Particles, drops, and bubbles moving across sharp interfaces and stratified layers. *Annual Review of Fluid Mechanics*, 52(1):61–91, 2020.

J. Martin, N. Rakotomalala, and D. Salin. Hydrodynamic dispersion broadening of a sedimentation front. *Physics of Fluids*, 6(10):3215–3217, Oct. 1994.

J. Mathew and A. J. Basu. Some characteristics of entrainment at a cylindrical turbulence boundary. *Physics of Fluids*, 14(7):2065–2072, July 2002.

M. R. Maxey. The gravitational settling of aerosol particles in homogeneous turbulence and random flow fields. *Journal of Fluid Mechanics*, 174:441–465, Jan. 1987.

M. R. Maxey and S. Corrsin. Gravitational settling of aerosol particles in randomly oriented cellular flow fields. *Journal of the Atmospheric Sciences*, 43(11):1112–1134, June 1986.

M. R. Maxey and J. J. Riley. Equation of motion for a small rigid sphere in a nonuniform flow. *The Physics of Fluids*, 26(4):883–889, Apr. 1983.

T. Maxworthy. The flow created by a sphere moving along the axis of a rotating, slightly-viscous fluid. *Journal of Fluid Mechanics*, 40(3):453–479, Feb. 1970.

I. M. Mazzitelli and D. Lohse. Evolution of energy in flow driven by rising bubbles. *Physical Review E*, 79(6):066317, June 2009.

C. D. McConnochie, C. Cenedese, and J. N. McElwaine. Entrainment into particle-laden turbulent plumes. *Physical Review Fluids*, 6(12):123502, Dec. 2021.

B. McKim, N. Jeevanjee, and D. Lecoanet. Buoyancy-driven entrainment in dry thermals. *Quarterly Journal of the Royal Meteorological Society*, 146(726):415–425, 2020.

H. Meheut, Z. Meliani, P. Varniere, and W. Benz. Dust-trapping Rossby vortices in protoplanetary disks. *Astronomy & Astrophysics*, 545:A134, Sept. 2012.

Y. Mezui, M. Obligado, and A. Cartellier. Buoyancy-driven bubbly flows: Scaling of velocities in bubble columns operated in the heterogeneous regime. *Journal of Fluid Mechanics*, 952: A10, Dec. 2022.

K. O. Mikaelian. Effect of viscosity on Rayleigh-Taylor and Richtmyer-Meshkov instabilities. *Physical Review E*, 47(1):375–383, Jan. 1993.

E. Minkov, M. Ungarish, and M. Israeli. The motion generated by a rising particle in a rotating fluid – numerical solutions. Part 2. The long container case. *Journal of Fluid Mechanics*, 454: 345–364, Mar. 2002.

M. Mizukami, R. N. Parthasarathy, and G. M. Faeth. Particle-generated turbulence in homogeneous dilute dispersed flows. *International Journal of Multiphase Flow*, 18(3):397–412, May 1992.

M. Moghadaripour, A. H. Azimi, and S. Elyasi. Experimental study of particle clouds in stagnant water. *Journal of Engineering Mechanics*, 143(9):04017082, Sept. 2017.

R. Monchaux and A. Dejoan. Settling velocity and preferential concentration of heavy particles under two-way coupling effects in homogeneous turbulence. *Physical Review Fluids*, 2(10): 104302, Oct. 2017.

D. W. Moore, P. G. Saffman, and K. Stewartson. The structure of free vertical shear layers in a rotating fluid and the motion produced by a slowly rising body. *Philosophical Transactions of the Royal Society of London. Series A, Mathematical and Physical Sciences*, 264(1156): 597–634, Sept. 1969.

B. R. Morton. Forced plumes. *Journal of Fluid Mechanics*, 5(1):151–163, Jan. 1959.

B. R. Morton, G. I. Taylor, and J. S. Turner. Turbulent gravitational convection from maintained and instantaneous sources. *Proceedings of the Royal Society of London. Series A. Mathematical and Physical Sciences*, 234(1196):1–23, Jan. 1956.

M. M. Mrokowska. Stratification-induced reorientation of disk settling through ambient density transition. *Scientific Reports*, 8(1):412, Jan. 2018.

R. F. Mudde. Gravity-Driven Bubbly Flows. *Annual Review of Fluid Mechanics*, 37(1):393–423, 2005.

C. Muller, D. Yang, G. Craig, T. Cronin, B. Fildier, J. O. Haerter, C. Hohenegger, B. Mapes, D. Randall, S. Shamekh, and S. C. Sherwood. Spontaneous aggregation of convective storms. *Annual Review of Fluid Mechanics*, 54(1):133–157, 2022.

Y. Murai and Y. Matsumoto. Numerical analysis of detailed flow structures of a bubble plume. *JSME International Journal Series B*, 41(3):568–574, 1998.

M. Nakajima, G. J. Golabek, K. Wünnemann, D. C. Rubie, C. Burger, H. J. Melosh, S. A. Jacobson, L. Manske, and S. D. Hull. Scaling laws for the geometry of an impact-induced magma ocean. *Earth and Planetary Science Letters*, 568:116983, Aug. 2021.

K. Nakamura, H. N. Yoshikawa, Y. Tasaka, and Y. Murai. Linear stability analysis of bubble-induced convection in a horizontal liquid layer. *Physical Review E*, 102(5):053102, Nov. 2020.

S. Nasab and P. Garaud. Preferential concentration by mechanically driven turbulence in the two-fluid formalism. *Physical Review Fluids*, 6(10):104303, Oct. 2021.

F. Necker, C. Härtel, L. Kleiser, and E. Meiburg. High-resolution simulations of particle-driven gravity currents. *International Journal of Multiphase Flow*, 28(2):279–300, Feb. 2002.

J. A. Neufeld, J. F. J. Bryson, and F. Nimmo. The top-down solidification of iron asteroids driving dynamo evolution. *Journal of Geophysical Research: Planets*, 124(5):1331–1356, 2019.

H. Nicolai and E. Guazzelli. Effect of the vessel size on the hydrodynamic diffusion of sedimenting spheres. *Physics of Fluids*, 7(1):3–5, Jan. 1995.

P. Nielsen. Turbulence effects on the settling of suspended particles. *Journal of Sedimentary Research*, 63(5):835–838, Sept. 1993.

V. V. Nikulin. Analytical model of motion of turbulent vortex rings in an incompressible fluid. *Journal of Applied Mechanics and Technical Physics*, 55(4):558–564, July 2014.

J. M. Nitsche and G. K. Batchelor. Break-up of a falling drop containing dispersed particles. *Journal of Fluid Mechanics*, 340:161–175, June 1997.

P. Odier, J. Chen, and R. E. Ecke. Understanding and modeling turbulent fluxes and entrainment in a gravity current. *Physica D: Nonlinear Phenomena*, 241(3):260–268, Feb. 2012.

P. Olson. 8.01 - Core Dynamics: An Introduction and Overview. In G. Schubert, editor, *Treatise on Geophysics (Second Edition)*, pages 1–25. Elsevier, Oxford, Jan. 2015. ISBN 978-0-444-53803-1.

P. Olson, M. Landeau, and B. H. Hirsh. Laboratory experiments on rain-driven convection: Implications for planetary dynamos. *Earth and Planetary Science Letters*, 457:403–411, Jan. 2017.

N. Otsu. A threshold selection method from gray-level histograms. *IEEE Transactions on Systems, Man, and Cybernetics*, 9(1):62–66, Jan. 1979.

R. Ouillon, E. Meiburg, and B. R. Sutherland. Turbidity currents propagating down a slope into a stratified saline ambient fluid. *Environmental Fluid Mechanics*, 19(5):1143–1166, Oct. 2019.

R. Pal, S. Sarkar, and A. Mukhopadhyay. Influence of ambient conditions on evaporation and transport of respiratory droplets in indoor environment. *International Communications in Heat and Mass Transfer*, 129:105750, Dec. 2021.

C. Patterson, G. Tilton, and M. Inghram. Age of the Earth. *Science*, 121(3134):69–75, Jan. 1955.

R. Paugam, M. Wooster, S. Freitas, and M. Val Martin. A review of approaches to estimate wildfire plume injection height within large-scale atmospheric chemical transport models. *Atmospheric Chemistry and Physics*, 16(2):907–925, Jan. 2016.

S. S. Pegler and M. S. D. Wykes. Shaping of melting and dissolving solids under natural convection. *Journal of Fluid Mechanics*, 900:A35, Oct. 2020.

P. Peñas, O. R. Enríquez, and J. Rodríguez-Rodríguez. Bubble-laden thermals in supersaturated water. *Journal of Fluid Mechanics*, 924, Oct. 2021.

J. Philippi, M. Berhanu, J. Derr, and S. Courrech du Pont. Solutal convection induced by dissolution. *Physical Review Fluids*, 4(10):103801, Oct. 2019.

F. Pignatel, M. Nicolas, and É. Guazzelli. A falling cloud of particles at a small but finite Reynolds number. *Journal of Fluid Mechanics*, 671:34–51, Mar. 2011.

M. S. Plesset and C. G. Whipple. Viscous effects in Rayleigh-Taylor instability. *The Physics of Fluids*, 17(1):1–7, Jan. 1974.

S. Popinet. An accurate adaptive solver for surface-tension-driven interfacial flows. *Journal of Computational Physics*, 228(16):5838–5866, Sept. 2009.

T. S. Pottebaum and M. Gharib. The pinch-off process in a starting buoyant plume. *Experiments in Fluids*, 37(1):87–94, July 2004.

M. Pozzo, C. Davies, D. Gubbins, and D. Alfè. Thermal and electrical conductivity of solid iron and iron–silicon mixtures at Earth's core conditions. *Earth and Planetary Science Letters*, 393:159–164, May 2014.

J. C. Prairie, K. Ziervogel, R. Camassa, R. M. McLaughlin, B. L. White, C. Dewald, and C. Arnosti. Delayed settling of marine snow: Effects of density gradient and particle properties and implications for carbon cycling. *Marine Chemistry*, 175:28–38, Oct. 2015.

H. C. Price, J. Mattsson, and B. J. Murray. Sucrose diffusion in aqueous solution. *Physical Chemistry Chemical Physics*, 18(28):19207–19216, July 2016.

C. H. B. Priestley and F. K. Ball. Continuous convection from an isolated source of heat. *Quarterly Journal of the Royal Meteorological Society*, 81(348):144–157, 1955.

B. Qaddah, J. Monteux, V. Clesi, M. A. Bouhifd, and M. Le Bars. Dynamics and stability of an iron drop falling in a magma ocean. *Physics of the Earth and Planetary Interiors*, 289: 75–89, Apr. 2019.

H. Rahimipour and D. Wilkinson. Dynamic behaviour of particle clouds. In *11th Australasian Fluid Mechanics Conference University of Tasmania, Hobart, Australia*, 1992.

W. E. Ranz and W. R. Marshall. Evaporation from drops: Part 1. *Chemical Engineering Progress*, 48(3):141–146, 1952.

J. F. Reali, P. Garaud, A. Alsinan, and E. Meiburg. Layer formation in sedimentary fingering convection. *Journal of Fluid Mechanics*, 816:268–305, Apr. 2017.

D. W. Rees Jones and A. J. Wells. Frazil-ice growth rate and dynamics in mixed layers and sub-ice-shelf plumes. *The Cryosphere*, 12(1):25–38, Jan. 2018.

A. Rivoldini, T. Van Hoolst, O. Verhoeven, A. Mocquet, and V. Dehant. Geodesy constraints on the interior structure and composition of Mars. *Icarus*, 213(2):451–472, June 2011.

C. Robert and R. Bousquet. *Géosciences. La dynamique du système Terre*. Belin edition, Sept. 2013. ISBN 978-2-7011-3816-9.

D. C. Rubie, H. J. Melosh, J. E. Reid, C. Liebske, and K. Righter. Mechanisms of metal–silicate equilibration in the terrestrial magma ocean. *Earth and Planetary Science Letters*, 205(3): 239–255, Jan. 2003.

D. C. Rubie, S. A. Jacobson, A. Morbidelli, D. P. O'Brien, E. D. Young, J. de Vries, F. Nimmo, H. Palme, and D. J. Frost. Accretion and differentiation of the terrestrial planets with implications for the compositions of early-formed Solar System bodies and accretion of water. *Icarus*, 248:89–108, Mar. 2015.

T. Rückriemen, D. Breuer, and T. Spohn. The Fe snow regime in Ganymede's core: A deep-seated dynamo below a stable snow zone. *Journal of Geophysical Research: Planets*, 120(6): 1095–1118, 2015.

T. Rückriemen, D. Breuer, and T. Spohn. Top-down freezing in a Fe–FeS core and Ganymede's present-day magnetic field. *Icarus*, 307:172–196, June 2018.

J. F. Rudge, T. Kleine, and B. Bourdon. Broad bounds on Earth's accretion and core formation constrained by geochemical models. *Nature Geoscience*, 3(6):439–443, June 2010.

G. J. Ruggaber. *Dynamics of Sediment Clouds Related to Open-Water Sediment Disposal*. PhD thesis, MIT, June 2000.

J. P. L. C. Salazar, J. D. Jong, L. Cao, S. H. Woodward, H. Meng, and L. R. Collins. Experimental and numerical investigation of inertial particle clustering in isotropic turbulence. *Journal of Fluid Mechanics*, 600:245–256, Apr. 2008.

H. Samuel. A re-evaluation of metal diapir breakup and equilibration in terrestrial magma oceans. *Earth and Planetary Science Letters*, 313–314:105–114, Jan. 2012.

G. Schubert, D. J. Stevenson, and K. Ellsworth. Internal structures of the Galilean satellites. *Icarus*, 47(1):46–59, July 1981.

G. Schubert, K. Zhang, M. G. Kivelson, and J. D. Anderson. The magnetic field and internal structure of Ganymede. *Nature*, 384(6609):544–545, Dec. 1996.

G. Schubert, J. Anderson, T. Spohn, and W. McKinnon. Interior composition, structure and dynamics of the Galilean satellites. 2004.

R. S. Scorer. Experiments on convection of isolated masses of buoyant fluid. *Journal of Fluid Mechanics*, 2(6):583–594, Aug. 1957.

H. P. Scott, Q. Williams, and F. J. Ryerson. Experimental constraints on the chemical evolution of large icy satellites. *Earth and Planetary Science Letters*, 203(1):399–412, Oct. 2002.

M. Z. Sheikh, K. Gustavsson, D. Lopez, E. Lévêque, B. Mehlig, A. Pumir, and A. Naso. Importance of fluid inertia for the orientation of spheroids settling in turbulent flow. *Journal of Fluid Mechanics*, 886:A9, Mar. 2020.

V. A. Sheremet. Laboratory experiments with tilted convective plumes on a centrifuge: A finite angle between the buoyancy force and the axis of rotation. *Journal of Fluid Mechanics*, 506: 217–244, May 2004.

J. Siebert, J. Badro, D. Antonangeli, and F. J. Ryerson. Metal–silicate partitioning of Ni and Co in a deep magma ocean. *Earth and Planetary Science Letters*, 321–322:189–197, Mar. 2012.

F. Sohl, T. Spohn, D. Breuer, and K. Nagel. Implications from Galileo Observations on the Interior Structure and Chemistry of the Galilean Satellites. *Icarus*, 157(1):104–119, May 2002.

M. Spada, O. Jorba, C. Pérez García-Pando, Z. Janjic, and J. M. Baldasano. Modeling and evaluation of the global sea-salt aerosol distribution: Sensitivity to size-resolved and sea-surface temperature dependent emission schemes. *Atmospheric Chemistry and Physics*, 13 (23):11735–11755, Dec. 2013.

R. C. Srivastava. A simple model of evaporatively driven downdraft: Application to microburst downdraft. *Journal of the Atmospheric Sciences*, 42(10):1004–1023, May 1985.

R. C. Srivastava. A model of intense downdrafts driven by the melting and evaporation of precipitation. *Journal of the Atmospheric Sciences*, 44(13):1752–1774, July 1987.

K. Stewartson. On the slow motion of a sphere along the axis of a rotating fluid. *Mathematical Proceedings of the Cambridge Philosophical Society*, 48(1):168–177, Jan. 1952.

B. Stiehl, R. Shrestha, S. Schroeder, J. Delgado, A. Bazzi, J. Reyes, M. Kinzel, and K. Ahmed. The effect of relative air humidity on the evaporation timescales of a human sneeze. *AIP Advances*, 12(7):075210, July 2022.

G. Subramanian and D. L. Koch. Evolution of clusters of sedimenting low-Reynolds-number particles with Oseen interactions. *Journal of Fluid Mechanics*, 603:63–100, May 2008.

B. R. Sutherland, Y. Ma, M. R. Flynn, D. Frank, P. F. Linden, D. Lemasquerier, M. Le Bars, C. Pacary, T. Jamin, T. Dauxois, and S. Joubaud. Plumes in rotating fluid and their transformation into tornados. *Journal of Fluid Mechanics*, 924, Oct. 2021.

J. J. Tao, X. T. He, W. H. Ye, and F. H. Busse. Nonlinear Rayleigh-Taylor instability of rotating inviscid fluids. *Physical Review E*, 87(1):013001, Jan. 2013.

G. I. Taylor. The motion of a sphere in a rotating liquid. *Proceedings of the Royal Society of London. Series A, Containing Papers of a Mathematical and Physical Character*, 102(715): 180–189, Nov. 1922.

G. R. Taylor and M. B. Baker. Entrainment and detrainment in cumulus clouds. *Journal of the Atmospheric Sciences*, 48(1):112–121, Jan. 1991.

L. Thompson, M. Smith, J. Thomson, S. Stammerjohn, S. Ackley, and B. Loose. Frazil ice growth and production during katabatic wind events in the Ross Sea, Antarctica. *The Cryosphere*, 14(10):3329–3347, Oct. 2020.

A. M. Tompkins. Organization of tropical convection in low vertical wind shears: The role of cold pools. *Journal of the Atmospheric Sciences*, 58(13):1650–1672, July 2001.

Z.-X. Tong, Y.-L. He, and W.-Q. Tao. A review of current progress in multiscale simulations for fluid flow and heat transfer problems: The frameworks, coupling techniques and future perspectives. *International Journal of Heat and Mass Transfer*, 137:1263–1289, July 2019.

W. B. Tonks and H. J. Melosh. Magma ocean formation due to giant impacts. *Journal of Geophysical Research: Planets*, 98(E3):5319–5333, 1993.

F. Toschi and E. Bodenschatz. Lagrangian properties of particles in turbulence. *Annual Review of Fluid Mechanics*, 41(1):375–404, 2009.

J. Touma and J. Wisdom. Evolution of the Earth-Moon system. *The Astronomical Journal*, 108:1943, Nov. 1994.

A. Townsend. LXXXI. The eddy viscosity in turbulent shear flow. *The London, Edinburgh, and Dublin Philosophical Magazine and Journal of Science*, 41(320):890–906, Sept. 1950.

Y. Tsuji, Y. Morikawa, and K. Terashima. Fluid-dynamic interaction between two spheres. *International Journal of Multiphase Flow*, 8(1):71–82, Feb. 1982.

D. L. Turcotte and G. Schubert. *Geodynamics*. Cambridge University Press, Mar. 2002. ISBN 978-0-521-66624-4.

J. S. Turner. The 'starting plume' in neutral surroundings. *Journal of Fluid Mechanics*, 13(3): 356–368, July 1962.

J. S. Turner. Turbulent entrainment: The development of the entrainment assumption, and its application to geophysical flows. *Journal of Fluid Mechanics*, 173:431–471, Dec. 1986.

J. S. Turner and G. I. Taylor. Buoyant vortex rings. *Proceedings of the Royal Society of London. Series A. Mathematical and Physical Sciences*, 239(1216):61–75, Jan. 1957.

M. Ulvrová, N. Coltice, Y. Ricard, S. Labrosse, F. Dubuffet, J. Velímský, and O. Šrámek. Compositional and thermal equilibration of particles, drops, and diapirs in geophysical flows. *Geochemistry, Geophysics, Geosystems*, 12(10), 2011.

M. van Reeuwijk and J. Craske. Energy-consistent entrainment relations for jets and plumes. *Journal of Fluid Mechanics*, 782:333–355, Nov. 2015.

M. van Reeuwijk, P. Salizzoni, G. R. Hunt, and J. Craske. Turbulent transport and entrainment in jets and plumes: A DNS study. *Physical Review Fluids*, 1(7):074301, Nov. 2016.

D. Vedensky and M. Ungarish. The motion generated by a slowly rising disk in an unbounded rotating fluid for arbitrary Taylor number. *Journal of Fluid Mechanics*, 262:1–26, Oct. 1994.

F. Veron. Ocean Spray. *Annual Review of Fluid Mechanics*, 47(1):507–538, 2015.

G. A. Voth and A. Soldati. Anisotropic particles in turbulence. *Annual Review of Fluid Mechanics*, 49(1):249–276, 2017.

J.-B. Wacheul and M. Le Bars. Experiments on fragmentation and thermo-chemical exchanges during planetary core formation. *Physics of the Earth and Planetary Interiors*, 276:134–144, Mar. 2018.

J. Wade and B. J. Wood. Core formation and the oxidation state of the Earth. *Earth and Planetary Science Letters*, 236(1):78–95, July 2005.

H. Wang and A. W.-K. Law. Second-order integral model for a round turbulent buoyant jet. *Journal of Fluid Mechanics*, 459:397–428, May 2002.

L.-P. Wang and M. R. Maxey. Settling velocity and concentration distribution of heavy particles in homogeneous isotropic turbulence. *Journal of Fluid Mechanics*, 256:27–68, Nov. 1993.

R.-Q. Wang, A. W.-K. Law, and E. E. Adams. Large-Eddy Simulation (LES) of settling particle cloud dynamics. *International Journal of Multiphase Flow*, 67:65–75, Dec. 2014.

J.-Z. Xue, E. Herbolzheimer, M. A. Rutgers, W. B. Russel, and P. M. Chaikin. Diffusion, dispersion, and settling of hard spheres. *Physical Review Letters*, 69(11):1715–1718, Sept. 1992.

Y. Yamamoto, F. Hisataka, and S. Harada. Numerical simulation of concentration interface in stratified suspension: Continuum–particle transition. *International Journal of Multiphase Flow*, 73:71–79, July 2015.

J.-I. Yano. Basic convective element: Bubble or plume? A historical review. *Atmospheric Chemistry and Physics*, 14(13):7019–7030, July 2014.

H. Yoshimoto and S. Goto. Self-similar clustering of inertial particles in homogeneous turbulence. *Journal of Fluid Mechanics*, 577:275–286, Apr. 2007.

X. Zhan and G. Schubert. Powering Ganymede's dynamo. *Journal of Geophysical Research: Planets*, 117(E8), 2012.

Y. Zhang and Z. Xu. Kinetics of convective crystal dissolution and melting, with applications to methane hydrate dissolution and dissociation in seawater. *Earth and Planetary Science Letters*, 213(1):133–148, Aug. 2003.

B. Zhao, A. W. K. Law, A. C. H. Lai, and E. E. Adams. On the internal vorticity and density structures of miscible thermals. *Journal of Fluid Mechanics*, 722:R5, May 2013.

B. Zhao, A. W. K. Law, E. E. Adams, and J. W. Er. Formation of particle clouds. *Journal of Fluid Mechanics*, 746:193–213, May 2014.

P. Zuidema, G. Torri, C. Muller, and A. Chandra. A survey of precipitation-Induced atmospheric cold pools over oceans and their interactions with the larger-scale environment. *Surveys in Geophysics*, 38(6):1283–1305, Nov. 2017.

T. Zürner, C. Toupoint, D. De Souza, D. Mezouane, and R. Monchaux. Settling of localized particle plumes in a quiescent water tank. *Physical Review Fluids*, 8(2):024301, Feb. 2023.